

MECHANOBIOLOGICAL REGULATION OF ATRIOVENTRICULAR
VALVE MORPHOGENESIS

A Dissertation

Presented to the Faculty of the Graduate School

of Cornell University

In Partial Fulfillment of the Requirements for the Degree of

Doctor of Philosophy

by

David Matthew Bassen

December 2019

© 2019 David Matthew Bassen

ALL RIGHTS RESERVED

MECHANOBIOLOGICAL REGULATION OF ATRIOVENTRICULAR VALVE MORPHOGENESIS

David Matthew Bassen, Ph. D.

Cornell University 2019

Around 1% of live births have a congenital heart defect (CHD), a majority of which include defects in the structure and function of heart valves [1]. Pediatric patients face years of surgical interventions and treatments because current replacement valves cannot grow with the heart throughout postnatal development [2]. Genetic causes for CHDs are insufficient to explain the prevalence, variety and concurrent combinations of these defects [3]. Heart valve development progresses in a tightly controlled, time dependent manner, in an intensifying hemodynamic environment. The fact that hemodynamic forces, including flow induced deformations and shear stresses, affect valve development has been well established. Yet, little is still known on how hemodynamic stresses interact with prescribed ligand signaling programs to orchestrate cellular activities that bring about valve morphogenesis. The objective of this thesis was to elucidate the influence of mechanical stress on the biology of valve embryonic cells to determine how mechanical stimuli regulate normal development and act as epigenetic causes of congenital disease. Using an osmotic stress method novel to valve developmental studies, we have identified unique roles

for tensile and compressive stresses in directing valve remodeling and sizing through changes in proliferation and cell contractility. Using *in silico* systems biology methods and *in vitro* bioreactor data, this work also elucidated on the roles of shear stress on regulating endothelial to mesenchymal transition in valve development. Additionally, this work contributed to the understanding of epithelial to mesenchymal driven metastasis by uncovering the signaling by which cells make decisions and acquire a collective, migratory phenotype. Overall, it is hoped that the findings and tool development set forth in this work will contribute to improving clinical outcomes for patients with congenital defects and in need of regenerative tissue engineered solutions.

BIOGRAPHICAL SKETCH

David Matthew Bassen graduated summa cum laude in 2013 from The State University of New York at Binghamton with a B.S. in Bioengineering. During his undergraduate studies, David received the Barry M. Goldwater Scholarship, a national award for excellence in undergraduate research and academic achievement. David started his undergraduate studies during his senior year of high school at Dutchess Community College where he was awarded two A.S. degrees in 2011. He was especially motivated by his tutoring experiences at the DCC Math Center to continue teaching and mentoring during his undergraduate and graduate work. David spent two summers at the Wadsworth Center, a research institution part of the NYS Department of Health, modeling amino-acid interactions within proteins called inteins and unique macromolecular structures of microtubules.

During his Ph.D. work at Cornell, David was awarded the National Science Foundation Graduate Research Fellowship, the Graduate Assistance in Areas of National Need Teaching Fellowship, and a National Science Foundation INTERN grant in support of his internship at Applied BioMath LLC. David has mentored multiple undergraduate and graduate students, assisted annually with the review of NSF GRFP applications, and worked as an English as a Second Language tutor for rural farmworkers around the Finger Lakes region. His research focused on how mechanical forces orchestrate molecular signaling during heart valve embryogenesis.

Dedicated to my lifelong friends and family

ACKNOWLEDGMENTS

First, I would like to acknowledge my mother Denise who has been supportive every step of the way in my education and has always challenged me to overcome my greatest obstacles. I would also like to thank my cousin Judy and her husband Eric for their wholehearted support of my doctoral progress and career development.

I would like to thank my labmates: Dan Cheung, Leah Pagnozzi, Terence Gee, Duc Pham, Ablajan Mahmut, Guy Scuderi, Chelsea Stephens, Chelsea Gregg, Russ Gould, Stephanie Lindsey, Kalay Seranthian and many others in the Varner lab for their comradery, friendship, training, and assistance over the years. I would like to give a special thanks to Duc Pham for his support and efforts during the second half of my thesis.

I thank my undergraduate students, Rishabh Singh, Hyunji Koo, Rashmi Rao, and Lina Yu for their contributions, and determination to undertake technically difficult projects. I hope they gained as much from my mentorship as I gained from mentoring them. I thank Rishabh and Rashmi specifically for help with Chapter 2.

I thank my undergraduate research mentors, Nilesh Banavali, Gretchen Mahler, and Walker Land who each gave me the best start possible to a scientific career and who each taught me, by example, what it takes to be an excellent mentor.

I would like to thank my mentors and colleagues, especially Fei Hua, Josh Apgar, and Jim Schaff, at Applied BioMath for helping me to take my first steps to a successful modeling career.

Thank you to my advisors Jonathan Butcher and Jeff Varner for standing by me, challenging me and giving me a path to succeed in my career. Jonathan and Jeff originally drew me to Cornell with their commitment to pushing the boundaries of computational tools in biology and their ambitious mindsets. I would like to thank my committee members Ben Cosgrove and Jan Lammerding, for their advice, patience and commitment to my career development.

Above all, I thank my wonderful partner Evie for her support, insights and for being at my side through the most difficult times.

Finally, I would like to acknowledge funding sources that have supported my work and stipend. The National Science Foundation made a profound impact on my Ph.D. life and career through their Graduate Research Fellowship and INTERN grant programs. The National Institutes of Health funded my research projects through grants to the Butcher Lab.

TABLE OF CONTENTS

BIOGRAPHICAL SKETCH.....	III
ACKNOWLEDGMENTS.....	V
TABLE OF CONTENTS	VII
LIST OF FIGURES.....	XI
LIST OF TABLES.....	XIII
LIST OF ABBREVIATIONS.....	XIV
CHAPTER 1. INTRODUCTION.....	16
1.1 CLINICAL SIGNIFICANCE OF CONGENITAL HEART DEFECTS	17
1.2 HEART VALVE MORPHOGENESIS	18
1.2.1 Rationale for the study of atrio-ventricular valves	20
1.2.2 Avian animal model	21
1.2.3 Canonical TGF β signaling.....	21
1.2.4 VEGF signaling	22
1.2.5 Other implicated pathways	23
1.3 HEMODYNAMICS DURING VALVE DEVELOPMENT	24
1.4 MECHANICAL SIGNALING PATHWAYS IN VALVE DEVELOPMENT	28
1.4.1 RhoGTPase signaling	28
1.4.2 Non-canonical TGF β signaling	31
1.4.3 Wnt and β -catenin signaling	32
1.4.4 Notch signaling.....	32
1.5 UNCOVERING THE MECHANOBIOLOGY BEHIND HEART VALVE DEFECTS	33
1.5.1 Role of pressure and tensile forces in directing tissue growth	33
1.6 PATHWAYS IMPLICATED IN CONGENITAL DEFECTS OF THE MITRAL VALVE	37
1.7 OBJECTIVES OF THIS WORK	39
1.8 REFERENCES.....	41
CHAPTER 2. COMPRESSIVE STRESS INDUCES BMP SIGNALING IN COOPERATION WITH MEK-ERK TO DRIVE GROWTH OF THE ATRIOVENTRICULAR VALVE	52
2.1 SUMMARY	53
2.2 INTRODUCTION	54
2.3 METHODS	57
2.3.1 Avian animal model	57
2.3.2 AV cushion isolation and hanging drop culture	57
2.3.3 Cushion compaction measurement.....	57
2.3.4 Media and application of osmotic stress	57
2.3.5 Cytokines and inhibitors.....	59
2.3.6 Left atrial ligation	60
2.3.7 Immunofluorescence/immunohistochemistry	60
2.3.8 Live Imaging	61
2.3.9 Stain localization analysis	61
2.4 RESULTS.....	63

2.4.1	Osmotic pressure controls compaction phenotype in vitro	63
2.5	67
2.5.1	Osmotic stress compaction phenotype is TGF β independent.....	68
2.5.2	NM-myosin-II drives compaction phenotype	72
2.5.3	Altered mechanical loading in vivo shows upregulation of BMP signaling	75
2.5.4	Spatial localization of Smad15, ERK, and Myosin activity	76
2.5.5	Stage independence of osmotic stress and role of matrix in tissue shaping and stiffness.....	79
2.6	DISCUSSION.....	81
2.7	ACKNOWLEDGEMENTS	89
2.8	REFERENCES.....	90
CHAPTER 3. POPULATION HETEROGENEITY IN THE EPITHELIAL TO MESENCHYMAL TRANSITION IS CONTROLLED BY NFAT AND PHOSPHORYLATED SP1		95
3.1	SUMMARY	96
3.2	ABSTRACT	97
3.3	INTRODUCTION	98
3.4	RESULTS.....	102
3.4.1	The model population captured key features of TGF- β induced EMT 102	
3.4.2	TGF- β 1/2 and VEGF-A exposure promotes phenotype heterogeneity through NFATc and phosphorylated Sp1	108
3.4.3	Identification of a novel LEF-1 regulator.....	110
3.4.4	Combined TGF- β 2 and VEGF-A exposure drives heterogeneity in MCF10A and DLD1 cells	113
3.4.5	Ductal branching during acini formation is dependent upon phenotype heterogeneity in MCF10A and DLD1 cells.....	117
3.5	DISCUSSION.....	121
3.6	MATERIALS AND METHODS.....	129
3.6.1	Signaling network connectivity	129
3.6.2	Formulation, solution and analysis of the EMT model equations.....	131
3.6.3	Cell culture and experimental interrogation	138
3.7	REFERENCES.....	143
CHAPTER 4. JUPOETS: A CONSTRAINED MULTIOBJECTIVE OPTIMIZATION APPROACH TO ESTIMATE BIOCHEMICAL MODEL ENSEMBLES IN THE JULIA PROGRAMMING LANGUAGE		152
4.1	SUMMARY	153
4.2	ABSTRACT	154
4.2.1	Background.....	154
4.2.2	Results	154
4.2.3	Conclusions	155
4.3	BACKGROUND	155
4.4	IMPLEMENTATION.....	157
4.4.1	JuPOETs optimization problem formulation.....	159

4.5	RESULTS AND DISCUSSION.....	166
4.6	CONCLUSIONS	175
4.7	AVAILABILITY AND REQUIREMENTS	176
4.8	REFERENCES.....	177
CHAPTER 5. SHEAR STRESS REGULATION OF ENDOTHELIAL TO		
MESENCHYMAL TRANSITION IN THE DEVELOPING		
ATRIOVENTRICULAR VALVE		
		181
5.1	SUMMARY	182
5.2	INTRODUCTION	184
5.3	METHODS	186
5.3.1	Model identification	186
5.3.2	Modeling Approach.....	187
5.3.3	Experimental methods	190
5.4	RESULTS.....	191
5.5	DISCUSSION.....	197
5.6	REFERENCES.....	203
CHAPTER 6. CONCLUSIONS AND FUTURE DIRECTIONS.....		
		209
6.1	CONCLUSIONS	210
6.2	FUTURE DIRECTIONS	215
6.2.1	Using osmotic stress in concert with shear flow	215
6.2.2	Adaptation of hanging drop system to study AV septation	216
6.2.3	Spatial Mechanical testing of <i>in situ</i> sample	216
6.2.4	Spatial modeling of valve development at the cellular level.....	217
6.2.5	Understanding the roles of multiple pathways in shear stress signaling	
	219	
6.3	REFERENCES.....	220
APPENDIX A. METHOD FOR MEASURING TISSUE DEPTH USING		
BRIGHTFIELD MICROSCOPY AND APPLICATION TO LIVE		
EMBRYONIC VALVE CUSHIONS.....		
		222
APPENDIX B. COMPUTATIONAL MODELING TO ADVANCE		
PHARMACEUTICAL DEVELOPMENT IN THE AREA OF IMMUNO-		
ONCOLOGY		
		228
APPENDIX C. MECHANICAL TESTING WITH MICROPIPETTE		
ASPIRATION: A BRIDGE TO COLLABORATIONS.....		
		230
C.1	SUMMARY	230
C.2	STIFFNESS RESPONSE FOR COMPARISON OF MOUSE AND HUMAN LYMPH	
	NODES: COLLABORATION WITH FNU APOORVA (ANKUR SINGH LAB).	231
C.3	COLLABORATION WITH DAN LUO'S GROUP (YUDI PARDO, DNA META	
	GELS)	232
C.4	UNCOVERING THE SIDE SPECIFIC MECHANOSENSITIVITY OF CXCR4:	
	COLLABORATION WITHIN THE BUTCHER LAB (DUC PHAM, OFT CXCR4 PROJECT)	
	233
C.5	REFERENCES.....	234
APPENDIX D. AUTOMATION OF DATA ACQUISITION FROM BASIC		
MICROSCOPY		
		235

D.1	SUMMARY	235
D.2	NEEDS IDENTIFICATION	235
D.3	CUSHION IMAGING EXPERIMENTAL MANAGER.....	236
D.4	MICRO-PIPETTE ASPIRATION EXPERIMENT MANAGER	237
D.5	THE SOFTWARE	238
D.6	CONCLUSION	238
APPENDIX E. CODE FOR ANALYSIS AND APPLICATIONS.....		239
E.1	FIJI ANALYSIS CODE FOR IF QUANTIFICATION OF IMAGE STACKS	239
E.1.1	Main Python-FIJI analysis script.....	239
E.1.2	Analysis code for experiment including auto threshold search.....	245
E.1.3	R Analysis for IF quantification of image stacks	249
E.2	R SPATIAL LOCALIZATION ANALYSIS CODE.....	252
E.2.1	Single sample spatial analysis	252
E.2.2	Experimental spatial analysis	255
E.2.3	Localization analysis for single experiment	257
E.3	ADDITIONAL MODEL CODE FOR SHEAR STRESS MODEL	259
E.3.1	Shear transfer functions	259
E.3.2	Model signal integration logic modifications.....	260
E.3.3	Modify control logic (using above logic flat file as input).....	261
E.4	MICROSCOPE CONTROLLER CLASS.....	266
E.5	GET Z-STACK CODE (USED IN APPENDIX A).....	277
APPENDIX F. RELEVANT PROTOCOLS.....		280
F.1	OSMOTIC MEDIA	280
F.2	3D IMMUNO-FLUORESCENCE OF AV OR OFT CUSHIONS	281
F.2.1	Whole Mount Staining of Embryonic Cushions or Cell Spheroids ...	281
F.3	STAINING PROTOCOL FOR COLLAGEN GEL EMBRYONIC PATCHES / SHEAR BIOREACTOR	284
F.3.1	Staining of embryonic patches in shear reactor.....	284
F.4	USE OF ZEISS STEREOSCOPE.....	287
APPENDIX G. SUPPLEMENT FOR CHAPTER 3.....		291
G.1	SUPPLEMENTAL MATERIALS AND METHODS.....	291

LIST OF FIGURES

Figure 1.1. Cross section of the developing chick atrio-ventricular canal.	20
Figure 1.2. Hemodynamic patterning at mid-stage development during a single cardiac cycle.	27
Figure 1.3. Hemodynamic patterning at late-stage development during a single cardiac cycle.	27
Figure 1.4. Flow mechanics can reinforce the developmental program or propagate defects.	28
Figure 1.5. Osmotic stress and its mechanical effects on cells. Black arrows refer to the net-forces being exerted on the cell.....	35
Figure 2.1. Osmotic stress regulates tissue compaction.	64
Figure 2.2. Osmotic stress regulates tissue growth	66
Figure 2.3. Proliferation and apoptosis largely similar during compaction phase	67
Figure 2.4. Osmotic stress does not alter tissue stiffness	68
Figure 2.5. Osmotic stress compaction phenotype is pSmad2/3 independent	69
Figure 2.6. Compressive stress regulates tissue compaction through BMP signaling .	71
Figure 2.7. Compressive stress regulates tissue compaction through BMP signaling .	73
Figure 2.8. BMP and compressive stress decrease NM-myosin-II activation	74
Figure 2.9. Osmotic stress affects endothelial RhoA-GTP patterning not activity	75
Figure 2.10. Increased pressure loading by left atrial ligation upregulates pSmad15 in association with hyperplastic valves	76
Figure 2.11. pSmad15 spatial quantification	77
Figure 2.12. pERK spatial quantification	78
Figure 2.13. pSER-19 spatial quantification	78
Figure 2.14. Osmotic stress acts to regulate tissue compaction across stages of valve maturation in collaboration with matrix scaffolding.....	80
Figure 2.15. Proposed pathways for osmotic stress regulation of valve morphogenesis	86
Figure 3.1. Model connectivity recreates the core architecture during EMT.....	104

Figure 3.2. Training and validation simulations. The population of EMT models qualitatively captured TGF- β -induced EMT signaling.	107
Figure 3.3. Simulated VEGF-A and TGF- β 1/2 exposure promoted phenotype heterogeneity.	112
Figure 3.4. Analysis of underlying signaling responses.	114
Figure 3.5. Simultaneous TGF- β 1/2 and VEGF-A treatment induced phenotype heterogeneity and is dependent upon NFAT activity <i>in-vitro</i>	116
Figure 3.6. Ductal branching is dependent upon phenotype heterogeneity within MCF10A in 3-D culture.	120
Figure 4.1. Schematic of multiobjective parameter mapping.	159
Figure 4.2. The performance of JuPOETs on the multi-objective test suite.	167
Figure 4.3. Representative JuPOETs performance comparison between JuPOETs and POETs in Octave for problems in the multi-objective test suite.	169
Figure 4.4. Proof of concept biochemical network study.	170
Figure 4.5. Experiment to experiment variation captured by the ensemble.	174
Figure 5.1. YAP1/ROCK/PECAM shear stress signaling network.	187
Figure 5.2. Mechanotransduction transfer function behaviors for different shear modes.	189
Figure 5.3. Bioreactor experimental set up in incubator.	190
Figure 5.4. Gene expression data showing activation of EMT related genes in response to different shear conditions.	192
Figure 5.5. Comparison of model fit to gene expression data.	193
Figure 5.6. Predictions for abundances of YAP1, Nuclear YAP1 (YAPN'), PECAM,	194
Figure 5.7. YAP1 nuclear translocation increases with 1 dyne/cm ² OSC stimulation.	195
Figure 5.8. YAP1 nuclear translocation increases with 10 dyne/cm ² LSS stimulation.	196
Figure 5.9. RhoA activity as measured by stained area per cell.	197
Figure 6.1. Agent-based model framework.	218

LIST OF TABLES

Table 1.1. Staging comparison chick to human with key valvulogenesis events.....	19
Table 1.2. Various molecular targets and observed defects in animal models and clinically.....	24
Table 2.1. Osmolality measurements for control, hypo, and hyper-osmotic medias acquiring using freezing point depression osmometry.....	58
Table 2.2. Summary table of inhibitors	59
Table 4.1. Multi-objective optimization test problems.....	166

LIST OF ABBREVIATIONS

AVC	Atrioventricular Canal
OFT	Outflow Tract
BMP	Bone morphogenic protein
BSA	Bovine serum albumin
CD	Cluster of differentiation
CS	Chicken serum
ECM	Extracellular matrix
EMT	Epithelial to Mesenchymal Transition
ERK	Extracellular signal-regulated kinase
EtOH	Ethanol
KLF	Krüppel-like factor
KO	Knockout
LSS	Laminar steady-state flow
MAPK	Mitogen-activated protein kinases
MEK	Mitogen-activated protein kinase kinase
MSC	Mesenchymal stem cell
MMP	Matrix metalloproteinase
OSC	Oscillatory flow
P/S	Penicillin/streptomycin
PBS	Phosphate-buffered saline
PDMS	Polydimethylsiloxane
PECAM	Platelet endothelial cell adhesion molecule (CD31)

PCR	Polymerase chain reaction
SMA	Smooth muscle actin
TBS	Tris-buffered saline
TGF	Tissue growth factor
VEGF	Vascular endothelial growth factor
Vim	Vimentin
WSS	Wall shear-stress
YAP	Yes associated protein

CHAPTER 1.
INTRODUCTION

* Figure 1.2 and Figure 1.3 reprinted with permission from “Hemodynamic patterning of the avian atrioventricular valve.,” Jan. 2011, H. C. Yalcin, A. Shekhar, T. C. McQuinn, and J. T. Butcher, *Dev. Dyn.*, vol. 240, no. 1, pp. 23–35,. Copywrite 2010 by John Wiley and Sons

1.1 Clinical significance of congenital heart defects

The human heart is a four chambered pump that relies on four valves to maintain unidirectional blood flow. These valves must maintain homeostasis while experiencing severe hemodynamic loads. During development, the heart valve primordia, often referred to as cushions, work to maintain a sufficient movement of blood in the embryo, even at the most nascent stages of valvulogenesis. The valve develops in complexity quickly in order to match the rate of embryonic growth. Failure of the valves to maintain unidirectional flow during development can lead to embryonic lethality or lifelong cardiac health conditions.

Around 1% of live births have a congenital heart defect (CHD), a majority of which include defects in the structure and function of heart valves [1]. Congenital diseases of the heart valves as a whole account for \$1 billion in healthcare costs, annually in the US [2]. Further, there is likely underreporting of the prevalence of congenital heart defects in lower income countries [3]. Around 20-30% of these defects occur with functionally impaired valves. Genetic causes for CHDs are insufficient to explain the prevalence, variety, and concurrent combinations of these defects, predicting only 10-20% of cases [4]. Pediatric patients face years of surgical interventions and treatments because current replacement valves cannot grow with the heart throughout postnatal development [5]. The lack of therapeutic treatments, e.g. pharmacologic agents, impose a significant burden on patients with CHDs, and especially those who do not have access to sophisticated surgical treatments throughout their lifetimes.

1.2 Heart valve morphogenesis

The development of cardiac valves can be characterized by the progressive maturation of cardiac jelly into fibrous and flexible leaflets, occurring in the rapidly folding and septating heart. The atrioventricular (AV) valves develop in parallel with AV septation and semilunar (out flow tract, or OFT) valve maturation. The developmental progression of both AV and OFT valves, while significantly different, share common developmental pathways and intermediate states that govern the initial population of the valve cushion through endothelial to mesenchymal transition (EndMT) and subsequent remodeling into thin, fibrous leaflets.

Table 1.1 provides a timeline for key valve developmental processes and their mapping to human development and chick staging. Valvulogenesis initiates around 28 days in humans, or at the start of day 3 in chick, when the myocardium localized at the atrio-ventricular canal begins to locally expand the cardiac jelly by producing glycosaminoglycans (GAGs) [6]. These GAG enriched structures are referred to as endocardial cushions. Valve cushions become populated with interstitial cells by the process of endothelial to mesenchymal transition (EndMT), in which endothelial cells separate from one another and invade the mesenchyme [7]. The resulting mesenchymal cells proliferate, yielding a tissue that is ~85% cellular. These cells then remodel the valve structure including deposition of collagen matrix. The molecular regulation of EndMT is precisely controlled in order to ensure proper onset and extent of cushion population.

Event	HH Stage (chick)	Timeframe (chick)	Timeframe (human)
Heartbeat onset	HH10-HH11	33 – 45 hpc	28 dpc
Cardiac jelly formation	HH13	49 – 52 hpc	28 dpc
Cushion population through EndMT	HH14-HH17	52 – 69 hpc	By 33-35 dpc
AV cushion fusion	HH25	4.5 – 5 dpc	37-42 dpc
Leaflet compaction and elongation	HH27-HH36	5 – 10 dpc	42-58 dpc

Table 1.1. Staging comparison chick to human with key valvulogenesis events*hpc = hours past conception, dpc = days past conception, EndMT = endothelial to mesenchymal transition [8]–[10]

For example, EndMT is suppressed by a myocardial gradient of vascular epithelial growth factor (VEGFA), until the cushion has grown large enough to bring the endocardial surface away from this gradient. At the same time, small amounts of VEGF ligand are required for EMT to occur [11]. The AV cushions fuse at HH25, septating the heart top to bottom and creating two subsets of cellular populations. Cells at the fusion plane will remodel into a fibrous septum, while the other set will generate the septal leaflets of the AV valves (mitral, left and tricuspid, right), see Figure 1.1. . Over time, these tissues become progressively stiffer and have higher proportions of matrix and a larger surface to volume ratio.

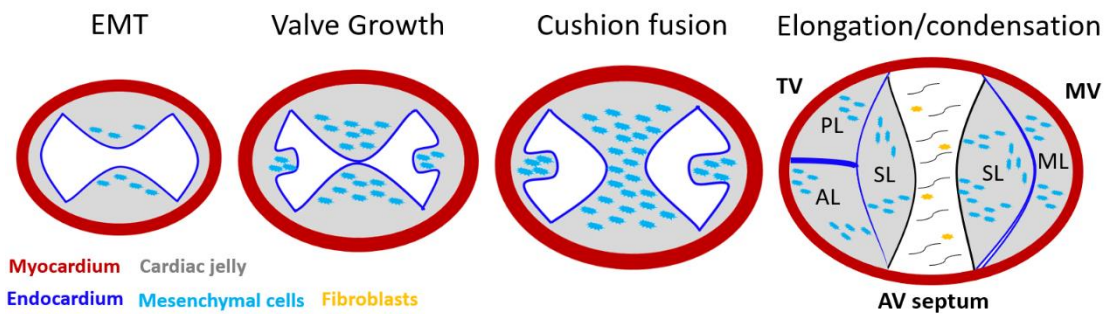


Figure 1.1. Cross section of the developing chick atrio-ventricular canal. Valve cushions are shown during key processes in development. *TV, tricuspid and MV, mitral valve, PL posterior leaflet (tricuspid), AL anterior leaflet (tricuspid), SL septal leaflet, mural leaflet (mitral)

1.2.1 Rationale for the study of atrio-ventricular valves

While the OFT valves (aortic and pulmonary) usually garner attention due to the prominence of aortic valve disease, the AV valves provide a system to study EndMT and valve remodeling in cells derived exclusively from the endocardium. Specifically, the mesenchymal stem cells in septal leaflets are purely of endocardial origin following EndMT cells [6]. The OFT system is substantially more complex, requiring neural crest cell invasion to produce both OFT septation and valve elongation [12]. Further, the AV valves are considerably larger and therefore provide a more robust population of cells, an especially important concern when attempting quantitative gene or protein analysis. It should be noted that the mural leaflets are known to be innervated by myocardial cells [13]. Finally, in addition to specific defects of the mitral valve and AV valvuloseptal apparatus, defects in AV valves can lead to other defects in the heart [1], [14], leading to further clinical burden [15].

1.2.2 Avian animal model

Chick and quail models are well-established tools for studying development [16]. The four chambered avian heart develops in a manner that mirrors that of human heart development. The chick model is staged using the Hamburger Hamilton staging system, developed in 1951, allowing for consistent assessment of embryos at a particular embryonic time point [8]. Chick embryos do not require maternal contributions and can be grown *in ovo* or *ex ovo* with the capacity to make surgical manipulations. Large numbers of embryos can be cultured at once to provide sufficient sample volumes for *in vitro* experiments. The ease of use and low cost of these embryos provides a reliable system for studying complex phenomena. Further, the morphologies of the chick heart correlate significantly with morphologies seen during human development [16]. While differences between mammalian and chick in cell lineages and cytokine isoforms exist, these differences are less distinct for the AV valves [17], [18].

1.2.3 Canonical TGF β signaling

Canonical TGF β signaling is initiated by TGF β 1/2/3 and primarily through Smad activation. Smad transcription factors collectively help to downregulate E-Cadherin, while upregulating transcription factors like LEF1 that can further downregulate epithelial markers, while also driving α SMA and vimentin expression for cell migration and invasion [19]. Specifically, several Smads, including Smads 2 and 3 will be phosphorylated by TGF β receptors, form Smad2/2 complexes and translocate into the nucleus [20]. Clearly, TGF β signaling plays a role in epithelial to mesenchymal transition (EMT), but also modulates later valve remodeling and

myofibroblastic differentiation [6]. At a higher level, the TGF β superfamily also includes bone morphogenic proteins (BMPs). These BMPs are required at each step of valve development, and have been shown to have both permissive and driving roles in allowing TGF β -1/2/3 ligands to activate transcriptional targets [21], [22]. For instance, during endocardium EMT, BMP2 secreted by the myocardium allows endocardial cells to undergo EMT in response to TGF β [23]. BMP signaling occurs through alk2/3 and BMP receptor complexes through Smads1/5/8, whereas TGF β factors bind to alk1/5 and TGF β 2 receptors [21]. In mid to late development, TGF β signaling through TGF β 2 receptors is critical for successful valve remodeling [24]. BMPs can work in parallel with TGF β isoforms or in concert to create cell and tissue phenotypes across stages of development.

1.2.4 VEGF signaling

Vascular epithelial growth factor (VEGF) stabilizes endothelial phenotypes and increases endothelial migration [25]. VEGF can thereby provide two critical functions: (1) the regulation of the timing and extent EMT related events and (2) maintenance of the endothelial layer as cells are lost to transformations and as the surface area of leaflets grows. VEGF signaling through nuclear factor of activated T-cells cytoplasmic 1 (NFATc1) has been shown to be important in both EMT and valve elongation [26]. Myocardial expression of NFATc1 has been shown to drive EMT, whereas, NFATc1 in endothelial cells is stabilizing and can lead to proliferation [23], [26]. In early development, VEGF receptor 1 is present but is replaced by VEGF receptor 2 post EMT and is thought to assist in valve elongation [27]. Generally, VEGF-A is the most commonly implicated isoform [28]. VEGF has also been shown

to signal through miRNAs to interfere with EMT and with elongation through the down regulation of Smad3 [27], [29].

VEGF has also been shown to crosstalk with the RAF/MAPK pathway through PKC, suggesting that VEGF signaling may be able to inhibit TGF β signaling downstream of RAS/RAF [30]. Lastly, in cancer cells, NFATc1 has been shown to form complexes with Smad3, thereby blocking TGF β signals [31].

1.2.5 Other implicated pathways

Wnt signaling is usually associated with a release of beta-catenin from the APC complex, allowing for increased expression of TGF β 3 and mesenchymal activation [32]. Interestingly, non-canonical signaling of TGF β through PI3K allows for a similar release of beta catenin, demonstrating a redundancy between these pathways [33]. GTPase signaling through RhoA and Rac1 have also shown to be key non-Smad players in TGF β signaling that affect differentiation and convey mechanical stimuli in valve development [34]. Notch signaling is key to the patterning and differentiation of cells that make up the outflow tract valves [35].

Notch, Wnt and BMP are also known to work together across multiple cell types to regulate early valve development [36]. While genetic information alone does not explain the occurrence of many defects, many signaling pathways have been implicated due to genetic abnormalities in subsets of patients [37]. A summary of the signaling pathways discussed above with their associated experimental and clinical defects is presented in Table 1.2. Many of these pathways will be discussed later in this chapter to elucidate their roles in responding to mechanical stresses.

Molecular target	Process involvement	KO effect in animal model	Clinical AV defect	References
TGFβ	EMT, Remodeling	MS: insufficient EMT MS: insufficient cushion remodeling	Marfan syndrome / mitral prolapse	[38] [24] [39]
VEGF	EMT, Endothelial growth, Valve elongation	MS:KO: stunted elongation	Endocardial cushion defect, Atrial septal defect	[27] [40]
BMP	EMT, Growth	MS:KO Valvular insufficiency	Atrioventricular septal defect	[41] [42]
NOTCH	Cell migration, differentiation	MS:KO lethality	Mitral valve stenosis	[36] [43]
KLF2	EMT, Shaping	MS:KO in sufficient EMT MS:KO lethality		[44] [45]
TRPV4	EMT	ZF: insufficient remodeling		[46]
Wnt/β-catenin	EMT, ECM production	CK:KO No EMT/no cushion formation		[47]
Rho-ROCK/Rac	Differentiation and migration	MS:inhibition decreased migration and insufficient cell alignment		[48]

Table 1.2. Various molecular targets and observed defects in animal models and clinically. Interactions between these pathways make it likely that those with undocumented genetic connections can likely give rise to similar defects. MS=mouse, CH=chick, KO=knockout, ZF=Zebrafish

1.3 Hemodynamics during valve development

Alterations to hemodynamic stresses provide a target for regulating development that can also explain why defects often occur in combination. Once hemodynamics are disrupted, the resulting defect will cause a feedback response that

further details the hemodynamic environment throughout the entire heart. Thereby, a septation defect could lead to a malfunctioning valve, or vice versa. Acquiring a complete understanding of mechanobiological regulation of heart valve morphogenesis first requires a consideration of the mechanical stresses placed on the entire valve annulus at the organ level.

At HH10 (35hrs), the embryonic heart begins to beat [49]. By HH11 (40hrs), there is effective blood flow and a clear heart rhythm [50]. Given the difficulties in measuring shear stress and pressure drops directly, Yalcin et al. examined shear profiles generated from CFD simulations of the AV valves that are calculated based off of ultrasound flow velocimetry [51]. From HH17 to HH30, shear stress on the AV valves goes from an average wall shear stress (WSS) of 3.62 to 9.11 dynes/cm². Peak WSS were significantly higher increasing from 19.34 to 287.18 dynes/cm². Peak pressure drops increase from 0.014 to 0.71 mmHg. As development progresses from HH23 and beyond, vortices and oscillatory flow are found on the ventricular side of the AVC. Prior to and during onset of EndMT, shear stresses develop from low oscillatory and pulsatile flows on the symmetric cushion. As development progresses, constrictions along the AV canal, which become narrower as the AV cushions grow (Figure 1.1), lead to peak shear stresses along the AV cushion endocardium (Figure 1.2). By late development (HH30+), there is a transition to spatially localized oscillatory flow on the ventricularis and pulsatile flow on the atrialis (Figure 1.3). Pressure loads across the valve annulus cause significant compressive stresses on the valve leaflets [52], in addition to bending moments that create regions of tissue under tension [53]. These spatial and temporal variations in shear stress and pressure

underscore the variety of hemodynamic stimuli that valve endothelial and mesenchymal cells experience *in vivo*. To decouple these effects, *in vitro* models have been used to select idealized modes of flow, namely oscillatory and steady-state flows, to isolate the specific effects of each stimulus [54]. It is also important to acknowledge that deflection of the AV cushions also occurs as a result of flow, which may result in internal deformations [55].

It has long been clear that both blood flow velocity and blood viscosity increase exponentially over the course of AV valve development [51], [56]. Further, because flow is characteristically dependent on geometry, a single point defect can disrupt the hemodynamic environment of the entire heart, leading to widespread defects [57]. Disruptions in hemodynamics may therefore have effects on mechanically induced signaling throughout the heart that become reinforced due to further dysregulation of the hemodynamic environment (Figure 1.4).

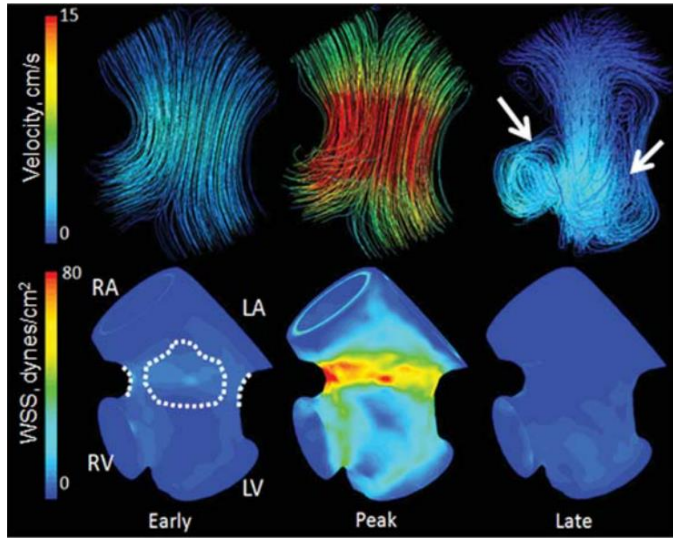


Figure 1.2. Hemodynamic patterning at mid-stage development during a single cardiac cycle. Velocity streamlines and wall-shear stress values through and on the AVC are shown Reprinted with permission from John Wiley & Sons, Inc. from [51].

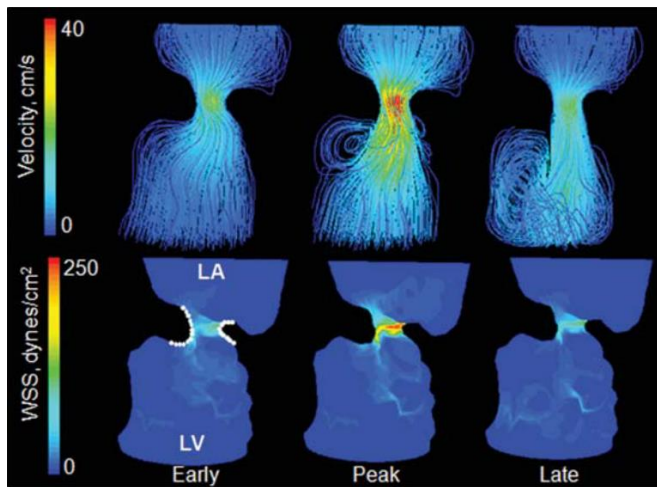


Figure 1.3. Hemodynamic patterning at late-stage development during a single cardiac cycle. Velocity streamlines and wall-shear stress values through and on the AVC are shown Reprinted with permission from John Wiley & Sons, Inc. from [51].

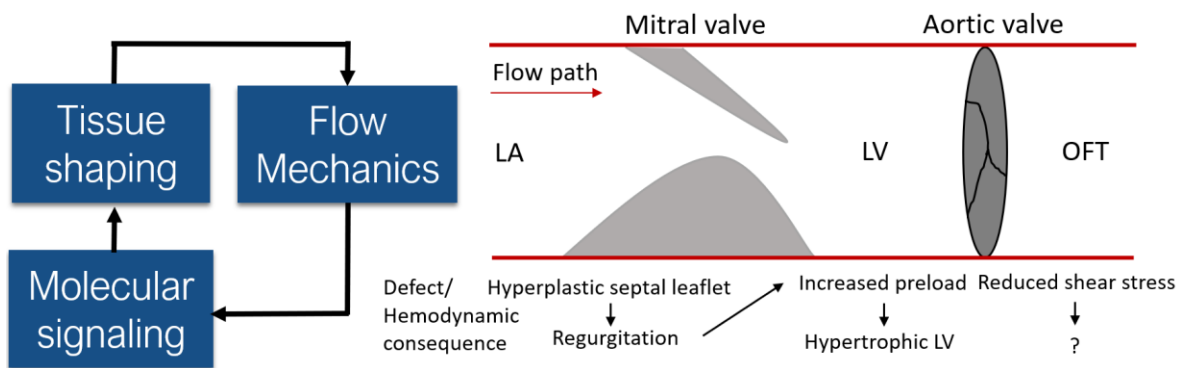


Figure 1.4. Flow mechanics can reinforce the developmental program or propagate defects. Schematic representing hemodynamic signaling feedback through shape changes (left). Model of disorganization of blood flow downstream of mitral defect seen in the entire heart (right).

1.4 Mechanical signaling pathways in valve development

Principally, it is not well understood how hemodynamic signals are processed by the valve endothelial or mesenchymal cells. Evidence for the role of flow in valve development is clear, but the specific molecular changes that result in spatial organization of the maturing tissues are not known. It is important to consider that there are multiple sources of mechanical loads on both the valve endothelium and mesenchyme. These include external normal (i.e, perpendicular to the tissue surface) and shear forces caused by flow, hydrostatic pressure, reaction forces at the valve annulus. Here, contributions from individual hemodynamic loads will be addressed in the context of mechanosensitive signaling pathways.

1.4.1 RhoGTPase signaling

Rho GTPases have been implicated numerous times with respect to stress affecting growth (proliferation, mass addition) and cellular properties during valve development, as well as in other developmental and cancer related processes. Previous work has shown that RhoA and Rac1 play central roles in mid to late stages (HH25 to

HH42) of valve development [34]. There is an inherent developmental transition from RhoA to Rac1 activity as valve condensation progresses and this transition appears to be necessary for valve interstitial cells to process signals from cyclic stretch [34]. Further evidence of RhoA and Rac1 in cyclic stretch has been found in fetal lung tissue, where RhoA was also seen as a quick acting (activating within 5 minutes), negative regulator of maturation and Rac1 associated with long term stress responses [58]. Tan et al. demonstrated that mid stage (HH25) cushions elongate in the direction of flow in a RhoA dependent manner [59]. In studies with gingival fibroblasts, Rac1 has been shown to influence migration through upregulation of actin polymerization and myosin activation, with these cells also responding to mechanical stretching through RhoGTPase signals [60], [61]. Rho and Rac interact to inhibit one another, excluding both from being active in the same location in a cell, aiding in cell polarization for apical-basal polarity maintenance and migration [62]. Rho-ROCK signaling downstream of focal adhesions and focal adhesion kinase (FAK) has shown to modulate proliferative behavior in response to mechanical stretch [63]. In endothelial cells, fluid shear stress has long been shown to induce cytoskeletal alignment in a Rho-dependent manner [64]. Lastly in valve development, RhoA has been shown to process signals from ECM components (namely periostin) to govern invasion into the AV mesenchyme [65].

Broadly, Rho and Rac GTPases are shown to play roles in many mechanically triggered cellular processes critical to development, making them attractive to study in a developmental context. These activities may rely heavily on cellular localization of these proteins (e.g. polarized contractile events) but may also act generally as

signaling mediators that simply transduce a signal, independent of their initial locations.

In addition to their presence at focal adhesions (cell-ECM interactions), the activation of RhoGTPases can occur at the epithelial junctions [66]. RhoA can specifically play a role in stabilizing these junctions [66], which is of interest to understanding shear driven EMT in development. Rac1 has also been shown to initiate recruitment of E-cadherin to adherin-junctions and to be subsequently activated by this recruitment [66].

Rho GTPases have long been implicated in their interactions with other pathways not directly related to the cytoskeleton [67]. RhoA has shown to be transcriptionally active, triggering nuclear translocation of the YAP1 transcription factor to drive cellular proliferation and apoptosis [68].

Overall, Rho-GTPase signaling has the ability to influence valve development through its regulation of cell adhesion and motility dynamics. Further, Rho-GTPases can act as key signaling intermediates with TGF β and BMP pathways to regulate processes such as collective migration, cell contractility, proliferation, and death. However, the links between the activities of these GTPases and mechanical stimuli remain to be fully elucidated.

1.4.2 Non-canonical TGF β signaling

It has been shown that TGF β signals can activate a variety of pathways aside from SMAD transcriptional signaling [69]. Notably, TGF β can activate Ras superfamily GTPases, including RAS-MEK-ERK and RhoA-ROCK [69], [70]. The MAPK/MEK-ERK pathway is well known to influence EMT [32], as well as tumor growth processes through cooperation with FAK (focal adhesion kinase) [71]. Additionally, ERK has shown to be regulated by micro-RNA-21 downstream of hemodynamic stress [72]. In gingival fibroblasts, RhoA-ROCK signaling is induced by TGF β -1 exposure and is required for myofibroblastic activation [73]. PI3K signaling has also shown to be required for EMT through GSK3 to permit release of beta-catenin to drive pro-EMT transcription [19], [74]. Further, PI3K and Rho have been shown to work together to regulate migration in developing heart tissue [65].

Klf2 is a shear stress sensitive transcription factor in zebrafish that can respond especially to oscillatory shear flow through TRPV4 calcium signaling [46], [75]. Activation of canonical TGF β signaling, through Alk5 receptors to SMADs, is required for shear activation of Klf2 [76]. TGF β is implicated as being upstream of a shear sensitive transcription factor, yet it is unclear how TGF β is activated in the first place. However, it is known that a non-canonical activation of the TGF β pathway can lead to autocrine TGF β 3 signals, which in turn lead to canonical SMAD signaling [19]. Primary cilia have also shown to be involved in shear driven EMT, where the absence of cilia is permissive for EMT and is also downstream of TGF β activation [77], [78]. RhoGTPases can also be activated by TGF β ligands [69].

1.4.3 Wnt and β -catenin signaling

Wnt/ β -catenin signals are often required for SMAD transcriptional activity in the nucleus and can affect processes in valve development, disease and in cancer [79]. Canonically, Wnt ligands bind receptors consisting of frizzled receptors and low density lipo-protein co-receptors, leading to inhibition of β -catenin degradation [80]. During valve development, active Wnt is required for successful EMT and FGF-driven AV cushion growth [81]. Wnt has also been shown to directly drive proliferation in valve interstitial cells [82]. Wnt mediated phosphorylation of GSK3 plays a key role in regulation of EMT by regulating β -catenin sequestration in the cytoplasm [83]. In valvulogenesis, Wnt expression in mesenchymal cells has been shown to correlate with endocardial KLF2 and implicated in a paracrine signal that transduces shear stress from the endothelial surface to the mesenchyme [84]. Myocardial BMP2 expression, which is required for EMT, was found to be reliant on myocardial Wnt expression [36]. Overall, Wnt signaling is a promising target that affects at least both early EMT and mid-stage cushion growth.

1.4.4 Notch signaling

Notch has been shown to be an important endothelial pathway required for EndMT in the AV cushion, which signals between adjacent cells via Delta-Notch interactions [36], [85]. In OFT development, Notch is essential to the maturation of neural crest cells into smooth muscle cells that are required for complete remodeling the of the OFT valves [86]. Deletion of Notch targets may cause septation defects or arch artery defects across the heart [86]. A large body of evidence also points to interactions between Notch and YAP/TAZ in multiple developmental systems [87]. It

should be noted that Notch, Wnt and Fibroblastic growth factor (FGF) signaling all play important roles in activating mesenchymal and fibroblastic phenotypes in valve development [23].

1.5 Uncovering the mechanobiology behind heart valve defects

The majority of CHDs are not explained by genetic factors, making the initial origins of valve malformations obscure. Observation of more subtle deviations in gene expression and maternal factors may be required to gain a predictive understanding of when and where defects will occur. Further, it is likely that no single small deviation contributes to defects, as there are large physiological ranges for many morphological readouts [88]. A systems biology approach can be used that acknowledges the complexities of many non-linear factors interacting to produce defects [89].

Given the emerging role of mechanics, with some evidence for the role of wall shear stresses and little work to explain the role of normal forces in development, it is crucial to decompose and establish the direct roles of mechanical forces to inform an integrative systems model of development.

1.5.1 Role of pressure and tensile forces in directing tissue growth

Generally, the cardiovascular field has focused on pressure loading in adult contexts as the transvalvular pressures are significantly higher in magnitude and are used directly as clinical readouts [90], leading to a gap in knowledge during development. However, several studies point to pressure sensitivity in embryonic valve cells.

TRPV4 calcium channels have been shown to play an important role in osmotic stress response, specifically to tissue swelling [91], [92]. TRPV4 receptors

have also shown sensitivity to mechanical stimuli (touch) [93], suggesting that these channels may be involved in common responses of osmotic and altering mechanical loads. Most interestingly, TRPV4 has been shown to act upstream of *klf2* in valve development to sense oscillatory shear [46].

Cyclic pressure has been shown to affect cell matrix secretion and cell contractility in adult porcine aortic valve cells [94], [95]. Static pressure was found to cause collagen secretion, but not an increase in contractile behavior [96]. On the other hand, sustained pressure alters focal adhesion-integrin co-localization and proliferation in human umbilical vein endothelial (HUVEC) cells, suggesting that embryonic tissues may be more sensitive than adult tissues to static pressure stimuli [97].

Buskohl et al. presents a model coupling tissue growth and shaping directly to hemodynamic loads [52]. This fluid-structure interaction model was calibrated using experimental mechanics and flow fields derived from day 5 (HH25) chicken embryos. The solid component contained a constitutive model containing a homeostatic stress by which stress is mapped to the inelastic deformation tensor (i.e. growth is modeled as inelastic deformation). Under these conditions a compressive stress was able to drive tissue growth and elongation in the direction of flow. Therefore, areas of the cushion experiencing only low levels of compression or tension will resorb while areas experiencing robust compression will expand. This specific role of compressive and tensile stresses motivates the experimental study to elucidate the underlying biological mechanisms that could link each type of mechanical stimulus to a growth response.

Osmotic stress has been used to apply hydrostatic pressures to cells to examine their mechanical responses [98]. Further, osmotic stress has been used to test the effects of hydrostatic pressure on chondrocytes suspended in extracellular matrix [99], [100]. Hypo-osmotic stress induces mechanical loads by creating a gradient of water into a cell, swelling the cell and thereby causing tensions on the membrane and cytoskeleton (Figure 1.5). Hyper-osmotic stress induces mechanical loads by creating a gradient of water out of a cell, contracting the cell and thereby causing compression of the membrane and cytoskeleton (Figure 1.5).

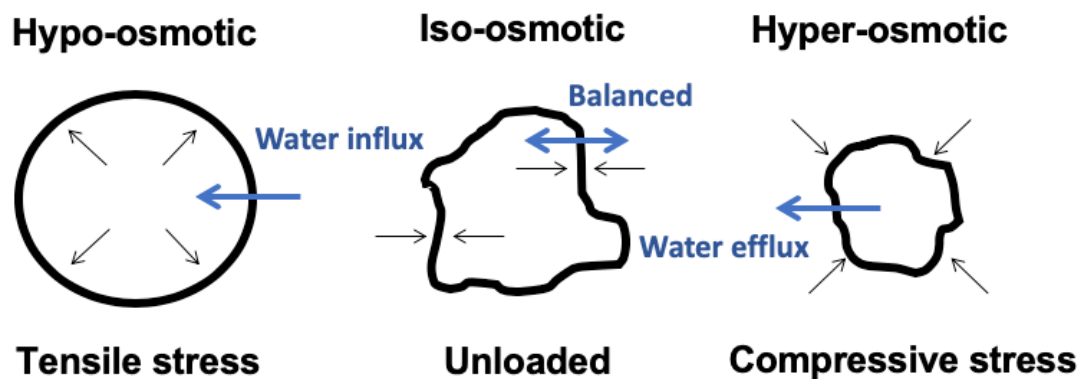


Figure 1.5. Osmotic stress and its mechanical effects on cells. Black arrows refer to the net-forces being exerted on the cell. Iso-osmotic conditions result in no load, while hypo-osmotic and hyper-osmotic stresses create volumetric strains due to the movement of water either into or out of the cell. The same principle can be applied to tissues, assuming the boundary is sufficiently defined, such as by an endothelial layer.

While blood osmolality is shown to be tightly controlled [101], the osmotic stresses felt by cushion cells will be a function of both the internal tissue environment and mechanical loads that may affect cellular volume. Conventionally, cells try to maintain their size by regulating ion concentrations [102]. In development, the homeostatic volume of a cell will likely change over time, especially in early development where amino acids are also used to balance osmotic stress [103].

Importantly, cells do not generally return to their initial homeostatic size when stressed. The homeostatic volume (“set-point”) of a cell has shown to be perturbed through protein phosphatase inhibition in swelling activation [104]. Notable causes of increased cell volume homeostasis include cell proliferation, contractile behavior and migration; causes of decreased volume homeostasis include secretion, differentiation and cell death [104].

Modest volume changes may act as signals for varied phenotypes [103].

Recent modeling has demonstrated that cells experiencing external mechanical loading will activate a complex response that alters cellular stiffness through pressure, volume and actin cortex adjustment [105]. These complex interactions are also seen in cells undergoing mitotic rounding and have shown to actively balance osmotic (hydrostatic) stress with actin myosin cortex contraction to control cell shape, volume and mechanical properties [98]. It is clear that external mechanical loads can affect the cellular osmotic environment and that alterations in external osmotic environment can affect the mechanics of cells. Osmotic stress may therefore be implicated in potentially all forms of mechanical activation. The specific effects of osmotic stress and resultant alterations to cellular behaviors is not well characterized in mammalian cells, excluding renal and cartilaginous cells, and especially in the area of valve development. The importance of ion channel signaling in mechanical stretching, shear stress signal transduction, and osmotic stress signaling point to a common mechanism that may underlie these signals.

1.6 Pathways implicated in congenital defects of the mitral valve

There have been several genes and pathways associated with congenital mitral valve defects, observed clinically in humans and through *in vivo* animal models. Disruption of genes associated with the TGF β pathway have been associated with multiple congenital defects. Marfan syndrome (MFS) is an autosomal dominant disorder that can affect multiple connective tissues in the body [106]. MFS often leads to several heart defects including thickening, shortened and stiffened valves throughout the heart, including mitral valve prolapse [107]. MFS has been associated with excess TGF- β /Smad2 activity [108]. Fibrillin 1, a connective tissue ECM component which aids in tissue elasticity, inhibits TGF- β activity by binding to TGF- β ligands [109], [110]. Consequently, defects in Fibrillin genes have been associated with a prevalence of MFS [111]. A direct role of Fibrillin regulation of TGF- β has been confirmed in mouse models lacking Fibrillin 1 [112]. Loays-Dietz (LDS) syndrome results in craniofacial and cardiovascular defects and is caused by genetic defects in TGF- β receptors (TGF- β R1 & TGF- β R2) [113]. Like in MFS, LDS can also result in mitral valve prolapse, TGF- β as necessary for the proper seating and sizing of the mitral valve [107].

Myxomatous mitral valve disease is a dysregulation of the valve ECM balance resulting in overly flexible leaflets with poor coaptation and regurgitation [114].

Myxomatous mitral valves leading to prolapse have been associated with bicuspid aortic valve (BAC) [115]. Disruption of Alk3 mediated BMP signaling in epicardially derived cells in the AV septal mesenchyme have shown to create a myxomatous phenotype in the mitral valve [116]. Over expression of in BMP4 was associated with

MVP patients and *in vitro* disruption of BMP4 could cause matrix disruption mimicking MVP phenotypes [117].

Noonan syndrome results in facial abnormalities and mitral valve prolapse [118]. Noonan syndrome disorders which also include atrial septal defects and pulmonary valve stenosis, can occur as a result from over activation in any 1 of 11 MAPK genes, including MEK1 and MEK2, which code for proteins which activate RAS-ERK signaling [118], [119]. Mouse models of Noonan syndrome have demonstrated that gain of function mutation of Ptpn11, which encodes a tyrosine phosphatase important in RAS/MAPK signaling, leads to enlarged mitral valves [120].

For CHDs with any known associated genetic defects, these genetic abnormalities can be reliably associated as poorly as 10% effectively as 100% [118]. Clearly, there is a need to better understand the epigenetic mechanisms that influence the complex cellular and mechanical interactions of cardiac tissues.

Hemodynamics has been shown to play a role in contributing to a myriad of defects including AV cushion, OFT cushion, and septal defects, either as an initial insult or as the downstream result of a gene mutation [50]. Several mechanically linked pathways have been implicated or directly involved in clinically relevant disease pathologies. For example, TGF β , RhoA, Klf2 and downstream effectors all show shear sensitivity leading to clinically relevant valve and heart defects [121]–[123].

The sources and downstream effects of hemodynamic defects are hard to decouple, but intrinsic sources beyond explicit genetic defects could also include minor genetic variabilities that may be patient specific. One extrinsic source of

hemodynamic variability may come from the placental or maternal contributions, which have been recapitulated in avian models by altering the vitelline vein network [124]. Identifying the signaling pathways underlying responses to specific hemodynamic stimuli could lead to new readouts *in vivo* that will describe how tissue morphogenesis is altered leading to defects.

1.7 Objectives of this work

The developmental programs that lead to cushion cellularization and ultimately precise valve morphogenesis require dynamically evolving signals from multiple cell populations to be processed correctly. Understanding these complex interactions is important to both understanding and predicting congenital defects, as well as for controlling tissue engineering processes. These interactions contain multiple types of mechanical loads as well as a plethora of genetically prescribed signaling pathways. In Chapter 2, we address the need to understand the roles of compressive and tensile loads on valve growth by applying a mechano-osmotic stress system for the time in the context of valve morphogenesis. Further, we identify osmotic stress as a potentially significant role in establishing a complete understanding of the mechanical fields present during valve morphogenesis. To address the complexities of mechanobiological interaction pathways, in Chapter 3 and Chapter 4, we develop a systems biology model framework capable of representing the interactions of multiple signaling pathways as derived from multi-scale data. Wall-shear stresses, although studied directly in an adult context, has not been characterized in development to describe the relationship between amplitudes and modes of flow to the acclimatization of morphogenic behaviors. In Chapter 5, we apply these different modes of WSS in a

flow bioreactor to uncover phenotypic insights and associated signaling responses. Further, we expand our systems biology model to include mechanical signaling pathways, allowing us to assess the relative importance of mechanosensitive pathways. My guiding hypothesis is that these mechanical forces have distinct influences on morphogenesis throughout development by controlling valve remodeling and valve homeostasis. The first purpose of this work is to identify from these signaling pathways, targets that respond to mechanical loads caused by hemodynamics through the use of in vitro culture systems, bioreactors, and in vivo surgical manipulations. The consequence of these responses will be measured by assessing the development of tissue size, shape, and critical cellular behaviors necessary for valve development in the presence of a varied mechanical environment. A further goal of this work was to generate computational tools to interrogate the integration of these mechanical signals into discernable cell phenotypes. My hope is that this research will inform clinical diagnostics *in utero*, support the ability of engineers to develop tissue engineered solutions for pediatric patients, and enable early interventions that prevent defects from occurring.

1.8 References

- [1] J. I. E. Hoffman, S. Kaplan, and R. R. Liberthson, "Prevalence of congenital heart disease," *Am. Heart J.*, vol. 147, no. 3, pp. 425–439, 2004.
- [2] V. T. Nkomo, J. M. Gardin, T. N. Skelton, J. S. Gottdiener, C. G. Scott, and M. Enriquez-Sarano, "Burden of valvular heart diseases: a population-based study," *Lancet*, vol. 368, no. 9540, pp. 1005–1011, Sep. 2006.
- [3] D. Van Der Linde *et al.*, "Birth prevalence of congenital heart disease worldwide: A systematic review and meta-analysis," *J. Am. Coll. Cardiol.*, vol. 58, no. 21, pp. 2241–2247, 2011.
- [4] B. G. Bruneau, "The developmental genetics of congenital heart disease.," *Nature*, vol. 451, no. 7181, pp. 943–8, Feb. 2008.
- [5] J. T. Butcher, G. J. Mahler, and L. a Hockaday, "Aortic valve disease and treatment: the need for naturally engineered solutions.," *Adv. Drug Deliv. Rev.*, vol. 63, no. 4–5, pp. 242–68, Apr. 2011.
- [6] J. T. Butcher and R. R. Markwald, "Valvulogenesis: the moving target.," *Philos. Trans. R. Soc. Lond. B. Biol. Sci.*, vol. 362, no. 1484, pp. 1489–503, Aug. 2007.
- [7] C.-J. Lin, C.-Y. Lin, C.-H. Chen, B. Zhou, and C.-P. Chang, "Partitioning the heart: mechanisms of cardiac septation and valve development.," *Development*, vol. 139, no. 18, pp. 3277–99, Sep. 2012.
- [8] B. J. Martinsen, "Reference guide to the stages of chick heart embryology.," *Dev. Dyn.*, vol. 233, no. 4, pp. 1217–37, Aug. 2005.
- [9] P. W. Oosthoek *et al.*, "Development of the atrioventricular valve tension apparatus in the human heart," *Anat. Embryol. (Berl.)*, vol. 198, no. 4, pp. 317–329, 1998.
- [10] A. Wessels, M. W. M. Markman, J. L. M. Vermeulen, R. H. Anderson, A. F. M. Moorman, and W. H. Lamers, "The development of the atrioventricular junction in the human heart," *Circ. Res.*, vol. 78, no. 1, pp. 110–117, 1996.
- [11] E. J. Armstrong and J. Bischoff, "Heart valve development: endothelial cell signaling and differentiation.," *Circ. Res.*, vol. 95, no. 5, pp. 459–70, Sep. 2004.
- [12] B. Wu, H. S. Baldwin, and B. Zhou, "Nfatc1 directs the endocardial progenitor cells to make heart valve primordium.," *Trends Cardiovasc. Med.*, vol. 23, no. 8, pp. 294–300, Nov. 2013.

- [13] A. Wessels *et al.*, “Epicardially derived fibroblasts preferentially contribute to the parietal leaflets of the atrioventricular valves in the murine heart.,” *Dev. Biol.*, vol. 366, no. 2, pp. 111–24, Jun. 2012.
- [14] A. Carpentier *et al.*, “Congenital malformations of the mitral valve in children. Pathology and surgical treatment.,” *J. Thorac. Cardiovasc. Surg.*, vol. 72, no. 6, pp. 854–866, Dec. 1976.
- [15] J. Lincoln and K. E. Yutzey, “Molecular and developmental mechanisms of congenital heart valve disease.,” *Birth Defects Res. A. Clin. Mol. Teratol.*, vol. 91, no. 6, pp. 526–34, Jun. 2011.
- [16] K. H. Kain *et al.*, “The chick embryo as an expanding experimental model for cancer and cardiovascular research.,” *Dev. Dyn.*, vol. 243, no. 2, pp. 216–28, Feb. 2014.
- [17] A. Wessels and D. Sedmera, “Developmental anatomy of the heart: a tale of mice and man.,” *Physiol. Genomics*, vol. 15, no. 3, pp. 165–76, Nov. 2003.
- [18] A. Krishnan *et al.*, “A detailed comparison of mouse and human cardiac development,” *Pediatr. Res.*, vol. 76, no. 6, pp. 500–507, 2014.
- [19] and B. R. O. Damian Medici, Elizabeth D. Hay, “Snail and Slug Promote Epithelial-Mesenchymal Transition through β -Catenin–T-Cell Factor-4-dependent Expression of Transforming Growth Factor- β 3,” *Seikagaku*, vol. 82, no. 4, pp. 327–331, 2010.
- [20] J. Zavadil and E. P. Böttinger, “TGF- β and epithelial-to-mesenchymal transitions,” *Oncogene*, vol. 24, no. 37, pp. 5764–5774, 2005.
- [21] A. von Gise and W. T. Pu, “Endocardial and epicardial epithelial to mesenchymal transitions in heart development and disease.,” *Circ. Res.*, vol. 110, no. 12, pp. 1628–45, Jun. 2012.
- [22] J. Wang *et al.*, “Atrioventricular cushion transformation is mediated by ALK2 in the developing mouse heart,” *Dev. Biol.*, vol. 286, no. 1, pp. 299–310, 2005.
- [23] M. D. Combs and K. E. Yutzey, “Heart valve development: regulatory networks in development and disease.,” *Circ. Res.*, vol. 105, no. 5, pp. 408–21, Aug. 2009.
- [24] K. Jiao, M. Langworthy, L. Batts, C. B. Brown, H. L. Moses, and H. S. Baldwin, “Tgfbeta signaling is required for atrioventricular cushion mesenchyme remodeling during in vivo cardiac development.,” *Development*, vol. 133, no. 22, pp. 4585–4593, 2006.
- [25] C. Ruhrberg, *VEGF in Development*. 2008.

- [26] C.-P. Chang *et al.*, “A field of myocardial-endocardial NFAT signaling underlies heart valve morphogenesis.” *Cell*, vol. 118, no. 5, pp. 649–663, Sep. 2004.
- [27] K. Stankunas, G. K. Ma, F. J. Kuhnert, C. J. Kuo, and C. P. Chang, “VEGF signaling has distinct spatiotemporal roles during heart valve development,” *Dev. Biol.*, vol. 347, no. 2, pp. 325–336, 2010.
- [28] Y.-N. Chiu, R. a Norris, G. Mahler, A. Recknagel, and J. T. Butcher, “Transforming growth factor β , bone morphogenetic protein, and vascular endothelial growth factor mediate phenotype maturation and tissue remodeling by embryonic valve progenitor cells: relevance for heart valve tissue engineering.” *Tissue Eng. Part A*, vol. 16, no. 11, pp. 3375–3383, 2010.
- [29] J. P. Hong, X. M. Li, M. X. Li, and F. L. Zheng, “VEGF suppresses epithelial-mesenchymal transition by inhibiting the expression of Smad3 and miR-192, a Smad3-dependent microRNA,” *Int. J. Mol. Med.*, vol. 31, no. 6, pp. 1436–1442, 2013.
- [30] K. C. Corbit, N. Trakul, E. M. Eves, B. Diaz, M. Marshall, and M. R. Rosner, “Activation of Raf-1 signaling by protein kinase C through a mechanism involving Raf kinase inhibitory protein.” *J. Biol. Chem.*, vol. 278, no. 15, pp. 13061–13068, 2003.
- [31] G. Singh *et al.*, “Sequential activation of NFAT and c-Myc transcription factors mediates the TGF- β switch from a suppressor to a promoter of cancer cell proliferation,” *J. Biol. Chem.*, vol. 285, no. 35, pp. 27241–27250, 2010.
- [32] J. Xu, S. Lamouille, and R. Derynck, “TGF-beta-induced epithelial to mesenchymal transition.” *Cell Res.*, vol. 19, no. 2, pp. 156–172, 2009.
- [33] B. C. Willis and Z. Borok, “TGF- beta -induced EMT : mechanisms and implications for fibrotic lung disease,” *Am. J. Physiol. Lung Cell. Mol. Physiol.*, vol. 293, no. 3, pp. L525-34, 2007.
- [34] R. A. Gould *et al.*, “Cyclic Mechanical Loading Is Essential for Rac1- Mediated Elongation and Remodeling of the Embryonic Mitral Valve Cyclic Mechanical Loading Is Essential for Rac1-Mediated Elongation and Remodeling of the Embryonic Mitral Valve,” *Curr. Biol.*, pp. 1–11, 2016.
- [35] V. C. Garside, A. C. Chang, A. Karsan, and P. A. Hoodless, “Co-ordinating Notch, BMP, and TGF- β signaling during heart valve development,” *Cell. Mol. Life Sci.*, vol. 70, no. 16, pp. 2899–2917, Aug. 2013.
- [36] Y. Wang *et al.*, “Endocardial to myocardial notch-wnt-bmp axis regulates early heart valve development.” *PLoS One*, vol. 8, no. 4, p. e60244, Jan. 2013.

- [37] I. C. Joziase *et al.*, “Genes in congenital heart disease: Atrioventricular valve formation,” *Basic Res. Cardiol.*, vol. 103, no. 3, pp. 216–227, 2008.
- [38] M. Azhar *et al.*, “Ligand-specific function of transforming growth factor beta in epithelial-mesenchymal transition in heart development,” *Dev. Dyn.*, vol. 238, no. 2, pp. 431–442, 2009.
- [39] E. R. Neptune *et al.*, “Dysregulation of TGF- β activation contributes to pathogenesis in Marfan syndrome,” *Nat. Genet.*, vol. 33, no. 3, pp. 407–411, 2003.
- [40] D. Lambrechts and P. Carmeliet, “Genetics in Zebrafish, Mice, and Humans to Dissect Congenital Heart Disease: Insights in the Role of VEGF,” *Curr. Top. Dev. Biol.*, vol. 62, pp. 189–224, 2004.
- [41] T. Yamagishi, K. Ando, and H. Nakamura, “Roles of TGF β and BMP during valvulo-septal endocardial cushion formation,” *Anat. Sci. Int.*, vol. 84, no. 3, pp. 77–87, Sep. 2009.
- [42] K. E. Roberts *et al.*, “BMP2 mutations in pulmonary arterial hypertension with congenital heart disease,” *Eur. Respir. J.*, vol. 24, no. 3, pp. 371–374, 2004.
- [43] V. Garg *et al.*, “Mutations in NOTCH1 cause aortic valve disease,” *Nature*, vol. 437, no. 7056, pp. 270–4, Sep. 2005.
- [44] A. R. Chiplunkar *et al.*, “Krüppel-Like Factor 2 Is Required for Normal Mouse Cardiac Development,” *PLoS One*, vol. 8, no. 2, 2013.
- [45] H. Nakajima and N. Mochizuki, “Flow pattern-dependent endothelial cell responses through transcriptional regulation,” *Cell Cycle*, vol. 16, no. 20, pp. 1893–1901, 2017.
- [46] E. Heckel *et al.*, “Oscillatory Flow Modulates Mechanosensitive *klf2a* Expression through *trpv4* and *trpp2* during Heart Valve Development,” *Curr. Biol.*, pp. 1–8, 2015.
- [47] A. D. Person, R. J. Garriock, P. A. Krieg, R. B. Runyan, and S. E. Klewer, “*Frzb* modulates Wnt-9a-mediated β -catenin signaling during avian atrioventricular cardiac cushion development,” *Dev. Biol.*, vol. 278, no. 1, pp. 35–48, 2005.
- [48] Z. Zhao and S. A. Rivkees, “Rho-associated kinases play a role in endocardial cell differentiation and migration,” *Dev. Biol.*, vol. 275, no. 1, pp. 183–191, 2004.
- [49] B. Hogers, M. C. Deruiter, A. C. G. Groot, and R. E. Poelmann,

- “Extraembryonic venous obstructions lead to cardiovascular malformations and can be embryolethal,” vol. 41, pp. 87–99, 1999.
- [50] J. T. Granados-Riveron and J. D. Brook, “The impact of mechanical forces in heart morphogenesis,” *Circ. Cardiovasc. Genet.*, vol. 5, no. 1, pp. 132–142, 2012.
- [51] H. C. Yalcin, A. Shekhar, T. C. McQuinn, and J. T. Butcher, “Hemodynamic patterning of the avian atrioventricular valve.,” *Dev. Dyn.*, vol. 240, no. 1, pp. 23–35, Jan. 2011.
- [52] P. R. Buskohl, J. T. Jenkins, and J. T. Butcher, “Computational simulation of hemodynamic-driven growth and remodeling of embryonic atrioventricular valves,” *Biomech. Model. Mechanobiol.*, vol. 11, no. 8, pp. 1205–1217, Nov. 2012.
- [53] I. Vesely and D. Boughner, “Analysis of the bending behaviour of porcine xenograft leaflets and of natural aortic valve material: Bending stiffness, neutral axis and shear measurements,” *J. Biomech.*, vol. 22, no. 6–7, 1989.
- [54] G. J. Mahler, C. M. Frendl, Q. Cao, and J. T. Butcher, “Effects of shear stress pattern and magnitude on mesenchymal transformation and invasion of aortic valve endothelial cells,” *Biotechnol. Bioeng.*, vol. 111, no. 11, pp. 2326–37, Nov. 2014.
- [55] P. R. Buskohl, R. a. Gould, and J. T. Butcher, “Quantification of embryonic atrioventricular valve biomechanics during morphogenesis,” *J. Biomech.*, vol. 45, no. 5, pp. 895–902, Mar. 2012.
- [56] N. Hu and E. B. Qark, “Hemodynamics of the Stage 12 to Stage 29 Chick Embryo,” 1989.
- [57] H. C. Yalcin, A. Shekhar, N. Nishimura, A. a Rane, C. B. Schaffer, and J. T. Butcher, “Two-photon microscopy-guided femtosecond-laser photoablation of avian cardiogenesis: noninvasive creation of localized heart defects.,” *Am. J. Physiol. Heart Circ. Physiol.*, vol. 299, no. 5, pp. H1728-35, Nov. 2010.
- [58] O. Silbert, Y. Wang, B. S. Maciejewski, H. Lee, S. K. Shaw, and J. Sanchez–Esteban, “ROLES OF RhoA AND Rac1 ON ACTIN REMODELING AND CELL ALIGNMENT AND DIFFERENTIATION IN FETAL TYPE II EPITHELIAL CELLS EXPOSED TO CYCLIC MECHANICAL STRETCH,” *Exp. Lung Res.*, vol. 34, no. 10, pp. 663–680, 2008.
- [59] H. Tan *et al.*, “Fluid flow forces and rhoA regulate fibrous development of the atrioventricular valves,” *Dev. Biol.*, vol. 374, no. 2, pp. 345–356, Feb. 2013.
- [60] Y. Fang and K. K. H. Svoboda, “Nicotine inhibits human gingival fibroblast

migration via modulation of Rac signalling pathways.," *J. Clin. Periodontol.*, vol. 32, no. 12, pp. 1200–7, Dec. 2005.

- [61] L. A. Huber, "Rab and rho GTPases are involved in specific response of periodontal ligament fibroblasts to mechanical stretching," vol. 1268, pp. 209–213, 1995.
- [62] J. T. Parsons, A. R. Horwitz, and M. a Schwartz, "Cell adhesion: integrating cytoskeletal dynamics and cellular tension.," *Nat. Rev. Mol. Cell Biol.*, vol. 11, no. 9, pp. 633–43, 2010.
- [63] P. P. Provenzano and P. J. Keely, "Mechanical signaling through the cytoskeleton regulates cell proliferation by coordinated focal adhesion and Rho GTPase signaling.," *J. Cell Sci.*, vol. 124, no. Pt 8, pp. 1195–1205, 2011.
- [64] E. Tzima, M. A. del Pozo, S. J. Shattil, S. Chien, and M. A. Schwartz, "Activation of integrins in endothelial cells by fluid shear stress mediates Rho-dependent cytoskeletal alignment.," *EMBO J.*, vol. 20, no. 17, pp. 4639–47, Sep. 2001.
- [65] J. T. Butcher, R. a. Norris, S. Hoffman, C. H. Mjaatvedt, and R. R. Markwald, "Periostin promotes atrioventricular mesenchyme matrix invasion and remodeling mediated by integrin signaling through Rho/PI 3-kinase," *Dev. Biol.*, vol. 302, no. 1, pp. 256–266, 2007.
- [66] S. Citi, D. Spadaro, Y. Schneider, J. Stutz, and P. Pulimeno, "Regulation of small GTPases at epithelial cell-cell junctions," *Mol. Membr. Biol.*, vol. 28, no. 7–8, pp. 427–444, 2011.
- [67] L. Van Aelst and C. D'Souza-Schorey, "Rho GTPases and signaling networks.," *Genes Dev.*, vol. 11, no. 18, pp. 2295–2322, 1997.
- [68] Y. Zhang *et al.*, "CD44 acts through RhoA to regulate YAP signaling.," *Cell. Signal.*, vol. 26, no. 11, pp. 2504–13, Nov. 2014.
- [69] Y. E. Zhang, "Non-Smad pathways in TGF-beta signaling.," *Cell Res.*, vol. 19, no. 1, pp. 128–39, 2009.
- [70] R. Derynck and Y. E. Zhang, "Smad-dependent and Smad-independent pathways in TGF-beta family signalling.," *Nature*, vol. 425, no. 6958, pp. 577–584, 2003.
- [71] P. P. Provenzano, D. R. Inman, K. W. Eliceiri, and P. J. Keely, "Matrix density-induced mechanoregulation of breast cell phenotype, signaling and gene expression through a FAK-ERK linkage," *Oncogene*, vol. 28, no. 49, pp. 4326–4343, 2009.

- [72] T. Banjo *et al.*, “Haemodynamically dependent valvulogenesis of zebrafish heart is mediated by flow-dependent expression of miR-21,” *Nat. Commun.*, vol. 4, no. May, p. 1978, Jan. 2013.
- [73] P. C. Smith, M. Cáceres, and J. Martinez, “Induction of the myofibroblastic phenotype in human gingival fibroblasts by transforming growth factor-beta1: role of RhoA-ROCK and c-Jun N-terminal kinase signaling pathways,” *J. Periodontal Res.*, vol. 41, no. 5, pp. 418–25, Oct. 2006.
- [74] A. V. Bakin, A. K. Tomlinson, N. A. Bhowmick, H. L. Moses, and C. L. Arteaga, “Phosphatidylinositol 3-kinase function is required for transforming growth factor ??-mediated epithelial to mesenchymal transition and cell migration,” *J. Biol. Chem.*, vol. 275, no. 47, pp. 36803–36810, 2000.
- [75] J. Vermot *et al.*, “Reversing blood flows act through klf2a to ensure normal valvulogenesis in the developing heart,” *PLoS Biol.*, vol. 7, no. 11, pp. 12–14, Nov. 2009.
- [76] A. D. Egorova *et al.*, “Tgf β /Alk5 signaling is required for shear stress induced klf2 expression in embryonic endothelial cells,” *Dev. Dyn.*, vol. 240, no. 7, pp. 1670–80, Jul. 2011.
- [77] P. Dijke, A. D. Egorova, M. T. H. Goumans, R. E. Poelmann, and B. P. Hierck, “TGF- β Signaling in Endothelial-to- Mesenchymal Transition : The Role of Shear Stress and Primary Cilia,” *Sci. Signal.*, vol. 5, no. 212, pp. 1–3, 2012.
- [78] A. D. Egorova *et al.*, “Lack of primary cilia primes shear-induced endothelial-to-mesenchymal transition,” *Circ. Res.*, vol. 108, no. 9, pp. 1093–1101, 2011.
- [79] A. Abuammah *et al.*, “New developments in mechanotransduction: Cross talk of the Wnt, TGF- β and Notch signalling pathways in reaction to shear stress,” *Curr. Opin. Biomed. Eng.*, vol. 5, pp. 96–104, 2018.
- [80] H. Clevers, “Wnt/ β -Catenin Signaling in Development and Disease,” *Cell*, vol. 127, no. 3, pp. 469–480, 2006.
- [81] F. M. Bosada, V. Devasthali, K. A. Jones, and K. Stankunas, “Wnt / β -catenin signaling enables developmental transitions during valvulogenesis,” pp. 1041–1054, 2016.
- [82] S. Xu and A. I. Gotlieb, “Wnt3a/??-catenin increases proliferation in heart valve interstitial cells,” *Cardiovasc. Pathol.*, vol. 22, no. 2, pp. 156–166, 2013.
- [83] D. Wu and W. Pan, “GSK3: a multifaceted kinase in Wnt signaling,” *Trends Biochem. Sci.*, vol. 35, no. 3, pp. 161–168, 2010.
- [84] L. M. Goddard *et al.*, “Hemodynamic Forces Sculpt Developing Heart Valves

- through a KLF2-WNT9B Paracrine Signaling Axis,” *Dev. Cell*, vol. 43, no. 3, pp. 274-289.e5, 2017.
- [85] A. C. Y. Chang *et al.*, “A Notch-dependent transcriptional hierarchy promotes mesenchymal transdifferentiation in the cardiac cushion,” *Dev. Dyn.*, vol. 243, no. 7, pp. 894–905, 2014.
- [86] F. a High *et al.*, “An essential role for Notch in neural crest during cardiovascular development and smooth muscle differentiation.,” *J. Clin. Invest.*, vol. 117, no. 2, pp. 353–363, 2007.
- [87] C. G. Hansen, T. Moroishi, and K. L. Guan, “YAP and TAZ: A nexus for Hippo signaling and beyond,” *Trends Cell Biol.*, vol. 25, no. 9, pp. 499–513, 2015.
- [88] S. E. Lindsey, J. T. Butcher, and H. C. Yalcin, “Mechanical regulation of cardiac development.,” *Front. Physiol.*, vol. 5, no. August, p. 318, Jan. 2014.
- [89] R. a. Gould, L. M. Aboulmouna, J. D. Varner, and J. T. Butcher, “Hierarchical approaches for systems modeling in cardiac development,” *Wiley Interdiscip. Rev. Syst. Biol. Med.*, vol. 5, no. 3, p. n/a-n/a, 2013.
- [90] J. Butcher, G. Mahler, and L. Hockaday, “Aortic valve disease and treatment: The need for naturally engineered solutions,” *Adv. Drug Deliv. Rev.*, vol. 63, no. 4–5, pp. 242–268, Apr. 2011.
- [91] A. Mizuno, N. Matsumoto, M. Imai, and M. Suzuki, “Impaired osmotic sensation in mice lacking TRPV4.,” *Am. J. Physiol. Cell Physiol.*, vol. 285, no. 1, pp. C96–C101, 2003.
- [92] W. Liedtke and J. M. Friedman, “Abnormal osmotic regulation in *trpv4*^{-/-} mice.,” *Proc. Natl. Acad. Sci. U. S. A.*, vol. 100, no. 23, pp. 13698–13703, 2003.
- [93] W. Liedtke, D. M. Tobin, C. I. Bargmann, and J. M. Friedman, “Mammalian TRPV4 (VR-OAC) directs behavioral responses to osmotic and mechanical stimuli in *Caenorhabditis elegans*.,” *Proc. Natl. Acad. Sci. U. S. A.*, vol. 100 Suppl, pp. 14531–14536, 2003.
- [94] K. J. Schipke, S. D. Filip To, and J. N. Warnock, “Design of a Cyclic Pressure Bioreactor for the *Ex Vivo* Study of Aortic Heart Valves.,” *J. Vis. Exp.*, no. 54, pp. 3–7, 2011.
- [95] Y. Xing, J. N. Warnock, Z. He, S. L. Hilbert, and A. P. Yoganathan, “Cyclic pressure affects the biological properties of porcine aortic valve leaflets in a magnitude and frequency dependent manner.,” *Ann. Biomed. Eng.*, vol. 32, no. 11, pp. 1461–70, Nov. 2004.

- [96] Y. Xing, Z. He, J. N. Warnock, S. L. Hilbert, and A. P. Yoganathan, “Effects of constant static pressure on the biological properties of porcine aortic valve leaflets.,” *Ann. Biomed. Eng.*, vol. 32, no. 4, pp. 555–62, Apr. 2004.
- [97] E. a. Schwartz, R. Bizios, M. S. Medow, and M. E. Gerritsen, “Exposure of Human Vascular Endothelial Cells to Sustained Hydrostatic Pressure Stimulates Proliferation : Involvement of the V Integrins,” *Circ. Res.*, vol. 84, no. 3, pp. 315–322, Feb. 1999.
- [98] M. P. Stewart, J. Helenius, Y. Toyoda, S. P. Ramanathan, D. J. Muller, and A. a Hyman, “Hydrostatic pressure and the actomyosin cortex drive mitotic cell rounding.,” *Nature*, vol. 469, no. 7329, pp. 226–230, 2011.
- [99] M. M. Knight, T. Toyoda, D. a Lee, and D. L. Bader, “Mechanical compression and hydrostatic pressure induce reversible changes in actin cytoskeletal organisation in chondrocytes in agarose.,” *J. Biomech.*, vol. 39, no. 8, pp. 1547–51, Jan. 2006.
- [100] M. a. Haider, R. C. Schugart, L. a. Setton, and F. Guilak, “A mechano-chemical model for the passive swelling response of an isolated chondron under osmotic loading,” *Biomech. Model. Mechanobiol.*, vol. 5, no. 2–3, pp. 160–171, 2006.
- [101] S. J. Andrewartha, H. Tazawa, and W. W. Burggren, “Hematocrit and blood osmolality in developing chicken embryos (*Gallus gallus*): In vivo and in vitro regulation,” *Respir. Physiol. Neurobiol.*, vol. 179, no. 2–3, pp. 142–150, 2011.
- [102] K. Strange, “Cellular volume homeostasis.,” *Adv. Physiol. Educ.*, vol. 28, no. 1–4, pp. 155–159, 2004.
- [103] J. M. Baltz and A. P. Tartia, “Cell volume regulation in oocytes and early embryos: Connecting physiology to successful culture media,” *Hum. Reprod. Update*, vol. 16, no. 2, pp. 166–176, 2009.
- [104] E. K. Hoffmann, I. H. Lambert, and S. F. Pedersen, “Physiology of cell volume regulation in vertebrates.,” *Physiol. Rev.*, vol. 89, no. 1, pp. 193–277, 2009.
- [105] H. Jiang and S. X. Sun, “Cellular pressure and volume regulation and implications for cell mechanics,” *Biophys. J.*, vol. 105, no. 3, pp. 609–619, 2013.
- [106] D. P. Judge and H. C. Dietz, “Marfan ’ s syndrome,” 2005.
- [107] M. Godfrey *et al.*, “Abnormal morphology of fibrillin microfibrils in fibroblast cultures from patients with neonatal Marfan syndrome,” *Am. J. Pathol.*, vol. 146, no. 6, pp. 1414–1421, 1995.
- [108] C. M. Ng *et al.*, “TGF- β -dependent pathogenesis of mitral valve prolapse in a

- mouse model of Marfan syndrome,” *J. Clin. Invest.*, vol. 114, no. 11, pp. 1586–1592, 2004.
- [109] A. Aleksandrova *et al.*, “Convective tissue movements play a major role in avian endocardial morphogenesis,” *Dev. Biol.*, vol. 363, no. 2, pp. 348–361, 2012.
- [110] S. Lahaye, J. Lincoln, and V. Garg, “Genetics of Valvular Heart Disease,” 2014.
- [111] B. Lee *et al.*, “Linkage of Marfan syndrome and a phenotypically related disorder to two different fibrillin genes,” *Nature*, vol. 352, no. 6333, pp. 330–334, 1991.
- [112] L. Pereira *et al.*, “Targetting of the gene encoding fibrillin-1 recapitulates the vascular aspect of marfan syndrome,” *Nat. Genet.*, vol. 17, no. 2, pp. 218–218, 1997.
- [113] B. L. Loeys *et al.*, “A syndrome of altered cardiovascular, craniofacial, neurocognitive and skeletal development caused by mutations in TGFBR1 or TGFBR2,” *Nat. Genet.*, vol. 37, no. 3, pp. 275–281, 2005.
- [114] K. Tamura, Y. Fukuda, M. Ishizaki, Y. Masuda, N. Yamanaka, and V. J. Ferrans, “Abnormalities in elastic fibers and other connective-tissue components of floppy mitral valve,” *Am. Heart J.*, vol. 129, no. 6, pp. 1149–1158, 1995.
- [115] J. C. Chisholm, “Mitral valve prolapse syndrome associated with congenital bicuspid aortic valve,” *J. Natl. Med. Assoc.*, vol. 73, no. 10, pp. 921–923, 1981.
- [116] M. M. Lockhart *et al.*, “Alk3 mediated Bmp signaling controls the contribution of epicardially derived cells to the tissues of the atrioventricular junction,” *Dev. Biol.*, vol. 396, no. 1, pp. 8–18, 2014.
- [117] R. Sainger *et al.*, “Human myxomatous mitral valve prolapse: Role of bone morphogenetic protein 4 in valvular interstitial cell activation,” *J. Cell. Physiol.*, vol. 227, no. 6, pp. 2595–2604, 2012.
- [118] T. Glass and H. Empty, “Genetics of Congenital Heart Disease The Glass Half Empty,” pp. 1270–1283, 2015.
- [119] M. Tartaglia *et al.*, “Mutations in PTPN11, encoding the protein tyrosine phosphatase SHP-2, cause Noonan syndrome,” *Nat. Genet.*, vol. 29, no. 4, pp. 465–468, 2001.
- [120] T. Araki *et al.*, “Mouse model of Noonan syndrome reveals cell type- and gene dosage-dependent effects of Ptpn11 mutation,” *Nat. Med.*, vol. 10, no. 8, pp.

849–857, 2004.

- [121] B. C. W. Groenendijk *et al.*, “Changes in shear stress-related gene expression after experimentally altered venous return in the chicken embryo,” *Circ. Res.*, vol. 96, no. 12, pp. 1291–8, Jun. 2005.
- [122] B. C. W. Groenendijk, B. P. Hierck, A. C. Gittenberger-De Groot, and R. E. Poelmann, “Development-related changes in the expression of shear stress responsive genes KLF-2, ET-1, and NOS-3 in the developing cardiovascular system of chicken embryos,” *Dev. Dyn.*, vol. 230, no. 1, pp. 57–68, May 2004.
- [123] V. Menon, J. Eberth, R. Goodwin, and J. Potts, “Altered Hemodynamics in the Embryonic Heart Affects Outflow Valve Development,” *J. Cardiovasc. Dev. Dis.*, vol. 2, no. 2, pp. 108–124, 2015.
- [124] K. K. Linask, M. Han, and N. J. M. Bravo-Valenzuela, “Changes in vitelline and utero-placental hemodynamics: implications for cardiovascular development,” *Front. Physiol.*, vol. 5, no. November, p. 390, Jan. 2014.

CHAPTER 2.

COMPRESSIVE STRESS INDUCES BMP SIGNALING IN COOPERATION
WITH MEK-ERK TO DRIVE GROWTH OF THE ATRIOVENTRICULAR VALVE

2.1 Summary

Successful morphogenesis and maturation of the atrioventricular (AV) valve requires the integration of multiple biomolecular signals including hemodynamically generated mechanical loads. While multiple sources of evidence support that mechanical forces influence and direct valve development, the roles of specific modes of stress, and how those signals are conveyed by cells into tissue phenotypes remains unclear. Here, we interrogated the roles of tensile and compressive loads on valve growth and shaping using osmotic pressure to induce the desired loads. We accomplished this by culturing AV cushions from HH25, HH34 and HH40 chicken embryos in hanging drop culture, isolating cushions from other stimuli and eliminating the need for tissue attachment. We found that compressive stress drives a growth phenotype that is 20%-30% larger than unloaded conditions and is characterized by additional proliferation and NM-myosin II activity during culture and reduced levels of compaction, whereas tensile stress increased compaction. We determined Compressive stress is acting through BMP signaling, as identified through pSmad15 activity, to increase proliferation and decrease cell contractility. We also identified MEK-ERK as being essential for both compressive stress and BMP2 mediation of compaction. We were able to identify a subsurface region within the cushion where this signaling was most pronounced. We further demonstrated that the effects of osmotic stress are conserved through the condensation and elongation stages of development where interactions with collagen matrix preserve leaflet morphology. We demonstrated osmotic stress as both a method for applying bulk tissues stresses and elucidated on its potential effects when induced by other mechanical loads. Overall,

our study establishes a mechanosensitive role for BMP in controlling AV valve morphogenesis in response to compressive stress.

2.2 Introduction

Defects of the valvuloseptal apparatus that form during embryogenesis can lead to many clinically impactful disorders of the valves themselves as well as the underlying heart muscle. Successful development of the atrioventricular (AV) valve requires the integration of multiple biomolecular signals to specify the precise shape and size of the AV septum and valve leaflets. Without these precise inputs, the heart will be subjected to undue stresses caused by reduced pumping efficiency and non-physiological mechanical loading. Evidence that disrupting physiological flow through the heart will lead to defective morphogenesis has been established for some time [1]. Quantitative study of the flow fields in valve development have led to a quantitative understanding of mechanical stress fields throughout development that include both shear stress profiles and pressure drops [2]. The role of shear stress has been studied as it applied to endothelial behavior and signaling [3]. Studies exposing valve cushion explants in a flow bioreactor have shown that the valve elongation can be promoted by unidirectional flow [4]. However, the influence of mechanical signaling on mid to late stages of development, during determine the growth, the elongation and condensation phases, is less understood [5]. Further, the mechanical environment of the valve in the full flow field includes multiple components that could have distinct and shared effects. The role of pressures and tensions, i.e. stresses arising from normal forces on the valve, has not been clearly defined, though these components increase rapidly in strength by mid development [2], [6]. Such forces arise from the valve resisting back

flow, experiencing surface tractions, and systemic pressure, and internal residual stresses. Normal forces (i.e. forces acting perpendicular to the tissue surface) have been implicated in adult disease clinically [7], as well as in adult valve models [8]. Finite element modeling has suggested a role for normal forces in driving valve growth in development but without resolving the biological mechanisms involved [6]. In this study, we seek to understand the role of the normal forces, which produce loads on the cushion in both compressive and tensile modes.

Osmotic stress is a long established method to study the effect of bulk tissue mechanical loads in cartilage, where tissue is too small and amorphous to secure on a traditional testing device [9]. Hypo-osmotic stress has been used to measure mechanical properties of collagenous matrix by inducing tensile loads [10]. Both hypo and hyper osmotic stresses have been used to assess mechanically induced signaling in chondrocytes [11]. Hyper osmotic stress was shown to regulate matrix composition in articular cartilage [12]. Further, this study demonstrated that sucrose is a way to induce hyper-osmotic stress without disrupting ion-balance [12].

Additionally, the osmotic stress method has been applied to embryonic organoids and tissue spheroid systems. Hyper-osmotic stress has been used to measure the mechanical behaviors of embryonic gut tissues [13]. Of important interest, osmotic stress has been used to identify pressure sensitive signaling pathways in tumor spheroid models [14], [15]. Overall, in these different systems, hyper-osmotic stress has been used to create compressive loads by inducing a net outward flow of water from the tissue and the underlying cells. On the other hand, hypo-osmotic stress has

been used to create tensile loads by inducing a net inward flow of water into the tissue and into the underlying cells.

Further, while the roles of TGF β and BMP signaling in remodeling are well established [16], the role of these central pathways in responding to mechanical signals is not well understood. Recent evidence supports that BMP is involved with signaling in the context of shear stress [17]. Equally important is how these pathways control cellular behaviors such as contractility, migration and traction forces through Non-muscle myosins and activating GTPases (e.g. Rho-ROCK) to produce a properly shaped and sized valve [18], [19].

Here, we use altered media formulations to induce osmotic stress and thereby apply whole-tissue, compressive (C) / hypertonic or tensile (T) / hypotonic loads to intact, freshly-isolated AV cushion explants. We apply these loads in a hanging drop culture system to isolate explants from surfaces that would induce migration or apply additional traction forces [20]. We further benefited from the osmotic stress method by eliminating the need for tissue anchorage that could lead to stress concentrations or cell migration. Based on a computational model of valve growth [6] and the matrix remodeling effects caused by hyper-osmotic stress in cartilage [12], we expected that compressive stress would drive the growth the valve. In this study, we demonstrated that mechanical stresses induced by osmotic stress can alter cushion size through changes in contractile and proliferative behaviors. We further identified that these mechanisms were mediated by BMP and MAPK signaling that is occurring near the cushion surface to elicit changes in remodeling.

2.3 Methods

2.3.1 Avian animal model

Chick and quail models are well-established tools for studying development [21]. The four chambered avian heart develops in a manner that mirrors that of human heart development [22]. The chick model is staged using the Hamburger Hamilton staging system, developed in 1951, allowing for consistent assessment of embryos at a particular embryonic time point [23].

2.3.2 AV cushion isolation and hanging drop culture

AV cushions were isolated from HH25, HH34, and HH40 chicken embryos. Whole tissue explants were cultured in 20 μ l hanging drops, where the explant would settle at the apex [24].

2.3.3 Cushion compaction measurement

Cushions were imaged fresh after placement in hanging drops and then again after 10h, 18h, or 24h in culture using an upright brightfield microscope (Zeiss V20 Stereoscope with Retiga 4000R camera). Tissue areas were measured in FIJI and a compaction ratio was measured by computing the ratio of final to initial area. In Appendix A, we demonstrate that tissue area is directly proportional to the tissue volume.

2.3.4 Media and application of osmotic stress

Control (unloaded condition) media consisted of 1xM199 (290 mOSM) with the following additives constant for all medias: 1% penicillin-streptomycin, 2.2g/L sodium bicarbonate, 1% chick serum and 0.1% insulin-transferrin-selenium. Hypoosmotic conditions were achieved using 0.5x M199 (173 mOSM, -40%).

Hyperosmotic media was made by making a 0.14 M solution in 1xM199 (446 mOSM, +50%). Osmolarities were measured using a freezing point depression osmometer courtesy of the Cornell vet school, calibrated using a 290 mOsm standard. Osmotic formulations were found to change stoichiometrically (linearly) with the addition or removal of solutes (Table 2.1).

Formulation	Reading (mOSM/kg)	Perturbation
STRD(290)	288	Standard
Media	295	0%
Hypo-osmotic (0.5xM199 with equal buffer)	174	-41%
Hyper-osmotic [0.14M] sucrose	446	51%

Table 2.1. Osmolality measurements for control, hypo, and hyper-osmotic medias acquiring using freezing point depression osmometry

2.3.5 Cytokines and inhibitors

The following cytokines were added to culture media: BMP2 (10ng/ml, Krackeler Scientific), TGF β 3 (2ng/ml, Peprotech). The following Inhibitors were added to culture media: ROCK inhibitor, Y-27632 (10 uM, Cell Signaling). Alk2/3 inhibitor, LDN193189 (1uM, Sigma), Alk 5/7 inhibitor SB431542 (2.6uM, Sigma), and MEK inhibitor, U0126 (10uM, Sigma), and NM-Myosin II inhibitor (+-) Blebbistatin (1uM-10uM, VWR/BioVision).

Target	Name	Concentration	Provider	Dosage reference
ROCK	Y-27632	10 uM	Cell Signaling	[18]
Alk2/3	LDN193189	1 uM	Sigma	[25], [26]
Alk 5/7	SB431542	2.6 uM	Sigma	[20]
MEK	U0126	10 uM	Sigma	[27]
NM-Myosin II	(+) (-) Blebbistatin	1uM-10uM	VWR BioVision	Manufacture solubility and empirical titration

Table 2.2. Summary table of inhibitors

2.3.6 Left atrial ligation

Fertilized White Leghorn chicken eggs were incubated in a 38°C forced-draft incubator to HH21 (3.5 days), at which point the eggs were windowed and embryos were incubated *in ovo* at 38°C in a Hovabator Styrofoam incubator. On day 4 and before AV septation, an overhand knot of 10-0 nylon suture loop was placed across a portion of either the left atrium and tightened (or removed for Sham control), resulting in a partially constricted the left AV orifice. In ovo incubation continued until HH31 (day 7). This method is described in further detail [28] and has been established as a means to decrease ventricular preload [18], [29].

2.3.7 Immunofluorescence/immunohistochemistry

Cushions were fixed in 4% PFA for 30 minutes at 4°C, permeabilized with 0.02% triton-x and blocked using 3% BSA, 20mM MgCl, 0.3% Tween 20, 0.3M Glycine, and 5% Donkey serum in 1xTBS. Samples were incubated with the following primary antibodies at 1:100 dilution unless noted: PHH3 (mouse or rat, Cell Signaling), Caspas3 (Mouse, Cell Signaling), alpha-smooth-muscle-actin-cy3 conjugated (Mouse, Sigma), RhoA-GTP (Mouse, Cell Signaling), Rac1-GTP (Mouse, Cell Signaling), pERK (Rabbit, Cell Signaling), pSmad2/3 (Rabbit, Cell Signaling), pSmad1/5 Cell Signaling, pSER19 on myosin light chain kinase (Rabbit, 1:50, Thermo-Scientific). Antibodies requiring amplification (pERK, pSmad1/5, pSmad2/3) were also incubated in 1% H₂O₂ in PBS for 40 minutes, stained with HRP secondaries and incubated using a TSA kit. Secondary antibodies were applied in 5% BSA in TBS. After staining, cushions were optically cleared using HISTO-M solution (Visikol).

Stained cushions were imaged in glass-bottomed 96-well plates using an inverted Zeiss LSM 710 microscope.

For LAL sections, whole day 7 chick hearts were flushed with TBS and fixed with 4% PFA for overnight, embedded with paraffin, and sectioned. Antigen retrieval was done with citrate buffer. Endogenous peroxidase was blocked with 1% H₂O₂ in PBS for 40 minutes. Sections were then permeabilized and blocked with the buffer as above. Sections were incubated with pSmad15 (rabbit, 1:100, Cell Signaling) or pERK12 (rabbit, 1:100, Cell Signaling), and MF20 (mouse, 1:100, Thermo-Scientific). Sections were then incubated with donkey anti-rabbit HRP (1:100, Thermo-Scientific) and donkey anti-mouse AF568 (1:100, Thermo-Scientific). Signal was amplified using TSA Amplification Kit (Perkin Elmer).

2.3.8 Live Imaging

Cushion explants were imaged at 150x in hanging drops using an upright Zeiss Discovery V.20 stereoscope after being freshly isolated and at 10, 18 and 24 hours. Live/Dead images were collected using Calcein AM green and Ethidium homodimer, using GFP and Texas red filters and a Halogen light source.

In order to extract spatial information from the cushion data, it was necessary to consider a simple way to partition the space that would allow for quantitative comparisons between cushions of different sizes and cell densities.

2.3.9 Stain localization analysis

We considered each nucleus or positive cell as an object existing at a radius (r) from a centroid calculated from the location of all nuclei. This approach allows for a ROI to be defined ad hoc from the raw data, as opposed to requiring predefined

segmentation steps to identify the total cushion area. The radii were then normalized on a per cushion basis by averaging the radii of M number of cells farthest from the tissue center (i.e. those with the largest radii) and dividing all radii by this average max radius R_{\max} creating r_{norm} values. This approach prevents small surface irregularities from greatly affecting normalization. With proper selection of M , this also leads to the inclusion of only surface/endothelial cells, defining a biologically reasonable condition for $r_{\text{norm}} = 1$. Cells at $r_{\text{norm}} > 1$ reflect deviations in the cushion size from a perfectly smooth circle. Outliers, e.g. due to another cushion at an image edge, will show up generally at $r_{\text{norm}} > 1.2$. The same procedure is applied to the objects from the stain image channel to create $r_{\text{norm, stain}}$. The resulting distributions can be binned into bins of equal area by computing radii of those circles with the following formula:

$$r_{\text{circle}}(i) = \sqrt{\frac{(i + 1) * A_0}{\pi}}$$

where i is the circle index, with the central circle being 0, and A_0 is a selected constant area.

The implementation used, written in R , can be found in Appendix E. The code includes a function to apply to one sample, a wrapper function for multiple samples, and these functions in use for a particular dataset.

2.4 Results

2.4.1 Osmotic pressure controls compaction phenotype in vitro

We use altered media formulations to induce osmotic stress and thereby apply whole-tissue, compressive (C) / hypertonic or tensile (T) / hypotonic loads to intact, freshly-isolated AV cushion explants. We refer to the osmotically balanced media control as the unloaded condition (U).

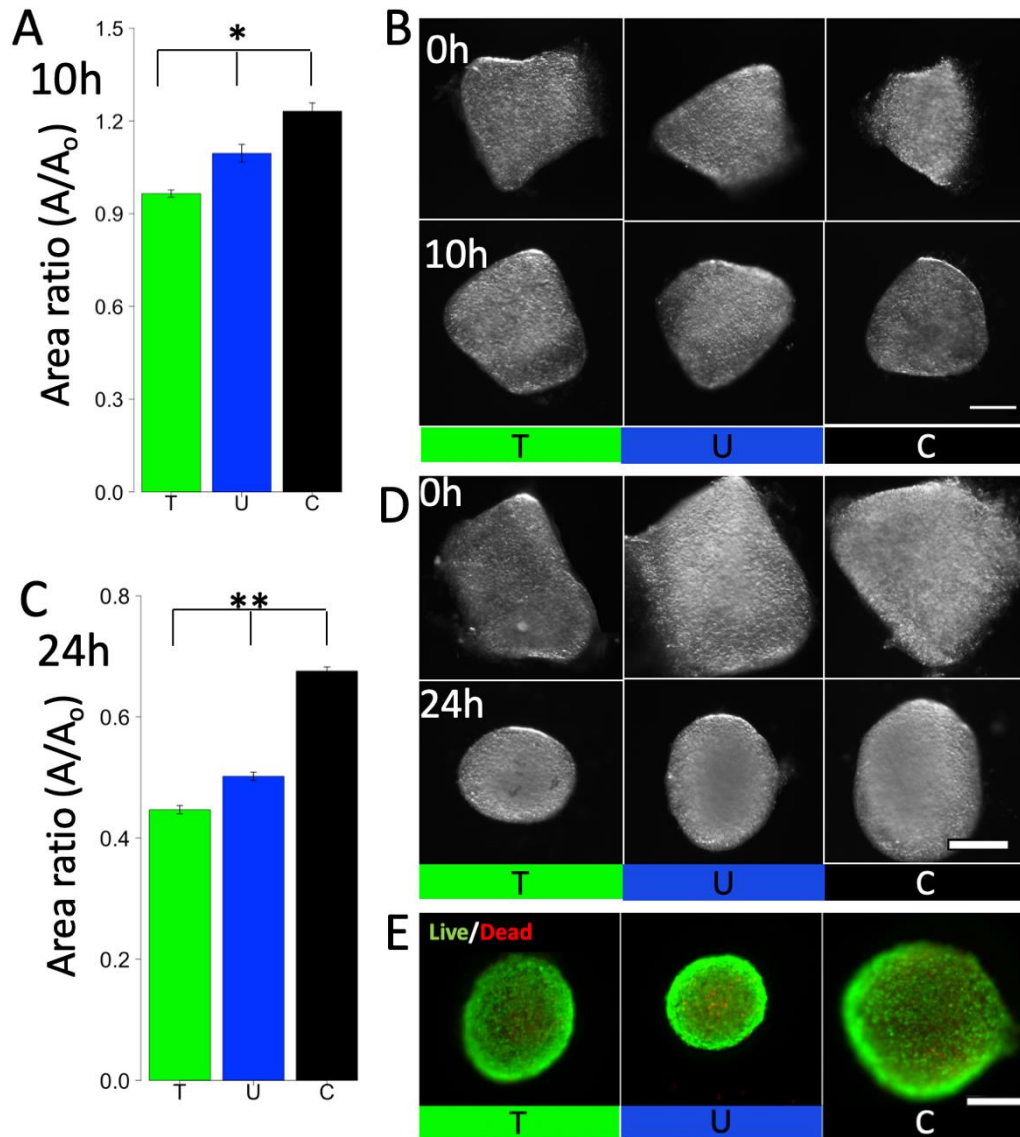


Figure 2.1. Osmotic stress regulates tissue compaction. (A) Compaction trend at 10h * $p < 0.05$ between conditions (B) Endpoint brightfield images of HH25 AV cushions compacting and rounding over 10h (C) Compaction trend at 24h ** $p < 0.005$ between conditions (D) Endpoint brightfield images of HH25 AV cushions compacting and rounding over 24h (E) Live dead at 24h showing $> 90\%$ viability (Live-calcian AM, dead-ethidium homodimer) Scale bars $200\mu\text{m}$, $n = 4-6$ cushions per condition from 3-6 independent experiments, SEM shown

Cushions initially continued to grow in culture, followed by a period of compaction. Osmotic pressure had effects during both periods. At 10hrs, compressive stress promoted a growth phenotype (area ratio larger than 1.0) (Figure 2.1A), whereas, unloaded and tensile loaded cushions compacted, with the compaction being significantly more for tensile loading. All cushions rounded at the edges but retained an overall trapezoidal shape (Figure 2.1B). At 24hrs, all tissues have compacted significantly, but compressive loaded cushions continued to be the largest and tensile loaded cushions, the smallest (Figure 2.1C). By 24hrs, all cushions rounded from a trapezoidal shape into a circular or elliptical shape (Figure 2.1D). We confirmed that cushions were viable in loaded and unloaded conditions at 24h (Figure 2.1E). Proliferation increased with compressive stress compaction at 10hrs (Figure 2.2A) whereas there is limited apoptosis until after 10hrs, with no differences between the conditions (Figure 2.3A). However, there were no significant differences in apoptosis or proliferation at 24hrs (Figure 2.3B). Osmotic stress did not significantly affect cell density (Figure 2.2D) or apparent tissue stiffness (Figure 2.4A,B).

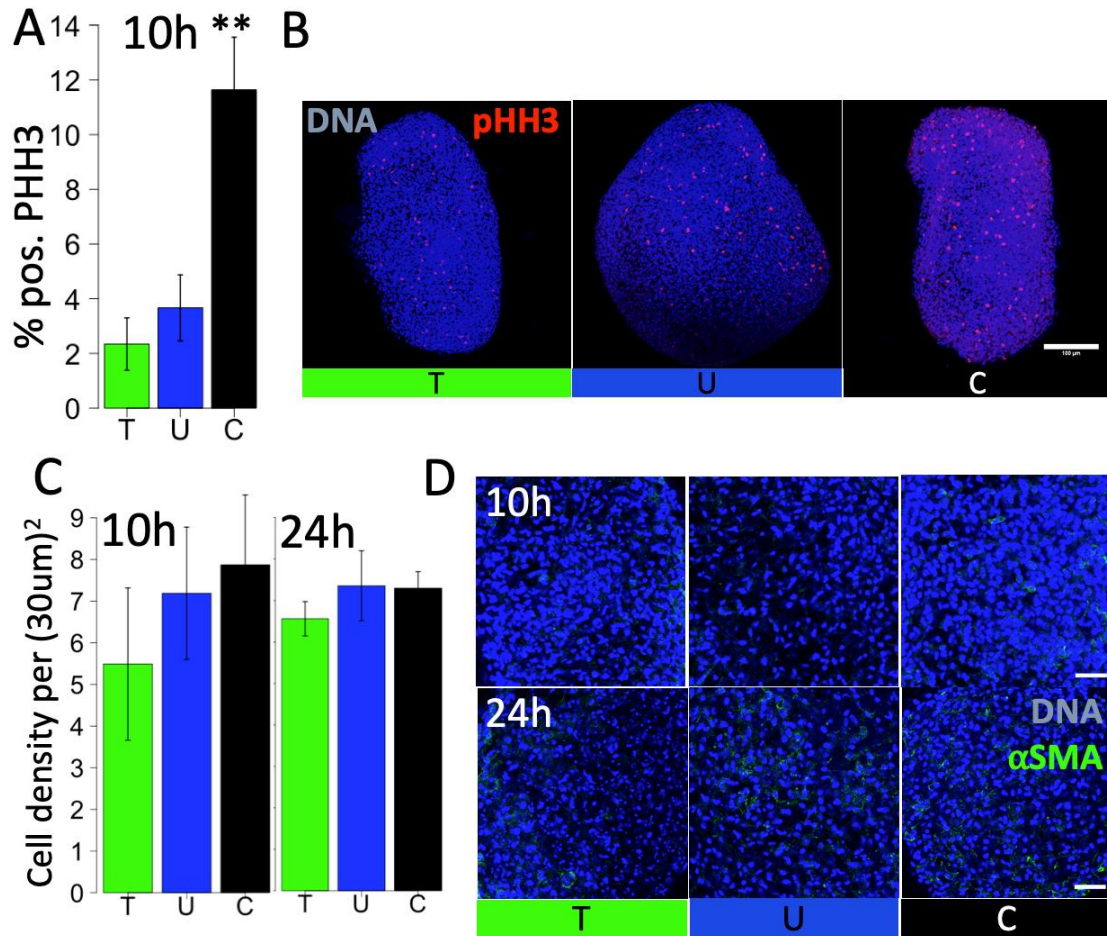


Figure 2.2. Osmotic stress regulates tissue growth (A) Cell densities at 10hrs and 24hrs, scale bar 200 μ m (B) Number of cells in mitosis (phosphohistone-3) at 10hrs ** $p < 0.005$ between conditions (C) Whole mount IF images of 10 hr cushions stained for pHH3 (D) Example images from cushions used to quantify density, $n = 3-4$ cushions per condition from 3 independent experiments, SEM shown

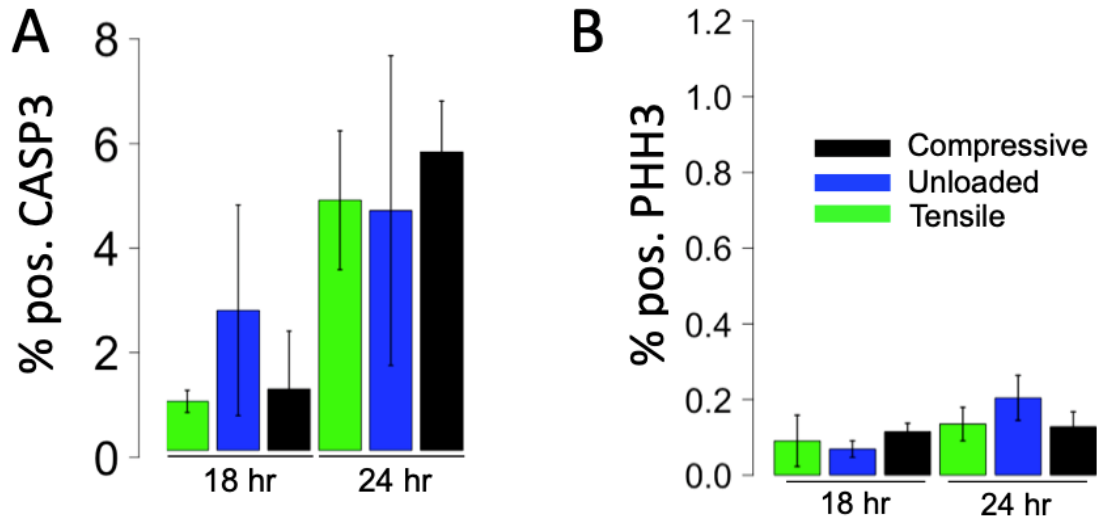


Figure 2.3. Proliferation and apoptosis largely similar during compaction phase(A) Apoptosis increases uniformly over the treatments at and beyond 18hrs (B) Proliferation is uniformly low after 10hrs, n = 4-6 cushions per condition, SD shown

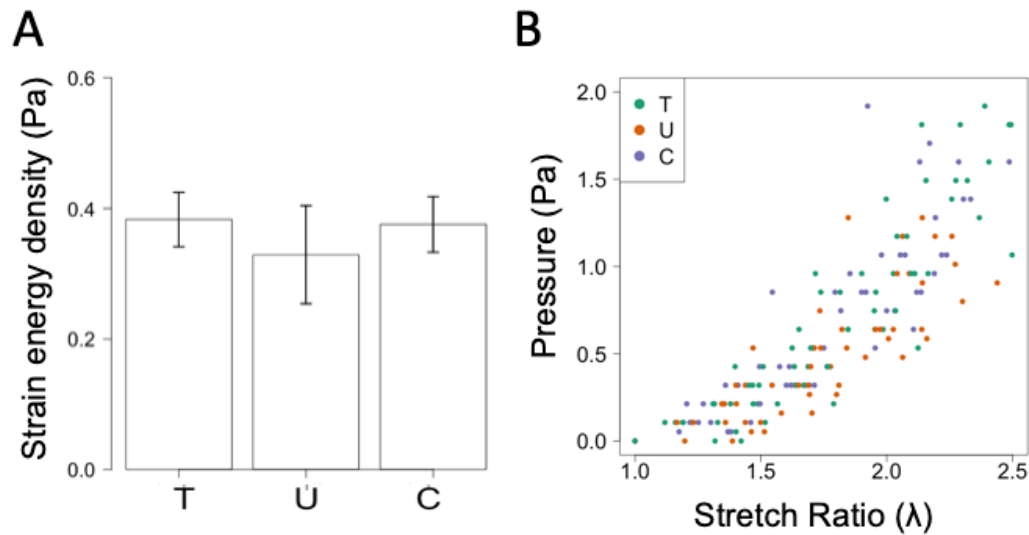


Figure 2.4. Osmotic stress does not alter tissue stiffness (A) Micropipette aspiration measurements of strain energy density, (B) Mechanical response curves for the cushions tested $n = 5-6$ cushions per condition per 3 independent experiments, SEM shown

2.4.2 Osmotic stress compaction phenotype is TGF β independent

Initially, we examined if TGF β , which we previously found could drive a growth phenotype, was being activated by compressive stress [20]. We however found no significant differences in pSmad2/3 nuclear localization between osmotic treatments (Figure 2.5A) Further, Alk5/7 inhibitor SB431542 (2.6 μ M), which blocks TGF β 2/3 signaling, did not alter the effects of compressive stress with confirmed successful inhibition of Smad2/3 phosphorylation (Figure 2.5B,C). BMP signaling modulates osmotic stress to drive tissue compaction

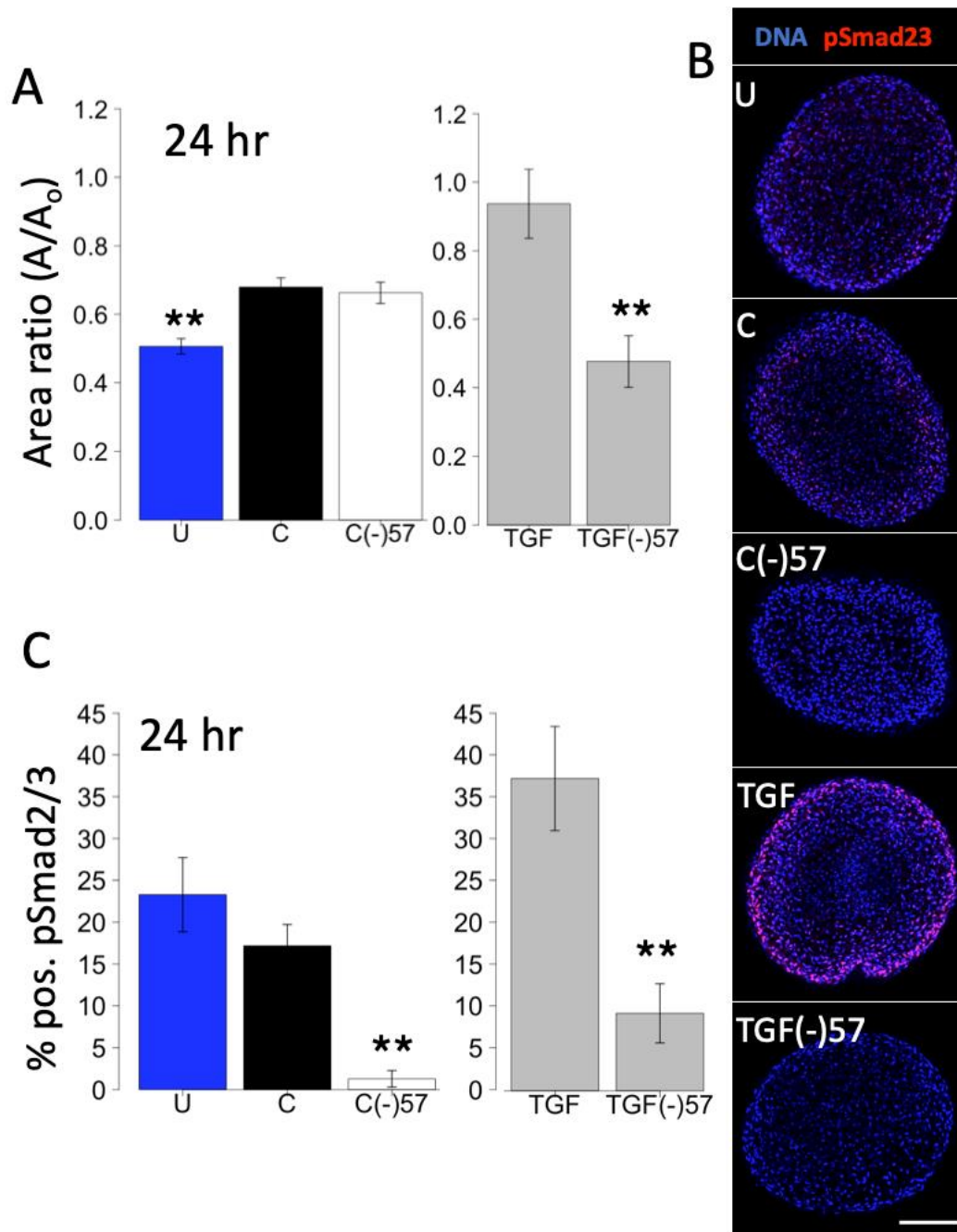


Figure 2.5. Osmotic stress compaction phenotype is pSmad2/3 independent (A) Compaction trend at 24hrs ** $p < 0.005$ between conditions (B) Number of cells positive for pSmad2/3 at 24hrs (D) Whole mount IF images of 24 hr cushions stained for pSmad2/3, scale bar 100uM, $n=6-8$ cushions per condition, SD shown

Given the role of BMPs in valve maturation, but unclear role in growth related mechanosensitive mechanisms, we examined the role of BMP2 signaling as an alternative to the TGF β pathway [30]. During the compaction timeframe (after 10hrs), we found significant differences in pSmad1/5 nuclear localization, with compressive stress showing the highest pSmad1/5 activity, suggesting elevated BMP signaling (Figure 2.6A,B). Combination of compressive stress with of Alk2/3 inhibitor LDN led to a significant reduction in cushion size (Figure 2.6C). A weaker effect was found with the more specific alk 2 inhibitor DMH1 (data not shown). We used BMP2 treatment to simultaneously explore the direct role of BMP in cushion remodeling and as an agonist the pSmad15 pathway. We found that BMP2 treatment (20ng/ml) markedly decreased compaction without affecting rounding (Figure 2.6D). As expected, BMP2 was blocked by co-treatment with alk2/3 inhibitor LDN (Figure 2.6D).

Additionally, we investigated a potential downstream kinase pathway of BMP2, MAPK MEK-ERK, which is implicated in mechano-signaling and mediation of Smad15 signaling [17]. MEK inhibition via U0126 has a large effect on the non-compaction phenotype, significantly blocking the effect of compressive stress (Figure 2.7A) and completely blocking BMP2 (Figure 2.7B). We examined ERK activation at 24hrs and 18hrs to assess an intermediate timepoint during remodeling compaction. At 18hrs, p-ERK is not significantly elevated in the compressive condition, but is clearly blocked successfully by MEK inhibition, and slightly by alk2/3 inhibition (Figure 2.7C,D).

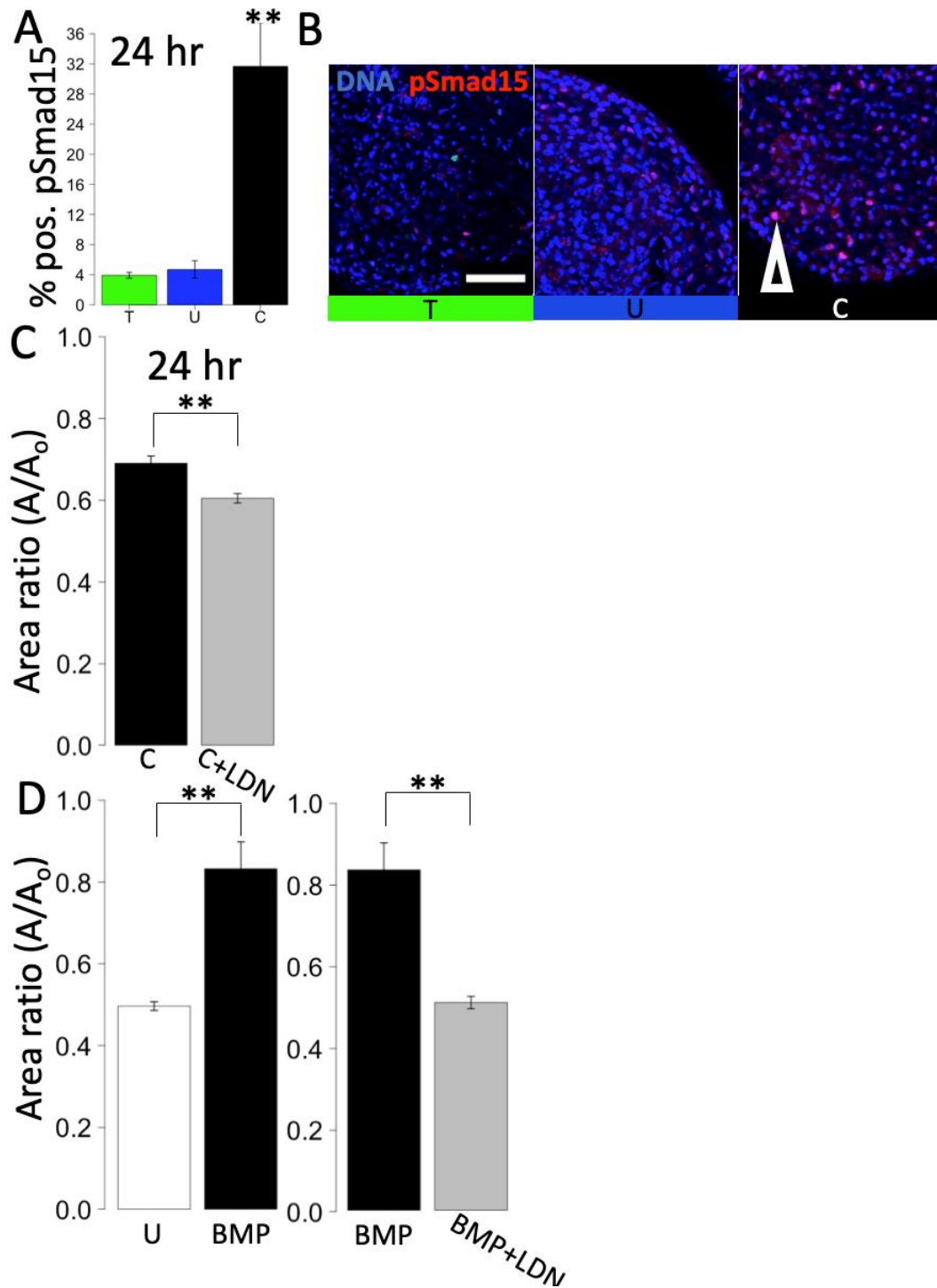


Figure 2.6. Compressive stress regulates tissue compaction through BMP signaling (A) Number of cells positive for pSmad15 at 24hrs, scale bar 50 μ m, ** $p < 0.005$ between treatment and control, $n=4-5$, SD shown (B) Whole mount IF images of 24 hr cushions stained for pSmad15 (C) Compaction trend for compressive stress combined with *alk2/3* inhibitor LDN (D) Compaction trend for BMP2 treatment combined with *alk2/3* inhibitor LDN, $n=4-5$ cushions per condition, SEM shown

2.4.3 NM-myosin-II drives compaction phenotype

To assess a contractile mechanism for osmotic and BMP non-compaction phenotypes, NM myosin II activation was assessed by staining for p-SER19 on the NM-myosin II light chain. pSER-19 decreased significantly in both the compressive and tensile conditions at 24hrs (Figure 2.8A,B). We then assessed the myosin activity when directly applying BMP2 ligand. BMP2 treatment significantly reduced SER-19 activation at 18hrs (Figure 2.8C), which could be restored slightly by LDN or significantly by MEK inhibition (Figure 8D).

Non-muscle myosin II was shown to be essential for tissue compaction as revealed by treatment with blebbistatin (Figure 2.8E). Further, we found a dose dependent effect of blebbistatin on tissue size (Figure 2.8E). Tissue compaction was inhibited at lower doses of blebbistatin (1uM) and was reversed at a higher doses (at or beyond 2uM). However, inhibition of ROCK using Y27362 led to a modest, statistically insignificant reduction in compaction when applied to either the unloaded condition and did not affect tissue rounding (Figure. 8F,G). Blebbistatin treatment could also block tissue rounding partially at 1uM and completely at 2uM (Figure 2.8G). To determine if there was a role for ROCK as an upstream kinase for contractile signaling, we staining for RhoA-GTP. We found Rho activity localized to the endothelial cells during compaction at 18hrs (Figure 2.9A). ROCK inhibition disrupted endothelial polarity resulting in clumped and disorganized surface cells (Figure 2.9B). We also observed honey-comb like RhoA-GTP staining patterns in the cytoplasm of cells under compressive (Figure 2.9B).

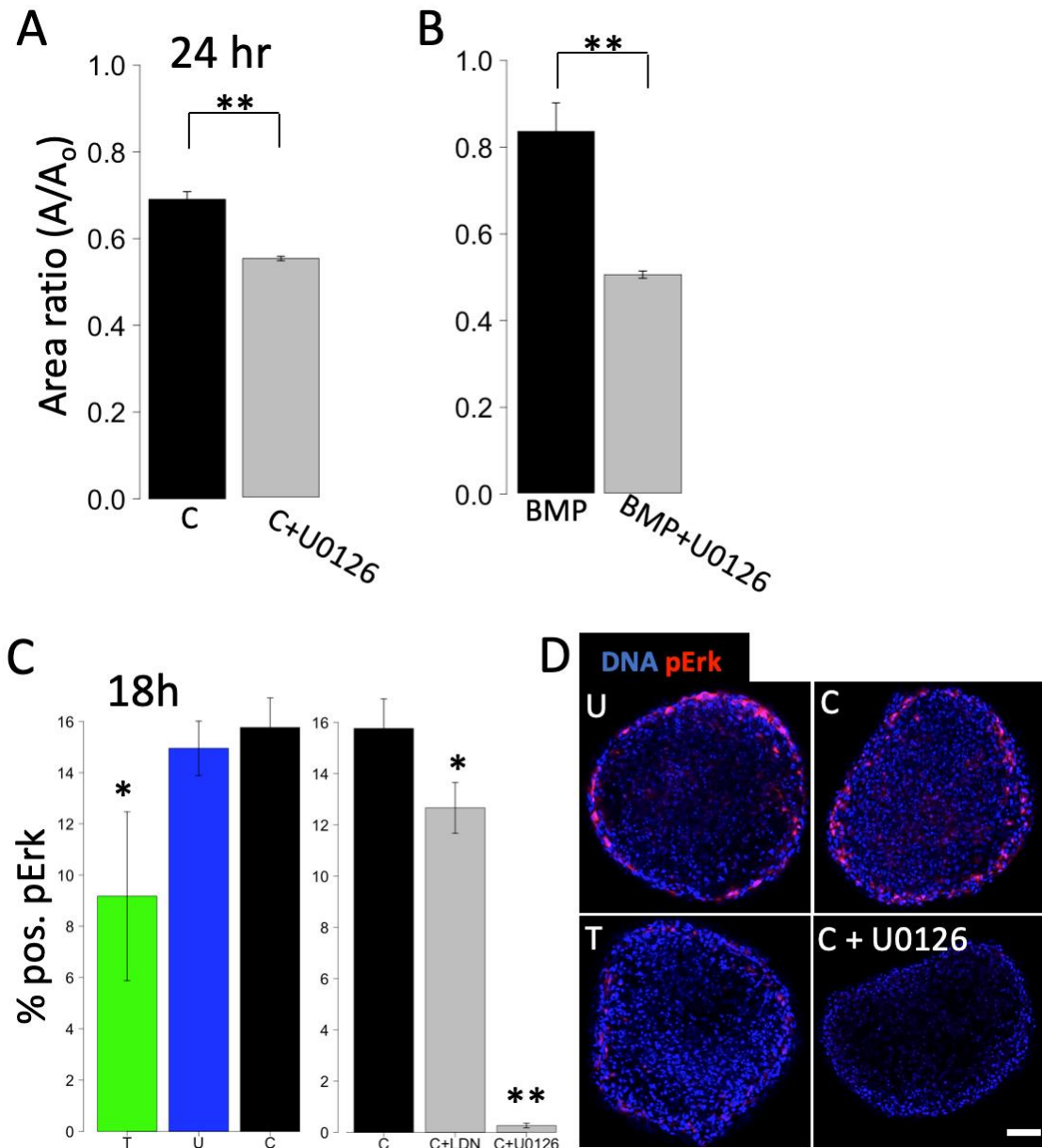


Figure 2.7. Compressive stress regulates tissue compaction through BMP signaling
 (A) Compaction trend for compressive stress combined with *alk2/3* and MEK inhibitors
 (B) Compaction trend for BMP2 treatment combined with and MEK inhibitor U0126
 (C) Number of cells positive for pERK at 18hrs, scale bar 50 μ m (D) Whole mount IF images of 18 hr cushions stained for pERK, n = 4-6 cushions per condition per 3 independent experiments, SEM shown

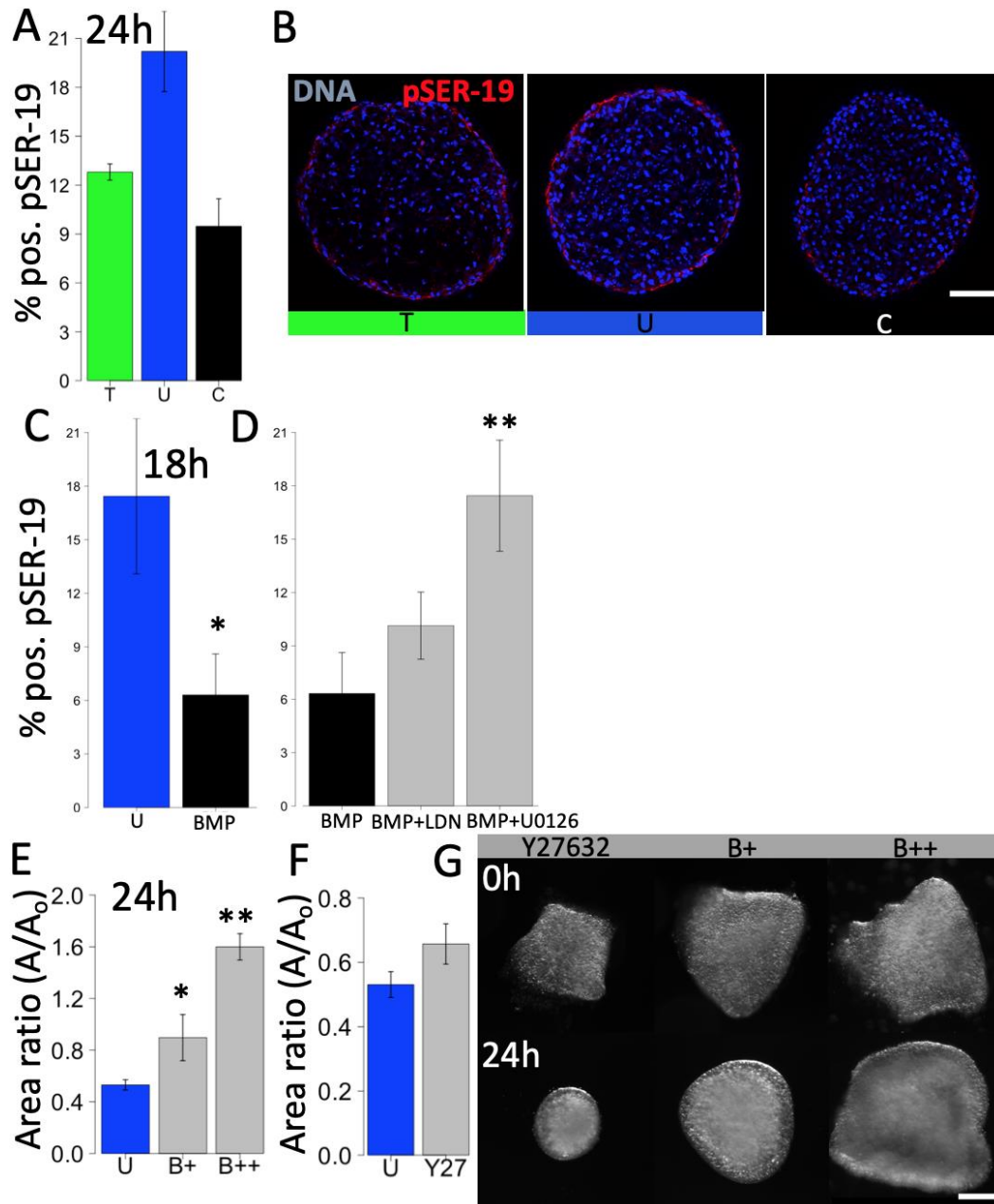


Figure 2.8. BMP and compressive stress decrease NM-myosin-II activation (A) Number of cells positive for pSER19 at 24hrs (B) Whole mount IF images of 24 hr cushions stained under osmotic stress for pSER19, scale bar 50 μ m (C) Compaction with ROCK inhibitor Y27632 (D) Area ratios for NM-myosin-II inhibition with blebbistatin 1 μ M (B+) and 10 μ M (B++) (E) Representative images of cushions treated with blebbistatin showing varied degrees of compaction and rounding (loss of jagged edges and initial shape) (F) Whole mount IF images of 18h cushions treated with BMP2 stained for pSER19, scale bar 50 μ m, n = 4-6 cushions per condition per 3 independent experiments, SEM shown (both IF and compaction data)

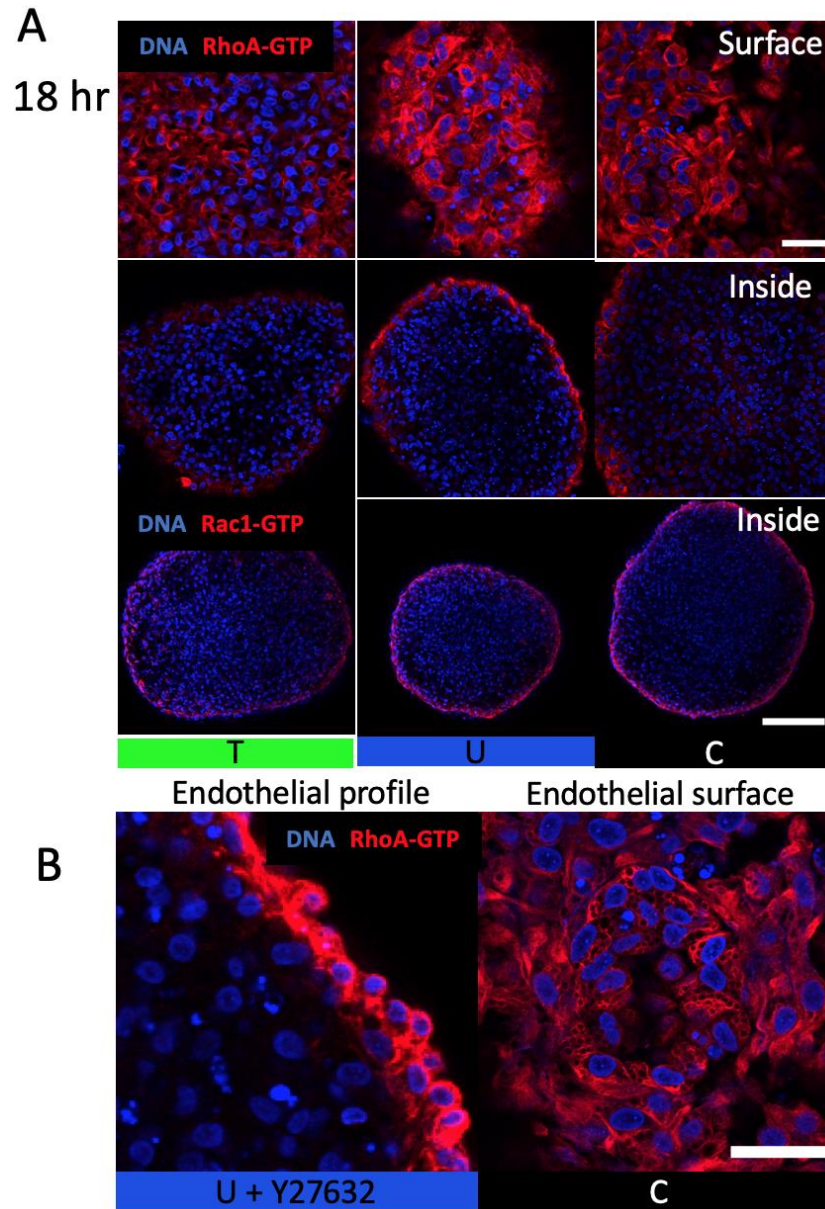


Figure 2.9. Osmotic stress affects endothelial RhoA-GTP patterning not activity (A) RhoA-GTP localization on cushion surface and 30 microns inside and Rac1-GTP inside (B) Disruption of apical-basal polarity at endothelium with ROCK inhibition (C) Honeycomb like pattern in RhoA-GTP stain associated with compressive stress

2.4.4 Altered mechanical loading in vivo shows upregulation of BMP signaling
 Left-atrial-ligation (LAL) is a method to surgically alter the hemodynamics placed on the atrioventricular valve [28], [31]. Under LAL, the mitral septal leaflet showed a

significant increase in pSmad1/5 when compared to left-ligation-sham surgery (Sham-L) (Figure 2.10A,B). The mural leaflets generally showed high pSmad1/5 activity with a statistically insignificant increase in the LAL condition (Figure 2.10B).

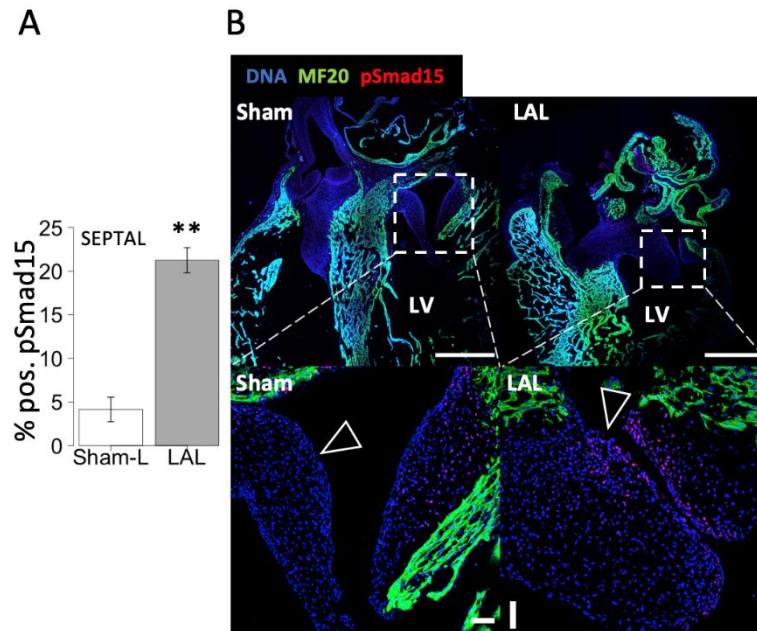


Figure 2.10. Increased pressure loading by left atrial ligation upregulates pSmad15 in association with hyperplastic valves (A) Number of cells positive for pSmad15, scale bar 50 μ m (B) IHC images of HH30 chick mitral valve stained for pSmad15 and MF20 (myocardial marker) with arrows indicating location on the atrial aspect with increased pSmad15 signaling under LAL, n = 3 sections from independent embryos per condition, SD shown, LV = left ventricle

2.4.5 Spatial localization of Smad15, ERK, and Myosin activity

We found significant differences in the spatial localization of the pSmad, pERK and pSER-19 signals found within the cushion. pSmad15 activation was observed throughout the outside and inner layers of the cushions when expressed. Compressive stress resulted in higher pSmad15 activity throughout the cushion (Figure 2.11A) that also correlated with greater expression near the tissue surface

Figure 2.11B). pERK activity was present across the cushions (Figure 2.12A). We found that pERK activity occurred in all conditions around a mean radius of 0.8 which corresponds to a sub-endocardial region (Figure 2.12B). We found that pSER-19 was present at or near the surface layers of the cushion and compressive stress resulted in a decrease in pSER-19 activity throughout the surface layers (Figure 2.13A). The mean normalized radius of pSER-19 positive cells was at or above 0.9 for all conditions (Figure 2.13B).

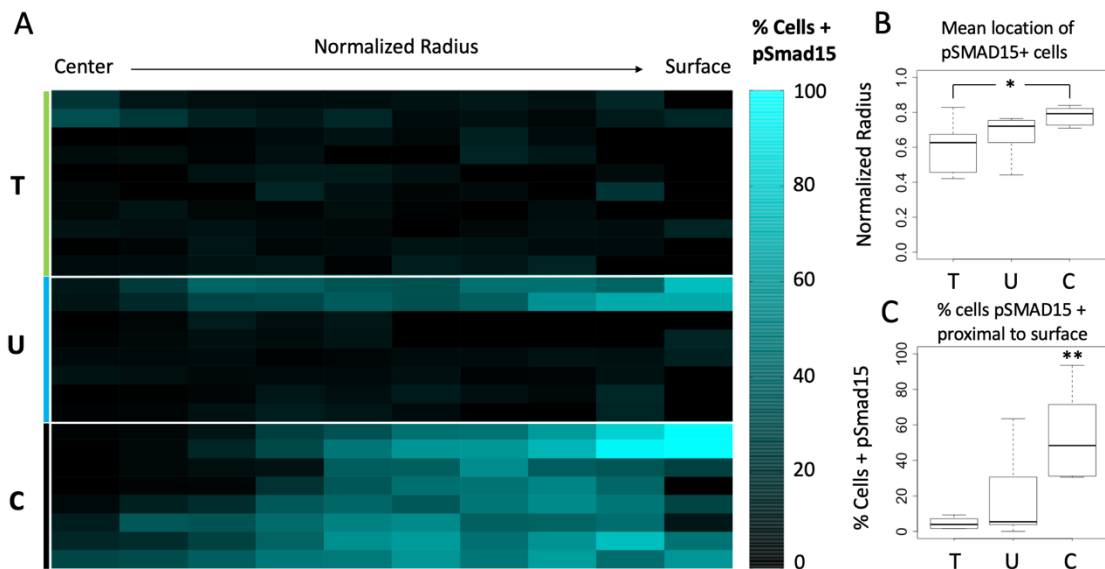


Figure 2.11. pSmad15 spatial quantification(A) colormap of pSmad15 distribution along a normalized cushion radius within 10 regions of interest of equal area. (B) The mean normalized radii for each osmotic condition (C) Signal at or near the cushion surface (last 3 bins), * $p < 0.05$, ** $p < 0.05$, $N=4-5$ cushions per group with 2 slices per cushion around 30 microns

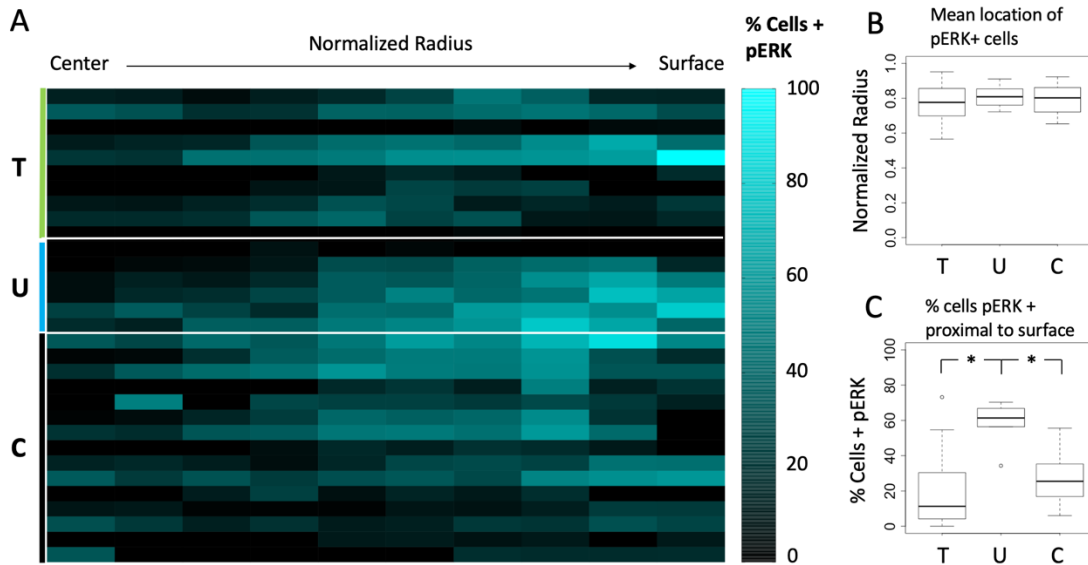


Figure 2.12. pERK spatial quantification (A) colormap of pERK distribution along a normalized cushion radius within 10 regions of interest of equal area. (B) The mean normalized radii for each osmotic condition (C) Signal at or near the cushion surface (last 3 bins), * $p < 0.05$, $N = 3-6$ cushions per group with 2 slices per cushion around 30 microns

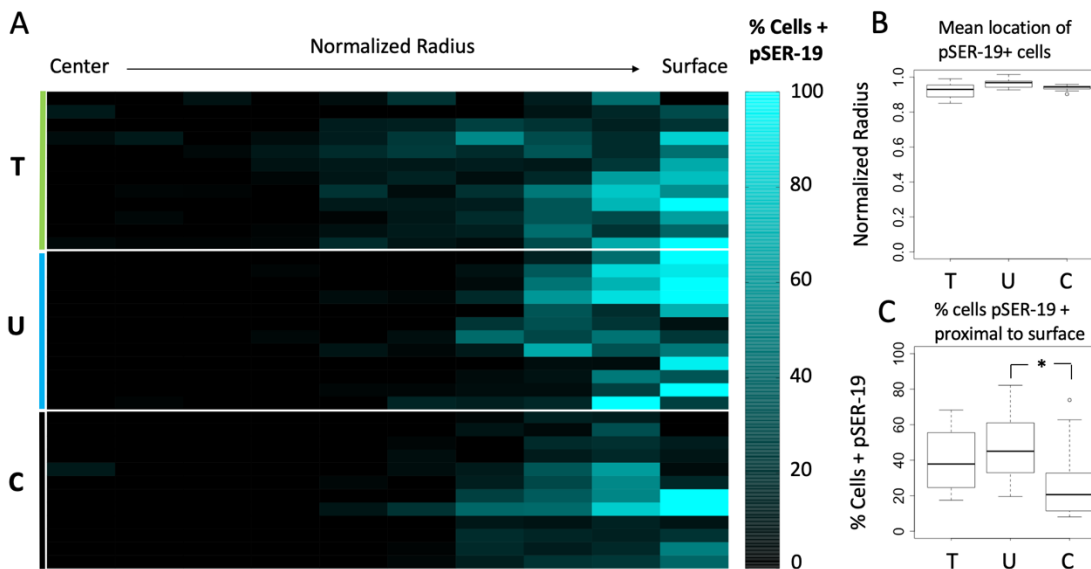


Figure 2.13. pSER-19 spatial quantification (A) colormap of pSER-19 distribution along a normalized cushion radius within 10 regions of interest of equal area. (B) The mean normalized radii for each osmotic condition (C) Signal at or near the cushion surface (last 3 bins), * $p < 0.05$, $N = 6-8$ cushions per group with 2 slices per cushion around 30 microns

2.4.6 Stage independence of osmotic stress and role of matrix in tissue shaping and stiffness

To determine the relative contributions of ECM and cell contractility in determining cushion shape, we assessed cushion compaction under osmotic loads at mid to late stages of development where collagen matrix begins to dominate [32]. Cushions in unloaded conditions compacted across all stages, from HH25 to HH36 by 50%, even given an increasing collagen matrix density, until after HH40 where compaction stops at 80% (Figure 2.14A). Cushions in hypotonic conditions compact 10% more than controls, an effect that diminishes at later stages. Cushions in compressive stress conditions compact between 70%-80% across all stages (Figure 2.14A). Degradation of collagen matrix via collagenase II in HH40 leaflets led the leaflets to compact by 50% over 24hrs, similar to unloaded cushions at HH25 (Figure 2.14B). Collagenase treatment also led to a loss in the thin, saddle-like morphology of HH 40 leaflets (Figure 2.14C). Interestingly, the HH40 leaflets still retained an elongated axis with an aspect ratio similar to HH34 leaflets (Figure 2.14D). Collagenase treated HH40 cushions had strain energy densities near those measured for unloaded HH25 cushions, around 0.4 Pa (Figure 2.14E,F).

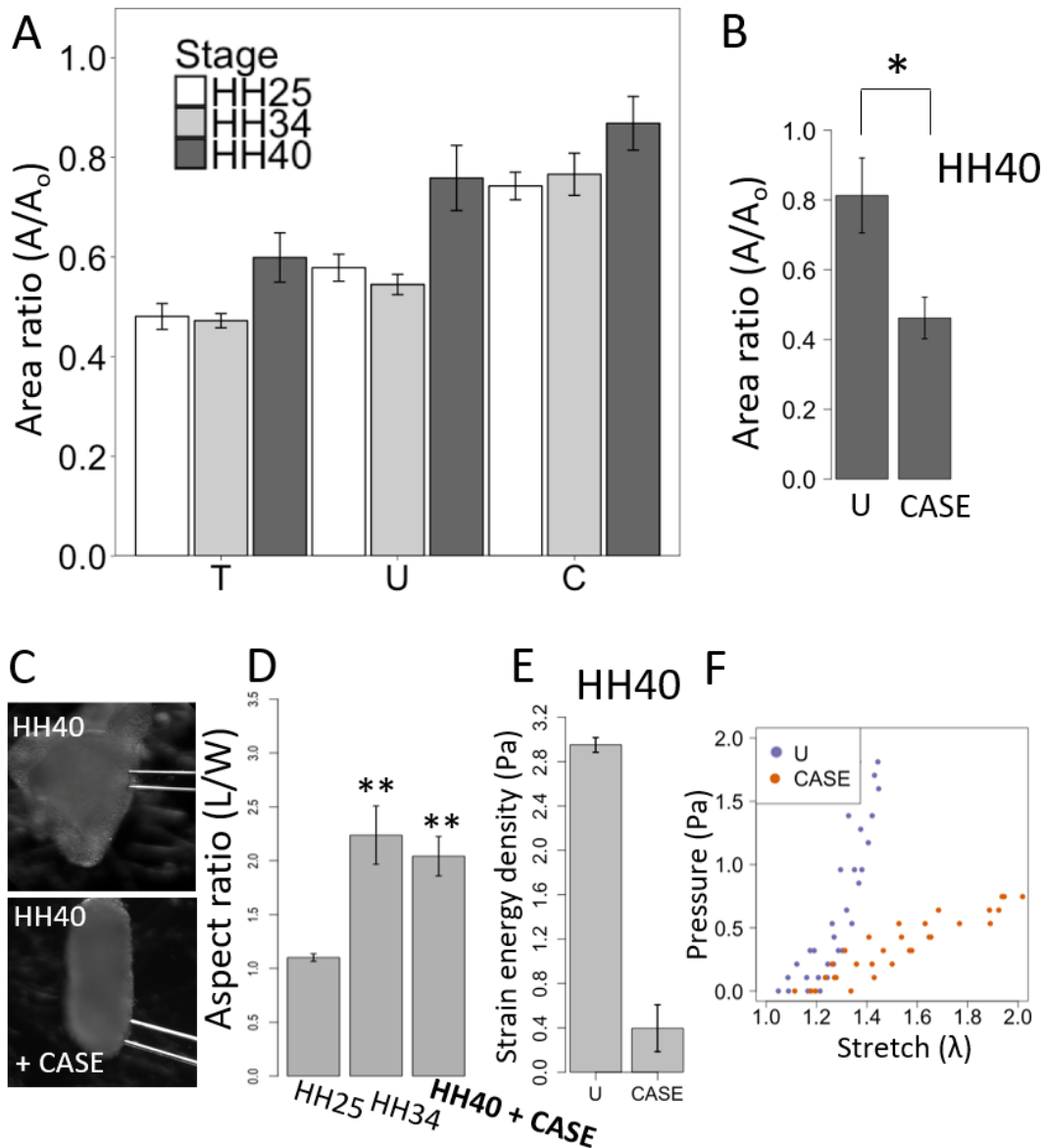


Figure 2.14. Osmotic stress acts to regulate tissue compaction across stages of valve maturation in collaboration with matrix scaffolding (A) Stage dependent compaction behavior under osmotic stress conditions showing added resistance to compaction at HH40 while still maintaining the general trend from tensile to compressive loading (24hrs, n=4-6 per 3 independent experiments), (B) Late stage (HH40) compaction with collagenase II treatment (300U) (C) Widefield images of a fresh HH40 leaflet and after 24 hour treatment with collagenase II, docked on glass pipette (D) Aspect ratio measurements demonstrate maintenance of elongation comparable to that seen at HH34 (D) HH40 mitral valve leaflet and collagenase II treated brightfield image docked on glass pipette after 24hrs, n = 4-6 cushions per condition per 3 independent experiments, SEM shown (E) Strain energy densities for control/unloaded and collagenase treated HH40 leaflets, 3-4 cushions per condition, SD shown. (F) Mechanical response curves for the cushions tested

2.5 Discussion

Long-term physiological valve function requires that fetal valve primordia morph into leaflets with the correct shape and size to maintain one-way blood flow through the heart. Understanding how mechanically driven signals and processes influence the outcome of valve morphogenesis first requires clarifying the role of individual stimuli. Using osmotic stress to understand the roles of the general tensile and compressive forces, we identify a role for pressures and bulk tensile loads on developing valve tissue that can govern tissue sizing and tissue shaping. We identified two roles for compressive stress in determining cushion size. We found that compressive stress promotes growth as characterized by increased tissue size (Figure 2.1) and proliferation (Figure 2.2) and that compressive stress promotes a homeostatic maintenance of size by mediating compaction. Conversely, we demonstrated that tensile stress can decrease cushion size (Figure 2.1). We identified that these processes were independent of TGF β (Figure 2.5). We further identified BMP2 as a mechanosensitive driver of valve growth and mid-stage development (Figure 2.6). This pathway involves the inhibition of NM-Myosin activity through cooperation with MEK-ERK signals (Figure 2.8)

We ruled out TGF β 3 as being responsible for the compressive stress non-compaction phenotype which was previously found to increase tissue size [20], but illustrated successful blockage of pSmad2/3 in both the compressive condition and TGF β 3 treatment case (Figure 2.5). On the other hand, pSmad1/5 was upregulated by compressive stress in combination with a reduction in tissue size with the application of Alk2/3 inhibitor (Figure 2.6). This supports TGF β and BMP both as independent

mediators of compaction, but that BMP is uniquely activated by compressive stress [20]. *In vivo*, decreased BMP signaling through Smad1/5/8 has been associated with size deficient valve leaflets. [34]

BMP2 treatment alone was found to produce a similar non-compaction phenotype (Figure 2.6). We examined MEK-ERK and p38 signaling as a which are both known to be downstream of BMP [17], [35]. We found only a partial response with p38 inhibitor and no significant differences in p38 alpha staining (data not shown). However, MEK inhibitor combined with either compressive stress or BMP2 led to a marked reduction in tissue size to unloaded control levels (Figure 2.7). We further considered an intermediate 18hr timepoint to identify mechanisms that might be transiently active during compaction. While tensile stress resulted in less pERK, the percentage of cells positive for pERK in unloaded and compressive conditions was nearly the same. The MEK inhibitor was able to successfully abolish pERK, demonstrating the effectiveness of the inhibitor and supporting that MEK-ERK is necessary to mediate the compaction phenotype.

Using blebbistatin, we identified the requirement of NM-myosin II for tissue compaction (Figure 2.8). Doses higher than 1uM not only arrest compaction but significantly alter the ability of the tissue to round, suggesting that cell contractility through NM-myosin II is the primary means of compaction remodeling.

To assess the potential regulation of NM-myosin II activity by compressive stress and BMP, we stained for p-SER19 on the NM myosin light chain. Light chain SER19 is phosphorylated whenever NM-myosin II is activated by upstream kinases [36]. Further, activation of inhibitory phosphorylation sites on the light chain by other

kinases such as PLC γ lead to dephosphorylation of pSER19, which positions this site as a reasonable readout of total activity [36]. We found that compressive stress significantly reduced pSER-19, at 24hrs (Figure 2.8A) but not 18hrs. Conversely, we found that BMP reduced pSER19 positive cells by 3-fold, which was restored slightly by alk2/3 inhibitor and completely by MEK inhibitor (Figure 2.7). This suggests a potential link between pERK and NM-myosin II activation. The temporal differences may be due to BMP having a more immediate effect on the growth/non-compactation phenotype earlier in culture.

We then investigated if BMP signaling was mechanically regulated in the AV cushions *in vivo* by using a left atrial ligation which shunts blood from the left side of the heart to the right and increases ventricular preload, resulting in stunted, thickened mitral valves [28], [29]. We found significantly increased pSmad1/5 activation throughout the mitral septal leaflet suggesting there is a role for BMP in a hyperplastic valve scenario *in vivo* (Figure 2.10).

We found generally high levels of pSmad1/5 in the mural leaflets, likely due to BMP ligand expression [37] from underlying myocardial cells [38]. Unregulated BMP signaling has also been associated with hyperplastic valves in mice [34].

To better understand the interactions of BMP and MAPK pathways and myosin activation, we performed spatial localization analysis to map signaling activity to normalized regions through the depth of the cushion as a function of a normalized radius (R_n). The movement of pSmad15 expression to nearer to the surface (R_n around 0.8) under compressive stress (Figure 2.11B) coincided with the layer of most active ERK activity, also around $R_n = 0.8$ (Figure 2.12B). This suggests that colocalization of

pERK and pSmad15 in the same cell or neighboring cells, may be required for compressive stress signaling. On the other hand, pSER-19 was on average closer to the surface/endothelium (Figure 2.13B), suggesting that there may be paracrine signals the underlying cells which can lead to myosin inhibition. A significant number of pSER positive cells were present at $R_n = 0.8$ (Figure 2.13A), suggesting that the mechanism may be autologous in some cells. The predominant localization of NM-myosin active cells in this sub-endocardial range supports that the observed tissue compaction is driven by mesenchymal cells in this outer layer. Endothelial cells have been shown to control tissue shaping in development [39]. Generally, we found 3 layers with different levels of activated proteins centered at: $R_n < 0.8$, $R_n = 0.8$, and $R_n > 0.8$. Colocalization of pERK and pSmad in the 0.8 layer may synergize to regulate the compaction phenotype as laid out in Figure 2.15A. The high degree of surface activation of NM-myosin may suggest that endothelial cell tensions are driving compaction, unless signaled to by the underlying cells as a result of BMP/MAPK signaling. This transduction is potentially through BMP ligands downstream secretion of Smad1/5/8 [40]. We have summarized the mechanism supported by these results in Figure 2.15B.

Originally, we were interested in the potential role of Rho/Rac given our recent work determining their roles in response to cyclic stretch [41]. We identified that RhoA-GTP and Rac1-GTP localize to the endocardium, likely where they are participating in maintaining apical/basal polarity [42]. Indeed, ROCK inhibitor disrupted the endothelium, resulting in loss of apical basal polarity and clumping of cells (Figure 2.9B). However, an interesting feature uncovered was the intracellular,

hexagonal staining pattern observed on the endothelium under compressive stress (Figure 2.9B), which may suggest a structural rearrangement in response to the load on the cell. Endothelial cells may be implicated as one source of mechanotransduction deeper into the tissue for shear stress [43], but may also play a role as they attempt to maintain surface integrity when faced with tissue swelling.

This work provides novel insights into the contributions and implicated signaling pathways relating to osmotic stress, hydrostatic pressure, and valve growth, and identifies new areas to address as to the exact mechanisms behind the interactions of BMP, MAPK and endpoint activities in this context. Multiple studies suggest interactions between BMP and MAPK. MAPK has the capacity to enhance the transcriptional activity of SMADs within the same cells by promoting Smad phosphorylation [44]. For example, activation of Smad1 by MAPK is required for normal embryogenesis in mice [27]. Overactive BMP signaling, achieved through deletion of regulator Smad6, results in a hyperplastic valve phenotype *in vivo* supporting the importance of BMP in regulating growth [45]. Integrin-FAK interactions have also been shown to activate Ras/MEK/ERK and to cooperate with SMAD signals [46]. Further, ERK has been shown not to be required for SMAD activation and nuclear translocation, while instead having interactions in the nucleus, suggesting that ERK may have synergistic effects at Smad transcriptional targets [47]. Targeting MEK-ERK has also proven effective at eliminating BMP driven malignant phenotypes in cancer cell lines, where Alk2/3 inhibition (via LDN) alone was ineffective [25]. In vascular endothelium, FAK/ERK was required to transduce shear stress downstream of BMPR-integrin interactions [17]. Conversely, BMP activation

of Smads can lead to upregulate the transcriptional activity of ERK in axon development [48]. In chondrocytes, integrins participate in osmotransduction and do so with or without being bound to matrix [11]. BMPR activation by BMP7 has also been correlated to myosin light chain expression [49]. The increased co-expression of pERK and pSmad15 in cells experiencing compressive stress (Figure 2.11 & Figure 2.12), combined with these data, support that the compressive stress phenotype may benefit from ERK enhancement in these cells, even though the level of ERK activity is similar between treatment groups (Figure 2.7).

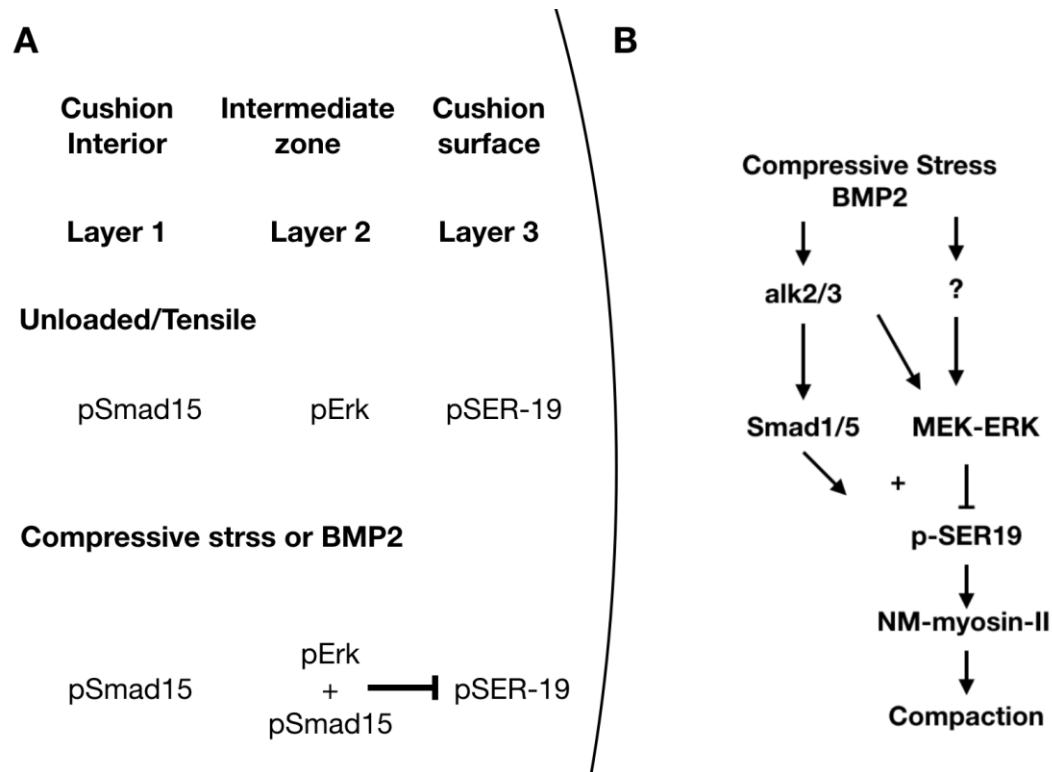


Figure 2.15. Proposed pathways for osmotic stress regulation of valve morphogenesis (A) Spatial distribution of active signaling elements and their consequences toward myosin activation (B) Overall interactions with Smad1/5 and MEK-ERK acting independently to regulate compaction

Finally, we explored whether osmotic stress had the potential to affect the later stages of fetal atrioventricular valve elongation and condensation. We found that the effects of tensile and compressive stresses were consistent from HH25-HH40 (Figure 2.14A). However, the increased collagen matrix content at HH40 restricted tissue compaction (Figure 2.14B). We further observed that degrading the collagen matrix was not sufficient to allow the tissue to completely round and it therefore maintained its elongated axis as measured by cushion aspect ratio (Figure 2.14C,D). This elongation was maintained despite a several fold decrease in tissue stiffness (Figure 2.14E,F) and supports other underlying matrix components or cellular alignments may be preventing contraction along the lengthened axis.

Tissue stiffness plays a critical role in the remodeling and function of the valve by limiting the rate of remodeling and the providing mechanical stability necessary for coaptation. TGF β 3 has been shown to increase valve stiffness in addition to regulating tissue size [20]. In the case of osmotic stress, we found no significant differences in tissues stiffness within the same stretch ranges (Figure 2.4). This supports a model where mechanical loading through BMP can control tissue size without affecting tissue stiffness. Clinically, Leoy-Dietz (LDS) syndrome results in overly elastic mitral septal leaflets and resulting from mutations in TGF- β receptors (TGF- β R1 & TGF- β R2) [50].

In vivo, valves are exposed to many modes of mechanical stress during the same cardiac cycle and many areas of the valve will be under tensile and compressive loads at the same time. Our work supports the hypothesis proposed by a computational

model of mechanically driven valve growth which suggested that compressive stress drives areas of localized growth [6].

It has been shown that interstitial osmotic stress can be induced by mechanical stretching that may further result in significant cellular tension or compression [51]. Cells experiencing these loads will attempt to compensate by varying their cytoskeletal stiffness and volume regulators such as aquaporins [52]. These results support a mechanism where external mechanical loads produce immediate secondary stresses on tissues and cells due to osmotic gradients. Therefore, osmotic stress, whether treated as a hydrostatic pressure or a response to blood flow induced tissue deformations has increasing relevance as a unifying stimulus for multiple sources of mechanical stimuli. Further, molecular readouts of the mechanical effects of osmotic stress can help to interpret these effects *in vivo*, when multiple loading modes are mixed. Given the relative simplicity and cost efficiency of applying osmotic loads, it is reasonable to consider using osmotic stress medias in shear stress and stretch bioreactors.

In summary, this study demonstrates that osmotic stress has developmentally relevant effects on valve shape fidelity and growth and reveals tensile and compressive stresses as signals that can act to control valve remodeling. Further, we demonstrated these effects have potential roles across multiple stages of development, from cushion growth to condensation and elongation.

2.6 Acknowledgements

We would like to acknowledge Jacque Nelson-Harrington and the Baker Institute for providing an osmometer. We would also like to acknowledge Visikol and Michael Johnson for providing protocol guidance and a free sample of their HISTO-M product. We acknowledge our funding sources: R01 HL110328, R01 HL128745, R01 HL143247, NSF GFRP, NSF CMMI-1635712 and core facility microscope funding from NIH S10RR025502.

2.7 References

- [1] A. S. Forouhar *et al.*, “Intracardiac fluid forces are an essential epigenetic factor for embryonic cardiogenesis.,” *Nature*, vol. 421, no. 6919, pp. 172–177, 2003.
- [2] H. C. Yalcin, A. Shekhar, T. C. McQuinn, and J. T. Butcher, “Hemodynamic patterning of the avian atrioventricular valve.,” *Dev. Dyn.*, vol. 240, no. 1, pp. 23–35, Jan. 2011.
- [3] G. J. Mahler, C. M. Frendl, Q. Cao, and J. T. Butcher, “Effects of shear stress pattern and magnitude on mesenchymal transformation and invasion of aortic valve endothelial cells.,” *Biotechnol. Bioeng.*, vol. 111, no. 11, pp. 2326–37, Nov. 2014.
- [4] H. Tan *et al.*, “Fluid flow forces and rhoA regulate fibrous development of the atrioventricular valves,” *Dev. Biol.*, vol. 374, no. 2, pp. 345–356, Feb. 2013.
- [5] S. E. Lindsey, J. T. Butcher, and H. C. Yalcin, “Mechanical regulation of cardiac development.,” *Front. Physiol.*, vol. 5, no. August, p. 318, Jan. 2014.
- [6] P. R. Buskohl, J. T. Jenkins, and J. T. Butcher, “Computational simulation of hemodynamic-driven growth and remodeling of embryonic atrioventricular valves,” *Biomech. Model. Mechanobiol.*, vol. 11, no. 8, pp. 1205–1217, Nov. 2012.
- [7] C. Henri, L. a Piérard, P. Lancellotti, F.-P. Mongeon, P. Pibarot, and A. J. Basmadjian, “Exercise testing and stress imaging in valvular heart disease.,” *Can. J. Cardiol.*, vol. 30, no. 9, pp. 1012–26, Sep. 2014.
- [8] K. J. Schipke, S. D. Filip To, and J. N. Warnock, “Design of a Cyclic Pressure Bioreactor for the *Ex Vivo* Study of Aortic Heart Valves.,” *J. Vis. Exp.*, no. 54, pp. 3–7, 2011.
- [9] P. J. Basser, R. Schneiderman, R. A. Bank, E. Wachtel, and A. Maroudas, “Mechanical properties of the collagen network in human articular cartilage as measured by osmotic stress technique.,” *Arch. Biochem. Biophys.*, vol. 351, no. 2, pp. 207–19, 1998.
- [10] D. a. Narmoneva, J. Y. Wang, and L. a. Setton, “Nonuniform swelling-induced residual strains in articular cartilage,” *J. Biomech.*, vol. 32, no. 4, pp. 401–408, 1999.
- [11] C. L. Jablonski, S. Ferguson, A. Pozzi, and A. L. Clark, “Integrin $\alpha 1\beta 1$ participates in chondrocyte transduction of osmotic stress,” *Biochem. Biophys. Res. Commun.*, vol. 445, no. 1, pp. 184–190, 2014.

- [12] Z. I. Johnson, I. M. Shapiro, and M. V. Risbud, “Extracellular osmolarity regulates matrix homeostasis in the intervertebral disc and articular cartilage: Evolving role of TonEBP,” *Matrix Biol.*, vol. 40, pp. 10–16, 2014.
- [13] N. R. Chevalier, E. Gazquez, S. Dufour, and V. Fleury, “Measuring the micromechanical properties of embryonic tissues,” *Methods*, pp. 1–9, 2015.
- [14] M. E. Dolega, M. Delarue, F. Ingremeau, J. Prost, A. Delon, and G. Cappello, “Cell-like pressure sensors reveal increase of mechanical stress towards the core of multicellular spheroids under compression,” *Nat. Commun.*, vol. 8, no. May 2016, pp. 1–9, 2017.
- [15] M. Delarue, F. Montel, D. Vignjevic, J. Prost, J. F. Joanny, and G. Cappello, “Compressive stress inhibits proliferation in tumor spheroids through a volume limitation,” *Biophys. J.*, vol. 107, no. 8, pp. 1821–1828, 2014.
- [16] V. C. Garside, A. C. Chang, A. Karsan, and P. A. Hoodless, “Co-ordinating Notch, BMP, and TGF- β signaling during heart valve development,” *Cell. Mol. Life Sci.*, vol. 70, no. 16, pp. 2899–2917, Aug. 2013.
- [17] J. Zhou *et al.*, “BMP receptor-integrin interaction mediates responses of vascular endothelial Smad1/5 and proliferation to disturbed flow,” *J. Thromb. Haemost.*, vol. 11, no. 4, pp. 741–755, 2013.
- [18] R. A. Gould *et al.*, “Cyclic Mechanical Loading Is Essential for Rac1- Mediated Elongation and Remodeling of the Embryonic Mitral Valve Cyclic Mechanical Loading Is Essential for Rac1-Mediated Elongation and Remodeling of the Embryonic Mitral Valve,” *Curr. Biol.*, pp. 1–11, 2016.
- [19] S. Kalogirou, N. Malissovass, E. Moro, F. Argenton, D. Y. R. Stainier, and D. Beis, “Intracardiac Flow Dynamics Regulate Atrioventricular Valve Morphogenesis,” *Cardiovasc. Res.*, pp. 1–34, 2014.
- [20] P. R. Buskohl, M. L. Sun, R. P. Thompson, and J. T. Butcher, “Serotonin potentiates transforming growth factor-beta3 induced biomechanical remodeling in avian embryonic atrioventricular valves,” *PLoS One*, vol. 7, no. 8, p. e42527, Jan. 2012.
- [21] K. H. Kain *et al.*, “The chick embryo as an expanding experimental model for cancer and cardiovascular research,” *Dev. Dyn.*, vol. 243, no. 2, pp. 216–28, Feb. 2014.
- [22] E. Aikawa *et al.*, “Human Semilunar Cardiac Valve Remodeling by Activated Cells From Fetus to Adult Implications for Postnatal Adaptation , Pathology , and Tissue Engineering,” vol. 02115, pp. 1344–1352, 2006.
- [23] B. J. Martinsen, “Reference guide to the stages of chick heart embryology.”

Dev. Dyn., vol. 233, no. 4, pp. 1217–37, Aug. 2005.

- [24] Y.-N. Chiu, R. a Norris, G. Mahler, A. Recknagel, and J. T. Butcher, “Transforming growth factor β , bone morphogenetic protein, and vascular endothelial growth factor mediate phenotype maturation and tissue remodeling by embryonic valve progenitor cells: relevance for heart valve tissue engineering.,” *Tissue Eng. Part A*, vol. 16, no. 11, pp. 3375–3383, 2010.
- [25] S. Ahsan, Y. Ge, and M. A. Tainsky, “Combinatorial therapeutic targeting of BMP2 and MEK-ERK pathways in NF1-associated malignant peripheral nerve sheath tumors,” *Oncotarget*, vol. 7, no. 35, 2016.
- [26] J. H. Boergermann, J. Kopf, P. B. Yu, and P. Knaus, “Dorsomorphin and LDN-193189 inhibit BMP-mediated Smad, p38 and Akt signalling in C2C12 cells,” *Int. J. Biochem. Cell Biol.*, vol. 42, no. 11, pp. 1802–1807, 2010.
- [27] J. Aubin, A. Davy, and P. Soriano, “In vivo convergence of BMP and MAPK signaling pathways: Impact of differential Smad1 phosphorylation on development and homeostasis,” *Genes Dev.*, vol. 18, no. 12, pp. 1482–1494, 2004.
- [28] D. Sedmera, T. Pexieder, V. Rychterova, N. Hu, and E. B. Clark, “Remodeling of chick embryonic ventricular myoarchitecture under experimentally changed loading conditions,” *Anat. Rec.*, vol. 254, no. 2, pp. 238–252, 1999.
- [29] A. DeAlmeida, T. McQuinn, and D. Sedmera, “Increased ventricular preload is compensated by myocyte proliferation in normal and hypoplastic fetal chick left ventricle,” *Circ. Res.*, vol. 100, no. 9, pp. 1363–1370, 2007.
- [30] H. Beppu, R. Malhotra, Y. Beppu, J. J. Lepore, M. S. Parmacek, and K. D. Bloch, “BMP type II receptor regulates positioning of out flow tract and remodeling of atrioventricular cushion during cardiogenesis,” *Dev. Biol.*, vol. 331, no. 2, pp. 167–175, 2009.
- [31] M. Midgett and S. Rugonyi, “Congenital heart malformations induced by hemodynamic altering surgical interventions.,” *Front. Physiol.*, vol. 5, no. August, p. 287, Jan. 2014.
- [32] J. T. Butcher, R. a Norris, S. Hoffman, C. H. Mjaatvedt, and R. R. Markwald, “Periostin promotes atrioventricular mesenchyme matrix invasion and remodeling mediated by integrin signaling through Rho/PI 3-kinase,” *Dev. Biol.*, vol. 302, no. 1, pp. 256–266, 2007.
- [33] M. M. Lockhart *et al.*, “Alk3 mediated Bmp signaling controls the contribution of epicardially derived cells to the tissues of the atrioventricular junction,” *Dev. Biol.*, vol. 396, no. 1, pp. 8–18, 2014.

- [34] L. F. Jackson *et al.*, “Defective valvulogenesis in HB-EGF and TACE-null mice is associated with aberrant BMP signaling,” vol. 22, no. 11, 2003.
- [35] K. Miyazono, S. Maeda, and T. Imamura, “BMP receptor signaling : Transcriptional targets , regulation of signals , and signaling cross-talk,” vol. 16, pp. 251–263, 2005.
- [36] M. A. Conti, K. Sachiyo, and R. S. Adelstein, *Myosins: A Superfamily of Molecular Motors*. 2008.
- [37] S. Somi, A. A. M. Buffing, A. F. M. Moorman, and M. J. B. Van Den Hoff, “Dynamic patterns of expression of BMP isoforms 2, 4, 5, 6, and 7 during chicken heart development,” *Anat. Rec. - Part A Discov. Mol. Cell. Evol. Biol.*, vol. 279, no. 1, pp. 636–651, 2004.
- [38] V. Gaussin *et al.*, “Alk3 / Bmpr1a Receptor Is Required for Development of the Atrioventricular Canal Into Valves and Annulus Fibrosus,” pp. 1–8, 2005.
- [39] H. Ninomiya and R. Winklbauer, “Epithelial coating controls mesenchymal shape change through tissue-positioning effects and reduction of surface-minimizing tension.,” *Nat. Cell Biol.*, vol. 10, no. 1, pp. 61–9, Jan. 2008.
- [40] L. Ye and W. G. Jiang, “Bone morphogenetic proteins in tumour associated angiogenesis and implication in cancer therapies,” *Cancer Lett.*, vol. 380, no. 2, pp. 586–597, 2016.
- [41] R. A. Gould *et al.*, “Cyclic Mechanical Loading Is Essential for Rac1-Mediated Elongation and Remodeling of the Embryonic Mitral Valve,” *Curr. Biol.*, vol. 26, no. 1, pp. 27–37, 2016.
- [42] J. Wojnacki *et al.*, “Rho GTPases at the crossroad of signaling networks in mammals Impact of Rho-GTPases on microtubule organization and dynamics Rho GTPases at the crossroad of signaling networks in mammals,” vol. 1248, no. September, 2017.
- [43] B. P. Hierck, K. Van der Heiden, C. Poelma, J. Westerweel, and R. E. Poelmann, “Fluid shear stress and inner curvature remodeling of the embryonic heart. Choosing the right lane!,” *ScientificWorldJournal.*, vol. 8, pp. 212–222, 2008.
- [44] M. P. De Caestecker *et al.*, “Smad2 transduces common signals from receptor serinethreonine and tyrosine kinases,” *Genes Dev.*, vol. 12, no. 11, pp. 1587–1592, 1998.
- [45] K. M. Galvin *et al.*, “A role for smad6 in development and homeostasis of the cardiovascular system.,” *Nat. Genet.*, vol. 24, no. 2, pp. 171–174, 2000.

- [46] M. Suzawa *et al.*, “Stimulation of Smad1 transcriptional activity by Ras-extracellular signal-regulated kinase pathway: A possible mechanism for collagen-dependent osteoblastic differentiation,” *J. Bone Miner. Res.*, vol. 17, no. 2, pp. 240–248, 2002.
- [47] Y. Tamura *et al.*, “Focal adhesion kinase activity is required for bone morphogenetic protein - Smad1 signaling and osteoblastic differentiation in murine MC3T3-E1 cells,” *J. Bone Miner. Res.*, vol. 16, no. 10, pp. 1772–1779, 2001.
- [48] M. J. Finelli, K. J. Murphy, L. Chen, and H. Zou, “Differential Phosphorylation of Smad1 Integrates BMP and Neurotrophin Pathways through Erk/Dusp in Axon Development,” *Cell Rep.*, vol. 3, no. 5, pp. 1592–1606, 2013.
- [49] G. Konstantinidis and A. Moustakas, “Cellular Physiology and Biochemistry Regulation of Myosin Light Chain Function by BMP Signaling Controls Actin Cytoskeleton Remodeling,” vol. 71110, 2011.
- [50] B. L. Loeys *et al.*, “A syndrome of altered cardiovascular, craniofacial, neurocognitive and skeletal development caused by mutations in TGFBR1 or TGFBR2,” *Nat. Genet.*, vol. 37, no. 3, pp. 275–281, 2005.
- [51] A. E. Ehret, K. Bircher, A. Stracuzzi, V. Marina, M. Zündel, and E. Mazza, “Inverse poroelasticity as a fundamental mechanism in biomechanics and mechanobiology,” *Nat. Commun.*, vol. 8, no. 1, p. 1002, 2017.
- [52] H. Jiang and S. X. Sun, “Cellular pressure and volume regulation and implications for cell mechanics,” *Biophys. J.*, vol. 105, no. 3, pp. 609–619, 2013.

CHAPTER 3.

POPULATION HETEROGENEITY IN THE EPITHELIAL TO MESENCHYMAL TRANSITION IS CONTROLLED BY NFAT AND PHOSPHORYLATED SP1

The work presented below was published in PLOS COMPUTATIONAL BIOLOGY in 2016 co-first authors Russel Gould & David Bassen. Dr. Russel Gould performed the experiments and I performed the modeling.

3.1 Summary

Identifying molecular determinants of behavioral heterogeneity in epithelial cell populations is a critical to interpreting diagnostics, understanding cellular responses to stimuli *in vivo* and to the mechanism of action or toxicity of drugs. Here, we developed a reduced order systems biology model of epithelial to mesenchymal (EMT) transition (251 parameters and 97 initial conditions) that captures how the integration of multiple external signals leads to multiple cell phenotypes. The parameters were constrained using characteristic rates derived from the literature allowing for a fully dimensioned model. To address parameter uncertainty in a way that captures inherent cell to cell variability, we generated ensembles of parameter sets using a Pareto Optimal Ensemble Technique (POET) implemented in the Julia programming language (shown in Chapter 4). The trained, cross-validated ensemble allowed us to derive test hypotheses that identified important network elements and elusive cell sub-populations. We found a hybrid phenotype in our simulations that supported the hypothesis of a group of cells that could simultaneously express both epithelial and mesenchymal protein, which could be driven by co-treatment with TGF β 2 and VEGFA. We further found that NFAT and phosphor-Sp-1 were master regulatory elements controlling the EMT hybrid phenotype. Through *in vitro* co-treatment of TGF β 2 and VEGFA, we confirmed both the hybrid phenotype and its regulators through flow cytometry and immune-fluorescence data. This work demonstrates the mechanisms driving EMT that have shown to be relevant for increasing monastic behavior and in understanding diverse populations of tumor cells.

Our work has further been used as a starting point for valvulogenesis specific EMT models through the capturing of conserved EMT signaling machinery (Appendix 1).

3.2 Abstract

Epithelial to mesenchymal transition (EMT) is an essential differentiation program during tissue morphogenesis and remodeling. EMT is induced by soluble transforming growth factor β (TGF- β) family members, and restricted by vascular endothelial growth factor family members. While many downstream molecular regulators of EMT have been identified, these have been largely evaluated individually without considering potential crosstalk. In this study, we created an ensemble of dynamic mathematical models describing TGF- β induced EMT to better understand the operational hierarchy of this complex molecular program. We used ordinary differential equations (ODEs) to describe the transcriptional and post-translational regulatory events driving EMT. Model parameters were estimated from multiple data sets using multiobjective optimization, in combination with cross-validation. TGF- β exposure drove the model population toward a mesenchymal phenotype, while an epithelial phenotype was enhanced following vascular endothelial growth factor A (VEGF-A) exposure. Simulations predicted that the transcription factors phosphorylated SP1 and NFAT were master regulators promoting or inhibiting EMT, respectively. Surprisingly, simulations also predicted that a cellular population could exhibit phenotypic heterogeneity (characterized by a significant fraction of the population with both high epithelial and mesenchymal marker expression) if treated simultaneously with TGF- β and VEGF-A. We tested this prediction experimentally in

both MCF10A and DLD1 cells and found that upwards of 45% of the cellular population acquired this hybrid state in the presence of both TGF- β and VEGF-A. We experimentally validated the predicted NFAT/Sp1 signaling axis for each phenotype response. Lastly, we found that cells in the hybrid state had significantly different functional behavior when compared to VEGF-A or TGF- β treatment alone. Together, these results establish a predictive mechanistic model of EMT susceptibility, and potentially reveal a novel signaling axis which regulates carcinoma progression through an EMT versus tubulogenesis response.

3.3 Introduction

The epithelial to mesenchymal transition (EMT) is a broadly participating, evolutionarily conserved differentiation program essential for tissue morphogenesis, remodeling and pathological processes such as cancer [1]. During EMT polarized, tightly adhered epithelial cell monolayers are transformed into non-interacting motile mesenchymal cells that simultaneously degrade and synthesize extracellular matrix (ECM) components and invade into the underlying tissue space [2]. EMT is the fundamental initiator of developmental processes such as embryonic gastrulation and valvulogenesis [3]. Transforming growth factor β (TGF- β) family members are important inducers of both developmental and pathological EMT [4, 5]. Decades of research has focused on identifying molecular regulators of EMT, but almost all on a single gene and in a nearly binary yes/no level of qualitative understanding. Medici and coworkers identified a core signaling program by which TGF- β isoforms induce EMT across a variety of cell lines [6, 7]. This program involves carefully orchestrated rounds of gene expression driven by the Smad and Snail families of transcription

factors as well as other key factors such as lymphoid enhancer-binding factor 1 (LEF-1), nuclear factor of activated T-cells, cytoplasmic 1 (NFATc1), and specificity protein 1 (Sp1). Coregulators such as β -catenin, NF- κ B, and the ErbB family of receptor tyrosine kinases however also participate in EMT regulation, but the degree of each's influence is difficult to ascertain in isolation [8–11]. EMT also exhibits complex temporal dynamics that are often intractable in gain/loss of function studies.

Elucidating the master regulatory architecture controlling EMT therefore requires inclusion of these complex overlapping and non-binary behaviors. Systems biology and mathematical modeling are essential tools for understanding complex developmental programs like EMT [12]. Previous computational models of TGF- β induced differentiation focused on single biological factors or EMT in single cells. For example, Chung *et al.*, constructed a model of TGF- β receptor activation and Smad signaling using ordinary differential equations and mass-action kinetics. Their model suggested that a reduction of functional TGF- β receptors in cancer cells may lead to an attenuated Smad2 signal [13]. Similarly, Vilar *et al.* suggested that specific changes in receptor trafficking patterns could lead to phenotypes that favor tumorigenesis [14]. Coarse grained modeling approaches have also been applied to EMT; Steinway *et al.* used discrete dynamic modeling to study developmental EMT and known dysregulation in invasive hepatocellular carcinoma [15]. Although these models provided insight into the role of receptor dynamics, EMT induction involves many other components, including competing second messengers and interconnected transcriptional regulatory loops. Integrating these additional scales of molecular signaling while maintaining the capacity for robust prediction requires a new and

expanded computational and experimental strategy. Data-driven systems approaches [16] or logical model formulations [17] are emerging paradigms that constrain model complexity through the incorporation of training and validation data. These are interesting techniques because the data informs model structure (which can be expanded as more data becomes available). Alternatively, Bailey proposed more than a decade ago that a qualitative understanding of a complex biological system should not require complete definition of its structural and parametric content [18]. Shortly thereafter, Sethna and coworkers showed that complex model behavior is often controlled by only a few parameter combinations, a characteristic seemingly universal to multi-parameter models referred to as “sloppiness” [19]. Thus, reasonable model predictions are often possible with only limited parameter information. Taking advantage of this property, we developed sloppy techniques for parameter identification using ensembles of deterministic models [20]. Furthermore, we proposed that the sloppy behavior of biological networks may also be seen as a source of cell-to-cell [21] or even patient-to-patient heterogeneity [22]. Bayesian parameter identification techniques have also been used to explore cell-to-cell heterogeneity [23, 24], where a population of cells could be viewed as a dynamic ensemble of context-specific biochemical networks [25].

In this study, we developed a family of mathematical models describing the induction of EMT by TGF- β isoforms in the presence and absence of vascular endothelial growth factor A (VEGF-A). We integrated a simple rule-based description of activity and gene expression regulation with traditional ordinary differential equation (ODE) modeling to describe an EMT interaction network containing 97 gene,

protein or mRNA components interconnected through 169 interactions. This integration allows the description of complex regulatory interactions in the absence of specific mechanistic information, it also allowed to build a predictive yet compact model. A family of model parameters was estimated using 41 molecular data sets generated in DLD1 colon carcinoma, MDCKII and A375 melanoma cells using the Pareto optimal ensemble technique (JuPOETs) multiobjective optimization algorithm. JuPOETs generated an ensemble of approximately 1400 models for analysis. Analysis of the model population suggested that both MCF10A and DLD1 cells could exhibit phenotypic heterogeneity if treated simultaneously with TGF- β 1/2 and VEGF-A. This heterogeneity was characterized by a significant fraction of the population being in a “hybrid state” having both high E-cadherin and high Vimentin expression. We tested these predictions using qRT-PCR and flow-cytometry studies in a variety of experimental conditions. Validation studies confirmed that upwards of 45% of the cellular population could be put into the hybrid state in the presence of both TGF- β 1/2 and VEGF-A. Moreover, this response depended upon both activation of Sp1 by MAPK and NFATc1 transcriptional activity consistent with the predicted molecular signaling. Lastly, the hybrid populations of both DLD1 and MCF10A cells exhibited different functional behavior than those from either TGF- β or VEGF-A treatment. The extent of ductal branch formation significantly increased with MCF10A cells in the hybrid phenotype, compared with cells treated with VEGF-A alone. Together, these results establish a predictive mechanistic model of EMT susceptibility, and reveal a novel signaling axis, which possibly regulates carcinoma progression through an EMT versus tubulogenesis response.

3.4 Results

3.4.1 The model population captured key features of TGF- β induced EMT

The EMT model architecture, based upon curated molecular connectivity, described the expression of 23 genes following exposure to TGF- β isoforms and VEGF-A (Figure 1). The EMT model contained 74 molecular species interconnected by 169 interactions. Model equations were formulated as ordinary differential equations (ODEs) augmented with rule-based descriptions of activity and gene expression regulation. ODEs are common tools to model biochemical pathways [26–28]. However, while ODE models can simulate complex intracellular behavior, they require estimates for model parameters which are often difficult to obtain. The EMT model had 251 unknown model parameters, 169 kinetic constants 38 control constants and 44 saturation constants. In addition to constants appearing in the signaling kinetics, characteristic gene expression and translation parameters were estimated from literature, and then corrected for each protein and transcript (four correction factors per gene product, see materials and methods). As expected, the unknown parameters were not uniquely identifiable given the training data [29]. Thus, instead of identifying a single best fit (but uncertain) model, we estimated a sloppy population of models (each consistent with the training data) by simultaneously minimizing the difference between model simulations and 41 molecular data sets using the Pareto Optimal Ensemble Technique (JuPOETs). The training data were generated in DLD1 colon carcinoma, MDCKII, and A375 melanoma cells following exposure to TGF- β isoforms [7]. We organized these data sets into 11 objective functions which were simultaneously minimized by JuPOETs. Additionally, we used data generated in this

study (S1 Figure), and 12 molecular data sets generated in HK-2 cells following VEGF-A exposure to train VEGF-A responsive model processes [30]. To guard against overfitting, we augmented the multiobjective optimization with leave-one-out cross validation to independently estimate both the training and prediction error for each objective. Thus, we generated 11 different model ensembles. Lastly, we compared model predictions with independent data sets not used during training (both at the molecular and model population levels) to evaluate the predictive power of the parameter ensemble.

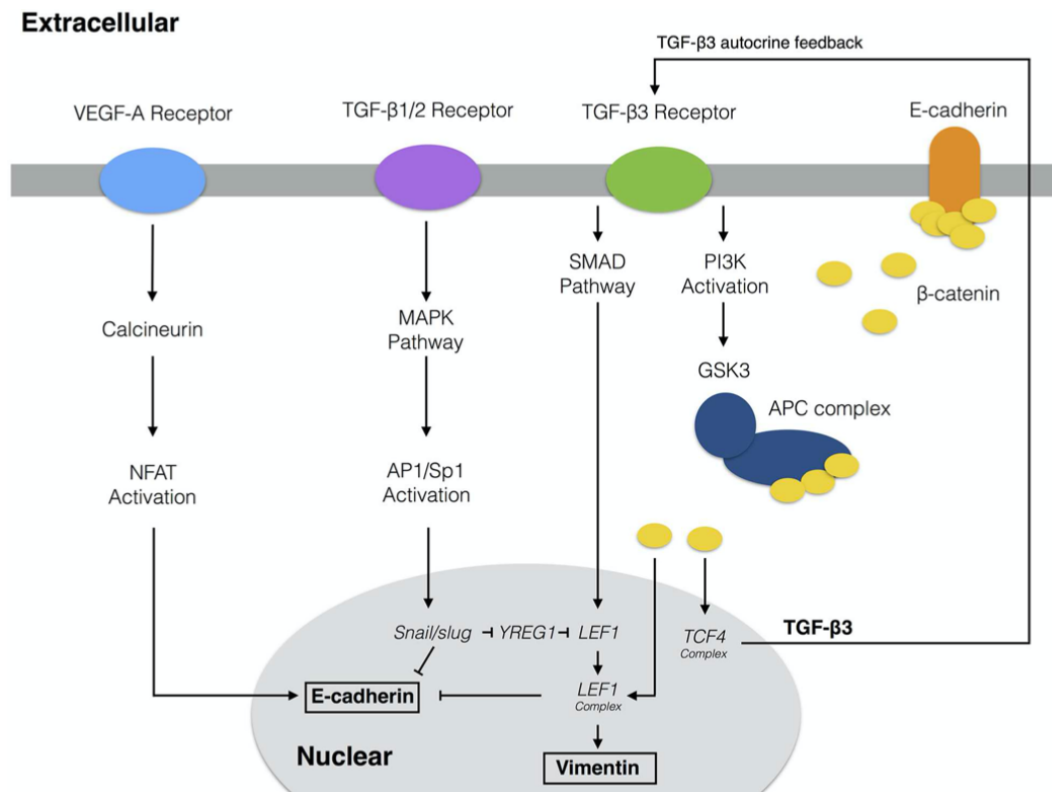


Figure 3.1. Model connectivity recreates the core architecture during EMT. The EMT network contains 97 nodes (proteins, mRNA, and genes) interconnected by 169 interactions. Central to EMT induction, activation of the MAPK cascade occurs through TGF- β 1/2 binding which activates the AP-1/Sp1 transcriptional axis. AP-1/Sp1 drives an autocrine response of TGF- β 3, which activates the Smad cascade, leading to phenotypic change. Conversely, VEGF-A binding can stabilize an epithelial phenotype through NFAT activation. Downstream activation of β -catenin signaling due to E-cadherin loss and GSK3 inactivation of β -catenin confinement is critical to the complete activation of the EMT program. The complete list of molecular interactions that comprise the model is given in the supplement.

JuPOETs generated a population of probable signaling models which captured the multiple phases of EMT induction (Figure 2). JuPOETs sampled well over 10^4 probable models during each stage of the cross-validation using global random sampling. From this analysis, $N \approx 1400$ models were selected for further analysis. The selected models all had the same possible molecular connectivity, but different values for model parameters. Transcription and translation rates, as well as mRNA and

protein degradation terms, were set using physical values from the literature [31], and allowed to vary by a scaling factor, see methods. Model selection was based upon Pareto rank, the prediction and training error across all objectives. The model population recapitulated key signaling events following TGF- β exposure. We subdivided the response to TGF- β exposure into two phases. First, TGF- β 1/2 signaling initiated a program which downregulated E-cadherin expression in a MAPK dependent manner while simultaneously upregulating TGF- β 3 expression. Second, TGF- β 3 secretion initiated an autocrine feedback which upregulated the expression of mesenchymal markers such as Vimentin and key upstream transcription factors such as LEF-1 in a SMAD dependent manner. TGF- β 3 expression was also able to sustain β -catenin release by inhibiting its sequestration by the APC complex through PI3K mediated GSK3, which was captured by the model (S2 Figure). Each phase involved the hierarchal expression and/or post-translational modification of several key transcription factors. During the first phase, stimulation with TGF- β 1/2 (10 a.u.) activated both the SMAD and MAPK pathways. MAPK activation resulted in the phosphorylation of the transcription factor activator protein 1 (AP-1), which in-turn upregulated the expression of Snail, a well established transcriptional repressor (Figure 2A). Snail expression was MAPK-dependent; the MEK inhibitor U0126 blocked AP-1 activation and Snail expression following TGF- β 1/2 exposure (Figure 2A, Lane 3). Overexpression of either Snail or Slug upregulated TGF- β 3 expression (Figure 2C) while simultaneously downregulating E-cadherin expression (Figure 2F). During the second phase, TGF- β 3 secretion and the subsequent autocrine signaling resulted in the upregulation of mesenchymal marker expression. The TGF- β 3 induced

gene expression program involves a complex hierarchy of transcriptional and post-translational regulatory events. Absence of E-cadherin indirectly promoted TGF- β 3 expression through the β -catenin/TCF4 complex following Snail or Slug expression (Figure 2C, Lane 2 or 3). Conversely, over-expression of E-cadherin inhibited the TGF- β 3 autocrine production by sequestering cytosolic β -catenin, thereby blocking EMT (Figure 2C, Lane 4 or 5). TGF- β 3 signaled through the Smad pathway to regulate LEF-1 expression and downstream target EMT genes (Figure 2G). TGF- β 3 (10 a.u.) in combination with downstream inhibitors (DN-Smad4 and DN-LEF-1) completely inhibited Vimentin expression, while elevating E-cadherin expression (Figure 2H and 2I).

The predictive power of the ensemble was tested using cross validation and by comparing simulations with data not used for model training. In whole, all of our training objectives were statistically significant (at a 95% confidence interval) compared to a randomized parameter family (N = 100) generated from a random starting point. Conversely, we *predicted* all of the training objectives, at a 95% confidence interval compared to randomized parameters (Wicoxon non-parametric test). The model also captured the temporal gene expression responses of E-cadherin, pSmad2, and LEF-1 (not used for model training) to within one-standard deviation (up to the 48 hr time-point) (Figure 2J–2L). Taken together, the model captured the key signaling events revealed by Medici *et al.* [7] that drive the phenotypic conversion. A listing of objective function values resulting from training, cross validation and the random parameter control is given in the supplement (S3 Figure).

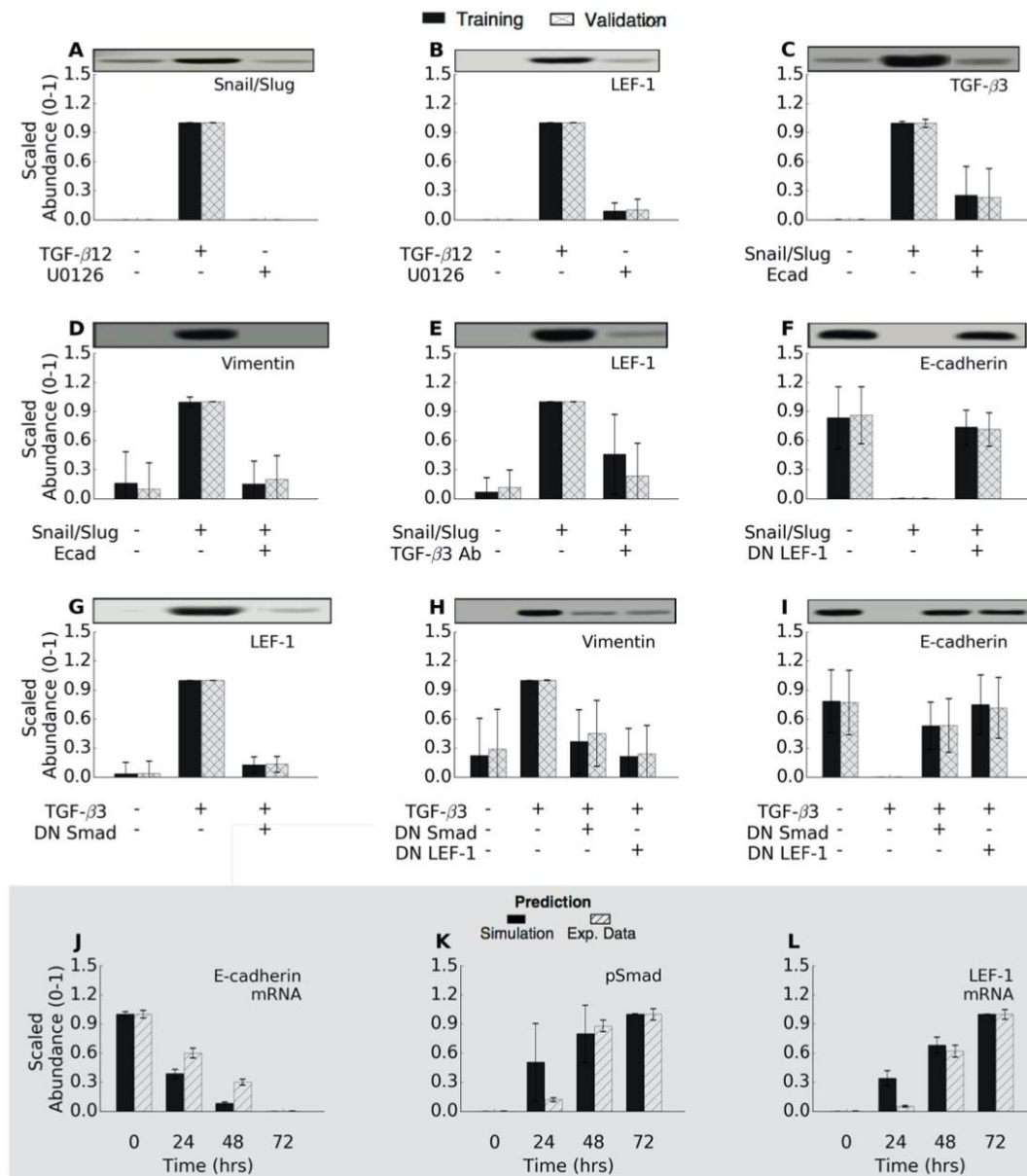


Figure 3.2. Training and validation simulations. The population of EMT models qualitatively captured TGF- β -induced EMT signaling. (A-I) The population was generated using JuPOETs and trained using 11 different objective functions (41 data sets) taken from Medici *et al.* [7]. The model captured the simulated experiments for all cases when compared to randomized controls. (J-L) The model populations were also compared against untrained temporal data to measure the effectiveness as a pure prediction. The western blot data was reproduced from Medici *et al.* [7]. The intensity of each band was estimated using the ImageJ program. These blot intensities were then used as the training data for the EMT parameter estimation studies.

3.4.2 TGF- β 1/2 and VEGF-A exposure promotes phenotype heterogeneity through NFATc and phosphorylated Sp1

While we captured the central tendency of many of the molecular features of EMT induction following TGF- β 1/2 exposure, an often neglected but important emergent feature of developmental and pathological programs is population heterogeneity [32]. We (and others) have previously hypothesized that deterministic model ensembles can simulate population behavior, at least at a coarse grained level [21]. We tested this hypothesis by analyzing the response of the population of EMT models to extracellular cues and then comparing this response to flow cytometry studies. We quantified the phenotypic response of the individual members of the ensemble to TGF- β 1/2 stimulation for two downstream phenotypic markers, Vimentin (mesenchymal) and E-cadherin (epithelial) following the addition of TGF- β 1/2 alone (Figure 3), and/or VEGF-A in combination with NFATc inhibitors (Figure 3). We identified model subpopulations that exhibited different behaviors following exposure to TGF- β 1/2 (Figure 3B). Analysis of the molecular signatures of these subpopulations suggested the abundance, localization and state of the Sp1, AP-1 and NFATc transcription factors controlled population heterogeneity. The majority of models (>80%) responded to treatment, moving away from the untreated population (Figure 3A–3F, gray). These models showed the classically expected behavior, a switch from an epithelial to mesenchymal phenotype following TGF- β 1/2 exposure. Some models resembled untreated cells; they had elevated phosphorylated Sp1, relative to non-induced cells, which decreased E-cadherin expression through Slug-mediated inhibition, which in turn increased Vimentin expression through TGF- β 3

autocrine signaling and the liberation of β -catenin. However, the most biologically interesting behavior was exhibited by cells achieving a hybrid phenotype, most notable in a dual treatment condition (Figure 3C, black arrow), but also present in a small percentage of untreated cells (Figure 3B, gray arrow). Models with this hybrid phenotype had elevated Sp1 and NFAT transcriptional activity, resulting in simultaneously increased Vimentin and E-cadherin expression (Figure 4A). However, these conclusions are likely sensitive to the components that we have included in the model, and could also involve proteins that we have not considered.

To better understand the hybrid phenotype, we simulated the response of the model population to TGF- β 1/2 and VEGF-A treatment with and without NFATc inhibitors (Figure 3). As expected, stimulation with VEGF-A (50 a.u.) maintained an epithelial population (Figure 3A), while TGF- β 1/2 (10 a.u.) exposure shifted the population from an epithelial to a mesenchymal phenotype (Figure 3B). On the other hand, combined stimulation with TGF- β 1/2 (10 a.u.) and VEGF-A (50 a.u.) increased both E-cadherin and Vimentin expression, resulting in a hybrid phenotype with both epithelial and mesenchymal characteristics (Figure 3C). Vimentin expression was correlated with high levels of nuclear phosphorylated Sp1, following TGF- β 1/2 exposure. Conversely, elevated E-cadherin expression depended upon the activity of NFAT transcription factors downstream of VEGF-A stimulation. To further isolate the role of NFAT on this hybrid state, we simulated the inhibition of NFAT transcriptional activity across all conditions (all else being equal). NFAT inhibition in combination with VEGF-A or TGF- β 1/2 treatments blocked increased E-cadherin expression in the case of VEGF-A (Figure 3D), but did not influence TGF- β 1/2 signaling (Figure 3E).

Lastly, NFATc inhibition in combination with simultaneous TGF- β 1/2 and VEGF-A exposure repressed nearly all E-cadherin expression, shifting nearly the entire population towards a mesenchymal phenotype (Figure 3F). Taken together, high levels of nuclear localized phosphorylated Sp1 correlated with Vimentin expression, while NFATc transcriptional activity was critical for maintaining E-cadherin expression in the presence of competing signals.

3.4.3 Identification of a novel LEF-1 regulator

During model identification, we found that consistent TGF- β induced EMT from a stable epithelial cell population required an additional regulatory protein. This protein, which we called hypothetical regulator 1 (YREG1), was required to mediate between SNAIL/SLUG transcriptional activity and the upregulation of LEF-1 expression following TGF- β 1/2 exposure. SNAIL/SLUG are well known transcriptional repressors [33–35], although there are a few studies which suggest that at least SNAIL can also act as a transcriptional activator [36]. In the model, we assumed the expression of SNAIL/SLUG was likely regulated by AP1/SP1 [37]. Thus, upon receiving direct SNAIL/SLUG and TGF- β 3 signals, the model predicted enhanced SNAIL/SLUG expression, consistent with experimental observations. TGF- β 1/2 stimulation also induces LEF-1 expression. However, literature evidence suggested that LEF-1 expression was not strongly dependent upon AP1/SP1 activity [38]. Thus, either SNAIL/SLUG are acting as inducers (contrary to substantial biochemical evidence) or, they are repressing the expression of an intermediate repressor. Given the biochemical evidence supporting SNAIL/SLUG as repressors, we created the hypothetical YREG1 repressor whose expression is downregulated by

SNAIL/SLUG. The literature data therefore suggested that YREG1 had two transcriptional targets, LEF-1 and TGF- β 3. By adding this regulator, our simulations became consistent with training and literature data. Medici et al. suggested that feedback between β -catenin and LEF-1 was likely, although this feedback had yet to be identified [7]. Low levels of YREG1 expression were present in all simulations to regulate the formation of the β -catenin-LEF-1 complex. To test the effect of YREG1 on the epithelial population, we conducted over-expression and knockdown simulations on untreated cells (Figure 4B and 4C). In the absence of YREG1, the population of models failed to consistently to retain a stable epithelial state (Figure 4B). Conversely, YREG1 amplification revealed an enhanced epithelial phenotype, while some inherently transformed cells moved towards a hybrid phenotype (Figure 4C). Elevated YREG1 repressed LEF-1 and TGF- β 3 expression, thereby not allowing free β -catenin to form the β -catenin-LEF-1 complex, or TGF- β 3 induced SMAD activation. Taken together, low YREG1 expression was required for the maintenance of a stable epithelial phenotype that was simultaneously inducible across TGF- β 1/2, TGF- β 3 and SNAI1/SLUG transfection.

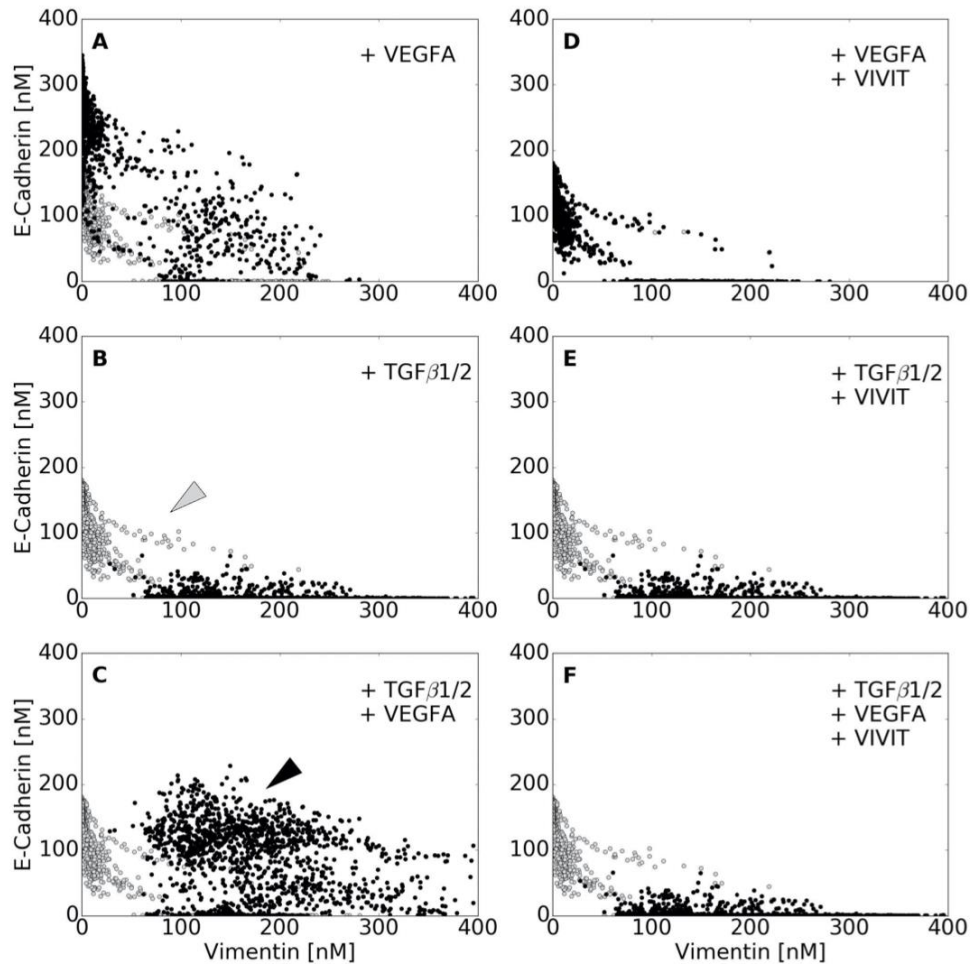


Figure 3.3. Simulated VEGF-A and TGF- β 1/2 exposure promoted phenotype heterogeneity. Simulated response to TGF- β 1/2 and VEGF-A exposure with and without axis specific inhibitors. Vimentin and E-cadherin abundances (in nM) were used to quantify the shift in population at 48 hrs. (A-C) VEGF-A (50 a.u.) treatment resulted in a population with enhanced epithelial properties. This was contrary to the addition of TGF- β 2 (10 a.u.), which shifted the population towards a mesenchymal phenotype. Interestingly, the combined effects of TGF- β 2 and VEGFA was found to increase both ecadherin and vimentin levels, creating a heterogeneous population (black arrow), which can also be seen in a minority of untreated cells (gray arrow). (D-F) To isolate the effect of NFAT, we inhibited NFAT de-phosphorylation in combination with VEGFA. This negated the increase in ecadherin expression and shifted the population towards a mesenchymal phenotype. Likewise, combining NFAT inhibition with TGF- β mitigated all VEGF enhanced ecadherin expression. Lastly, combination of TGF- β 2, VEGFA, and NFAT inhibition nearly mitigated all effects of VEGFA, shifting the heterogeneous population towards a mesenchymal phenotype. In whole, high levels of phosphorylated-Sp1 correlated with vimentin expression, while NFAT was responsible for maintaining E-cadherin expression in the presence of other factors, although neither were mutually exclusive.

3.4.4 Combined TGF- β 2 and VEGF-A exposure drives heterogeneity in MCF10A and DLD1 cells

The EMT model simulations suggested the transcriptional activity of NFATc and Sp1 could be independently tuned to generate a hybrid cell population with both epithelial and mesenchymal characteristics. To test this hypothesis, we exposed either quiescent epithelial (MCF10, Figure 5) or transformed epithelial cells (DLD1, S4 Figure) to combinations of TGF- β 1/2 and/or VEGF-A. As expected, TGF- β 1/2 treatment (10ng/ml) increased Slug and Vimentin expression, while repressing E-cadherin expression both at the transcript and protein levels in MCF10A (Figure 5A and 5B) and DLD1 cells (S5C Figure). Both MCF10A (Figure 5C) and DLD1 cells (S4E and S4G Figure) transitioned from quiescent cobblestone morphology to spread spindle shapes, consistent with EMT. As predicted, we found increased nuclear localization of phosphorylated Sp1 following TGF- β 1/2 stimulation in both MCF10A (Figure 5B and 5C) and DLD1 cells (S4E and S4F Figure). Consistent with model predictions, VEGF-A (50ng/ml) treatment increased the abundance of NFATc1 and E-cadherin at both the transcript and protein level in both MCF10A (Figure 5A) and DLD1 cells (S4 Figure). We also found that NFATc1 nuclear localization significantly increased in both MCF10 (Figure 5B and 5C) and DLD1 (S4C and S4E Figure) cells treated with VEGF-A. Interestingly, combining VEGF-A (50ng/ml) with TGF- β 1/2 (10ng/ml) resulted in significantly elevated expression of both E-cadherin and Vimentin at the transcript and protein levels in both MCF10A (Figure 5A and 5B) and DLD1 cells (S4 and S5 Figs). NFATc1 expression increased, while Sp1 expression was similar to the TGF- β 1/2 case alone (Figure 5A and 5B, S4D and S4E Figure),

supporting their independent regulation. The expression of Slug, and Vimentin significantly increased, while E-cadherin levels were increased in MCF10A cells (Figure 5A) and maintained at control levels in DLD1 cells (S4D Figure). As predicted, nuclear co-localization of both NFATc1 and phosphorylated Sp1 were apparent in MCF10A (Figure 5B and 5C) and DLD1 (S4E and S4F Figure) cells treated with both ligands. Taken together, combined VEGF-A and TGF- β 1/2 treatment elicited a hybrid phenotype expressing both mesenchymal and epithelial characteristics in both MCF10A and DLD1 cells. This phenotype was driven by the transcriptional activity of two key transcription factors, Sp1 and NFATc, which could be modulated independently by TGF- β 1/2 and VEGF-A exposure.

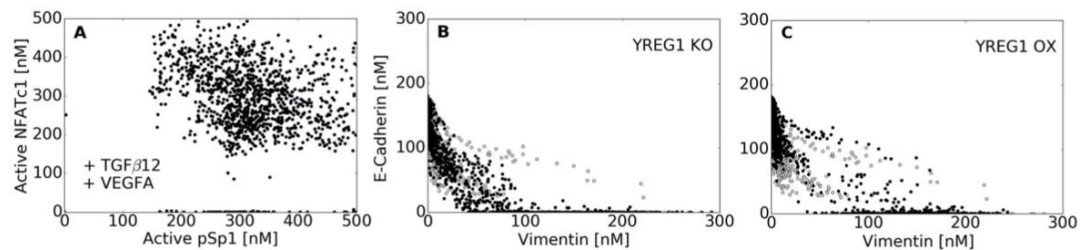


Figure 3.4. Analysis of underlying signaling responses. We examined the distribution of NFATc1 and AP1/SP1 in cells containing the hybrid phenotype (VEGF-A + TGF- β 2 case), showing the potential for cells to express both SP1 and NFATc1 in a non exclusive manner. (B) In the absence of YREG1, most of the population failed to consistently to retain a stable epithelial state. (C) We identified a novel regulator of LEF1 called YREG1 that allows Snail/ Slug to emulate an inducer by repressing YREG1, which was required to stabilize the untreated population. YREG1 overexpression revealed an enhanced epithelial phenotype, while some inherently transformed cells moved towards a hybrid phenotype.

Our phenotypic analysis predicted that NFATc transcriptional activity was critical to maintaining E-cadherin expression in the presence of both VEGF-A and TGF- β 1/2. We experimentally tested this hypothesis by exposing both MCF10A (Figure 5E and 5F) and DLD1 cells (S5 Figure) to combinations of VEGF-A and TGF- β 1/2 in the

presence or absence of VIVIT, a soluble peptide inhibitor of NFATc transcriptional activity [39]. Treatment with VEGF-A (50ng/ml) and VIVIT (10 μ M) in MCF10A cells significantly reduced E-cadherin expression compared to VEGF-A alone (Figure 5D and 5E). Co-treatment with VIVIT and TGF- β 1/2 did not enhance EMT capacity of MCF10A cells above that of TGF- β 1/2 alone (Figure 5A, 5B and 5E). Likewise, VIVIT in combination with both TGF- β 1/2 and VEGF-A resulted in a loss of E-cadherin gene and protein expression, while Slug and Vimentin levels remained increased (Figure 5D and 5E). Quantitative flow cytometry confirmed these results in both MCF10A (Figure 5F) and DLD1 cells (S5C Figure). Both epithelial cell lines initially had high levels of E-cadherin expression, and low Vimentin abundance (Q1–99.5%), but both MCF10A and DLD1 cells shifted from an epithelial to mesenchymal phenotype (Q1–33.4%, Q4–42.8%) following TGF- β 1/2 exposure. As expected, NFATc nuclear localization was repressed with VIVIT treatment regardless of ligand stimulation, while the abundance of nuclear phosphorylated Sp1 increased for both TGF- β 1/2 and TGF- β 1/2 + VIVIT conditions (Figure 5C and 5E). Combined TGF- β 1/2 and VEGF-A increased both Vimentin and E-cadherin expression (Q1–42.1%, Q2–52.3%) compared to TGF- β 1/2 alone. Together, these results demonstrate that NFATc and phosphorylated Sp1 are critical for regulating E-cadherin and Vimentin expression during phenotype heterogeneity in MCF10A and DLD1.

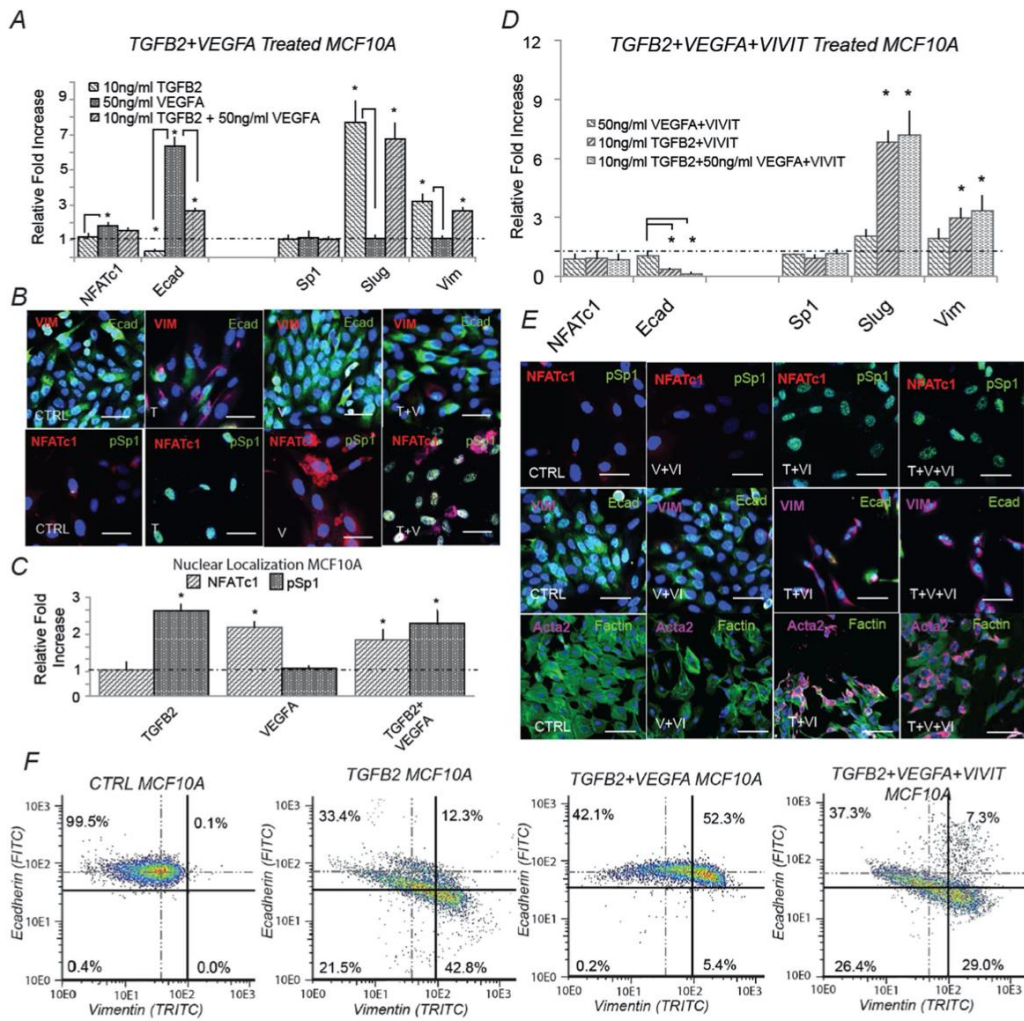


Figure 3.5. Simultaneous TGF- β 1/2 and VEGF-A treatment induced phenotype heterogeneity and is dependent upon NFAT activity *in-vitro*. (A) In MCF10A, treatment with (10ng/ml) TGF- β 2 increased Slug and vimentin, while ecadherin expression was inhibited at both the gene and protein level at 48 hrs. Conversely, VEGFA alone increased both NFATc1 and ecadherin gene expression. Simultaneous TGF- β 2 (10ng/ml) and VEGFA (50ng/ml) treatment increased Slug, NFATc1, and vimentin expression, while also increasing ecadherin levels via qPCR. (B-C) Immunofluorescence confirmed these results and nuclear co-localization of both phospho-Sp1 and NFAT were found dependent upon TGF- β 2 and VEGFA, respectively. (D) To isolate the effect of NFAT, treatment of VEGFA (50ng/ml) and VIVIT (10 μ M) reduced ecadherin expression at 48hrs (control-dashed line). Similarly, combined TGF- β 2, VEGFA and VIVIT treatment increased Slug and vimentin expression, while inhibiting ecadherin levels via qPCR. (E) These findings were confirmed via immunofluorescence as the VIVIT peptide inhibited ecadherin and nuclear localization of NFATc1 in all three cases. (F) Quantitative flow cytometry also confirmed this trend. Similar experiments in DLD1 followed a similar trend (supplement). Magnification, 40x. Scale bars: 50 μ m.

C = Control, T = TGF- β 2, V = VEGFA, VI = NFAT inhibitor (VIVIT). Asterisks signify statistical differences from each other according to a one-way ANOVA with Tukey's post hoc ($p < 0.05$).

3.4.5 Ductal branching during acini formation is dependent upon phenotype heterogeneity in MCF10A and DLD1 cells

We finally employed established three-dimensional (3D) *in vitro* models of invasion, migration, compaction, and tubulogenesis [40] to determine the functional consequences of the hybrid phenotype (Figure 6). MCF10A and DLD1 cells were aggregated via hanging drop, placed on the surface of a collagen gel, and cultured for 72 hrs under various biochemical treatments. TGF- β 1/2 stimulation significantly enhanced cell matrix invasion and matrix compaction, while in contrast VEGF-A stimulation promoted surface migration but no invasion or compaction (Figure 6B–6D). Interestingly, combined TGF- β 1/2 and VEGF-A stimulation significantly increased cell migration potential above that of VEGF-A alone while maintaining 3D matrix compaction, though with decreased magnitude compared to TGF- β 1/2 alone. Inhibition of NFATc transcriptional activity by VIVIT decreased migration following treatment with VEGF-A alone (Figure 6B). Co-treatment of VIVIT significantly decreased migration, while complementarily increasing invasion and compaction, when MCF10A cells were stimulated with both VEGF-A and TGF- β 1/2 (Figure 6B–6D). The responses of DLD1 cells followed a similar trend to MCF10A, although the magnitudes of migration, invasion, and compaction were less. Cell circularity within 3D gels strongly and negatively correlated with both invasion and compaction regardless of treatment (Figure 6E). Circularity refers to the morphology of the cells.

In general, a quiescent epithelial cell assumes a circular morphology in culture, while an active mesenchymal cell is highly elongated. The circularity index, a common means of quantifying cell morphology, relates cell area to perimeter. A perfect circle has a circularity index equal to 1.0, while a straight line has a circularity index equal to 0.0, see Butcher et al. [41]. TGF- β 1/2 treatment alone resulted in irregular and spindle shaped morphology, while VEGF-A exposure promoted round quiescent cells (Figure 6A). Combined VEGF-A and TGF- β 1/2 promoted morphology between these extremes. VIVIT mediated NFATc inhibition significantly reduced the circularity index, similar to TGF- β 1/2 treatment (Figure 6F). VEGF-A treatment also induced the formation of tubular structures (acini), but the number of tubular branches relative to total acini was significantly increased upon combined TGF- β 1/2 and VEGF-A. No tubular structures were identified within the DLD1 constructs during the 7 day tubulogenesis endpoints, supporting that MCF10A and DLD1 cells have some cell-type specific EMT sensitivity despite their underlying competency for acquiring a heterogeneous phenotype. This suggests that initial EMT sensitivity of a cell influences downstream functional response from TGF- β and VEGFA stimulation. Together, these results establish that VEGF-A and TGF- β 1/2 ligand concentrations potentiate between acini and ductal branch formation in 3D culture, and are dependent upon NFATc activity.

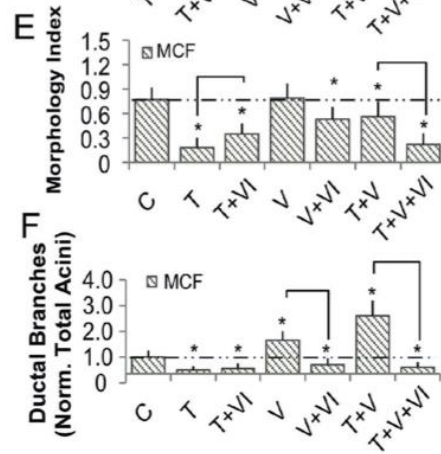
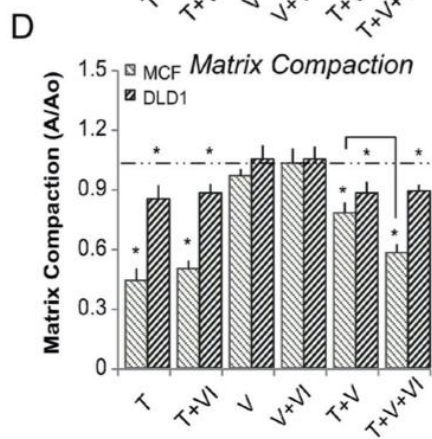
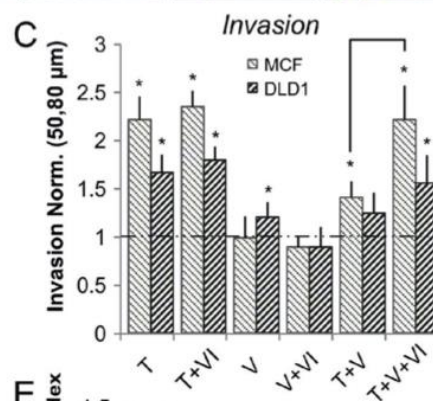
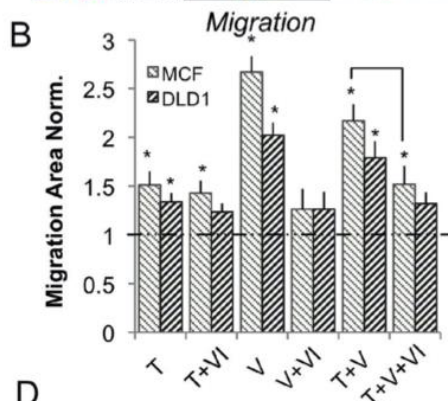
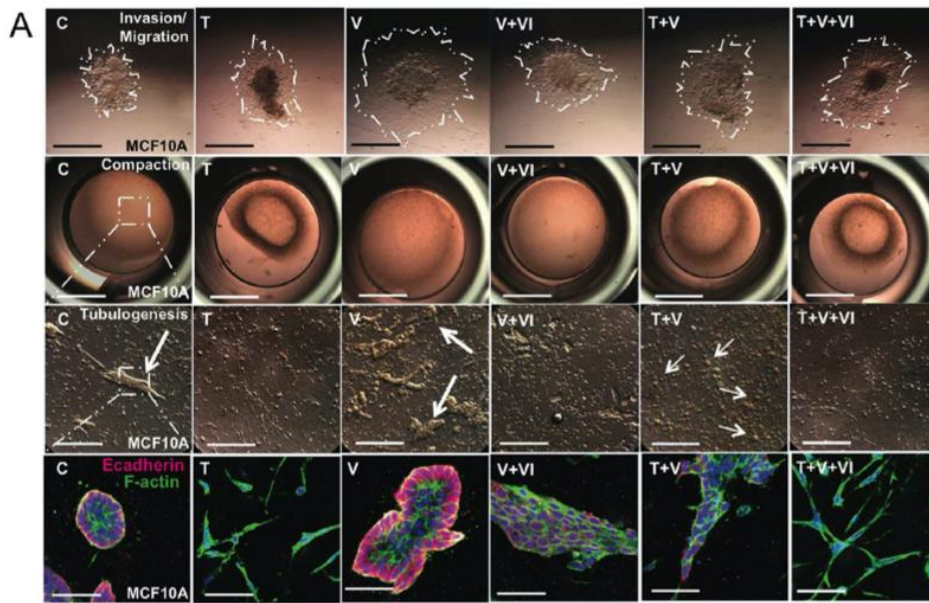


Figure 3.6. Ductal branching is dependent upon phenotype heterogeneity within MCF10A in 3-D culture. MCF10A and DLD1 were formed into spheroids overnight and explanted to a collagen gel for 72 hrs. For compaction and tubular assays, cells were embedded into collagen gels for 72 hrs, and the extent of tubulogenesis was measured at 7 days. (A-D) Within MCF10A, TGF- β 2 (10ng/ml) enhanced invasion and contractile properties while, VEGFA (50ng/ml) promoted increased migration. TGF- β 2 with VEGFA significantly increased migration, while limiting with compaction. VIVIT (10 μ M) in combination with VEGFA and TGF- β 2 decreased migration and compaction, while increasing invasion. (D) Likewise, cell morphology (circularity index) correlated with both invasion and compaction in MCF10A. (E-F) The size of tubular structures (acini) also increased significantly upon addition of VEGFA, while the number of ductal branches was most significant upon simultaneous TGF- β 2 and VEGFA treatment (Red-Ecadherin, Green-Factin, Blue- Nuclear). DLD1 cells followed a similar trend, although the degree of migration, invasion, and compaction was less significant. In addition, no tubular structures were identified during the 7 day tubulogenesis endpoints. Scale bars: 500 μ m, 1000 μ m, 250 μ m, and 80 μ m, respectively. C = Control, T = TGF- β 2, V = VEGFA, VI = NFAT inhibitor (VIVIT). Asterisks signify statistical differences from each other according to a one-way ANOVA with Tukey's post hoc ($p \leq 0.05$). Boxes in the left-most panel identify regions identified by arrows that were then imaged in greater zoom in the panel immediately below. The box diagram was not repeated for arrows in the other panels for clarity, but the same method was applied.

3.5 Discussion

In this study, we developed a family of mathematical models describing the induction of EMT by TGF- β isoforms in the presence and absence of VEGF-A. The model, which contained 74 molecular species interconnected by 169 interactions, described the expression of 23 genes in response to growth factor stimulation. We estimated an ensemble of likely model parameters using the JuPOETs multiobjective optimization framework. The model population was trained and cross-validated to prescribe biological significance using 41 data sets generated in DLD1 colon carcinoma, MDCKII, and A375 melanoma cell lines [7]. Analysis of this population predicted possible phenotypic modes (and their associated signaling) that cells could exhibit when stimulated with TGF- β and/or VEGF-A. The most novel hypothesis generated from the analysis was that cells could operate in a hybrid state defined by both epithelial and mesenchymal traits when stimulated simultaneously with TGF- β and VEGF-A. We tested this hypothesis in MCF10A and DLD1 cells stimulated with combinations of TGF- β and VEGF-A. As expected, in the presence of TGF- β or VEGF-A alone, MCF10A and DLD1 cells were either mesenchymal or epithelial, respectively. However, with both TGF- β and VEGF-A, MCF10A and DLD1 cells exhibited a hybrid phenotype, having both epithelial and mesenchymal characteristics. Furthermore, we found that functional traits such as tubulogenesis and ductal branching were different for cells in this hybrid phenotype. Together, this study established a predictive model of EMT induction, determined that deterministic model ensembles could predict population heterogeneity, and proved the existence of a

unique hybrid phenotype resulting from the simultaneous integration of extracellular growth factor signals.

Cells routinely process a multitude of signals simultaneously, especially when coordinating developmental or pathological programs. For example, oncogenic cells integrate both mechanical and chemical cues in their local microenvironment during tumorigenesis, including cytokines VEGF and TGF- β [42]. VEGF-A mediates pathological angiogenic remodeling of tumors [43], while TGF- β can elicit both protective and oncogenic responses [44, 45]. While much research has tested signaling pathways individually, far less is understood about combinatorial stimulation, such as with both VEGF-A and TGF- β . Both *in vitro* and *in vivo* studies have suggested that epithelial cells can exhibit heterogeneous phenotypes in addition to classically defined epithelial or mesenchymal states [46, 47]. For example, expression profiling in human epithelial cancer cell lines demonstrated a spectrum of phenotypes, including some that expressed both E-cadherin and Vimentin simultaneously [48, 49]. Zajchowski *et al.*, speculated that these expression profiles were somehow important for maintaining epithelial properties, while simultaneously allowing other functional behavior such as proliferation and migration [50]. Whether and how heterogeneous phenotypes arise and participate in cancer progression, as well as their response to pharmacological inhibition are fundamental questions that should receive increased attention. In this study, we determined that a hybrid phenotype could be obtained through combined treatment with VEGF-A and TGF- β , both common factors localized in the tumor microenvironment. Furthermore, our systematic simulation-experimentation strategy identified that the transcriptional activity of Sp1 and NFATc were the critical factors

controlling this phenotypic heterogeneity. Several studies have highlighted the importance of NFATc as a key transcription factor involved in cell growth, survival, invasion, angiogenesis and cancer [51]. For example, proliferation and anchorage-independent growth of pancreatic tumor cells is dependent on calcineurin and NFATc1 activity, consistent with the high levels of nuclear NFATc1 found in pancreatic tumors [52]. Likewise, our results found that VEGF-A was a potent inducer of NFATc1 expression, which may be required for epithelial cell migration and tubulogenesis. Although specific NFATc isoforms were not distinguished in the model, our simulations suggested that NFATc transcriptional activity was capable of maintaining epithelial traits, even during TGF- β induced EMT. Experimentally, we found that E-cadherin expression was dependent upon NFATc dephosphorylation in response to simultaneous VEGF-A and TGF- β 1/2 treatment. Thus, these results support the hypothesis that NFATc activity plays a critical role in maintaining cell-cell contacts, even during partial EMT.

Epithelial cells reproduce tissue-like organization when grown in a three-dimensional extracellular matrix (ECM) environment, and therefore are an attractive model to study morphogenic mechanisms. It is well established that MCF10A cells form structures that closely resemble acini (multi-lobed cluster of cells) in three-dimensional *in vitro* cultures [53]. It has been postulated that a cellular response reminiscent of partial EMT underlies this process, stimulating further branching and formation of acini [54]. Normally well controlled process such as tubulogenesis can be co-opted by cancer cells to break away from a primary lesion and invade through the surrounding stroma [55]. However, by retaining a transient hybrid EMT-like state,

clusters of these tube-forming tumor cells can reform at a high rate after invasion, possibly explaining why invasive human carcinomas frequently appear to be cellular collections with varying degrees of gland-like differentiation [56]. In this study, we showed that our predicted hybrid phenotype generated by simultaneous treatment of epithelial cells with VEGF-A and TGF- β possessed altered migration and invasion, which enhanced tubular branching. A salient feature of this behavior, however, was the retention of cell-cell contacts that allowed cells to migrate without completely dissociating from their neighbors. Thus, our results support a mechanism in which hybrid cells can maintain some functional characteristics of epithelial cells such as cell-cell adhesion, which are normally lost in a fully differentiated mesenchymal state.

The tumor microenvironment contains many soluble signals simultaneously, including VEGF and TGF- β . Thus, it is likely that some cancerous epithelial cells could exhibit hybrid EMT phenotypic states. This may explain why fibroblastoid morphology, a classical feature of EMT, is not commonly observed in human carcinomas [56]. This study focused on the combinatorial effects of two very different ligand families present together in the tumor environment. Additional modeling studies are required to unravel the global response of epithelial cells to the full spectrum of chemical, substrate, and mechanical cues. The simulation strategy presented here is readily adaptable to larger species sets, with the major advantage that experimentally testable hypotheses can be generated regarding how signals get integrated to produce global cellular response. Furthermore, by simulating multiple ensembles of parameter sets, subpopulations across a constellation of phenotypes can be created and mined for common and/or divergent signaling characteristics. This is a

significant advantage over forced convergence to a single unique solution and thereby generating a potentially non-physiological homogeneous population.

The deterministic population of EMT models predicted heterogeneous behavior that was qualitatively consistent with experimental studies. There is a diversity of algorithmic approaches to estimate model parameters [57], as well as many strategies to integrate model identification with experimental design [58, 59]. However, despite these advances, the identification of models describing intracellular network behavior remains challenging. There are different schools of thought to deal with this challenge. One school has focused on model reduction. Data-driven approaches [16], boolean [60] or other logical model formulations [17, 61] are emerging paradigms that constrain model complexity by the availability of the training and validation data. Other techniques such as constraints based modeling, which is commonly used to model metabolic networks, have also been applied to model transcriptional networks, although primarily in lower eukaryotes and prokaryotes [62]. These techniques (and many others, see review [63]) are certainly exciting, with many interesting properties. Here, we used a traditional approach of mass action kinetics within an ordinary differential equation framework that also included transfer functions to simplify scenarios where reactions involving one species are controlled by several others (e.g. E-cadherin transcription). The identification problem for the EMT model was underdetermined (not uncommon for differential equation based models). However, a central criticism leveled by biologists is that model simplification is often done at the cost of biological reality, or done for reasons of computational expediency [64]. To avoid this criticism, we systematically identified an ensemble of likely

models each consistent with the training data, instead of a single but uncertain best fit model. Previously, we (and others) have suggested that deterministic ensembles could model heterogeneous populations in situations where stochastic computation was not feasible [21]. Population heterogeneity using deterministic model families has previously been explored for bacterial growth in batch cultures [65]. In that case, distributions were generated because the model parameters varied over the ensemble, i.e., extrinsic noise led to population heterogeneity. In this study, parameters controlling physical interactions such as disassociation rates, or processes such as gene expression were distributed over the ensemble. Population heterogeneity can also arise from intrinsic thermal fluctuations, which are not captured by a deterministic population of models [66]. Thus, deterministic ensembles, provide a coarse-grained or extrinsic-only ability to simulate population diversity. Despite this limitation, our prediction of phenotypic heterogeneity (and the underlying signaling events responsible for the heterogeneity) was consistent with experimental observations. This suggested that deterministic ensembles could simulate disease or developmental processes in which heterogeneity plays an important role, without having to resort to stochastic simulation.

A common criticism of ODE modeling has been the poorly characterized effect of structural and parametric uncertainty. In this study, parametric uncertainty was addressed by developing an ensemble of probable models instead of a single best-fit but uncertain model using multiobjective optimization. While computationally complex, multiobjective optimization is an important tool to address qualitative conflicts in training data that arise from experimental error or cell line artifacts [67].

On the other hand, structural uncertainty is defined as uncertainty in the biological connectivity. The EMT model connectivity was assembled from an extensive literature review. However, several potentially important signaling mechanisms were not included. First, we identified a potential gap in biological knowledge surrounding the regulation of LEF-1 expression, that was filled by the addition of the hypothetical YREG1 transcriptional repressor. The LEF-1 transcription factor is expressed in tissues that undergo EMT during embryogenesis [68, 69], and has been suggested to promote an invasive phenotype in cancer cells [8, 70]. Low levels of YREG1 were important for stabilizing the interaction between LEF-1 and β -catenin, while elevated levels inhibited EMT by downregulating LEF-1 transcriptional activity. Recent evidence has established a complex role of Amino terminal Enhancer of Split (AES) and Groucho/TLE on suppressing LEF-1 activity. AES opposes LEF-1 transcriptional activation while Groucho/TLE binds with LEF-1 for a histone deacetylase repression. In addition, β -catenin directly displaces Groucho/TLE repressors from TCF/LEF-1 in Wnt-mediated transcription activation [71, 72]. Our model agrees with this newly discovered feedback system, as YREG1 regulates LEF-1 activity leading to EMT stabilization.

NF- κ B may also play an essential role of in the epithelial transformation. NF- κ B may influence Snail expression through the AKT pathway and directly stabilize Snail activity [73]. This is particularly important for integrating inflammation pathways, such as interleukin-6 (IL-6) and tumor necrosis factor- α (TNF- α), which have been linked to EMT in pathological conditions [74]. Other pathways such as Notch have also been shown to act synergistically with TGF- β to express Slug in the

developing embryo [75]. In addition, other regulatory proteins such as ZEB1 could be added to the next generation model. ZEB1 can activate the expression of mesenchymal genes such as collagens, smooth muscle actin and myosin, Vimentin while simultaneously contributing to the repression of epithelial genes [76]. Therefore, ZEB1 can act in parallel to SNAIL and is an alternative to the canonical signaling paradigm presented here. Hong et al. developed an ODE model of ZEB1 signaling in MCF10A cells which also demonstrated intermediate EMT states [77]. Thus, there may be alternative modes resulting in a hybrid phenotype that should be included in future model architecture. Lastly, while we have modeled classical protein signaling, we have not considered the role of regulatory RNAs on EMT. There is growing evidence that microRNAs (miRNAs) play a strong role in EMT, where several miRNAs, for example miR-21 and miR-31 are strongly associated with TGF- β exposure [78], and have suggested that the EMT process is driven by a miR-34/SNAIL and/or miR-200/ZEB feedback circuit [79–81]. Addressing missing structural components like these (and potentially others), could generate more insight into TGF- β signaling and its role in phenotypic transformation.

3.6 Materials and Methods

The model code and parameter ensemble is freely available under an MIT software license and can be downloaded from <http://www.varnerlab.org>.

3.6.1 Signaling network connectivity

The EMT model described the gene expression program resulting from TGF- β and VEGF-A signaling in a prototypical epithelial cell. The TGF- β -EMT network contained 97 nodes (proteins, mRNA or genes) and 169 interactions. The network connectivity was curated from more than 40 primary literature sources in combination with on-line databases [82, 83]. The model interactome was not specific to a single epithelial cell line. Rather, we assembled canonical pathways involved in TGF- β and VEGF-A signaling, defaulting to human connectivity when possible. Using a canonical architecture allowed us to explore general features of TGF- β induced EMT without cell line specific artifacts.

Our signaling network reconstruction was based on Medici et al. who identified the pathways through which MDCKII, DLD1 colon carcinoma, and A375 melanoma cells transition towards a mesenchymal phenotype [7]. Sequential activation of MAPK and Smad pathways were initiated upon addition of TGF- β 1/2. Briefly, TGF- β 2 signals through the RAS-RAF-MEK-ERK pathway to up-regulate Snail and Slug expression [6]. Snail, a known repressor of junctional proteins, inhibits the expression of E-cadherin [70]. This initial repression of E-cadherin leads to a release of β -catenin from the cell membrane. This release of β -catenin can then translocate to the nucleus and form transcriptional complexes with TCF-4 to drive TGF- β 3 expression [7]. The PI3K to GSK3 pathway was included and acted as an

activating mechanism of β -catenin signaling through TGF- β 3 signaling [7]. GSK3 is known to act on β -catenin signaling through the ubiquitin-proteasome pathway [84, 85]. Thereby, further β -catenin release also resulted from by TGF- β 3 signals to the cells interior by binding to type II receptors, which form heterodimers with type I receptors (ALK5) [86]. This activates the receptors serine/threonine kinase activity to phosphorylate and activate the receptor Smads 2/3 [87]. In the model, receptors are simplified and represented as either bound or unbound complexes with their ligands. Phosphorylated Smads 2/3 (pSmad2/3) form heterodimers and translocate to the nucleus. pSmads complexes up-regulate other transcription factors, such as LEF-1. The pSmad2/4-LEF-1 complex has been shown to directly repress the E-cadherin gene [88]. LEF-1 also binds with β -catenin to upregulate mesenchymal proteins such as fibronectin [89]. In the model, Smad signaling is consolidated into a single Smad species that can act in a co-dependent fashion with LEF1 to downregulate E-cadherin via a transfer function, eliminating the need for an explicit LEF-1, pSmad complex. The EMT gene expression program was initiated by the binding of TGF- β isoforms to TGF- β surface receptors, starting the downstream signaling program. Repression of E-cadherin expression is the central event in the transition from an epithelial to a mesenchymal phenotype [70]. However, this transition is not solely driven by transcriptional events. At the protein level, the repression of E-cadherin leads to a release of β -catenin from cell membrane. Cytosolic β -catenin then translocates to the nucleus and forms transcriptionally-active complexes with immunoglobulin transcription factor 2 (TCF-4) to drive TGF- β 3 expression [7]. The PI3K to GSK3 pathway was included and acted as an activating mechanism of β -catenin signaling

through TGF- β 3 signaling [7]. GSK3 is known to act on β -catenin signaling through APC complex associated ubiquitin-proteasome pathway. The APC complex is represented in our model and serves as a second reservoir of β -catenin in untransformed cells whose sequestration is regulated by GSK3 [7, 84, 85]. Lastly, VEGF-A activation of NFATc1 takes place through calcineurin signaling leading to an enhancement of E-cadherin expression [90], as supported by our VEGF-A experimental data (S1 Figure).

3.6.2 Formulation, solution and analysis of the EMT model equations

The EMT model integrated kinetic ODE modeling with a rule-based description of signaling activity and gene expression regulation. Regulation of enzyme activity or gene expression processes was modeled by combining individual regulatory contributions, quantified by transfer-functions, into control coefficients using an integration rule. These control coefficients then modified the kinetic rates that appeared in the model. This strategy is similar in spirit to the Constrained Fuzzy Logic (cFL) approach of Lauffenburger and coworkers which has been used to effectively model signal transduction pathways important in human health [17]. In our formulation, Hill-like transfer functions $0 \leq f(\mathbf{x}) \leq 1$ were used to calculate the influence of factor abundance upon enzyme activity or a gene expression process. In this context, factors can be individual metabolite or protein levels or some function of abundance, e.g., the product of metabolite or proteins levels. However, more generally, factors can also correspond to non-modeled influences, categorial variables or other abstract quantities. In the current study, we let factors correspond to the abundance of individual proteins, inhibitors or transcription factors, as well as

products of transcription factors where it is necessary to represent a co-dependent regulatory activity. When a protein or gene was potentially sensitive to more than one regulatory input, logical integration rules were used to select which regulatory transfer function influenced enzyme activity at any given time. Thus, our EMT network model encoded complex signaling and regulatory features with a relatively small number of equations. This model formulation has been used previously to construct reduced order kinetic models of synthetic RNA circuits [91], cell free metabolic models [92] and reduced-order models of blood coagulation [93]. In this study, we extended this approach to describe gene expression processes in addition to signal transduction events.

3.6.2.1 EMT signaling events.

EMT signaling events were modeled using either saturation or mass-action kinetics within an ordinary differential equation (ODE) framework:

$$\frac{1}{\tau_i} \frac{dx_i}{dt} = \sum_{j=1}^{\mathcal{R}} \sigma_{ij} r_j(\mathbf{x}, \boldsymbol{\epsilon}, \mathbf{k}) - \mu x_i \quad i = 1, 2, \dots, \mathcal{M} \quad (1)$$

where \mathcal{R} denotes the number of signaling reactions and \mathcal{M} denotes the number of signaling proteins in the model. The quantity τ_i denotes a time scale parameter for species i which captures un-modeled effects; in the current study $\tau_i = 1$ for all species. The quantity $r_j(\mathbf{x}, \boldsymbol{\epsilon}, \mathbf{k})$ denotes the rate of reaction j . Typically, reaction j is a non-linear function of biochemical and enzyme species abundance, as well as unknown model parameters \mathbf{k} ($\mathcal{K} \times 1$). The quantity σ_{ij} denotes the stoichiometric coefficient for species i in reaction j . If $\sigma_{ij} > 0$, species i is produced by reaction j . Conversely,

if $\sigma_{ij} < 0$, species i is consumed by reaction j , while $\sigma_{ij} = 0$ indicates species i is not connected with reaction j . Species balances were subject to the initial conditions $\mathbf{x}(t_0) = \mathbf{x}_0$.

Rate processes were written as the product of a kinetic term (\bar{r}_j) and a control term (v_j) in the EMT model. The rate of enzyme catalyzed reactions was modeled using saturation kinetics:

$$\bar{r}_j = k_j^{cat} \epsilon_i \left(\frac{x_s}{K_{js} + x_s} \right) \quad (2)$$

where k_j^{cat} denotes the catalytic rate constant for reaction j , ϵ_i denotes the abundance of the enzyme catalyzing reaction j , and K_{js} denotes the saturation constant for species s in reaction j . On the other hand, mass action kinetics were used to model protein-protein binding interactions within the network:

$$\bar{r}_j = k_j^{max} \prod_{s \in m_j^-} x_s^{-\sigma_{sj}} \quad (3)$$

where k_j^{max} denotes the maximum rate for reaction j , σ_{sj} denotes the stoichiometric coefficient for species s in reaction j , and $s \in m_j^-$ denotes the set of *reactants* for reaction j . Reversible binding was decomposed into two irreversible steps.

The control terms $0 \leq v_j \leq 1$ depended upon the combination of factors which influenced rate process j . For each rate, we used a rule-based approach to select from competing control factors. If rate j was influenced by $1, \dots, m$ factors, we modeled this relationship as $v_j = \mathcal{I}_j(f_{1j}(\cdot), \dots, f_{mj}(\cdot))$ where $0 \leq f_{ij}(\cdot) \leq 1$ denotes a regulatory

transfer function quantifying the influence of factor i on rate j . The function $\mathcal{I}_j(\cdot)$ is an integration rule which maps the output of regulatory transfer functions into a control variable. In this study, we used $\mathcal{I}_j \in \{\min, \max\}$ and hill transfer functions [92, 93]. If a process had no modifying factors, $v_j = 1$.

3.6.2.2 EMT gene expression processes.

The EMT model described both signal transduction and gene expression events following the addition of TGF- β and VEGF-A. For each gene of the $\mathcal{G} = 23$ we considered, we modeled both the resulting mRNA (m_j) and protein (p_j):

$$\frac{dm_j}{dt} = r_{Tj} - (\mu + \theta_{m_j})m_j + \lambda_j \quad (4)$$

$$\frac{dp_j}{dt} = r_{Xj} - (\mu + \theta_{p_j})p_j \quad (5)$$

where $j = 1, 2, \dots, \mathcal{G}$. The terms r_{Tj} and r_{Xj} denote the specific rates of transcription, and translation while the terms θ_{m_j} and θ_{p_j} denote first-order degradation constants for mRNA and protein, respectively. Lastly, μ denotes the specific growth rate, and λ_j denotes the constitutive rate of gene expression for gene j . The specific transcription rate was modeled as the product of a kinetic term \bar{r}_{Tj} and a control term u_j which described how the abundance of transcription factors, or other regulators influenced the expression of gene j . The kinetic rate of transcription was modeled as:

$$\bar{r}_{Tj} = \alpha_j \left[V_T^{\max} \left(\frac{G_j}{K_T + G_j} \right) \right] \quad (6)$$

where the maximum gene expression rate was defined as the product of a characteristic transcription rate constant (k_T) and the abundance of RNA polymerase, $V_T^{max} = k_T (\text{RNAP})$. The parameter α_j denotes the gene specific correction to the characteristic transcription rate (estimated in this study). Similar to the signaling processes, the gene expression control term $0 \leq u_j \leq 1$ depended upon the combination of factors which influenced rate process j . For each rate, we used a rule-based approach to select from competing control factors. If the expression of gene j was influenced by $1, \dots, m$ factors, we modeled this relationship as $u_j = \mathcal{I}_j(f_{1j}(\cdot), \dots, f_{mj}(\cdot))$ where $0 \leq f_{ij}(\cdot) \leq 1$ denotes a regulatory transfer function quantifying the influence of factor i on the expression of gene j . The function $\mathcal{I}_j(\cdot)$ is an integration rule which maps the output of regulatory transfer functions into a control variable. In this study, we used $\mathcal{I}_j \in \{\min, \max\}$ and hill transfer functions [92, 93]. If a gene expression process has no modifying factors, $u_j = 1$. The degradation rate constants were defined as $\theta_{m,j} = \delta_j k_{d,m}$ and $\theta_{p,j} = \gamma_j k_{d,p}$ where $k_{d,m}$ and $k_{d,p}$ denote characteristic degradation constants for mRNA and protein, respectively and δ_j and γ_j denote transcript and protein specific correction factors to these constants. Lastly, the specific translation rate was modeled as:

$$r_{X,j} = \beta_j \left[V_X^{max} \left(\frac{m_j}{K_X + m_j} \right) \right] \quad (7)$$

where V_X^{max} denotes a characteristic maximum translation rate estimated from literature, β_j denotes the transcript specific correction the characteristic translation rate, and K_X denotes a translation saturation constant. The characteristic maximum translation rate was defined as the product of a characteristic translation rate constant (k_X) and the abundance of ribosomes (RIBO), $V_X^{max} = k_X (\text{RIBO})$.

In this study, we estimated k_T , k_X , $k_{d,m}$, $k_{d,p}$, RNAP and RIBO directly from literature using estimates of transcription and translation rates, the half-life of a typical mRNA and protein and a typical value for the copies per cell of RNA polymerase and ribosomes. The saturation constants K_X and K_T were adjusted so that gene expression and translation resulted in gene products on a biologically realistic concentration scale. Next, we calculated the concentration for gene j by assuming, on average, that a cell had two copies of each gene at any given time. Thus, the bulk of our gene expression parameters were based directly upon literature values, and were not adjusted during model identification. The values used for the characteristic transcription/translation parameters, degradation constants and macromolecular copy number are given in the supplement along with the specific formulas required to calculate all derived constants.

The signaling and gene expression model equations were implemented in Julia and solved using the CVODE routine of the Sundials package [94, 95]. The model code and parameter ensemble is freely available under an MIT software license and can be downloaded from <http://www.varnerlab.org>.

3.6.2.3 Estimation of model parameters using multiobjective optimization.

We estimated a population of likely EMT model parameter sets (each consistent with the training data) using 41 data sets generated in DLD1 colon carcinoma, MDCKII, and A375 melanoma cells taken from Medici *et al.* [7]. In addition to rate and saturation constants appearing in the signal transduction equations, we estimate the transcript/protein specific correction factors α_j , β_j , δ_j and δ_j and control coefficients from these data. We used the Pareto Optimal Ensemble Technique (JuPOETs) multiobjective optimization framework in combination with leave-one-out cross-validation to estimate an ensemble of model parameters [20, 96]. Model parameter values were adjusted to minimize the residual between simulations and experimental measurements. Cross-validation was used to calculate both training and prediction error during the parameter estimation procedure [97]. The 41 intracellular protein and mRNA data-sets used for identification were organized into 11 objective functions. These 11 objective functions were then partitioned, where each partition contained ten training objectives and one validation objective. The training and validation data were Western blots. We achieved a biologically realistic concentration scale by establishing characteristic rates of transcription, translation, mRNA and protein degradation, as well as characteristic concentrations of ribosomes and RNAPs using the Bionumbers database [31], (supplemental materials). The overall concentration scale was nM, with proteins ranging from 10–1000nM and mRNA ranging from 0.01 to 1nM, reflecting the true abundances and ratios between each species. An initial nominal parameter set was established by inspection. JuPOETs was then allowed to search in a neighborhood of $\pm 30\%$ of this nominal set. The correction

factors estimated by JuPOETs were in the range of 0.1–10, with the mean value of 1.68; thus, the characteristic rate parameters estimated from literature were consistent with measurements. The parameter ensemble estimated by JuPOETs is available with the model source code. JuPOETs is open source and freely available for download under an MIT software license from <http://www.varnerlab.org>.

3.6.3 Cell culture and experimental interrogation

DLD1 colon carcinoma and MCF10A cells were acquired from the American Tissue Culture Collection (Manassas, VA). Cells were grown in culture with RPMI-1640 medium with 10% fetal bovine serum and 1% penicillin/streptomycin or MGEM-2 supplemented with insulin, bovine pituitary extract, cholera toxin, hEGF, hydrocortisone, 5% horse serum, and 1% penicillin/streptomycin, respectively. Cells were passaged 1:3 or 1:4 every 3–6 d and used between passages 4 and 8. During treatment regime, DLD1 and MCF10A cells aggregated overnight in hanging drop culture (20 μ L; 20,000 cells). The spherical aggregates were placed on the surface of neutralized type I collagen hydrogels (1.5mg/mL) and allowed to adhere. Cultures were then serum starved (1% serum) for 24 hours. Recombinant human TGF- β 2 (R & D Systems, Minneapolis, MN) was added to the culture medium at a concentration of 10 ng/ml and recombinant VEGFA165 at a concentration of (5ng/ml, 50ng/ml) for all relative experiments. NFAT inhibitor (VIVIT peptide) (EMDBiosciences, Darmstadt, Germany), was added to the culture medium at a concentration of 10 μ M for all relative experiments. mRNA was then harvested at both the 3hr and 48hr time-point.

3.6.3.1 RT-PCR.

RNA extractions were performed using a Qiagen total RNA purification kit (Qiagen, Valencia, CA) and RNA was reverse transcribed to cDNA using the SuperScript III RT-PCR kit with oligo(dT) primer (Invitrogen). Sufficient quality RNA was determined by an absorbance ratio A260/A280 of 1.8–2.1, while the quantity of RNA was determined by measuring the absorbance at 260nm (A260). Real-time PCR experiments were conducted using the SYBR Green PCR system (Biorad, Hercules, CA) on a Biorad CFX96 cycler, with 40 cycles per sample. Cycling temperatures were as follows: denaturing, 95C; annealing, 60C; and extension, 70C. Primers were designed to detect GAPDH, E-cadherin, vimentin, Slug, Sp1, and NFATc1 in cDNA clones: Sp1 (F-TTG AAA AAG GAG TTG GTG GC, R-TGC TGG TTC TGT AAG TTG GG, Accession NG030361.1), NFATc1 (F-GCA TCA CAG GGA AGA CCG TGT C, R-GAA GTT CAA TGT CGG AGT TTC TGA G, Accession NG029226.1). GAPDH, E-cadherin, vimentin, and Slug primers were taken from previously published literature [7].

3.6.3.2 Antibody staining.

Samples were fixed in 4% PFA overnight at 4C. Samples were then washed for 15 minutes on a rocker 3 times with PBS, permeabilized with 0.2% Triton-X 100 (VWR International, Radnor, PA) for 10 minutes, and washed another 3 times with PBS. Samples were incubated overnight at 4C in a 1% BSA (Rockland Immunochemicals, Inc., Gilbertsville, PA) blocking solution followed by another 4C overnight incubation with either rabbit anti-human E-cadherin 1:100 (Abcam, ab53033), mouse anti-human phospho-Sp1 1:100 (Abcam, ab37707), mouse anti-

human vimentin 1:100 (Invitrogen, V9), and rabbit anti-human NFATc1 (Santa Cruz, sc-7294) 1:100. After 3 washes for 15 minutes with PBS, samples were exposed to Alexa Fluor 488 or 568 conjugated (Invitrogen), species specific secondary antibodies at 1:100 in 1% BSA for 2 hours at room temperature. Three more washes with PBS for 15 minutes were followed by incubation with either DRAQ5 far red nuclear stain (Enzo Life Sciences, Plymouth Meeting, PA) at 1:1000.

3.6.3.3 FACS.

Flow cytometry for E-cadherin 1:100 (Abcam) and vimentin 1:100 expressing cells was performed. Briefly, cells were trypsinized, fixed with 4% PFA for 10 min and then preserved in 50% methanol/PBS. Cells were kept in the -20C until antibody staining was performed. Samples were divided into multiple aliquots in order to stain the proteins separately and compensate for secondary antibody non-specific binding. Cells were incubated for 24 hrs at 4 C in primary antibody diluted in either PBS (extracellular) or 0.2% saponin-PBS (intracellular). Cells were then washed 3 times with PBS and incubated with appropriate secondary antibodies and imaged using a Coulter Epics XL-MCL Flow Cytometer (Coulter). All samples were compensated using appropriate background subtraction and all samples were normalized using 7500 cells per flow condition.

3.6.3.4 Three-dimensional culture and tubulogenesis assays.

For invasion/migration assays, cells were resuspended in culture media, and allowed to aggregate overnight in hanging drop culture (20 μ L; 20,000 cells). The spherical aggregates were placed on the surface of neutralized type I collagen hydrogels (1.5mg/mL) and allowed to adhere for 2 hrs before adding treatments.

Cultures were maintained for 72 hrs, after which they were fixed in 4% PFA and slowly rehydrated using PBS. For compaction assays, cells were pelleted via centrifugation and resuspended within a neutralized collagen hydrogel (1.5mg/mL) solution at a density of 400,000 cells/mL. 250 μ L of gel was inoculated into culture wells, which solidified after 60min. Treatments were then added within 800 μ L of the culture medium without serum. Gels were liberated from the surfaces of the culture wells the next day and cultured free floating for an additional 3–7 days, exchanging serum free media with appropriate factors every 48 hrs.

Tubulogenesis was defined as a typical nonmalignant acini structure. This includes a polarized epithelial cell, hollow lumen, and the basal sides of the cell are surrounded by ECM proteins (Figure 6A, Controls or VEGF treated). Previous work has shown that change in the morphological characteristics of nontumorigenic MCF10A epithelial acini occur over time and exploiting them to growth in 3D culture can be quantified. For example, using image segmentation, Chang et al. [98] examined the elongation of the MCF10A acini at 6, 12, and 96 hours after a particular treatment. Polizzotti et al. [99] also suggested a computational method to quantify acini structure based on morphological characteristics in nonmalignant, noninvasive, and invasive conditions. Adapted from these approaches, we first fluorescently labeled our cultures and captured the acini structures by 3D confocal microscopy. Next individual acini structures in the images were segmented by imageJ and labeled. We then extracted the number of ductal branches. Ductal branching was defined as any elongated cell cluster extending away from the total acini structure, which was manually segmented and counted using ImageJ. A total of 5 images for each condition were used, and

approximately 12 acini were analyzed in each image. Total branching was normalized to the amount of acini present, and provides an overall general assessment to the extent of acini remodeling.

3.6.3.5 Statistics.

Results are expressed as mean \pm standard error, $n \geq 6$. Data was analyzed with the GraphPad Prism version 4.00 for Windows (GraphPad Software, San Diego, CA) and SAS (Statistical Analysis Software, Cary, NC). A one-way ANOVA with Tukey's post hoc was used to compare differences between means and data was transformed when necessary to obtain equal sample variances. Differences between means were considered significant at $p < 0.05$.

3.7 References

1. Thiery JP. Epithelial-mesenchymal transitions in development and pathologies. *Curr Opin Cell Biol.* 2003;15(6):740–6. pmid:14644200
2. Stahl PJ, Felsen D. Transforming growth factor-beta, basement membrane, and epithelial-mesenchymal transdifferentiation: implications for fibrosis in kidney disease. *Am J Pathol.* 2001;159(4):1187–92. pmid:11583944
3. Eisenberg LM, Markwald RR. Molecular regulation of atrioventricular valvuloseptal morphogenesis. *Circ Res.* 1995;77(1):1–6. pmid:7788867
4. Zavadil J, Böttinger EP. TGF-beta and epithelial-to-mesenchymal transitions. *Oncogene.* 2005;24(37):5764–74. pmid:16123809
5. Xu J, Lamouille S, Derynck R. TGF-beta-induced epithelial to mesenchymal transition. *Cell Res.* 2009;19(2):156–72. pmid:19153598
6. Medici D, Hay ED, Goodenough DA. Cooperation between snail and LEF-1 transcription factors is essential for TGF-beta1-induced epithelial-mesenchymal transition. *Mol Biol Cell.* 2006;17(4):1871–9. pmid:16467384
7. Medici D, Hay ED, Olsen BR. Snail and Slug promote epithelial-mesenchymal transition through beta-catenin-T-cell factor-4-dependent expression of transforming growth factor-beta3. *Mol Biol Cell.* 2008;19(11):4875–87. pmid:18799618
8. Kim K, Lu Z, Hay ED. Direct evidence for a role of beta-catenin/LEF-1 signaling pathway in induction of EMT. *Cell Biol Int.* 2002;26(5):463–76. pmid:12095232
9. Jiang YG, Luo Y, He DL, Li X, Zhang LI, Peng T, et al. Role of Wnt/beta-catenin signaling pathway in epithelial-mesenchymal transition of human prostate cancer induced by hypoxia-inducible factor-1alpha. *Int J Urol.* 2007;14(11):1034–9. pmid:17956532
10. Huber MA, Azoitei N, Baumann B, Grünert S, Sommer A, Pehamberger H, et al. NF-kappaB is essential for epithelial-mesenchymal transition and metastasis in a model of breast cancer progression. *J Clin Invest.* 2004;114(4):569–81. pmid:15314694
11. Hardy KM, Booth BW, Hendrix MJC, Salomon DS, Strizzi L. ErbB/EGF signaling and EMT in mammary development and breast cancer. *J Mammary Gland Biol Neoplasia.* 2010;15(2):191–9. pmid:20369376
12. Ahmed S, Nawshad A. Complexity in interpretation of embryonic epithelial-mesenchymal transition in response to transforming growth factor-beta signaling. *Cells Tissues Organs.* 2007;185(1–3):131–45. pmid:17587819

13. Chung SW, Miles FL, Sikes RA, Cooper CR, Farach-Carson MC, Ogunnaike BA. Quantitative modeling and analysis of the transforming growth factor beta signaling pathway. *Biophys J*. 2009;96(5):1733–50. pmid:19254534
14. Vilar JMG, Jansen R, Sander C. Signal processing in the TGF-beta superfamily ligand-receptor network. *PLoS Comput Biol*. 2006;2(1):e3. pmid:16446785
15. Steinway SN, Zañudo JGT, Ding W, Rountree CB, Feith DJ, Loughran TP Jr, et al. Network modeling of TGFB signaling in hepatocellular carcinoma epithelial-to-mesenchymal transition reveals joint sonic hedgehog and Wnt pathway activation. *Cancer Res*. 2014;74(21):5963–77. pmid:25189528
16. Cirit M, Haugh JM. Data-driven modelling of receptor tyrosine kinase signalling networks quantifies receptor-specific potencies of PI3K- and Ras-dependent ERK activation. *Biochem J*. 2012;441(1):77–85. pmid:21943356
17. Morris MK, Saez-Rodriguez J, Clarke DC, Sorger PK, Lauffenburger DA. Training signaling pathway maps to biochemical data with constrained fuzzy logic: quantitative analysis of liver cell responses to inflammatory stimuli. *PLoS Comput Biol*. 2011;7(3):e1001099. pmid:21408212
18. Bailey JE. Complex biology with no parameters. *Nat Biotechnol*. 2001;19(6):503–4. pmid:11385433
19. Machta BB, Chachra R, Transtrum MK, Sethna JP. Parameter space compression underlies emergent theories and predictive models. *Science*. 2013;342(6158):604–7. pmid:24179222
20. Song SO, Chakrabarti A, Varner JD. Ensembles of signal transduction models using Pareto Optimal Ensemble Techniques (POETs). *Biotechnol J*. 2010;5(7):768–80. pmid:20665647
21. Lequieu J, Chakrabarti A, Nayak S, Varner JD. Computational modeling and analysis of insulin induced eukaryotic translation initiation. *PLoS Comput Biol*. 2011;7(11):e1002263. pmid:22102801
22. Luan D, Szlam F, Tanaka KA, Barie PS, Varner JD. Ensembles of uncertain mathematical models can identify network response to therapeutic interventions. *Mol Biosyst*. 2010;6(11):2272–86. pmid:20844798
23. Kalita MK, Sargsyan K, Tian B, Paulucci-Holthauzen A, Najm HN, Debusschere BJ, et al. Sources of cell-to-cell variability in canonical nuclear factor-kB (NF-kB) signaling pathway inferred from single cell dynamic images. *J Biol Chem*. 2011;286(43):37741–57. pmid:21868381

24. Hasenauer J, Waldherr S, Doszczak M, Radde N, Scheurich P, Allgöwer F. Identification of models of heterogeneous cell populations from population snapshot data. *BMC Bioinformatics*. 2011;12:125. pmid:21527025
25. Creixell P, Schoof EM, Erler JT, Linding R. Navigating cancer network attractors for tumor-specific therapy. *Nat Biotechnol*. 2012;30(9):842–8. pmid:22965061
26. Schoeberl B, Eichler-Jonsson C, Gilles ED, Müller G. Computational modeling of the dynamics of the MAP kinase cascade activated by surface and internalized EGF receptors. *Nat Biotechnol*. 2002;20(4):370–375. pmid:11923843
27. Chen WW, Schoeberl B, Jasper PJ, Niepel M, Nielsen UB, Lauffenburger DA, et al. Input-output behavior of ErbB signaling pathways as revealed by a mass action model trained against dynamic data. *Mol Syst Biol*. 2009;5:239. pmid:19156131
28. Tasseff R, Nayak S, Song SO, Yen A, Varner JD. Modeling and analysis of retinoic acid induced differentiation of uncommitted precursor cells. *Integr Biol (Camb)*. 2011;3(5):578–591.
29. Gadkar KG, Varner J, Doyle FJ 3rd. Model identification of signal transduction networks from data using a state regulator problem. *Syst Biol (Stevenage)*. 2005;2(1):17–30.
30. Lian Yg, Zhou Qg, Zhang Yj, Zheng Fl. VEGF ameliorates tubulointerstitial fibrosis in unilateral ureteral obstruction mice via inhibition of epithelial-mesenchymal transition. *Acta Pharmacol Sin*. 2011;32(12):1513–21. pmid:21986574
31. Milo R, Jorgensen P, Moran U, Weber G, Springer M. BioNumbers—the database of key numbers in molecular and cell biology. *Nucleic Acids Res*. 2010;38(Database issue):D750–3. pmid:19854939
32. Park SY, Lee HE, Li H, Shipitsin M, Gelman R, Polyak K. Heterogeneity for stem cell-related markers according to tumor subtype and histologic stage in breast cancer. *Clin Cancer Res*. 2010;16(3):876–87. pmid:20103682
33. Hemavathy K, Ashraf SI, Ip YT. Snail/slug family of repressors: slowly going into the fast lane of development and cancer. *Gene*. 2000;257(1):1–12. pmid:11054563
34. Hemavathy K, Guru SC, Harris J, Chen JD, Ip YT. Human Slug is a repressor that localizes to sites of active transcription. *Mol Cell Biol*. 2000;20(14):5087–95. pmid:10866665
35. Dhasarathy A, Phadke D, Mav D, Shah RR, Wade PA. The transcription factors Snail and Slug activate the transforming growth factor-beta signaling pathway in breast cancer. *PLoS One*. 2011;6(10):e26514. pmid:22028892

36. Guaita S, Puig I, Franci C, Garrido M, Dominguez D, Batlle E, et al. Snail induction of epithelial to mesenchymal transition in tumor cells is accompanied by MUC1 repression and ZEB1 expression. *J Biol Chem*. 2002;277(42):39209–16. pmid:12161443
37. Jackstadt R, Röh S, Neumann J, Jung P, Hoffmann R, Horst D, et al. AP4 is a mediator of epithelial-mesenchymal transition and metastasis in colorectal cancer. *J Exp Med*. 2013;210(7):1331–50. pmid:23752226
38. Eastman Q, Grosschedl R. Regulation of LEF-1/TCF transcription factors by Wnt and other signals. *Curr Opin Cell Biol*. 1999;11(2):233–40. pmid:10209158
39. Aramburu J, Yaffe MB, López-Rodríguez C, Cantley LC, Hogan PG, Rao A. Affinity-driven peptide selection of an NFAT inhibitor more selective than cyclosporin A. *Science*. 1999;285(5436):2129–33. pmid:10497131
40. Dhimolea E, Maffini MV, Soto AM, Sonnenschein C. The role of collagen reorganization on mammary epithelial morphogenesis in a 3D culture model. *Biomaterials*. 2010;31(13):3622–3630. pmid:20149444
41. Butcher JT, Penrod AM, García AJ, Nerem RM. Unique morphology and focal adhesion development of valvular endothelial cells in static and fluid flow environments. *Arterioscler Thromb Vasc Biol*. 2004;24(8):1429–34. pmid:15117733
42. Hong JP, Li XM, Li MX, Zheng FL. VEGF suppresses epithelial-mesenchymal transition by inhibiting the expression of Smad3 and miR-192 a Smad3-dependent microRNA. *Int J Mol Med*. 2013;31(6):1436–42. pmid:23588932
43. Nagy JA, Dvorak AM, Dvorak HF. VEGF-A and the induction of pathological angiogenesis. *Annu Rev Pathol*. 2007;2:251–75. pmid:18039100
44. Ferrara N. VEGF and the quest for tumour angiogenesis factors. *Nat Rev Cancer*. 2002;2(10):795–803. pmid:12360282
45. Willis BC, Borok Z. TGF-beta-induced EMT: mechanisms and implications for fibrotic lung disease. *Am J Physiol Lung Cell Mol Physiol*. 2007;293(3):L525–34. pmid:17631612
46. Polyak K, Weinberg RA. Transitions between epithelial and mesenchymal states: acquisition of malignant and stem cell traits. *Nat Rev Cancer*. 2009;9(4):265–273. pmid:19262571
47. Strauss R, Li ZY, Liu Y, Beyer I, Persson J, Sova P, et al. Analysis of epithelial and mesenchymal markers in ovarian cancer reveals phenotypic heterogeneity and plasticity. *PLoS One*. 2011;6(1):e16186. pmid:21264259

48. Neve RM, Chin K, Fridlyand J, Yeh J, Baehner FL, Fevr T, et al. A collection of breast cancer cell lines for the study of functionally distinct cancer subtypes. *Cancer Cell*. 2006;10(6):515–27. pmid:17157791
49. Welch-Reardon KM, Wu N, Hughes CCW. A Role for Partial Endothelial-Mesenchymal Transitions in Angiogenesis? *Arterioscler Thromb Vasc Biol*. 2014; pmid:25425619
50. Zajchowski DA, Bartholdi MF, Gong Y, Webster L, Liu HL, Munishkin A, et al. Identification of gene expression profiles that predict the aggressive behavior of breast cancer cells. *Cancer Res*. 2001;61(13):5168–78. pmid:11431356
51. Mancini M, Toker A. NFAT proteins: emerging roles in cancer progression. *Nat Rev Cancer*. 2009;9(11):810–820. pmid:19851316
52. Singh G, Singh SK, König A, Reutlinger K, Nye MD, Adhikary T, et al. Sequential activation of NFAT and c-Myc transcription factors mediates the TGF-beta switch from a suppressor to a promoter of cancer cell proliferation. *J Biol Chem*. 2010;285(35):27241–50. pmid:20516082
53. Debnath J, Muthuswamy SK, Brugge JS. Morphogenesis and oncogenesis of MCF-10A mammary epithelial acini grown in three-dimensional basement membrane cultures. *Methods*. 2003;30(3):256–268. pmid:12798140
54. Pearson GW, Hunter T. Real-time imaging reveals that noninvasive mammary epithelial acini can contain motile cells. *J Cell Biol*. 2007;179(7):1555–67. pmid:18166657
55. O'Brien LE, Tang K, Kats ES, Schutz-Geschwender A, Lipschutz JH, Mostov KE. ERK and MMPs sequentially regulate distinct stages of epithelial tubule development. *Dev Cell*. 2004;7(1):21–32. pmid:15239951
56. Debnath J, Brugge JS. Modelling glandular epithelial cancers in three-dimensional cultures. *Nat Rev Cancer*. 2005;5(9):675–88. pmid:16148884
57. Moles CG, Mendes P, Banga JR. Parameter estimation in biochemical pathways: a comparison of global optimization methods. *Genome Res*. 2003;13(11):2467–74. pmid:14559783
58. Rodriguez-Fernandez M, Rehberg M, Kremling A, Banga JR. Simultaneous model discrimination and parameter estimation in dynamic models of cellular systems. *BMC Syst Biol*. 2013;7:76. pmid:23938131
59. Villaverde AF, Banga JR. Reverse engineering and identification in systems biology: strategies, perspectives and challenges. *J R Soc Interface*. 2014;11(91):20130505. pmid:24307566

60. Choi M, Shi J, Jung SH, Chen X, Cho KH. Attractor landscape analysis reveals feedback loops in the p53 network that control the cellular response to DNA damage. *Sci Signal*. 2012;5(251):ra83. pmid:23169817
61. Terfve C, Cokelaer T, Henriques D, MacNamara A, Goncalves E, Morris MK, et al. CellNOptR: a flexible toolkit to train protein signaling networks to data using multiple logic formalisms. *BMC Syst Biol*. 2012;6:133. pmid:23079107
62. Hyduke DR, Palsson BØ. Towards genome-scale signalling network reconstructions. *Nat Rev Genet*. 2010;11(4):297–307. pmid:20177425
63. Wayman J, Varner J. Biological systems modeling of metabolic and signaling networks. *Curr Opin Chem Eng*. 2013;2:365–372.
64. Sainani KL. Meet the Skeptics: Why some doubt biomedical models—and what it takes to win them over. *Biomedical Computation Review*. 2012; p. 12–18.
65. Lee MW, Vassiliadis VS, Park JM. Individual-based and stochastic modeling of cell population dynamics considering substrate dependency. *Biotechnol Bioeng*. 2009;103(5):891–9. pmid:19365871
66. Swain PS, Elowitz MB, Siggia ED. Intrinsic and extrinsic contributions to stochasticity in gene expression. *Proc Natl Acad Sci U S A*. 2002;99(20):12795–800. pmid:12237400
67. Handl J, Kell DB, Knowles J. Multiobjective optimization in bioinformatics and computational biology. *IEEE/ACM Trans Comput Biol Bioinform*. 2007;4(2):279–92. pmid:17473320
68. Vega S, Morales AV, Ocaña OH, Valdés F, Fabregat I, Nieto MA. Snail blocks the cell cycle and confers resistance to cell death. *Genes Dev*. 2004;18(10):1131–43. pmid:15155580
69. Nawshad A, Hay ED. TGFbeta3 signaling activates transcription of the LEF1 gene to induce epithelial mesenchymal transformation during mouse palate development. *J Cell Biol*. 2003;163(6):1291–301. pmid:14691138
70. Cano A, Pérez-Moreno MA, Rodrigo I, Locascio A, Blanco MJ, del Barrio MG, et al. The transcription factor snail controls epithelial-mesenchymal transitions by repressing E-cadherin expression. *Nat Cell Biol*. 2000;2(2):76–83. pmid:10655586
71. Arce L, Pate KT, Waterman ML. Groucho binds two conserved regions of LEF-1 for HDAC-dependent repression. *BMC Cancer*. 2009;9:159. pmid:19460168
72. Grumolato L, Liu G, Haremake T, Mungamuri SK, Mong P, Akiri G, et al. β -Catenin-Independent Activation of TCF1/LEF1 in Human Hematopoietic Tumor

- Cells through Interaction with ATF2 Transcription Factors. *PLoS Genet.* 2013;9(8):e1003603. pmid:23966864
73. Wu Y, Deng J, Rychahou PG, Qiu S, Evers BM, Zhou BP. Stabilization of snail by NF-kappaB is required for inflammation-induced cell migration and invasion. *Cancer Cell.* 2009;15(5):416–28. pmid:19411070
 74. Sullivan NJ, Sasser AK, Axel AE, Vesuna F, Raman V, Ramirez N, et al. Interleukin-6 induces an epithelial-mesenchymal transition phenotype in human breast cancer cells. *Oncogene.* 2009;28(33):2940–7. pmid:19581928
 75. Niessen K, Fu Y, Chang L, Hoodless PA, McFadden D, Karsan A. Slug is a direct Notch target required for initiation of cardiac cushion cellularization. *J Cell Biol.* 2008;182(2):315–25. pmid:18663143
 76. Liu Y, El-Naggar S, Darling DS, Higashi Y, Dean DC. Zeb1 links epithelial-mesenchymal transition and cellular senescence. *Development.* 2008;135(3):579–88. pmid:18192284
 77. Hong T, Watanabe K, Ta CH, Villarreal-Ponce A, Nie Q, Dai X. An Ovol2-Zeb1 Mutual Inhibitory Circuit Governs Bidirectional and Multi-step Transition between Epithelial and Mesenchymal States. *PLoS Comput Biol.* 2015;11(11):e1004569. pmid:26554584
 78. Bullock MD, Sayan AE, Packham GK, Mirnezami AH. MicroRNAs: critical regulators of epithelial to mesenchymal (EMT) and mesenchymal to epithelial transition (MET) in cancer progression. *Biol Cell.* 2012;104(1):3–12. pmid:22188537
 79. Lu M, Jolly MK, Levine H, Onuchic JN, Ben-Jacob E. MicroRNA-based regulation of epithelial-hybrid-mesenchymal fate determination. *Proc Natl Acad Sci U S A.* 2013;110(45):18144–9. pmid:24154725
 80. Zhang J, Tian XJ, Zhang H, Teng Y, Li R, Bai F, et al. TGF-beta-induced epithelial-to-mesenchymal transition proceeds through stepwise activation of multiple feedback loops. *Sci Signal.* 2014;7(345):ra91. pmid:25270257
 81. Tian XJ, Zhang H, Xing J. Coupled reversible and irreversible bistable switches underlying TGFb-induced epithelial to mesenchymal transition. *Biophys J.* 2013;105(4):1079–89. pmid:23972859
 82. Linding R, Jensen LJ, Ostheimer GJ, van Vugt MATM, Jørgensen C, Miron IM, et al. Systematic discovery of in vivo phosphorylation networks. *Cell.* 2007;129(7):1415–26. pmid:17570479

83. Jensen LJ, Kuhn M, Stark M, Chaffron S, Creevey C, Muller J, et al. STRING 8—a global view on proteins and their functional interactions in 630 organisms. *Nucleic Acids Res.* 2009;37(Database issue):D412–6.
84. Zhou BP, Deng J, Xia W, Xu J, Li YM, Gunduz M, et al. Dual regulation of Snail by GSK-3 β -mediated phosphorylation in control of epithelial-mesenchymal transition. *Nat Cell Biol.* 2004;6(10):931–40. pmid:15448698
85. Larue L, Bellacosa A. Epithelial-mesenchymal transition in development and cancer: role of phosphatidylinositol 3' kinase/AKT pathways. *Oncogene.* 2005;24(50):7443–54. pmid:16288291
86. Derynck R, Zhang YE. Smad-dependent and Smad-independent pathways in TGF- β family signalling. *Nature.* 2003;425(6958):577–84. pmid:14534577
87. Massagué J, Seoane J, Wotton D. Smad transcription factors. *Genes Dev.* 2005;19(23):2783–810. pmid:16322555
88. Nawshad A, Medici D, Liu CC, Hay ED. TGF β 3 inhibits E-cadherin gene expression in palate medial-edge epithelial cells through a Smad2-Smad4-LEF1 transcription complex. *J Cell Sci.* 2007;120(Pt 9):1646–53. pmid:17452626
89. Medici D, Potenta S, Kalluri R. Transforming growth factor- β 2 promotes Snail-mediated endothelial-mesenchymal transition through convergence of Smad-dependent and Smad-independent signalling. *Biochem J.* 2011;437(3):515–520. pmid:21585337
90. Suehiro Ji, Kanki Y, Makihara C, Schadler K, Miura M, Manabe Y, et al. Genome-wide approaches reveal functional vascular endothelial growth factor (VEGF)-inducible nuclear factor of activated T cells (NFAT) c1 binding to angiogenesis-related genes in the endothelium. *J Biol Chem.* 2014;289(42):29044–59. pmid:25157100
91. Hu CY, Varner JD, Lucks JB. Generating Effective Models and Parameters for RNA Genetic Circuits. *ACS Synth Biol.* 2015;4(8):914–26. pmid:26046393
92. Wayman JA, Sagar A, Varner JD. Dynamic Modeling of Cell-Free Biochemical Networks Using Effective Kinetic Models. *Processes.* 2015;3(1):138.
93. Sagar A, Varner JD. Dynamic Modeling of the Human Coagulation Cascade Using Reduced Order Effective Kinetic Models. *Processes.* 2015;3(1):178.
94. Bezanson J, Edelman A, Karpinski S, Shah VB. Julia: A Fresh Approach to Numerical Computing. *CoRR.* 2014;abs/1411.1607.

95. Hindmarsh A, Brown P, Grant K, Lee S, Serban R, Shumaker D, et al. SUNDIALS: Suite of nonlinear and differential/algebraic equation solvers. *ACM Transactions on Mathematical Software*. 2005;31:363–396.
96. Bassen D, Vilkhovoy M, Minot M, Butcher JT, Varner JD. JuPOETS: A Constrained Multiobjective Optimization Approach to Estimate Biochemical Model Ensembles in the Julia Programming Language. *bioRxiv*. 2016;
97. Kohavi R. A study of cross-validation and bootstrap for accuracy estimation and model selection. In: *International joint Conference on artificial intelligence*. vol. 14. Citeseer; 1995. p. 1137–1145.
98. Chang H, Park C, Parvin B. Quantitative Representation of Three-dimensional Cell Culture Models. In: *Proceedings of the 2007 IEEE International Symposium on Biomedical Imaging: From Nano to Macro, Washington, DC, USA, April 12–16, 2007*; 2007. p. 89–92. Available from: <http://dx.doi.org/10.1109/ISBI.2007.356795>.
99. Polizzotti L, Basak O, Bjornsson C, Shubert K, Yener B, Plopper G. Novel Image Analysis Approach Quantifies Morphological Characteristics of 3D Breast Culture Acini with Varying Metastatic Potentials. *J Biomed Biotech*. 2012;2012:1–16.

CHAPTER 4.

JUPOETS: A CONSTRAINED MULTIOBJECTIVE OPTIMIZATION APPROACH TO ESTIMATE BIOCHEMICAL MODEL ENSEMBLES IN THE JULIA PROGRAMMING LANGUAGE

The work presented below was published in BMC SYSTEMS BIOLOGY in 2016.

I was the primary user of the JuPOETs during its development while I applied it to the work in Chapter 3 and supported its development. The final implementation of the code and simulations were written and performed by the other authors.

4.1 Summary

Julia is a high level, high performance language that has gained significant popularity in recent years due to its successful blend of straightforward syntax, debugging tools and C-like performance. Accessible modeling tools are essential to ensuring the advancement of modeling techniques and modeling endeavors by non-computer centric scientists. Ensemble approaches address model uncertainty by using several or model families instead of single best-fit parameters or fixed model structures. Parameter ensembles can then be used to understand the distribution of simulation error or leveraged to uncover biological variability. Here, we presented an implementation of the Pareto Optimal Ensemble Technique in Julia. We demonstrated the performance advantages of the Julia implementation over Octave on provided test problems. The test functions are also provided to the user for testing and validation purposes. Overall, we provided an open-source model optimization tool applicable to many biological systems and to solving high-dimensional problems with many valid local minima.

4.2 Abstract

4.2.1 Background

Ensemble modeling is a promising approach for obtaining robust predictions and coarse grained population behavior in deterministic mathematical models.

Ensemble approaches address model uncertainty by using parameter or model families instead of single best-fit parameters or fixed model structures. Parameter ensembles can be selected based upon simulation error, along with other criteria such as diversity or steady-state performance. Simulations using parameter ensembles can estimate confidence intervals on model variables, and robustly constrain model predictions, despite having many poorly constrained parameters.

4.2.2 Results

In this software note, we present a multiobjective based technique to estimate parameter or models ensembles, the Pareto Optimal Ensemble Technique in the Julia programming language (JuPOETs). JuPOETs integrates simulated annealing with Pareto optimality to estimate ensembles on or near the optimal tradeoff surface between competing training objectives. We demonstrate JuPOETs on a suite of multiobjective problems, including test functions with parameter bounds and system constraints as well as for the identification of a proof-of-concept biochemical model with four conflicting training objectives. JuPOETs identified optimal or near optimal solutions approximately six-fold faster than a corresponding implementation in Octave for the suite of test functions. For the proof-of-concept biochemical model, JuPOETs produced an ensemble of parameters that gave both the mean of the training data for

conflicting data sets, while simultaneously estimating parameter sets that performed well on each of the individual objective functions.

4.2.3 Conclusions

JuPOETs is a promising approach for the estimation of parameter and model ensembles using multiobjective optimization. JuPOETs can be adapted to solve many problem types, including mixed binary and continuous variable types, bilevel optimization problems and constrained problems without altering the base algorithm. JuPOETs is open source, available under an MIT license, and can be installed using the Julia package manager from the JuPOETs GitHub repository

4.3 Background

Ensemble modeling is a promising approach for obtaining robust predictions and coarse grained population behavior in deterministic mathematical models. It is often not possible to uniquely identify all the parameters in biochemical models, even when given extensive training data [1]. Thus, despite significant advances in standardizing biochemical model identification [2], the problem of estimating model parameters from experimental data remains challenging. Ensemble approaches address parameter uncertainty in systems biology and other fields like weather prediction [3–6] by using parameter families instead of single best-fit parameter sets. Parameter families can be selected based upon simulation error, along with other criteria such as diversity or steady-state performance. Simulations using parameter ensembles can estimate confidence intervals on model variables, and robustly constrain model predictions, despite having many poorly constrained parameters [7, 8]. There are many techniques to generate parameter ensembles. Battogtokh et al., Brown et al., and later

Tasseff et al. generated experimentally constrained parameter ensembles using a Metropolis-type random walk [3, 5, 9, 10]. Liao and coworkers developed methods to generate ensembles that all approach the same steady-state, for example one determined by fluxomics measurements [11]. They have used this approach for model reduction [12], strain engineering [13, 14] and to study the robustness of non-native pathways and network failure [15]. Maranas and coworkers have also applied this method to develop a comprehensive kinetic model of bacterial central carbon metabolism, including mutant data [16]. We and others have used ensemble approaches, generated using both sampling and optimization techniques, that have robustly simulated a wide variety of signal transduction processes [9, 10, 17–19], neutrophil trafficking in sepsis [20], patient specific coagulation behavior [21], uncertainty quantification in metabolic kinetic models [22] and to capture cell to cell variation [23]. Further, ensemble approaches have been used in synthetic biology to sample possible biocircuit configurations [24]. Thus, ensemble approaches are widely used to robustly simulate a variety of biochemical systems.

Identification of biochemical models requires significant training data perhaps taken from diverse sources. These real-world data sets often contain intrinsic conflicts resulting from, for example, the use of different cell lines, different measurement technologies, different reagent vendors or lots, uncontrollable experimental artifacts or general cross laboratory variability. Parameter ensembles that optimally balance these inherent conflicts lead to more robust model performance. Multiobjective optimization is an ensemble generation technique that naturally balances conflicts in noisy training data [25]. Multiobjective optimization has been used to identify signal transduction

models [18, 23], for the design of synthetic circuits [24], to design the folding behaviors of novel RNAs [26], to design bioprocesses [27], and to understand bacterial adaptation [28]. Thus, it is a widely used approach for a variety of biochemical applications. Previously, we developed the Pareto Optimal Ensemble Technique (POETs) algorithm to address the challenge of competing or conflicting training objectives. POETs, which integrates simulated annealing (SA) and multiobjective optimization through the notion of Pareto rank, estimates parameter ensembles which optimally trade-off between competing (and potentially conflicting) experimental objectives [29]. However, the previous implementation of POETs, in the Octave programming language [30], suffered from poor performance and was not configurable. For example, Octave-POETs does not accommodate user definable objective functions, bounds and problem constraints, cooling schedules, different variable types e.g., a mixture of binary and continuous design variables or custom diversity generation routines. Octave-POETs was also not well integrated into a package or source code management (SCM) system. Thus, upgrades to the approach containing new features, or bug fixes were not centrally managed.

4.4 Implementation

In this software note, we present an open-source implementation of the Pareto optimal ensemble technique in the Julia programming language (JuPOETs). JuPOETs takes advantage of the unique features of Julia to address many of the shortcomings of the previous implementation. Julia is a cross-platform, high-performance programming language for technical computing that has performance comparable to C but with syntax similar to MATLAB/Octave and Python [31]. Julia also offers a

sophisticated compiler, distributed parallel execution, numerical accuracy, and an extensive function library. Further, the architecture of JuPOETs takes advantage of the first-class function type in Julia allowing user definable behavior for all key aspects of the algorithm, including objective functions, custom diversity generation logic, linear/non-linear parameter constraints (and parameter bounds constraints) as well as custom cooling schedules. Julia's ability to naturally call other languages such as Python or C also allows JuPOETs to be used with models implemented in a variety of languages across many platforms. Additionally, Julia offers a built-in package manager which is directly integrated with GitHub, a popular web-based Git repository hosting service offering distributed revision control and source code management. Thus, JuPOETs can be adapted to many problem types, including mixed binary and continuous variable types, bilevel problems and constrained problems without altering the base algorithm, as was required in the previous POETs implementation.

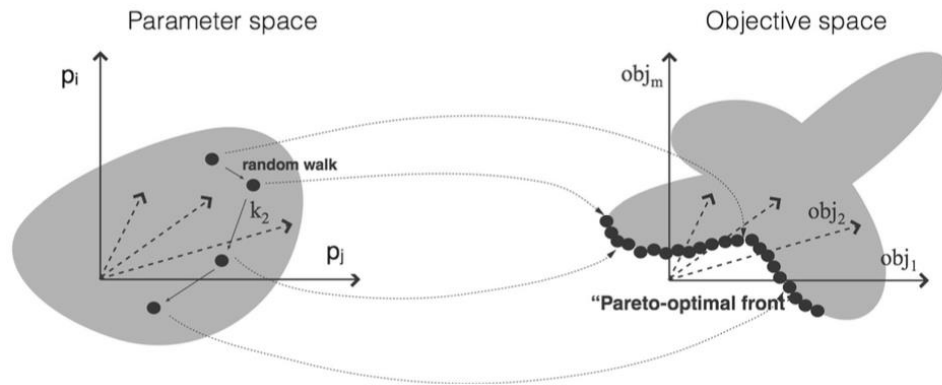


Figure 4.1. Schematic of multiobjective parameter mapping. The performance of any given parameter set is mapped into an objective space using a ranking function which quantifies the quality of the parameters. The distance away from the optimal tradeoff surface is quantified using the Pareto ranking scheme of Fonseca and Fleming in JuPOETs

4.4.1 JuPOETs optimization problem formulation

JuPOETs solves the K -dimensional constrained multiobjective optimization problem:

$$\min_{\mathbf{p}} \begin{cases} O_1(\mathbf{x}(t, \mathbf{p}), \mathbf{p}) \\ \vdots \\ O_K(\mathbf{x}(t, \mathbf{p}), \mathbf{p}) \end{cases} \quad (1)$$

subject to the model equations and constraints:

$$\begin{aligned} \mathbf{f}(t, \mathbf{x}(t, \mathbf{p}), \dot{\mathbf{x}}(t, \mathbf{p}), \mathbf{u}(t), \mathbf{p}) &= \mathbf{0} \\ g_1(t, \mathbf{x}(t, \mathbf{p}), \mathbf{u}(t), \mathbf{p}) &\geq 0 \\ &\vdots \\ g_C(t, \mathbf{x}(t, \mathbf{p}), \mathbf{u}(t), \mathbf{p}) &\geq 0 \end{aligned}$$

and parameter bound constraints:

$$\mathcal{L} \leq \mathbf{p} \leq \mathcal{U}$$

The quantity O_j denotes the j^{th} objective function ($j=1,2,\dots,K$), typically the sum of squared errors for the j^{th} data set for biochemical modeling applications. The terms $\mathbf{f}(t,\mathbf{x}(t,\mathbf{p}),\mathbf{x}'(t,\mathbf{p}),\mathbf{u}(t,\mathbf{p}))$ denote the system of model equations (e.g., differential equations, differential algebraic equations or linear/non-linear algebraic equations) where \mathbf{p} denotes the decision variable vector e.g., unknown model parameters ($D \times 1$). In typical biochemical modeling applications, the model equations $\mathbf{f}(\cdot)$ are a system of continuous real-valued non-linear differential equations that comprise a kinetic model, but other types of models e.g., stoichiometric models are also common. The quantity t denotes time, $\mathbf{x}(t,\mathbf{p})$ denotes the model state (with an initial state $\mathbf{x}(0)$), and $\mathbf{u}(t)$ denotes an input vector. The decision variables (e.g., kinetic parameters) can be subject to bounds constraints, where L and U denote the lower and upper bounds, respectively as well as C problem specific constraints $g_i(t,\mathbf{x}(t,\mathbf{p}),\mathbf{u}(t,\mathbf{p}))$, $i=1,\dots,C$. The decision variables \mathbf{p} are typically real-valued kinetic constants, or metabolic fluxes in the case of stoichiometric models. However, other variables types e.g., binary or categorical decision variables can also be accommodated.

Algorithm 1: Pseudo-code for the JuPOETs run-loop. The user must specify the objective function and an initial parameter guess. The user can optionally specify the neighbor, acceptance, cooling and refinement functions (or use the default implementations). The rank archive \mathcal{R} , solution archive \mathcal{S} and objective archive \mathcal{O} are initialized from the initial guess. The initial guess (potentially following a single objective local refinement step) is perturbed in the neighbor function, which generates a new solution whose performance is evaluated using the user supplied objective function. The new solution and objective values are then added to the respective archives and ranked using the builtin rank function. If the new solution is accepted (based upon a probability calculated with the user supplied acceptance function) it is added to the solution and objective archive. This solution is then perturbed during the next iteration of the algorithm. However, if the solution is not accepted, it is removed from the archive and discarded. The temperature is adjusted using the user supplied cooling function after each \mathcal{I} iterations. When JuPOETs terminates, the parameter solution archive \mathcal{S} , objective archive \mathcal{O} and rank archive \mathcal{R} are returned to the caller.

input : User specified objective function, and initial guess ($\mathcal{D} \times 1$). User can also specify custom neighbor, acceptance, cooling and refinement functions or use the default functions provided.

Output: Rank archive \mathcal{R} ($\mathcal{A} \times 1$), parameter solution archive \mathcal{S} ($\mathcal{D} \times \mathcal{A}$) and objective archive \mathcal{O} ($\mathcal{K} \times \mathcal{A}$), where \mathcal{A} denotes the number of accepted solutions

```

1 initialize:  $\mathcal{R}$ ,  $\mathcal{S}$  and  $\mathcal{O}$  using initial guess  $\mathbf{p}_0$ ;
2 initialize:  $T \leftarrow 1.0$ ;
3 initialize:  $T_{min} \leftarrow 1/10000$ ;
4 initialize: Maximum number of steps per temperature  $\mathcal{I}$ ;

// Call to local refinement function (single objective problem)
5  $\mathbf{p}_0 \leftarrow \text{user-function::refinement}(\mathbf{p}_0)$ ;

6 while  $T > T_{min}$  do
7    $i \leftarrow 1$ ;
8   while  $i < \mathcal{I}$  do
9     // Generate a new parameter solution using user neighbor function
10     $\mathbf{p}_{i+1} \leftarrow \text{user-function::neighbor}(\mathbf{p}^*)$ ;
11    // Evaluate  $\mathbf{p}_{i+1}$  using user objective function
12     $\mathbf{o}_{i+1} \leftarrow \text{user-function::objective}(\mathbf{p}_{i+1})$ ;
13    Add  $\mathbf{p}_{i+1}$  to solution archive  $\mathcal{S}$ ;
14    Add  $\mathbf{o}_{i+1}$  to objective archive  $\mathcal{O}$ ;
15    // Calculate Pareto rank of solutions in  $\mathcal{O}$  using builtin rank function
16     $\mathcal{R} \leftarrow \text{builtin-function::rank}(\mathcal{O})$ ;
17    // Accept  $\mathbf{p}_{i+1}$  into the archive with user defined probability
18     $\mathcal{P} \leftarrow \text{user-function::acceptance}(\mathcal{R}, T)$ ;
19    if  $\mathcal{P} > \text{rand}$  then
20      // Update the best solution with  $\mathbf{p}_{i+1}$ 
21       $\mathbf{p}^* \leftarrow \mathbf{p}_{i+1}$ ;
22      prune  $\mathcal{S}$ ,  $\mathcal{R}$  and  $\mathcal{O}$  of all solutions above a rank threshold;
23    else
24      Remove  $\mathbf{p}_{i+1}$  from solution archive  $\mathcal{S}$ ;
25      Remove  $\mathbf{o}_{i+1}$  from error archive  $\mathcal{O}$ ;
26    end
27     $i \leftarrow i + 1$ ;
28  end
29  // Update  $T$  using the user cooling function
30   $T \leftarrow \text{user-function::cooling}(T)$ ;
31 end

```

JuPOETs integrates simulated annealing (SA) [32] with Pareto ranking to estimate decision variables on or near the optimal tradeoff surface between competing

objectives (Figure 4.1 and Algorithm 1). A tradeoff surface defines the best possible performance for every conflicting objective, such that an increase in the performance of one objective does not decrease the performance of at least one other objective. Pareto rank is a scalar measure of distance away from the optimal tradeoff surface (low rank is near the surface, while higher ranks are progressively further away). Thus, the central idea underlying POETs is a mapping between the value of the objective vector evaluated at p_{i+1} (decision variable guess at iteration $i+1$) and the scalar Pareto rank (Figure 4.1). Traditional simulated annealing uses a scalar performance value e.g., simulation error to make a probabilistic decision to keep or reject a set of decision variables; decision variables with better performance are always accepted, while those with worse performance are sometimes accepted depending upon a parameter called the temperature. On the other hand, JuPOETs makes this same decision using the Pareto rank instead of a single performance objective. The problem of estimating biochemical model parameters from experimental data is typically posed as an error minimization problem over continuous real-valued decision variables (model parameters) subject to the model equations. A parameter set p_{i+1} lies along the optimal tradeoff surface if no other parameter guess leads to decreased error for every objective. JuPOETs calculates the performance of a candidate parameter set p_{i+1} by calling the user defined objective function; objective takes a parameter set as an input, evaluates the model equations, and using this solution, returns the $K \times 1$ objective vector. Candidate parameter sets are generated by the user supplied neighbor function; the default implementation of neighbor is a random perturbation, however other perturbation

logic can be implemented by the user. The error vector associated with \mathbf{p}_{i+1} is ranked using the builtin Pareto rank function, by comparing the error at iteration $i+1$ to the error archive \mathcal{O}_i (all error vectors up to iteration i meeting a ranking criterion).

Parameter sets on or near the optimal trade-off surface between the objectives have a rank equal to 0 (no other current parameter sets are better). These rank zero parameter sets define the Pareto optimal group for the ensemble, wherein Pareto optimality is defined as a parameter set not being dominated by any other sets within the ensemble. Sets with increasing non-zero rank are progressively further away from the optimal trade-off surface. Thus, a parameter set with a rank =0 is *better* in a trade-off sense than rank >0. We implemented the Fonseca and Fleming ranking scheme in the builtin rank function [33]:

$$\text{rank}(\mathcal{O}_{i+1}(\mathbf{p}_{i+1}) \mid \mathcal{O}_i) = r \quad (2)$$

where rank r is the number of parameter sets that dominate (are better than) parameter set \mathbf{p}_{i+1} , and $\mathcal{O}_{i+1}(\mathbf{p}_{i+1})$ denotes the objective vector evaluated at \mathbf{p}_{i+1} . We used the Pareto rank to inform the SA calculation. The parameter set \mathbf{p}_{i+1} was accepted or rejected by the SA at each iteration, by calculating an acceptance probability $P(\mathbf{p}_{i+1})$:

$$\mathcal{P}(\mathbf{p}_{i+1}) \equiv \exp\{-\text{rank}(\mathcal{O}_{i+1}(\mathbf{p}_{i+1}) \mid \mathcal{O}_i) / T\} \quad (3)$$

where T is the simulated annealing temperature; the temperature provides control over how strictly decreasing Pareto rank is enforced. As $\text{rank}(\mathcal{O}_{i+1}(\mathbf{p}_{i+1}) \mid \mathcal{O}_i) \rightarrow 0$, the acceptance probability moves toward one, ensuring that we explore parameter sets

along the Pareto surface. Occasionally, (depending upon T) a parameter set with a high Pareto rank is accepted by the SA allowing a more diverse search of the parameter space. However, as T is reduced as a function of iteration count (using the cooling function), the probability of accepting a high-rank set decreases. Parameter sets could also be accepted by the SA but *not* permanently archived in S_i , where S_i is the solution archive. Only parameter sets with rank less than or equal to a threshold (rank ≤ 4 by default) are included in S_i , where the archive is re-ranked and filtered after accepting every new parameter set. Parameter bounds were implemented in the neighbor function as box constraints, while problem specific constraints were implemented in objective using a penalty method:

$$O_i + \lambda \sum_{j=1}^c \min \{0, g_j(t, \mathbf{x}(t, \mathbf{p}), \mathbf{u}(t), \mathbf{p})\} \quad i = 1, \dots, \mathcal{K} \quad (4)$$

where λ denotes the penalty parameter ($\lambda=100$ by default). However, because both the neighbor and objective functions are user defined, different constraint implementations are easily defined.

To use JuPOETs, the user specifies the neighbor, acceptance, cooling and objective functions along with an initial decision variable guess. Default implementations of the neighbor, acceptance and cooling functions can be used directly, or they can be overridden by user defined logic. However, the user must provide an implementation of the objective function and provide an initial decision variable guess. Lastly, if the user is operating JuPOETs in hybrid mode, then a refinement function pointer must

also be specified. Hybrid mode temporarily switches the search from a multiobjective to a single objective problem, where the sum of the objective functions can be used to update the best (or initial) parameter guess. The specific hybrid mode search logic is up to the user; by default hybrid mode is off, and the default refinement implementation is simply a pass through function. However, we have shown previously that POETs operated in hybrid mode (where the single objective problem used a pattern search approach) had better performance than POETs alone [29]. Thus, hybrid mode is generally recommended for most applications. In addition, there are several user configurable parameters that can be adjusted to control the performance of JuPOETs: `maximum_number_of_iterations` controls the number of iterations per temperature (default 20); `rank_cutoff` controls the upper rank bound on the solution archive (default 5); `temperature_min` controls the minimum temperature after which JuPOETs returns the error and solution archives (default 0.001); `show_trace` controls the level of output shown to the user (default true). After the completion of the run, JuPOETs returns the parameter solution archive S , objective archive O and rank archive R . The parameter solution archive S contains is an $D \times A$ array, where A denotes the number of solutions in the archive when JuPOETs terminated. On the other hand, the objective archive O is an $K \times A$ array containing the performance values for each objective corresponding the columns of S . Lastly, JuPOETs returns the rank archive R which is an $A \times 1$ array of Pareto ranks corresponding to the columns of S . One technical note, if JuPOETs is run from multiple starting locations, and the archives from each of these runs is combined into a single collective archive, the combined parameter rank archive may become invalid. In

these cases, it is required to re-rank the parameter sets using the built-in rank function to produce a collective parameter ranking.

Name	Dimension	Function	Domain	Constraints
Schaffer function	1	$O_1(x) = x^2$ $O_2(x) = (x - 2)^2$	$-10 \leq x \leq 10$	
Binh and Korn function	2	$O_1(x, y) = 4x^2 + 4y^2$ $O_2(x, y) = (x - 5)^2 + (y - 5)^2$	$0 \leq x \leq 5$ $0 \leq y \leq 3$	$g_1(x, y) = (x - 5)^2 + y^2 \leq 25$ $g_2(x, y) = (x - 8)^2 + (y + 3)^2 \leq 7.7$
Fonseca and Fleming function	3	$O_1(x_i) = 1 - \exp\left(-\sum_{i=1}^N \left(x_i - \frac{1}{\sqrt{N}}\right)^2\right)$ $O_2(x_i) = 1 - \exp\left(-\sum_{i=1}^N \left(x_i + \frac{1}{\sqrt{N}}\right)^2\right)$	$-4 \leq x_i \leq 4$	

Table 4.1. Multi-objective optimization test problems. We tested the JuPOETs implementation on three two-dimensional test problems, with one-, two- and three-dimensional parameter vectors. Each problem had parameter bounds constraints, however, on the Binh and Korn function had additional non-linear problem constraints. For the Fonesca and Fleming problem, $N = 3$

4.5 Results and discussion

JuPOETs identified optimal or nearly optimal solutions significantly faster than Octave-POETs for a suite of multiobjective algebraic test problems (Table 1). The algebraic test problems were constrained non-linear functions with bound constraints and additional non-linear constraints on the decision variables in one case. The problems had up to three-dimensional continuous real-valued decision vectors, and each case had two objective functions. The wall-clock time for JuPOETs and Octave-POETs was measured for 10 independent trials for each of the test problems. The same cooling, neighbor, acceptance, and objective logic was employed between the implementations, and all other parameters were held constant. For each test function, the search domain was partitioned into 10 segments, where an initial parameter guess was drawn from each partition. The number of search steps for each temperate was $\square I = 10$ for all cases, and the cooling parameter was $\alpha = 0.9$. On

average, JuPOETs identified optimal or near optimal solutions for the suite of test problems six-fold faster (60s versus 400s) than Octave-POETs (Figure 4.2). JuPOETs produced the characteristic tradeoff curves for each test problem, given both decision variable bound and problem constraints (Figure 4.3). Thus, JuPOETs estimated an ensemble of solutions to constrained multiobjective algebraic test problems significantly faster than the current Octave implementation. Next, we tested JuPOETs on a proof-of-concept biochemical model identification problem.

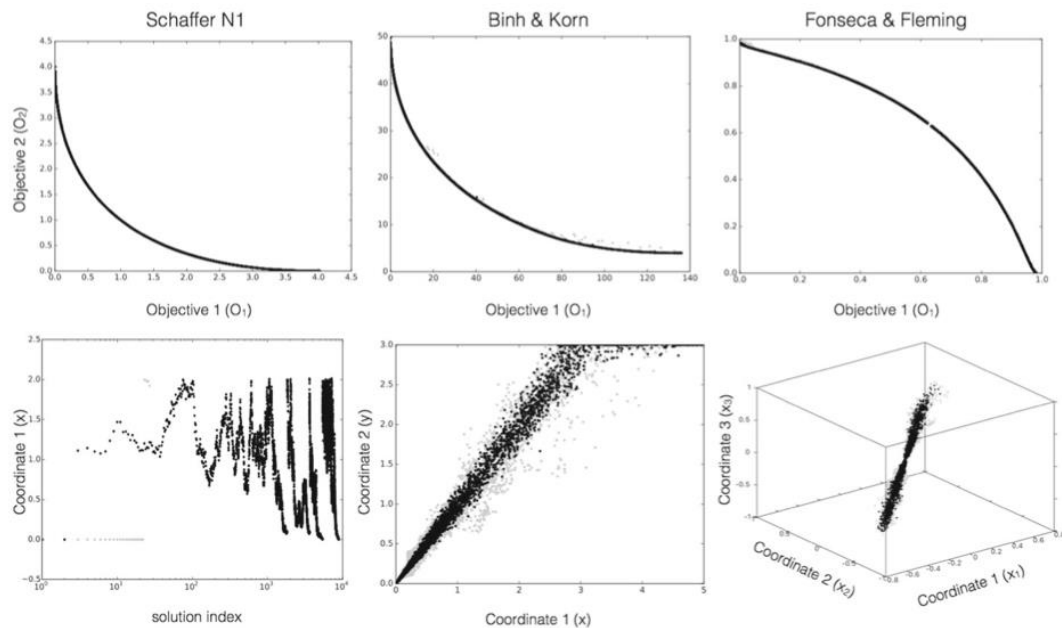


Figure 4.2. The performance of JuPOETs on the multi-objective test suite. The execution time (wall-clock) for JuPOETs and POETs implemented in Octave was measured for 10 independent trials for the suite of test problems. The number of steps per temperature $I = 10$, and the cooling parameter $\alpha = 0.9$ for all cases. The problem domain was partitioned into 10 equal segments, an initial guess was drawn from each segment. For each of the test functions, JuPOETs estimated solutions on (rank zero solutions, *black*) or near (*gray*) the optimal tradeoff surface, subject to bounds and problem constraints

JuPOETs estimated an ensemble of biochemical model parameters that were consistent with the mean of synthetic training data (Figure 4.4). Four synthetic training data sets were generated from a prototypical biochemical network consisting of 6 metabolites and 7 reactions (Figure 4.4, inset right). We considered a common case in which the same extracellular measurements of A_e, B_e, C_e and cellmass were made on four hypothetical cell types, each having the same biological connectivity but different performance. Network dynamics were modeled using the hybrid cybernetic model with elementary modes (HCM) approach of Ramkrishna and coworkers [34]. In the HCM approach, metabolic networks are first decomposed into a set of elementary modes (EMs) (chemically balanced steady-state pathways, see [35]). Dynamic combinations of elementary modes are then used to characterize network behavior. Each elementary mode is catalyzed by a pseudo enzyme; thus, each mode has both kinetic and enzyme synthesis parameters. The proof of concept network generated 6 EMs, resulting in 13 model parameters (continuous real-valued decision variables). The synthetic training data was generated by randomly varying these parameters.

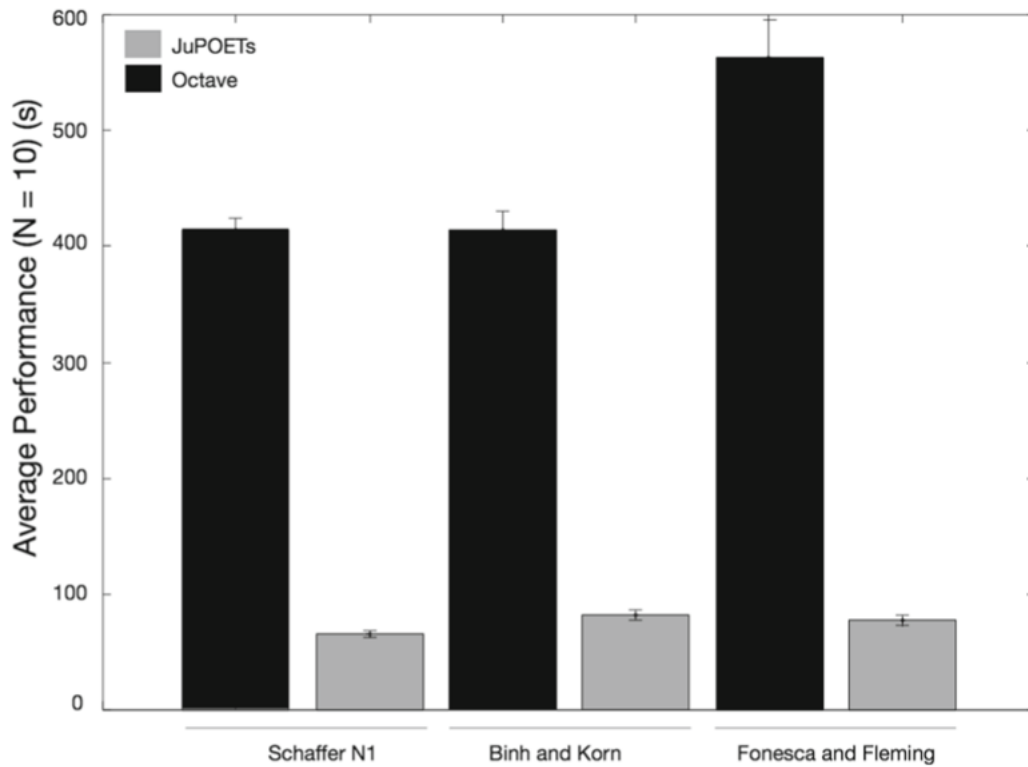


Figure 4.3. Representative JuPOETs performance comparison between JuPOETs and POETs in Octave for problems in the multi-objective test suite. JuPOETs performed roughly 8-fold faster across the three test functions. The number of steps per temperature $I = 10$, and the cooling parameter $\alpha = 0.9$ for all cases. The problem domain was partitioned into 10 equal segments, an initial guess was drawn from each segment. For each of the test functions, JuPOETs estimated solutions on the optimal tradeoff surface, subject to bounds and problem constraints

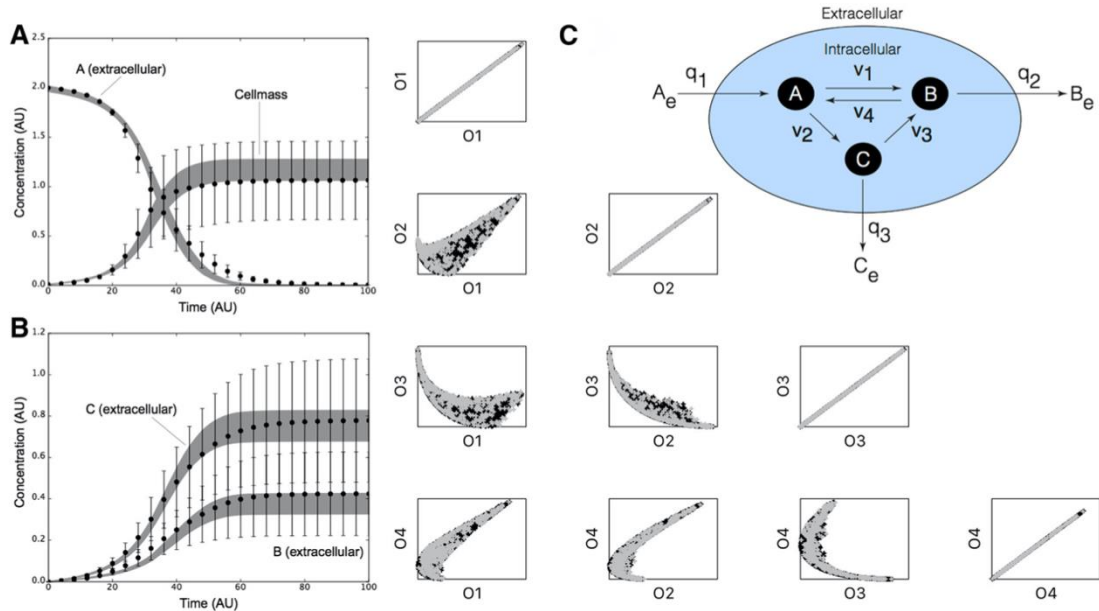


Figure 4.4. Proof of concept biochemical network study. Inset right: Prototypical biochemical network with six metabolites and seven reactions modeled using the hybrid cybernetic approach (HCM). Intracellular cellmass precursors A , B , and C are balanced (no accumulation) while the extracellular metabolites A_e , B_e , and C_e are dynamic. The oval denotes the cell boundary, q_j is the j th flux across the boundary, and v_k denotes the k th intracellular flux. Four data sets (each with A_e , B_e , C_e and cellmass measurements) were generated by varying the kinetic constants for each biochemical mode. Each data set was a single objective in the JuPOETs procedure. **a** Ensemble simulation of extracellular substrate A_e and cellmass versus time. **b** Ensemble simulation of extracellular substrate B_e and C_e versus time. The gray region denotes the 95% confidence estimate of the mean ensemble simulation. The data points denote mean synthetic measurements, while the error bars denote the 95% confidence estimate of the measurement computed over the four training data sets. **c** Trade-off plots between the four training objectives. The quantity O_j denotes the j th training objective. Each point represents a member of the parameter ensemble, where *gray* denotes rank 0 sets, while *black* denotes rank 1 sets. Ensembles were generated using POETs without employing local refinement

The general form of the biochemical test problem was given by:

$$\min_{\mathbf{p}} (O_1, \dots, O_{\mathcal{K}}) \quad (5)$$

subject to model and bounds constraints. We considered four training data sets ($\mathcal{K}=4$), each of which contained time-series measurements of A_e, B_e, C_e and cellmass. Each objective $O_j, j=1, \dots, \mathcal{K}$ quantified the squared difference between the simulated (x_i) and measured extracellular species abundance (y_i) in the j^{th} data set:

$$O_j = \sum_i \sum_{\tau} (x_i(\tau) - y_i(\tau))^2 \quad j = 1, \dots, \mathcal{K} \quad (6)$$

where, i denotes the species index and τ denotes the time index. The abundance of extracellular species i (x_i), the pseudo enzyme e_l (catalyzes flux through mode l), and cellmass were governed by the model equations:

$$\begin{aligned} \frac{dx_i}{dt} &= \sum_{j=1}^{\mathcal{R}} \sum_{l=1}^{\mathcal{L}} \sigma_{ij} z_{jl} q_l(\mathbf{e}, \mathbf{p}, \mathbf{x}) c \quad i = 1, \dots, \mathcal{M} \\ \frac{de_l}{dt} &= \alpha_l + r_{El}(\mathbf{p}, \mathbf{x}) u_l - (\beta_l + r_G) e_l \quad l = 1, \dots, \mathcal{L} \\ \frac{dc}{dt} &= r_G c \end{aligned}$$

where \mathcal{R} and \mathcal{M} denote the number of reactions and extracellular species in the model and \mathcal{L} denotes the number of elementary modes. The quantity σ_{ij} denotes the stoichiometric coefficient for species i in reaction j and z_{jl} denotes the normalized flux for reaction j in mode l . If $\sigma_{ij} > 0$, species i is produced by reaction j ; if $\sigma_{ij} < 0$,

species i is consumed by reaction j ; if $\sigma_{ij}=0$, species i is not connected with reaction j . Extracellular species, cellmass and pseudo-enzyme were subject to the initial conditions $\mathbf{x}(t_0)=\mathbf{x}_0$, $c(t_0)=c_0$ and $e_l=0.5$, respectively. The term $q_l(\mathbf{e},\mathbf{p},\mathbf{x})$ denotes the specific uptake/secretion rate for mode l where \mathbf{e} denotes the pseudo enzyme vector, \mathbf{p} denotes the unknown kinetic parameter vector (decision variables), \mathbf{x} denotes the extracellular species vector, and c denotes the cell mass; $q_l(\mathbf{e},\mathbf{p},\mathbf{x})$ is the product of a kinetic term ($q^- lq^- 1$) and a control variable governing enzyme activity. Flux through each mode was catalyzed by a pseudo enzyme e_l , synthesized at the regulated specific rate $r_{E,l}(\mathbf{p},\mathbf{x})$, and constitutively at the rate α_l . The term u_l denotes the cybernetic variable controlling the synthesis of enzyme l . The term β_l denotes the rate constant governing non-specific enzyme degradation, and r_G denotes the specific growth rate through all modes.

The specific uptake/secretion rates and the specific rate of enzyme synthesis were modeled using saturation kinetics. The specific growth rate was given by:

$$r_G = \sum_{l=1}^{\mathcal{L}} z_{\mu l} q_l(\mathbf{e}, \mathbf{p}, \mathbf{x})$$

where $z_{\mu l}$ denotes the growth flux μ through mode l . The control variables u_l and v_l , which control the synthesis and activity of each enzyme respectively, were given by:

$$u_l = \frac{z_{sl} \bar{q}_l}{\sum_{l=1}^{\mathcal{L}} z_{sl} \bar{q}_l} \quad (7)$$

and

$$v_l = \frac{z_{sl} \bar{q}_l}{\max_{l=1, \dots, \mathcal{L}} z_{sl} \bar{q}_l} \quad (8)$$

where z_{sl} denotes the uptake flux of substrate s through mode l . Each unknown kinetic parameter was continuous and real-valued, and subject to bounds constraints: $L \leq p \leq U$.

JuPOETs produced an ensemble of approximately $\dim S \simeq 13,000$ parameter sets that captured the mean of the measured data sets for extracellular metabolites and cellmass (Figure 4.4 a and b). JuPOETs minimized the difference between the simulated and measured values for extracellular metabolites A_e , B_e , C_e and cellmass, where the residual for each data set was treated as a single objective (leading to four objectives). The 95% confidence estimate produced by the ensemble was consistent with the mean of the measured data, despite having significant uncertainty in the training data.

JuPOETs produced a consensus estimate of the synthetic data by calculating optimal trade-offs between the training data sets (Figure 4.4 c). Multiple trade-off fronts were visible in the objective plots, for example between data set 3 (O_3) and data set 2 (O_2). Thus, without a multiobjective approach, it would be challenging to capture these data sets as fitting one leads to decreased performance on the other. However, the ensemble contained parameter sets that described each data set independently (Figure. 5). Thus, JuPOETs produced an ensemble of parameters that gave the mean of the training data

for conflicting data sets, while simultaneously estimating parameter sets that performed well on each individual objective function.

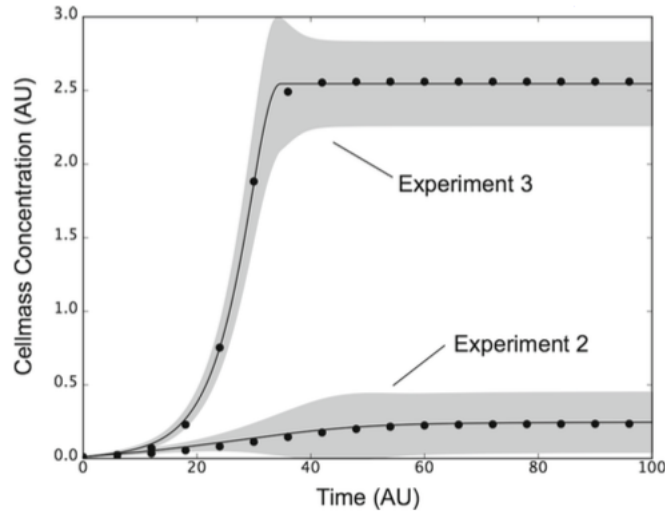


Figure 4.5. Experiment to experiment variation captured by the ensemble. Cellmass measurements (*points*) versus time for experiment 2 and 3 were compared with ensemble simulations. The full ensemble was sorted by simultaneously selecting the top 25% of solutions for each objective with rank ≤ 1 . The best fit solution for each objective (*line*) ± 1 -standard deviation (*gray region*) for experiment 2 and 3 brackets the training data despite significant differences the training values between the two data sets

Currently, JuPOETs does not consider parameter identifiability when constructing parameter ensembles. Although JuPOETs produces parameter estimates that give model performance similar to the training data, we do not have strict statistical confidence that the *true* parameter values are contained within the ensemble. However, despite this, ensembles produced by POETs can be predictive [18, 23]. Thus, JuPOETs produces a collection of parameters that are constrained by the performance of the model, and not by specific hypotheses regarding the individual values of the raw model parameters. Of course, knowledge of specific parameter values, or the relationship between parameter combinations, can be used to inform the

search through either bounds or problem specific constraints (for example, as demonstrated in the first example problem).

4.6 Conclusions

In this software note, we presented JuPOETs, a multiobjective technique to estimate parameter ensembles in the Julia programming language. JuPOETs is open source, and available for download under an MIT license from the JuPOETs GitHub repository at <https://github.com/varnerlab/POETs.jl>. We demonstrated JuPOETs on a suite of algebraic test problems, and a proof-of-concept ODE based biochemical model. While JuPOETs outperformed (and was significantly more flexible) than the previous Octave implementation, there are several areas that could be explored further. First, JuPOETs should be compared with other multiobjective evolutionary algorithms (MOEAs) to determine its relative performance on test and real world problems. Many evolutionary approaches e.g., the non-dominated sorting genetic algorithm (NSGA) family of algorithms, have been adapted to solve multiobjective problems [36, 37]. However, since there is a lack of open source Julia implementations of these alternative approaches, we did not benchmark the relative performance of JuPOETs in this note. One advantage that JuPOETs may have when compared to a strictly evolutionary approaches, is the inclusion of a local refinement step (hybrid mode), which temporarily reduces the problem to a single objective formulation. Previously, POETs run in hybrid mode led to better convergence on a proof-of-concept signal transduction model compared to the same approach without the hybrid refinement step [29]. Other hybrid multiobjective methods have also been shown to be more efficient than evolutionary approaches alone, for a variety of biochemical optimization

problems [24, 38]. Thus, there are several different algorithms that we can use to benchmark, and improve the performance of JuPOETs, after we implement them in Julia. Another strategy to improve the performance of JuPOETs is to reduce the number (or cost) of function evaluations that are required to obtain optimal or near optimal solutions. For example, in many real world parameter estimation problems, the bulk of the execution time is spent evaluating the objective functions. One strategy to improve JuPOETs performance could be to optimize surrogates [39], while another would be parallel execution of the objective functions. Currently, JuPOETs serially evaluates the objective function vector. However, parallel evaluation of the objective functions e.g., using the parallel Julia macro or other techniques, could be implemented without significantly changing the JuPOETs run loop. Taken together, JuPOETs demonstrated improved flexibility, and performance over POETs in parameter identification and ensemble generation for multiple objectives. JuPOETs has the potential for widespread use due to the flexibility of the implementation, and the high level syntax and distribution tools native to the Julia programming language.

4.7 Availability and requirements

JuPOETs is open source, available under an MIT software license. The JuPOETs source code is freely available from the JuPOETs GitHub repository at <https://github.com/varnerlab/POETs.jl>. All samples used in this study are included in the sample/biochemical and sample/test_functions subdirectories of the JuPOETs GitHub repository. JuPOETs can be run on all common. **Operating system environments:** (Linux, Mac OS, Windows).

4.8 References

1. Gadkar KG, Varner J, Doyle FJ. Model identification of signal transduction networks from data using a state regulator problem. *Syst Biol (Stevenage)*. 2005;2(1):17–30.
2. Gennemark P, Wedelin D. Benchmarks for identification of ordinary differential equations from time series data. *Bioinformatics*. 2009;25(6): 780–6. doi:10.1093/bioinformatics/btp050.
3. Battogtokh D, Asch DK, Case ME, Arnold J, Shüttler HB. An ensemble method for identifying regulatory circuits with special reference to the qa gene cluster of *Neurospora crassa*. *Proc Natl Acad Sci USA*. 2002;99(26): 16904–9.
4. Kuepfer L, Peter M, Sauer U, Stelling J. Ensemble modeling for analysis of cell signaling dynamics. *Nat Biotechnol*. 2007;25(9):1001–6. doi:10.1038/nbt1330.
5. Brown KS, Sethna JP. Statistical mechanical approaches to models with many poorly known parameters. *Phys Rev E*. 2003;68:021904–19.
6. Palmer TN, Shutts GJ, Hagedorn R, Doblas-Reyes FJ, Jung T, Leutbecher M. Representing model uncertainty in weather and climate prediction. *Ann Rev Earth Planetary Sci*. 2005;33:163–93.
7. Gutenkunst RN, Waterfall JJ, Casey FP, Brown KS, Myers CR, Sethna JP. Universally sloppy parameter sensitivities in systems biology models. *PLoS Comput Biol*. 2007;3(10):1871–8. doi:10.1371/journal.pcbi.0030189.
8. Song S, Varner J. Modeling and analysis of the molecular basis of pain in sensory neurons. *PLoS ONE*. 2009;4:6758–72.
9. Tasseff R, Nayak S, Salim S, Kaushik P, Rizvi N, Varner JD. Analysis of the molecular networks in androgen dependent and independent prostate cancer revealed fragile and robust subsystems. *PLoS ONE*. 2010;5(1):8864. doi:10.1371/journal.pone.0008864.
10. Tasseff R, Nayak S, Song SO, Yen A, Varner JD. Modeling and analysis of retinoic acid induced differentiation of uncommitted precursor cells. *Integr Biol (Camb)*. 2011;3(5):578–91. doi:10.1039/c0ib00141d.
11. Tran LM, Rizk ML, Liao JC. Ensemble modeling of metabolic networks. *Biophys J*. 2008;95(12):5606–17. doi:10.1529/biophysj.108.135442.
12. Tan Y, Rivera JGL, Contador CA, Asenjo JA, Liao JC. Reducing the

- allowable kinetic space by constructing ensemble of dynamic models with the same steady-state flux. *Metab Eng.* 2011;13(1):60–75. doi:10.1016/j.ymben.2010.11.001.
13. Contador CA, Rizk ML, Asenjo JA, Liao JC. Ensemble modeling for strain development of l-lysine-producing *escherichia coli*. *Metab Eng.* 2009;11(4–5):221–33. doi:10.1016/j.ymben.2009.04.002.
 14. Tan Y, Liao JC. Metabolic ensemble modeling for strain engineers. *Biotechnol J.* 2012;7(3):343–53. doi:10.1002/biot.201100186.
 15. Lee Y, Lafontaine Rivera JG, Liao JC. Ensemble modeling for robustness analysis in engineering non-native metabolic pathways. *Metab Eng.* 2014;25:63–71. doi:10.1016/j.ymben.2014.06.006.
 16. Khodayari A, Zomorodi AR, Liao JC, Maranas CD. A kinetic model of *escherichia coli* core metabolism satisfying multiple sets of mutant flux data. *Metab Eng.* 2014;25:50–62. doi:10.1016/j.ymben.2014.05.014.
 17. Luan D, Zai M, Varner JD. Computationally derived points of fragility of a human cascade are consistent with current therapeutic strategies. *PLoS Comput Biol.* 2007;3(7):142. doi:10.1371/journal.pcbi.0030142.
 18. Song SO, Varner J. Modeling and analysis of the molecular basis of pain in sensory neurons. *PLoS ONE.* 2009;4(9):6758. doi:10.1371/journal.pone.0006758.
 19. Nayak S, Siddiqui JK, Varner JD. Modelling and analysis of an ensemble of eukaryotic translation initiation models. *IET Syst Biol.* 2011;5(1):2. doi:10.1049/iet-syb.2009.0065.
 20. Song SO, Song SOK, Hogg J, Peng ZY, Parker R, Kellum JA, Clermont G. Ensemble models of neutrophil trafficking in severe sepsis. *PLoS Comput Biol.* 2012;8(3):1002422. doi:10.1371/journal.pcbi.1002422.
 21. Luan D, Szlam F, Tanaka KA, Barie PS, Varner JD. Ensembles of uncertain mathematical models can identify network response to therapeutic interventions. *Mol Biosyst.* 2010;6(11):2272–86. doi:10.1039/b920693k.
 22. Andreozzi S, Miskovic L, Hatzimanikatis V. iSCHRUNK—in silico approach to characterization and reduction of uncertainty in the kinetic models of genome-scale metabolic networks. *Metab Eng.* 2016;33:158–68. doi:10.1016/j.ymben.2015.10.002.
 23. Lequieu J, Chakrabarti A, Nayak S, Varner JD. Computational modeling and analysis of insulin induced eukaryotic translation initiation. *PLoS Comput Biol.* 2011;7(11):1002263. doi:10.1371/journal.pcbi.1002263.

24. Otero-Muras I, Banga JR. Multicriteria global optimization for biocircuit design. *BMC Syst Biol.* 2014;8:113. doi:10.1186/s12918-014-0113-3.
25. Handl J, Kell DB, Knowles J. Multiobjective optimization in bioinformatics and computational biology. *IEEE/ACM Trans Comput Biol Bioinform.* 2007;4(2):279–92. doi:10.1109/TCBB.2007.070203.
26. Taneda A. Multi-objective optimization for RNA design with multiple target secondary structures. *BMC Bioinformatics.* 2015;16(1):280. doi:10.1186/s12859-015-0706-x.
27. Sendin J, Otero-Muras I, Alonso AA, Banga J. Improved Optimization Methods for the Multiobjective Design of Bioprocesses. *Ind Eng Chem Res.* 2006;45:8594–603.
28. Angione C, Lió P. Predictive analytics of environmental adaptability in multi-omic network models. *Sci Rep.* 2015;5:15147. doi:10.1038/srep15147.
29. Song SO, Chakrabarti A, Varner JD. Ensembles of signal transduction models using pareto optimal ensemble techniques (poets). *Biotechnol J.* 2010;5(7):768–80. doi:10.1002/biot.201000059.
30. Eaton JW, Bateman D, Hauberg S. GNU octave version 3.0.1 manual: a high-level interactive language for numerical computations. North Charleston: CreateSpace Independent Publishing Platform; 2009.
31. Bezanson J, Edelman A, Karpinski S, Shah VB. Julia: A fresh approach to numerical computing. *arXiv CoRR.* abs/1411.1607. Ithaca: Cornell University; 2014.
32. Kirkpatrick S, Gelatt Jr CD, Vecchi MP. Optimization by simulated annealing. *Science.* 1983;220(4598):671–80. doi:10.1126/science.220.4598.671.
33. Fonseca CM, Fleming PJ. Genetic Algorithms for Multiobjective Optimization: Formulation, Discussion and Generalization. *arXiv CoRR Publisher.* In: *Proceedings of the 5th International Conference on Genetic Algorithms.* Ithaca: Cornell University; 1993. p. 416–23.
34. Kim J, Varner J, Ramkrishna D. A hybrid model of anaerobic e. coli gjt001: Combination of elementary flux modes and cybernetic variables. *Biotechnol Prog.* 2008;24(5):993–1006. doi:10.1002/btpr.73.
35. Schuster S, Fell DA, Dandekar T. A general definition of metabolic pathways useful for systematic organization and analysis of complex metabolic networks. *Nat Biotechnol.* 2000;18(3):326–2. doi:10.1038/73786.

36. Kalyanmoy D, Pratap A, Agarwal S, Meyarivan T. A Fast and Elitist Multiobjective Genetic Algorithm: NSGA-II. *IEEE Trans Evol Comp.* 2002;6: 182–97.
37. Huband S, Hingston P, Barone L, While L. A review of multiobjective test problems and a scalable test problem toolkit. *IEEE Trans Evol Comp.* 2006;10:477–506.
38. Sendin JOH, Otero-Muras I, Alonso AA, Banga JR. Improved optimization methods for multiple objective design of bioprocesses. *Ind Eng Chem Res.* 2006;45:8594–603.
39. Booker AJ, Dennis JE, Frank PD, Serafini DB, Torczon V, Trosset MW. A rigorous framework for optimization of expensive functions by surrogates. *Struct Optim.* 1999;17:1–13.

CHAPTER 5.

SHEAR STRESS REGULATION OF ENDOTHELIAL TO MESENCHYMAL TRANSITION IN THE DEVELOPING ATRIOVENTRICULAR VALVE

I would like to thank Dr. Gretchen Mahler for providing the gene expression data used to train the model in this chapter.

5.1 Summary

Endothelial to mesenchymal transition is a key initiating step in valvulogenesis, populating the valve cushion with cells that will grow and elongate this primitive tissue into a leaflet [1]. The precise initiation and cessation of EMT is critical to achieving proper valve homeostasis. Surface shear stresses have been shown to have roles in activating and switching off EMT in adult aortic valve endocardial cells [2]. In this study, we assessed the responsiveness of AV endocardial cells to shear stress using a flow bioreactor system. We extended the computational model of EMT published previously to include a rule-based representation of mechanotransduction and trained it on gene expression data acquired from our *in vitro* bioreactor experiments [3]. We used this model to show that a balance of YAP activity and PECAM expression could capture the behaviors of the shear stress response. We confirmed that YAP1 was shear stress sensitive in valve endocardial cells by observing nuclear localization of YAP1 under both OSC and LSS modes of shear stress. Using our *in silico* model, we predicted that RhoA-ROCK activity, commonly associated with YAP1 activation, is not required for this YAP1 nuclear translocation in response to shear stress. This was unexpected based on YAP1 responses to changes in matrix stiffness [4]. Instead, a decrease in RhoA-ROCK activity supports shear stress as being sufficient to permit nuclear translocation, verifying our prediction, and supporting fluid shear stress as an additional mechanism to mechanically drive YAP1 translocation [5]. Overall, we have shown that developmental valve EndMT can be induced by low magnitude OSC shear stress and repressed by high magnitude LSS shear stress through TGF β transcription. The complementary *in vitro* and *in silico* tools

that we have developed will allow for a more complete understanding of how tissue scale biomechanical loads orchestrate cellular signals to govern valve morphogenesis.

5.2 Introduction

Successful development of both AV and OFT valves requires precisely timed initiation and cessation of EMT in order to populate the valve mesenchyme without compromising the endothelium [6]. Consequences of dysregulated EMT include valve insufficiency, severe septal defects, and embryonic lethality [7], [8]. The developmental control of EMT is achieved through the interaction of signaling pathways, including TGF β , BMP and VEGF, across cell types [9], [10]. It is well established that TGF β ligands are pro-EMT signals in both embryogenesis and in cancer [11]. TGF β induced EMT is conserved in multiple endothelial cell types [12]. Further, EMT through TGF β signals is implicated in aortic aneurysms when abhorrently activated by non-physiological hemodynamic signals [13]. Recently, shear stress has been shown to regulate adult valve EMT through the activation of TGF β transcripts in aortic valve endothelial cells [2]. In response to shear stress, primary cilia have been shown to be directly connected to TGF β -induced EMT, though the relationship between stress magnitude and this relationship remains unclear [14]. At the same time, several signaling pathways have been implicated in shear transduction. KLF2 is a transcription factor responsive to oscillatory shear stress that can regulate key regulatory proteins in valve development [15]. YAP1 acts as a mechanosensor at cadherin junctions in vascular endothelium [16] and has been established as a mechanosensor for matrix stiffness downstream of Rho-ROCK activation [4]. Further, YAP1 has recently been established as a required transcription factor for canonical TGF β to activate EMT in AV valve development [17]. However, there has been no direct assessment on the mechanosensitivity of YAP to shear stress in the context of valve endocardial cells.

Further, while there has been exploration of the responses of YAP1 to flow in endothelial cells [18], the relationship between the flow profile, namely magnitude and waveform, and a YAP response is unclear.

Current data on the responsiveness of embryonic endothelial cells to shear stress does not explore the axes of magnitude and frequency and, instead, has focused on whole flow field responses either *in vivo* or in whole cushion explants [19], [20]. However, it has been established that shear stress mechanosensitivity can have a non-linear behavior, resulting in optimal values of shear stress magnitude for EMT induction [2]. Therefore, there is a need to interrogate how flow magnitude and frequency, which define a shear stimulus, each contribute to a biological response in a complex, *in vivo* flow environment. Systems level signaling models can be used to infer how such complex behavior can emerge from the intersection of multiple signals [21]. Principally, signaling models can provide an understanding of how inductive and inhibitor pathways interact to achieve a quantitative balance leading to an optimal response range of a given magnitude [3]. Here, we were able to predict and verify novel EMT phenotypes and their underlying signaling pathways using a hybrid ODE-rule-based model in the context of cancer biology [3].

In this work, we set out to establish the relationship between different shear stress modes and EMT in AV cushion endothelial cells. We established that AV endothelial cells are sensitive to shear stress in two modes, one inductive and one repressive, depending on the type and magnitude of the flow applied. Through computational modeling and *in vitro* experiments, we identified YAP1 and PECAM as upstream signals that are involved in shear stress EMT transcriptional regulation.

5.3 Methods

5.3.1 Model identification

YAP1 is a mechanosensitive transcription factor that is becoming of increasing interest for its roles in organ size regulation, tumor formation and developmental processes [22]–[24]. Recently, YAP1 was identified as required for endothelial EMT in chick, acting to enable snail/slug transcriptional activity at the E-cadherin promoter [25]. This was particularly impactful as this introduced YAP1 as a key player in what was thought to be well understood pathway of BMP to TGF β induced EndMT [12]. YAP1 signaling has also been shown to be downstream of Rho/ROCK during responses to varied substrate stiffnesses [22], [26]. Therefore, we hypothesized that YAP1 would be activated in a ROCK dependent manner. Shear stress has been shown to signal through PECAM (CD31) through tension created between VE-cadherin and PECAM-1 [27]. We therefore hypothesized that the role of PECAM was to stabilize the endothelial state in the presence of shear stress and that its upregulation and subsequent increase in number would increasingly drive a suppressive effect. This approach was supported by the ability for PECAM to phosphorylate Akt in response to shear stress [28], which in turn can regulate sequestration of YAP1 on 14-3-3 via phosphorylation of YAP1 [29]. With these insights and assumptions from the literature, we arrived at the hypothetical YAP1 model shown in Figure 5.1.

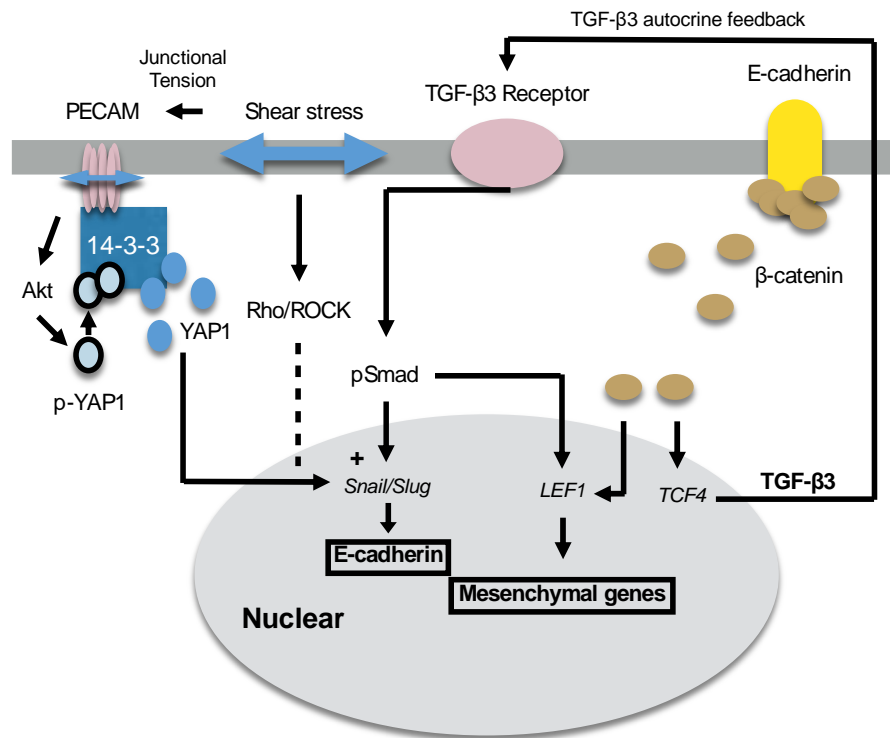


Figure 5.1. YAP1/ROCK/PECAM shear stress signaling network

5.3.2 Modeling Approach

After model identification from the literature in the background section, the following modifications were made to our previous EMT model in Chapter 3 [3]. First, TGFβ12 signaling was linked to pSmad2/3 activation, as opposed to the MAPK activation pathway seen in the cancer cell systems. New species were then added to the model. YAP1 regulation: PECAM(CD31), 14-3-3, Akt, p-Akt, YAP1, p-YAP1, RhoAGTP, ROCK. Mechanical signaling: Frequency and magnitude of shear stress

profile. The frequency and magnitude were related to the YAP1 activation and YAP1 inhibition by a transfer function with the following functional form:

$$f(M, F) = k * M^a * b^{-F}$$

where $M = \text{magnitude}$, $F = \text{frequency}$ $k = \text{gain}$, $a = \text{magnitude scale parameter}$,
 $b = \text{frequency scale parameter}$

which is then assembled as

$$T = \frac{f(M, F)}{K - f(M, F)}$$

where K is the saturation constant

The transfer function was designed to provide a functional form that could encode steady state ($F=0$) and oscillatory flows ($F>0$), and which would give no signal for no flow ($M=0$). Activators directly correlate with the transfer function, while inhibitors correlate to the reciprocal, since inhibitors which are off have a transfer function value of 1. Figure 5.2 shows the behavior of the shear stress transfer functions under OSC and LLS loading modes across a range of shear stress magnitudes for the parameterization used during simulations.

Incorporating qPCR readouts as training data was a challenge since fold changes from very small or near zero concentrations of species can make it difficult to capture control states with no stimuli. To accomplish this, a characteristic minimum

concentration of mRNA species was assumed on a species by species basis for PECAM, Slug and TGF β 3.

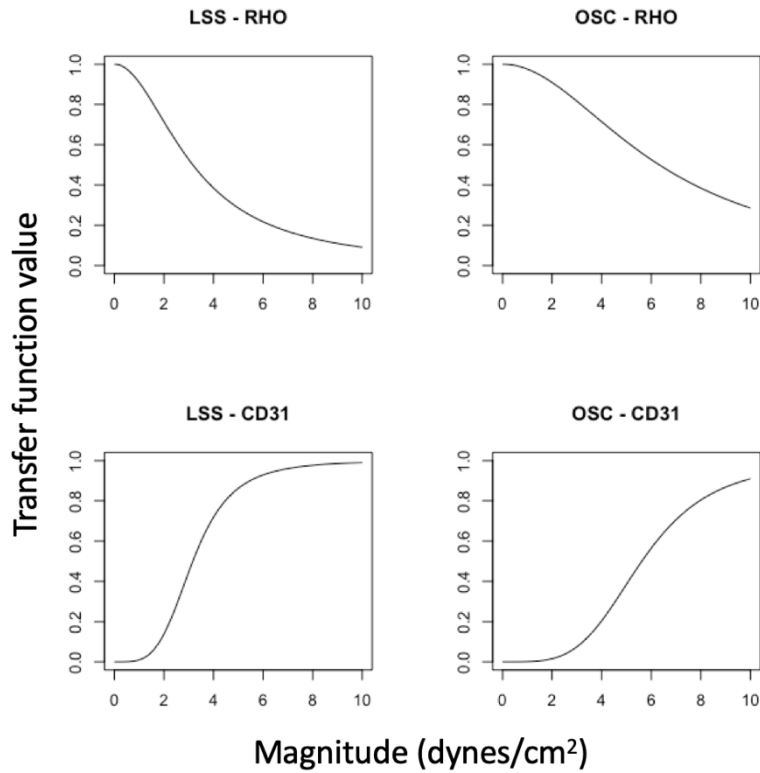


Figure 5.2. Mechanotransduction transfer function behaviors for different shear modes. Shown as applied to RhoA activation or CD31 (PECAM) transcriptional activation RhoA: $a=2$, $k=1$, $b=4$, $K=10$; CD31: $a=4$, $k=0.1$, $b=10$, $K=10$

The new model contains 119 species. JuPOETs as published and in Chapter 4 was used as the parameter optimization technique [30]. The model generated in Chapter 3 was adapted to contain the above model components, requiring the above new transfer functions as well as reactions governing the transcription, translation,

activation and deactivation of new species [3]. Model code can be found at https://github.com/dbassen/emt_gen_3.

5.3.3 Experimental methods

Flow reactor experiments

Shear stress experiments were performed using embryonic endocardial AV patches isolated from HH14 and HH16 chicken embryos which have been used to study induction and inhibition of EMT respectively [31]. A novel shear stress bioreactor system was used to apply shear stresses of varying magnitudes in combination with a syringe pump (oscillatory) or a peristaltic pump (steady-state) [2]. Oscillatory set up is shown in Figure 5.3. Assembly protocol is in Appendix E.

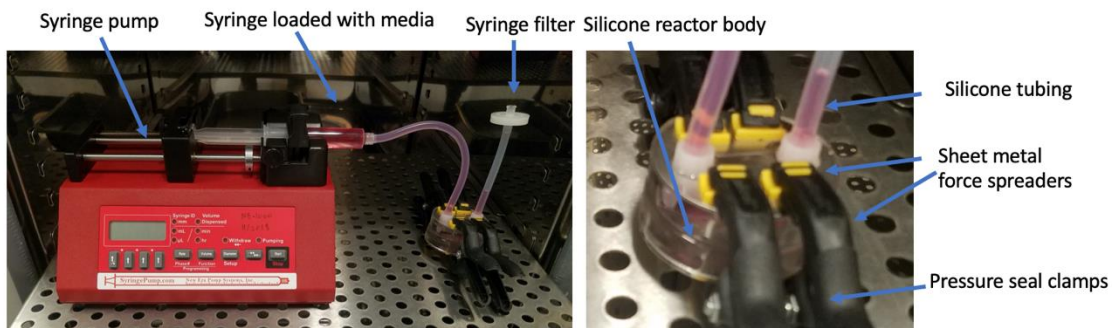


Figure 5.3. Bioreactor experimental set up in incubator

Immunofluorescence for protein expression and activity

Patches were fixed in place in 4% PFA for 60 minutes at 4°C, permeabilized with 0.02% triton-x and blocked using 3% BSA, 20mM MgCl, 0.3% Tween 20, 0.3M Glycine, and 5% Donkey serum in 1xTBS. Samples were incubated with the following primary antibodies at 1:100 dilution unless noted: YAP1 (mouse or rat, Santa Cruz),

alpha-smooth-muscle-actin-cy3 conjugated (Mouse, Sigma), RhoA-GTP (Mouse, Cell Signaling), Rac1-GTP (Mouse, Cell Signaling), pERK (Rabbit, Cell Signaling), pSmad2/3 (Rabbit, Cell Signaling), pSmad1/5 Cell Signaling, pSER19 on myosin light chain kinase (Rabbit, 1:50, Thermo-Scientific). Antibodies requiring amplification (YAP) were also incubated in 1% H₂O₂ in PBS for 40 minutes, stained with HRP secondaries and incubated using a TSA kit. Secondary antibodies were applied in 5% BSA in TBS.

Stained patches were imaged using a 20x dipping lens with TBS buffer on an upright Zeiss LSM 880 microscope.

Statistical comparisons were made using two-way t-tests and Wilcoxon-Mann-Whitney non-parametric tests.

5.4 Results

We applied a range of shear stress profiles to endocardial patches from HH14 quail embryos. We applied both steady-state (SS) and oscillatory (OSC) flows, at 3 magnitudes corresponding to average shear stress levels from early to mid-stages of development [32]. For SS flows, 1 dyne/cm² was the modestly inductive, leading to a 15-fold increase in Slug expression but with no increase in TGFβ3 transcription (Figure 5.4A). Mid to high magnitudes led to no significant increase in Slug or TGFβ3, but instead led to increased PECAM expression. For OSC flows, 1 dyne/cm²

was the most inductive condition, as it led to a 100+ fold increase in Slug expression, as well as a significant increase in TGFβ3 expression. An OSC flow at 5 dyne/cm² was still able to induce Slug but led to only a modest increase in TGFβ3 transcription. The high 10 dyne/cm² OSC condition showed similar behavior to the mid to high SS conditions, with increased PECAM expression and no increases in Slug or TGFβ3 (Figure 5.4B).

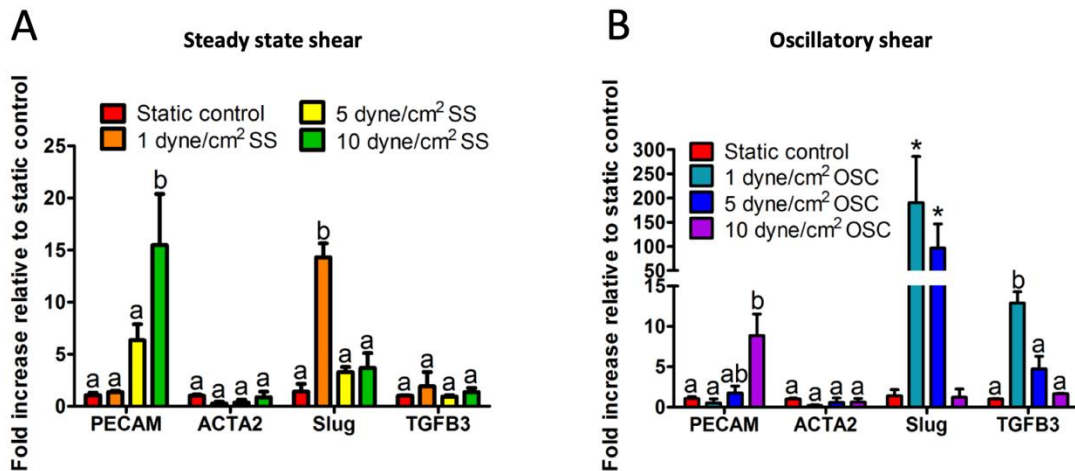


Figure 5.4. Gene expression data showing activation of EMT related genes in response to different shear conditions. Fold change in EMT gene expression values found from embryonic exposed to (A) steady state shear and (B) oscillatory shear in a flow bioreactor for 48hrs. n= 3-4 patches per condition, SD shown

The shear-YAP1 model trained on the gene expression data (Figure 5.4) objectives using POETs across the 7 experimental conditions (static, OSC and LSS over 3 magnitudes) was able to recapitulate the general trends of the gene expression data at 48hrs (Figure 5.5). The model struggled to capture the sensitivity of TGFβ signaling to inhibition by high magnitude and frequency conditions and could not capture the order of magnitude jump in fold change by snail/slug in the oscillatory condition.

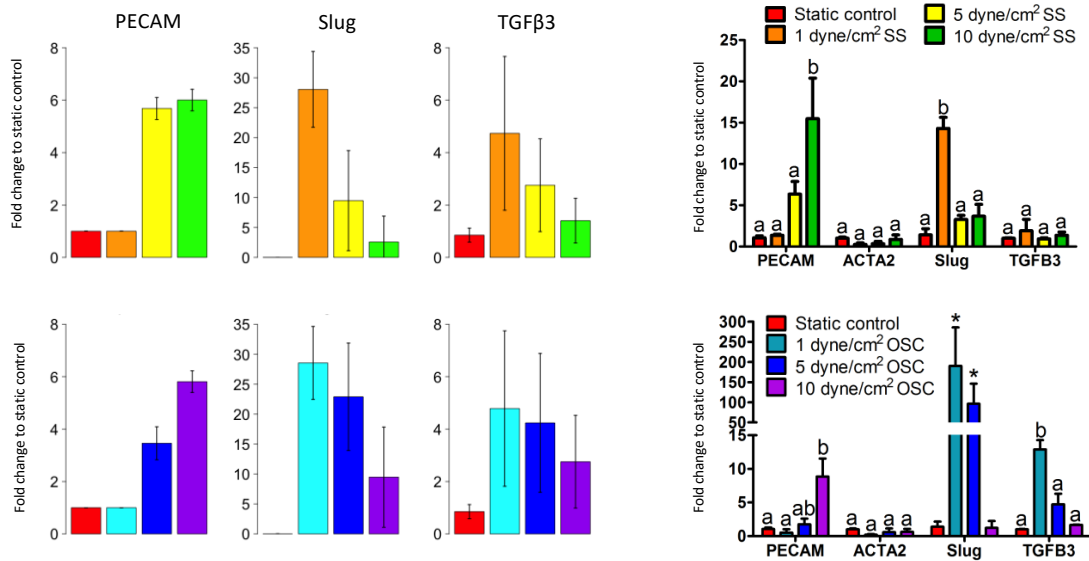


Figure 5.5. Comparison of model fit to gene expression data. Fold change values generated by model (left 6 plots) Fold change values found from patches in flow bioreactor at 48hrs (right two plots) Error bars represent variability between models in the ensemble

The model simulated the objectives while conforming to a YAP1 driven mechanism where YAP nuclear translocation is the primary driver of an EMT phenotype (low E-cadherin) (Figure 5.6). The model predicted that elevated PECAM expression and subsequent YAP sequestration would drive down YAP nuclear translocation (Figure 5.6.). The signaling model predicted deactivation of RhoA-GTP in the OSC condition (Figure 5.6), which was counter intuitive given the role of YAP in matrix mechanotransduction.

YAP1 nuclear localization increased from the static control for both the 1 OSC (Figure 5.7) condition and 10 LSS condition (Figure 5.8). RhoA activity decreased in the 1 OSC condition as quantified by area per cell from RhoA-GTP stain from $51.5 \pm 16.4 \mu\text{m}^2/\text{cell}$ to $8.35 \pm 6.35 \mu\text{m}^2/\text{cell}$ (Figure 5.9), verifying the prediction by the model.

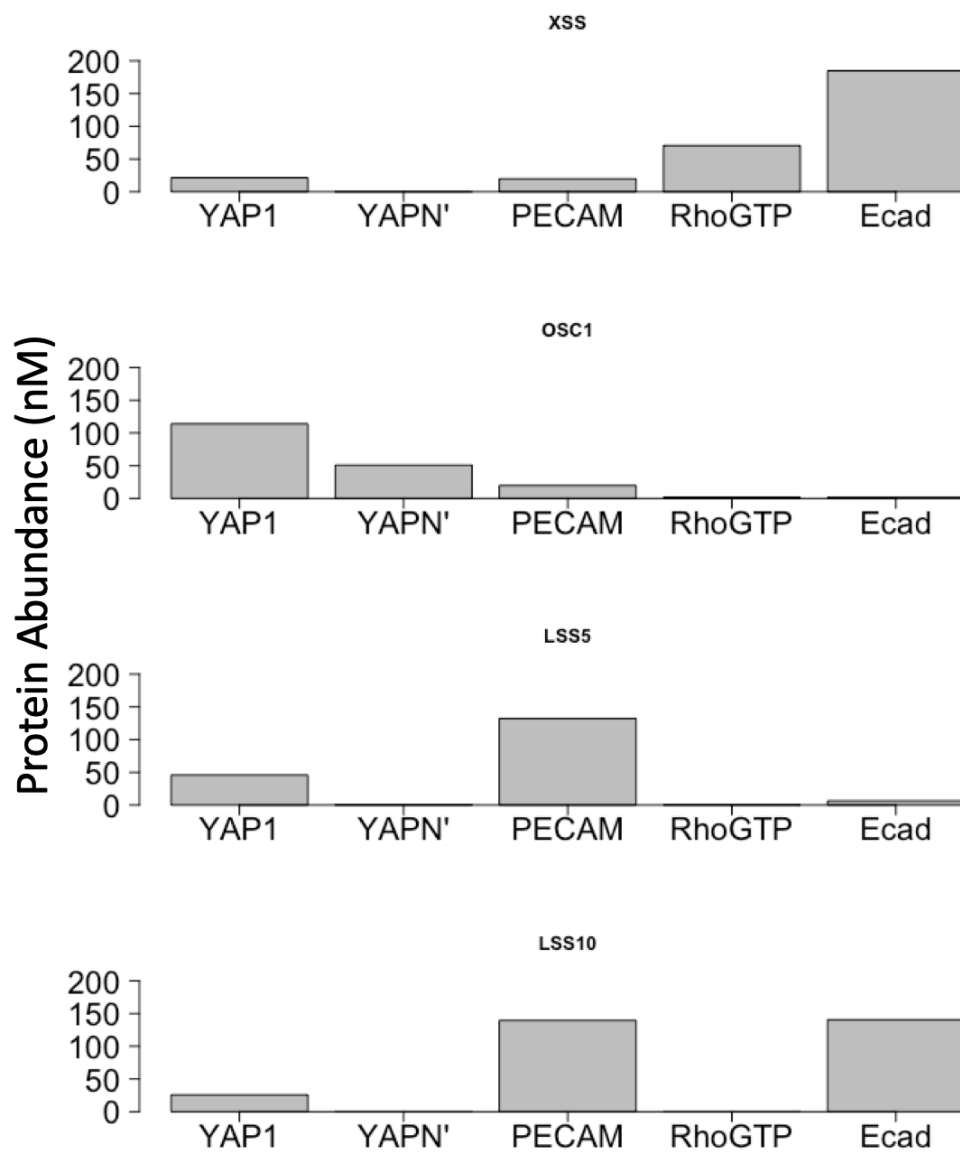


Figure 5.6. Predictions for abundances of YAP1, Nuclear YAP1 (YAPN'), PECAM, RhoGTP, and E-cadherin (Ecad) for a single parameter set at from the hand fit model used to generate ensemble

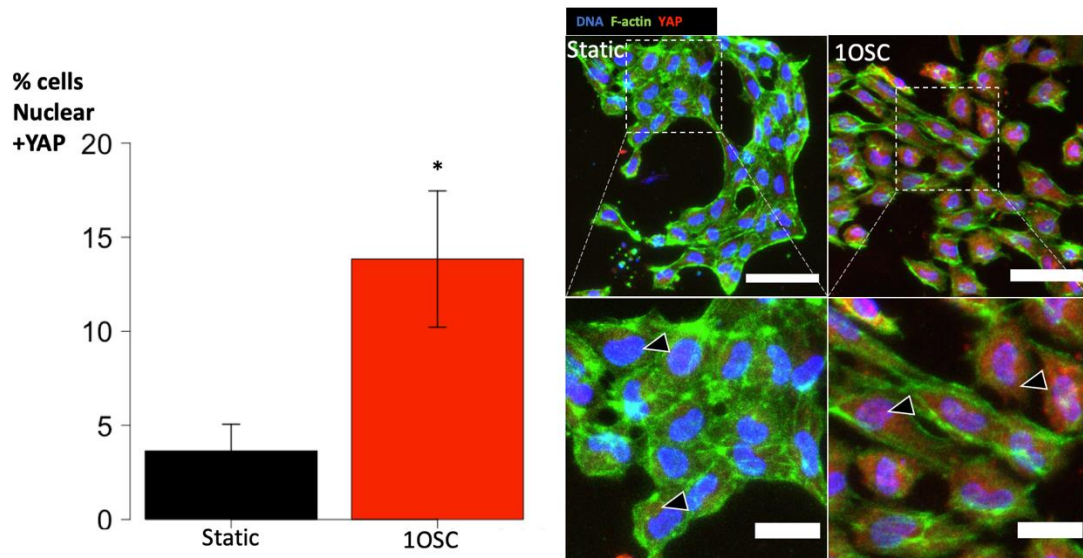


Figure 5.7. YAP1 nuclear translocation increases with 1 dyne/cm² OSC stimulation. Percent cells YAP1 positive in the nucleus (left). Immunofluorescence images of endocardial patches with nuclear quantification of YAP1 (right) Arrows point to cytoplasmic and nuclear areas of no YAP signal (static) and YAP signal (10SC). $p < 0.05$, $n=3-4$ patches, SD shown

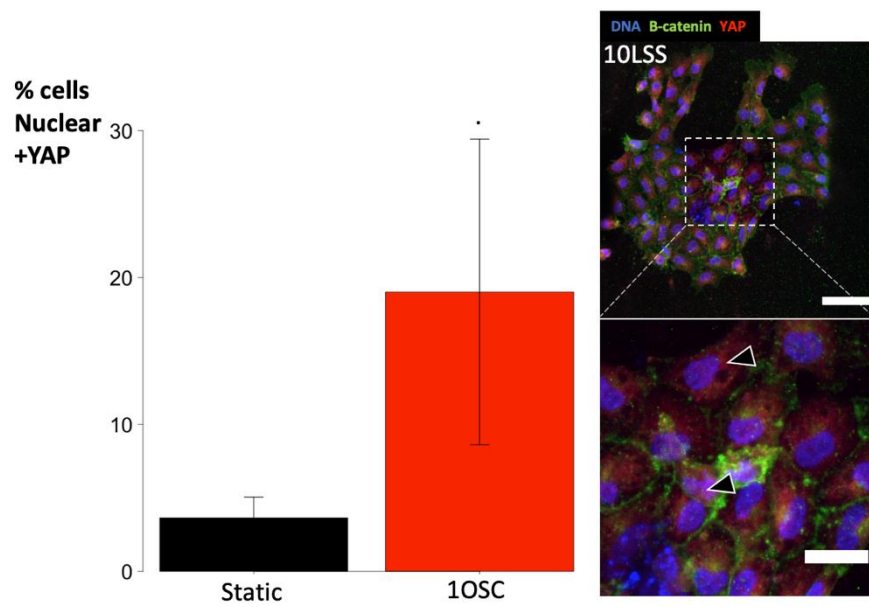


Figure 5.8. YAP1 nuclear translocation increases with 10 dyne/cm² LSS stimulation. Percent cells YAP1 positive in the nucleus (left) Immunofluorescence images of endocardial patches stained for YAP1 (right). Arrows indicate nuclear and cytoplasmic YAP signal . $p < 0.07$ $n=3-4$ patches, SD shown

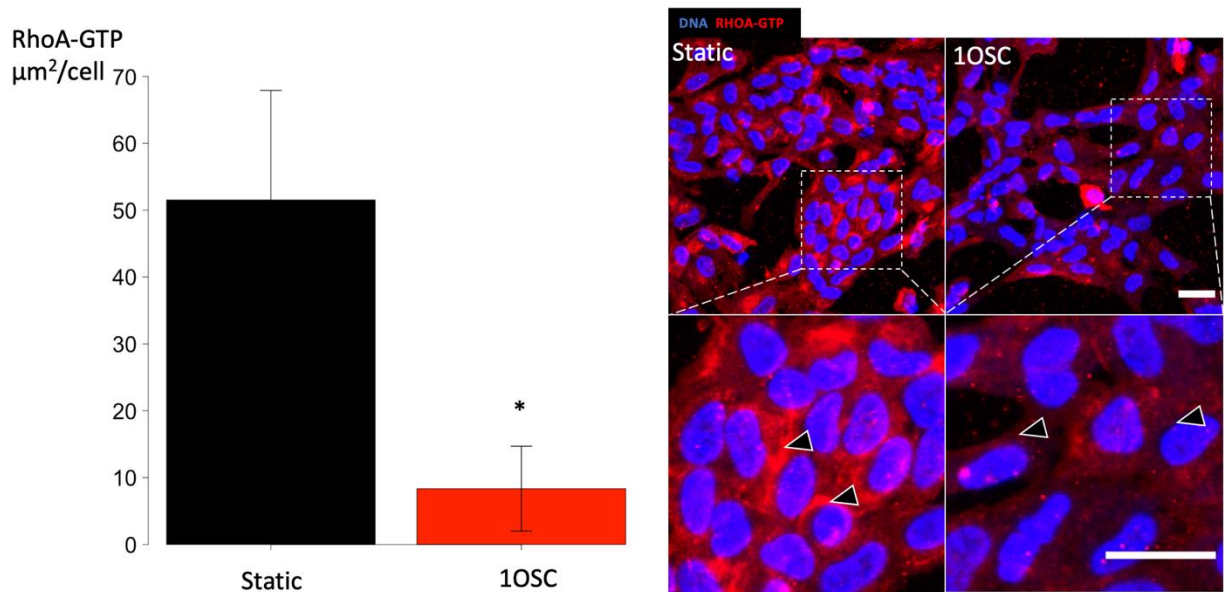


Figure 5.9. RhoA activity as measured by stained area per cell. RhoA activity decreases with 1 dyne/cm² OSC stimulation * $p < 0.05$, $n=3$ patches per group. Arrows show locations of cytoplasmic or perinuclear expression, either high or low in the static or OSC conditions respectively

5.5 Discussion

Endothelial to mesenchymal transition is a key initiating step in valvulogenesis and is the sole source of valve interstitial cells in the septal AV leaflets [6].

Insufficient EMT leads to stunted valves, improper AV septation, and often embryonic lethality [8]. Prolonged and excessive EMT can lead to hypertrophic valves and a compromised valve endothelium that cannot grow to meet the increasing surface area of the growing valve [33]. Therefore, determining the mechanisms by which EMT can be precisely controlled in time and extent is critical to understanding defects of the valve and valve apparatus. Further, evidence has grown supporting the interaction of mechanical signals with pathways central to developmental EMT such as YAP1 in TGF β Smad2/3 to snail/slugg transcription [17] and in the ciliary aggregation TGF β receptors to activate Smad2/3 and ERK transcription [34]. Wall-shear stress is a

complex signal that evolves rapidly during development and that has shown to be a regulator of EMT in adult porcine valves [2]. In this study, we set out to establish the responsiveness of endocardial valve cells to differing modes of shear stress and to identify underlying signaling pathways to explain this behavior. We found that HH14 and HH16 endothelial cells were transcriptionally sensitive to both LSS and OSC shear stress (Figure 5.4). Specifically, we found that low (1 dyne/cm²) levels of oscillatory shear stress induced EMT, while a high magnitude (10 dyne/cm²) of laminar steady shear flow stimulated PECAM, which represents an anti-EMT response [27]. Overall, we identified a non-linear/quadratic response to the shear stress magnitude in which low magnitudes are inductive and high magnitudes are repressive of EMT. Interestingly, this behavior has been reported in adult porcine valve cells [2] and in human bone marrow stem cells [35], supporting that a “sweet spot” of shear stress magnitude is a conserved feature of shear stress signal transduction. These optimal stimulus ranges occur at different magnitudes depending on the cell type and adult or developmental contexts. Therefore, it is important to identify the underlying signaling landscapes that define these optimal stimulus ranges.

Preliminary exploration of the YAP/shear model suggests that differential YAP1 signaling may play a role in manifesting the quadratic shear stress response in the context valvulogenesis (Figure 5.5). Since other signals through KLF2 [35] and BMP [36] are also implicated in a quadratic shear response, one hypothesis is that differential regulation across these pathways causes an overall non-linear response. It is however unclear if these pathways can produce the same shear responsiveness in isolation. If signaling elements can be identified that correlate more strongly with

either frequency or magnitude of the signal, then the functional form used in the model could be simplified to apply frequency or magnitude exclusively to only a specific signaling element. This would have the advantage of allowing the quadratic response to shear stress to emerge from the data, rather than being enforced by the function form. While YAP1 nuclear translocation appeared to be increased in both activating (1 OSC) (Figure 5.7) and inhibitory (10 LSS) (Figure 5.8) shear levels, there is also the potential for higher YAP1 expression in the OSC condition, in addition to higher nuclear localization. These conditions were predicted by the model even though the YAP1 nuclear species was near zero (Figure 5.6). YAP1 expression has been found to also vary, in addition to nuclear localization, under differing mechanical loads [37]. While RhoA activity was expected to correlate with YAP1, this expectation was from a static context [22]. Interestingly, our model predicted a drop in RhoA-GTP activity in response to shear stress (Figure 5.6), where we would have expected an increase that would correlate with YAP1 nuclear localization [26]. We confirmed this prediction by observing a reduction in RhoA activity in the 1 OSC with increased YAP1 activation (Figure 5.9). Assuming that YAP1 translocation in this system is caused directly by a mechanical stimulus, two candidate sources of stress to cause YAP1 nuclear translocation are (1) the external shear forces directly or (2) Rac1 activity which tends to inversely relate to RhoA activity [38]. Rac1 can interact with $\beta 1$ integrin to activate PAK-LATS and dephosphorylate YAP1, allowing for YAP1 cytoplasmic release and nuclear shuttling [39]. A Rac1 mediated 14-3-3 sequestration mechanism be added to work in parallel of the proposed PECAM-Akt mechanism in the current model. Rac1 can also alter which co-transcription factors that YAP1 can

bind to in the nucleus [40]. There may also be a temporal difference in Rho-ROCK expression. In cancer cells, ROCK-LIMK-YAP1 activation that occurs more immediately (minutes to hours) after shear stress exposure is necessary to induce changes in cell motility [37]. CD44, a primary hyaluronic acid adhesion receptor, can act to promote YAP1 signaling by activating Rho/ROCK [25], supporting a mechanosensitive role for CD44 as an upstream regulator of YAP1 signaling. This may be particularly relevant for valve EMT as the valve mesenchyme is made almost entirely from glycosaminoglycans [41]. It should also be noted that SRC kinases can control YAP nuclear shuttling, TEAD interactions, and nuclear export with known timescales that would be informative for a systems based model [42].

Several other pathways could be incorporated into the modeling framework to help identify the influence of each respective pathway on determining an inductive or repressive response to wall-shear stress in different contexts. In general, it will be necessary to consider carefully whether interactions between pathways will be implemented as integration rules and transfer functions or as more traditional mass action expressions. The primary cilium of an endothelial cell is a primary sensing and signaling organelle that sits on the apical side of the cell. In response to shear stress, primary cilia have been shown to be directly connected to TGF β -induced EMT, though the relationship between shear profile and the effect remains unclear [14]. However, loss of the of primary cilium seems to enable or “prime” TGF β -induced EMT [43]. Primary cilium can also activate TGF β signaling through SMAD2/3 [44] whereas stunted cilia lost this effect [34], suggesting that intact cilia may also to initiate an EMT signaling response. Further, cilia are temporally regulated in valve

development to coincide with phases of EMT and ablation of ciliary signaling leads to myxomatous mitral valve disease and prolapse [45]. KLF2 is a transcription factor responsive to oscillatory shear stress that can regulate key regulatory proteins in valve development [15]. It is a regulator downstream of TGF β /Alk5 signaling which is also upstream of MEK-ERK, making it a consequence of non-canonical TGF β /MAPK signaling [46]. Interestingly, data in human HBMCs show a quadratic response similar to the gene expression data shown in Figure 4 that is dependent on KLF2 [35]. This same study uses oscillatory shear index (OSI) developed by [47] to compare shear stress exposure between CFD simulations, *in vitro* results, and *in vivo* benchmarks, which may be useful as an additional way to represent shear stress as an input [35]. However, using OSI can make it more difficult to compare to results presented as magnitudes and modes (e.g. 5 dyne/cm² OSC).

KLF2 expression in the endothelium has been shown to activate WNT in the underlying MSCs Zebrafish [19]. With *klf2* KO, decreased WNT correlated with a thickened valves [19]. In human umbilical vein endothelial cells and porcine aortic endothelial cells, shear stress induces endothelial-to-mesenchymal transition via the transcription factor Snail/Slug and *klf2* [48]. Additionally, chick *klf2* primers are readily attainable for gene expression analysis contains [31]

The relationship that *klf2* has with TGF, BMP, MAPK, and AP1/SP1 pathways make it an ideal candidate for further exploration. Additionally, the papers cited above contain relative protein and gene expression data that could be used to train a baseline

model to predict dosing and inhibitor concentration requirements for *in vitro* experiments.

It may also be useful in the future to consider data from other organ systems exposed to shear stress including the lymphatic system, which also contains valves, the renal system, which is exposed to both shear and osmotic stresses, and the [49], [50]. YAP1 is a mechanosensor at cadherin junctions in mouse vascular endothelial cells [16]. In lymphatic valves, *Foxc2*, drives endothelial stability in response to oscillatory stress [49], [51]. *Klf2* can also be seen acting in venous endothelial cells and in the lymphatic endothelium [52].

Overall, we have shown that developmental valve EndMT can be both induced and repressed via shear stress through $TGF\beta$ transcription. The complementary *in vitro* and *in silico* tools that we have developed will allow for the integration of tissue scale biomechanical loads and cellular signals to determine predict spatially distinct tissue development.

5.6 References

- [1] A. von Gise and W. T. Pu, “Endocardial and epicardial epithelial to mesenchymal transitions in heart development and disease.,” *Circ. Res.*, vol. 110, no. 12, pp. 1628–45, Jun. 2012.
- [2] G. J. Mahler, C. M. Frenzl, Q. Cao, and J. T. Butcher, “Effects of shear stress pattern and magnitude on mesenchymal transformation and invasion of aortic valve endothelial cells.,” *Biotechnol. Bioeng.*, vol. 111, no. 11, pp. 2326–37, Nov. 2014.
- [3] R. Gould, D. Bassen, A. Chakrabarti, J. Varner, and J. Butcher, “Population heterogeneity in the epithelial to mesenchymal transition is controlled by NFAT and phosphorylated Sp1,” *bioRxiv*, Oct. 2016.
- [4] S. Dupont, “Role of YAP/TAZ in cell-matrix adhesion-mediated signalling and mechanotransduction,” *Exp. Cell Res.*, vol. 343, no. 1, pp. 42–53, 2015.
- [5] A. Elosegui-Artola *et al.*, “Force Triggers YAP Nuclear Entry by Regulating Transport across Nuclear Pores,” *Cell*, vol. 171, no. 6, pp. 1397-1410.e14, 2017.
- [6] C.-J. Lin, C.-Y. Lin, C.-H. Chen, B. Zhou, and C.-P. Chang, “Partitioning the heart: mechanisms of cardiac septation and valve development.,” *Development*, vol. 139, no. 18, pp. 3277–99, Sep. 2012.
- [7] D. Lambrechts and P. Carmeliet, “Genetics in Zebrafish, Mice, and Humans to Dissect Congenital Heart Disease: Insights in the Role of VEGF,” *Curr. Top. Dev. Biol.*, vol. 62, pp. 189–224, 2004.
- [8] M. Azhar *et al.*, “Ligand-specific function of transforming growth factor beta in epithelial-mesenchymal transition in heart development,” *Dev. Dyn.*, vol. 238, no. 2, pp. 431–442, 2009.
- [9] S. J. Conway, T. Doetschman, and M. Azhar, “The Inter-Relationship of Periostin , TGF β , and BMP in Heart Valve Development and Valvular Heart Diseases,” pp. 1509–1524, 2011.
- [10] K. Balachandran *et al.*, “Cyclic strain induces dual-mode endothelial-mesenchymal transformation of the cardiac valve.,” *Proc. Natl. Acad. Sci. U. S.*

A., vol. 108, no. 50, pp. 19943–8, Dec. 2011.

- [11] D. S. Micalizzi, S. M. Farabaugh, and H. L. Ford, “Epithelial-mesenchymal transition in cancer: parallels between normal development and tumor progression,” *J. Mammary Gland Biol. Neoplasia*, vol. 15, no. 2, pp. 117–34, Jun. 2010.
- [12] J. Xu, S. Lamouille, and R. Derynck, “TGF-beta-induced epithelial to mesenchymal transition,” *Cell Res.*, vol. 19, no. 2, pp. 156–172, 2009.
- [13] S. Maleki *et al.*, “Mesenchymal state of intimal cells may explain higher propensity to ascending aortic aneurysm in bicuspid aortic valves,” *Sci. Rep.*, vol. 6, no. June, pp. 1–16, 2016.
- [14] P. Dijke, A. D. Egorova, M. T. H. Goumans, R. E. Poelmann, and B. P. Hierck, “TGF- b Signaling in Endothelial-to- Mesenchymal Transition : The Role of Shear Stress and Primary Cilia,” *Sci. Signal.*, vol. 5, no. 212, pp. 1–3, 2012.
- [15] J. Vermot *et al.*, “Reversing blood flows act through klf2a to ensure normal valvulogenesis in the developing heart,” *PLoS Biol.*, vol. 7, no. 11, pp. 12–14, Nov. 2009.
- [16] H. J. Choi *et al.*, “Yes-associated protein regulates endothelial cell contact-mediated expression of angiopoietin-2,” *Nat. Commun.*, vol. 6, no. May, pp. 1–14, 2015.
- [17] H. Zhang *et al.*, “Yap1 is required for endothelial to mesenchymal transition of the atrioventricular cushion,” *J. Biol. Chem.*, vol. 289, no. 27, pp. 18681–92, Jul. 2014.
- [18] H. Nakajima and N. Mochizuki, “Flow pattern-dependent endothelial cell responses through transcriptional regulation,” *Cell Cycle*, vol. 16, no. 20, pp. 1893–1901, 2017.
- [19] L. M. Goddard *et al.*, “Hemodynamic Forces Sculpt Developing Heart Valves through a KLF2-WNT9B Paracrine Signaling Axis,” *Dev. Cell*, vol. 43, no. 3, pp. 274-289.e5, 2017.
- [20] T. Banjo *et al.*, “Haemodynamically dependent valvulogenesis of zebrafish heart is mediated by flow-dependent expression of miR-21,” *Nat. Commun.*, vol. 4, no. May, p. 1978, Jan. 2013.

- [21] R. a. Gould, L. M. Aboulmouna, J. D. Varner, and J. T. Butcher, “Hierarchical approaches for systems modeling in cardiac development,” *Wiley Interdiscip. Rev. Syst. Biol. Med.*, vol. 5, no. 3, p. n/a-n/a, 2013.
- [22] S. Dupont *et al.*, “Role of YAP/TAZ in mechanotransduction,” *Nature*, vol. 474, no. 7350, pp. 179–184, 2011.
- [23] B. C. Low, C. Q. Pan, G. V. Shivashankar, A. Bershadsky, M. Sudol, and M. Sheetz, “YAP/TAZ as mechanosensors and mechanotransducers in regulating organ size and tumor growth,” *FEBS Lett.*, vol. 588, no. 16, pp. 2663–2670, 2014.
- [24] T. Moroishi, C. G. Hansen, and K. L. Guan, “The emerging roles of YAP and TAZ in cancer,” *Nat. Rev. Cancer*, vol. 15, no. 2, pp. 73–79, 2015.
- [25] Y. Zhang *et al.*, “CD44 acts through RhoA to regulate YAP signaling,” *Cell. Signal.*, vol. 26, no. 11, pp. 2504–13, Nov. 2014.
- [26] S. C. Wei *et al.*, “Matrix stiffness drives epithelial–mesenchymal transition and tumour metastasis through a TWIST1–G3BP2 mechanotransduction pathway,” *Nat. Cell Biol.*, vol. 17, no. 5, pp. 678–688, 2015.
- [27] D. E. Conway and M. A. Schwartz, “Mechanotransduction of shear stress occurs through changes in ve-cadherin and pecam-1 tension: Implications for cell migration,” *Cell Adhes. Migr.*, vol. 9, no. 5, pp. 335–339, 2015.
- [28] I. Fleming, B. Fisslthaler, M. Dixit, and R. Busse, “Role of PECAM-1 in the shear-stress-induced activation of Akt and the endothelial nitric oxide synthase (eNOS) in endothelial cells,” *J. Cell Sci.*, vol. 118, no. 18, pp. 4103–4111, 2005.
- [29] S. Basu, N. F. Totty, M. S. Irwin, M. Sudol, and J. Downward, “Akt phosphorylates the Yes-associated protein, YAP, to induce interaction with 14-3-3 and attenuation of p73-mediated apoptosis,” *Mol. Cell*, vol. 11, no. 1, pp. 11–23, 2003.
- [30] D. Bassen, M. Vilkhovoy, M. Minot, J. T. Butcher, and J. D. Varner, “JuPOETs : A Constrained Multiobjective Optimization Approach to Estimate Biochemical Model Ensembles in the Julia Programming Language
Corresponding author :,” no. 607, 2016.
- [31] K. L. Pang, M. Parnall, and S. Loughna, “Effect of altered haemodynamics on

- the developing mitral valve in chick embryonic heart,” *J. Mol. Cell. Cardiol.*, vol. 108, pp. 114–126, 2017.
- [32] H. C. Yalcin, A. Shekhar, T. C. McQuinn, and J. T. Butcher, “Hemodynamic patterning of the avian atrioventricular valve,” *Dev. Dyn.*, vol. 240, no. 1, pp. 23–35, Jan. 2011.
- [33] K. Stankunas, G. K. Ma, F. J. Kuhnert, C. J. Kuo, and C. P. Chang, “VEGF signaling has distinct spatiotemporal roles during heart valve development,” *Dev. Biol.*, vol. 347, no. 2, pp. 325–336, 2010.
- [34] C. Clement *et al.*, “TGF- β Signaling Is Associated with Endocytosis at the Pocket Region of the Primary Cilium,” *Cell Rep.*, vol. 3, no. 6, pp. 1806–1814, 2013.
- [35] A. Williams, S. Nasim, M. Salinas, A. Moshkforoush, N. Tsoukias, and S. Ramaswamy, “A ‘sweet-spot’ for fluid-induced oscillations in the conditioning of stem cell-based engineered heart valve tissues,” *J. Biomech.*, vol. 65, pp. 40–48, 2017.
- [36] J. Zhou, Y.-S. Li, and S. Chien, “Shear Stress-Initiated Signaling and Its Regulation of Endothelial Function,” *Arterioscler. Thromb. Vasc. Biol.*, vol. 34, no. 10, pp. 2191–2198, 2014.
- [37] H. J. Lee *et al.*, “Fluid shear stress activates YAP1 to promote cancer cell motility,” *Nat. Commun.*, vol. 8, 2017.
- [38] R. A. Gould *et al.*, “Cyclic Mechanical Loading Is Essential for Rac1-Mediated Elongation and Remodeling of the Embryonic Mitral Valve,” *Curr. Biol.*, vol. 26, no. 1, pp. 27–37, 2016.
- [39] H. Sabra *et al.*, “ β 1 integrin-dependent Rac/group I PAK signaling mediates YAP activation of Yes-associated protein 1 (YAP1) via NF2/merlin,” *J. Biol. Chem.*, vol. 292, no. 47, pp. 19179–19197, 2017.
- [40] J. W. Jang *et al.*, “RAC-LATS1/2 signaling regulates YAP activity by switching between the YAP-binding partners TEAD4 and RUNX3,” *Oncogene*, vol. 36, no. 7, pp. 999–1011, 2017.
- [41] J. T. Butcher, R. a. Norris, S. Hoffman, C. H. Mjaatvedt, and R. R. Markwald, “Periostin promotes atrioventricular mesenchyme matrix invasion and remodeling mediated by integrin signaling through Rho/PI 3-kinase,” *Dev.*

Biol., vol. 302, no. 1, pp. 256–266, 2007.

- [42] N. Ege *et al.*, “Quantitative Analysis Reveals that Actin and Src- Family Kinases Regulate Nuclear YAP1 and Its Export Article Quantitative Analysis Reveals that Actin and Src-Family Kinases Regulate Nuclear YAP1 and Its Export,” *Cell Syst.*, vol. 6, no. 6, pp. 692-708.e13, 2018.
- [43] A. D. Egorova *et al.*, “Lack of primary cilia primes shear-induced endothelial-to-mesenchymal transition,” *Circ. Res.*, vol. 108, no. 9, pp. 1093–1101, 2011.
- [44] K. Koefoed, I. R. Veland, L. B. Pedersen, L. A. Larsen, and S. T. Christensen, “Cilia and coordination of signaling networks during heart development,” *Organogenesis*, vol. 10, no. 1, pp. 108–125, 2014.
- [45] K. A. Toomer *et al.*, “Primary cilia defects causing mitral valve prolapse,” *Sci. Transl. Med.*, vol. 11, no. 493, 2019.
- [46] A. D. Egorova *et al.*, “Tgf β /Alk5 signaling is required for shear stress induced klf2 expression in embryonic endothelial cells.,” *Dev. Dyn.*, vol. 240, no. 7, pp. 1670–80, Jul. 2011.
- [47] D. N. Ku, D. P. Giddens, C. K. Zarins, S. Glagov, and M. A. Y. June, “Pulsatile Flow and Atherosclerosis in the Human Carotid Bifurcation Positive Correlation between Plaque Location and Low and Oscillating Shear Stress,” *ARTERIOSCLEROSIS*, 1985.
- [48] M. M. Mahmoud *et al.*, “Shear stress induces endothelial-To-mesenchymal transition via the transcription factor Snail,” *Sci. Rep.*, vol. 7, no. 1, pp. 1–12, 2017.
- [49] A. Sabine *et al.*, “FOXC2 and fluid shear stress stabilize postnatal lymphatic vasculature,” *J. Clin. Invest.*, vol. 125, no. 10, pp. 3861–3877, 2015.
- [50] S. J. Kunnen *et al.*, “Fluid shear stress-induced TGF- β /ALK5 signaling in renal epithelial cells is modulated by MEK1/2,” *Cell. Mol. Life Sci.*, vol. 74, no. 12, pp. 2283–2298, 2017.
- [51] J. Kazenwadel *et al.*, “GATA2 is required for lymphatic vessel valve development and maintenance,” *J. Clin. Invest.*, vol. 125, no. 8, pp. 2879–2994, 2015.

- [52] G. García-Cardena and B. R. Slegtenhorst, “Hemodynamic Control of Endothelial Cell Fates in Development,” *Annu. Rev. Cell Dev. Biol.*, vol. 32, no. 1, pp. 633–648, 2016.

CHAPTER 6.

CONCLUSIONS AND FUTURE DIRECTIONS

6.1 Conclusions

Around 1% of live births have a congenital heart defect (CHD), resulting in the loss of 200,000 years of productive life [1], [2] By better understanding heart valve development, we as a field can advance both the treatment of pediatric and adult patients. Defects of the heart and heart valve are innately mechanical in nature. In development, we may be able to prevent or to reverse congenital defects by better understanding the physiological range of parameters that allow signaling feedback loops to drive development forward instead of propagating errors. These same insights can help us to understand degenerative valve diseases that involve the reactivation of what should be strictly developmental processes [3].

Normal valve development proceeds in a way that takes an amorphous and symmetric cushion and morphogenically evolves it into thin, fibrous leaflets, and a valvuloseptal apparatus [4]. During this time, a diverse set of mechanical forces is applied to the valve tissue in a material sense, as well as to the surface endothelium and underlying mesenchymal cells [5]. While there is significant evidence that mechanical forces drive valve development, it is still unclear how individual modes of force application, such as shear, stretch and pressures are directly affecting cellular decision making [5]–[7]. It is even less clear how these signals are integrated to perform a full orchestrated, healthy morphogenic process. The ultimate goal of this thesis was to investigate the roles of normal and shear stresses on valvulogenesis while developing new in vitro systems and computational tools to directly assess valve mechanobiology. The completion of this work contributed to insights into the types of mechanical stimuli that can act at various developmental targets and underlying

signaling pathways, which could be used to identify new therapeutic targets and to develop new diagnostics for tracking embryo health *in utero*.

Under compressive stress conditions, AV cushion growth was found to be promoted through a BMP and contractile signaling (Chapter 2). Next, a computational model of epithelial to mesenchymal transition was used to discover new EMT phenotypes and uncover key signaling players (Chapter 3). The optimization method used to fit the EMT models to experimental data, POETs, was published to make the method readily available in the Julia programming language (Chapter 4). These tools and models were then leveraged to test a mechanotransduction hypothesis and to motivate follow-up experiments (Chapter 5). This chapter discusses the major findings of this work while also identifying avenues for the field.

In Chapter 2, we investigated the role of normal-directed forces in regulating valve growth using an osmotic stress system novel in its application to valve development. The hanging-drop osmotic stress system developed can be applied to mechanically load valve primordia from various stages of development in a non-destructive manner conducive to live imaging. Using this system, we demonstrated that compressive stress promoted growth while tensile stress promoted compaction. We further identified BMP signaling as a key signaling pathway activated by osmotic stress that drove the compressive stress response. This result demonstrated that the tissue could respond to compression or tension by compensating with an opposing force. We further explored how different BMP signals and contractility readouts correlated through development of a spatial quantification method for 3D spheroidal tissues. Specifically, we found that the interplay of pSmad15 and MEK-ERK signaling

could regulate tissue compaction through regulation of non-muscle myosin activation. In addressing the morphology of the valves, we found that collagen matrix is critical to maintaining tissue shape under varying levels of mechanically induced remodeling. Hence, cushion and leaflet elongation could be maintained due to increased collagen, even in conditions of added compaction. Additionally, we found that these mechanical loads did not alter the inherent tissues stiffness. On the other hand, previous work has shown TGF β to affect both size and stiffness [8]. This suggests a delineation between BMP and TGF signaling whereby a balance of BMP and TGF may lead to cushions of the precise shapes and sizes for normal development. This work also identified pathways that may be working in parallel with RhoA to regulate growth in the flow field [9]. Recent evidence has suggested that mechanical stress and osmotic stress are inseparably linked [10]. This work is some of the first elucidation on the signaling processes that could be involved in mechano-osmotic stress regulation. In the future, readouts that clearly correspond to the mechanical aspects of osmotic stress, i.e. separate from explicit osmotic balance control, could be used to decouple the complex mechanical effects occurring even during simple uniaxial loading. Lastly, in Appendix C, we leveraged the mechanical testing technique used in this chapter, and the software developed in Appendix D, to address in a diverse set of systems, the mechanical properties of small, viscoelastic living or biofabricated materials.

In Chapter 3, we developed a semi-mechanistic computational model of epithelial to mesenchymal transition which we identified from the cancer biology literature. We predicted and verified the existence of a hybrid population of cells that simultaneously express epithelial and mesenchymal markers. In identifying the model,

we hypothesized that NFATc1 and Ap1/Sp1 were key signaling axis regulating the EMT phenotype. We found that this hypothesis replicated the training data and verified experimentally that the VEG/TGF axes could be independently activated to induce the hybrid phenotype. This phenotype, which allows cells to adhere tightly to each other and to migrate, has now been implicated as a power mechanism of collective migration from a tumor and subsequently higher odds of metastasis [11]. This model stands as an example of a systems biology approach to support experimental design and discovery. We were then able to adapt this model to serve as a starting point for a developmental EMT model, used to test varied signaling hypothesis and explore the sensitivity of multi-pathway systems to various signals and drugs, which is presented in Chapter 5.

In Chapter 4, we presented the parameter optimization paradigm utilized in Chapter 3 as a modular implementation in Julia with associated test functions and performance benchmarking. The approach presented here addresses one of the key difficulties in biological modeling: how to handle sloppy data and inherent biological variability. Pareto optimal ensemble techniques allow multiple parameter sets to be optimized simultaneously against multiple objective functions. These objective functions represent the distance of the model performance from individual pieces of experimental data or whole experimental panels. These methods can be leveraged alongside other global/multi-objective optimization tools like particle swarm optimization to find diverse sets of parameters that can satisfy different biological states [12]. We also demonstrated the power the upcoming language Julia for developing high performance code without sacrificing readability, portability or access.

In Chapter 5, we expanded and modified the model in Chapter 3 to explore shear stress signaling mechanisms directly in the context of valve development. We identified YAP1 as a shear stress sensitive mechanosensitive transcription factor. Our preliminary modeling work suggests that a system with a balance of YAP1 and PECAM expression is able to capture the trends in EMT activation under various shear conditions. Through flow bioreactor experiments, we confirmed that YAP1 is sensitive to shear stress and suggested a Rho/ROCK independent pathway to YAP1 activation. This work contributes to the growing evidence that wall shear stress acts at specific target ranges to induce in EMT [13]–[15]. This model establishes the architecture required to integrate signals from several pathways that are currently implicated in shear regulated EMT. Taken together, the results in Chapter 5 and Chapter 2 support a role for BMP-MEK-ERK in regulating tissue growth as a function of pressures and tensions, and a role for Rho-ROCK regulating EMT as a function of wall shear stresses.

Overall, the works laid out in this thesis have the potential for broad impacts in the areas of etiological congenital heart valve research, tissue engineering and mechanobiology. Little is still known about the origins of most congenital heart defects. As the role of mechanical signaling has been established as essential to a physiological morphogenic process, it is critical to uncover the signaling elements responsible. Further, due to the complexities of the mechanical field *in vivo*, it is critical to understand the contributions of individual components as well as their synergistic interactions. The main works in Chapter 2, Chapter 3, and Chapter 5, have demonstrated distinct roles for wall shear stresses to regulate endothelial stability and

normal stresses to regulate tissue growth. We have also developed new methods of reducing model complexity that can help the mechanistic modeling field to better identify the balance between all-inclusive mass-action models and coarse-grained approaches. Further, in Chapter 2, we, to our knowledge, provide the first evidence that osmotic stress targets key and canonical pathways in valve development, leading to a new way to interpret previous studies that investigated the roles of mechanical deformation on tissue growth. We have also, through work in Chapter 4 and Appendix C, provided a wider availability of computational tools for models and scientists at the bench. The parameter optimization framework in Chapter 4 can be applied to a wide variety of biological problems in which conflicting data from experiments needs to be reconciled. The microscope automation software in Appendix C enables data acquisition from live samples from custom set-ups where expeditious acquisition is required, such as during mechanical testing.

6.2 Future Directions

The work presented in this dissertation provides insights that can lead to numerous avenues to further expand our knowledge of valve mechanobiology in embryogenesis. Future directions of this work include expanding the systems modeling approach and continuing to explore the role of osmotic stress signaling in development.

6.2.1 Using osmotic stress in concert with shear flow

The osmotic stress system as used in Chapter 2 provides a simple method to apply a static mechanical load. Medias used in flow bioreactors could be replaced by medias with different osmolarities. In a similar fashion, hypo-osmotic tensile loads

could be created by reducing media solutes, and hyper-osmotic compressive loads could be created using sucrose. These conditions would allow for precise control over a large component of the normal forces independent of the flow velocity.

6.2.2 Adaptation of hanging drop system to study AV septation

While conducting hanging drop experiments in Chapter 2, occasionally two cushions would be placed in the same hanging drop. We observed that AV cushions at HH25 would merge into a single spheroid after 24 hours, while cushions from later stages would form a seam. By intentionally adding multiple cushions per drop, it would be possible to study AV cushion fusion by analyzing cell migration and by preconditioning cushions with different mechanical stresses or chemical treatments before the two-cushion culture period. This work could help to elucidate what causes embryonic tissues to behave like a liquid versus forming distinct boundaries [16].

6.2.3 Spatial Mechanical testing of *in situ* sample

Methods like left and right atrial ligations and outflow tract banding have been shown to affect ventricular stiffness [17], yet to our knowledge, the stiffness of valve leaflets has not been measured. By combining these *in vivo* surgical manipulations with micro pipette aspiration, stiffnesses of healthy and defective valves could be measured in a valve-side specific manner. These insights could be used to help identify the causal relationships between tissue rigidity and tissue size.

Immunofluorescence and confocal reflectance microscopy could be used to further characterize the underlying microstructure in these locations. In total, this data would elucidate how changes in stiffness lead to functional valve primordia while also providing necessary mechanical cues to underlying cell types. This localized stiffness

information could also inform the creation of defect specific computational models, going beyond the assumption of a uniform material structure [18].

6.2.4 Spatial modeling of valve development at the cellular level

Given the critical morphological features of a developed valve, spatial modeling has an opportunity to capture how cellular mechanisms interact to form a spatially purposed and heterogeneous valve. Buskohl et al. 2012 presents a finite element based model of the developing heart valve, governed by a constitutive law that allows for tissue growth [18]. This model contains one bulk biological parameter, a homeostatic stress, at which no growth will occur. Therefore, while this model can map hemodynamic stresses onto the valve and coarsely capture the feed forward nature of the mechanical stimuli, it cannot relate how individual cell behaviors might lead to the processing of these signals and to remodeling.

Agent-based modeling provides a framework to capture emergent behaviors arising from the collective activities of cells over a physical landscape[19], [20]. The spatial component of agent-based modeling allows for the capturing of morphological growth and localization of specific hemodynamics signals. Further, ABMs can take advantage of existing signaling models to help predict model outcomes, extending its multiscale nature.

The essential components for an agent based model are (1) a definition for the agents, in this case cells, (2) moves or tasks that agents can perform, (3) rules that dictate the probability that a given move will be taken, and (4) an environment defined by a spatial grid and chemokine or mechanical gradients generated by cells. A general schematic of how an agent-based model framework can integrate data and modeling techniques from multiple biological scales is presented in Figure 6.1.

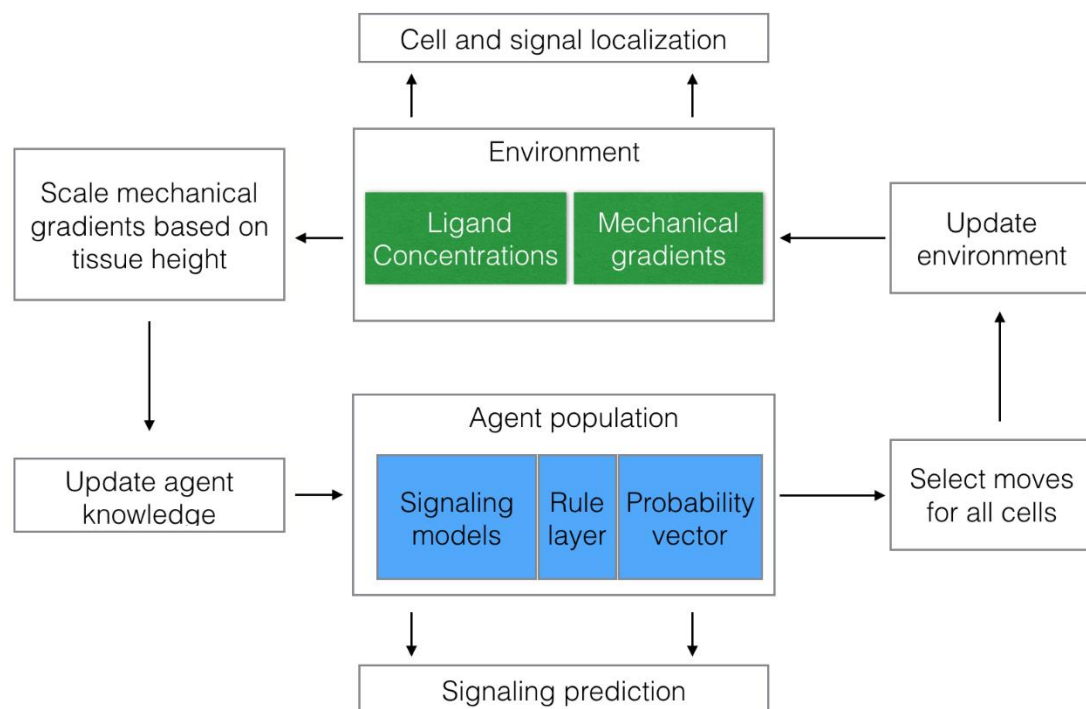


Figure 6.1. Agent-based model framework Molecular and cell level data inform the components in blue while tissue scale data on cytokine expression and hemodynamics can inform the components in green

It is hoped that these multi-scale models, trained by data describing cellular phenotypes, such as from live IF or IHC images, will help to describe and quantify the intermediate stages of valve development beyond the coarse levels of grow-elongate-condensate.

6.2.5 Understanding the roles of multiple pathways in shear stress signaling

Chapter 5 outlines signaling pathways to be incorporated into a next generation shear stress model. One key pathway to prioritize will be *klf2*, which is a transcription factor that is known to be shear sensitive [21]. This will require the addition of increasingly complex integration rules for transcriptional activation of TGF pathways. The new model could be trained on data from these separate pathways, allowing new rules and transfer functions to be identified as required to accommodate signal integration and independence. By testing the new model under more experimental constraints, i.e. conforming to data from multiple pathways, it will be more straightforward to rule out certain mechanisms by assessing which what data can be satisfied in the same cell. In addition to POETs, fitting the parameters could be done with particle swarm optimization or other global optimization techniques to broaden the parameter identification process. By employing more than one optimization framework at the same time, more confidence can be gained in situations when multiple, biologically relevant minima exist in the parameter space. An optimization scheme that allows for periodic use of gradient descent may help to avoid over-reliance on the original hand fit model [22].

6.3 References

- [1] J. I. E. Hoffman, S. Kaplan, and R. R. Liberthson, "Prevalence of congenital heart disease," *Am. Heart J.*, vol. 147, no. 3, pp. 425–439, 2004.
- [2] V. T. Nkomo, J. M. Gardin, T. N. Skelton, J. S. Gottdiener, C. G. Scott, and M. Enriquez-Sarano, "Burden of valvular heart diseases: a population-based study," *Lancet*, vol. 368, no. 9540, pp. 1005–1011, Sep. 2006.
- [3] G. J. Mahler, E. J. Farrar, and J. T. Butcher, "Inflammatory cytokines promote mesenchymal transformation in embryonic and adult valve endothelial cells," *Arterioscler. Thromb. Vasc. Biol.*, vol. 33, no. 1, pp. 121–130, 2013.
- [4] S. E. Lindsey and J. T. Butcher, "The cycle of form and function in cardiac valvulogenesis," *Aswan Hear. Cent. Sci. Pract. Ser.*, vol. 2011, no. 2, p. 10, 2011.
- [5] S. Lindsey, "Hemodynamic Regulation of Outflow Tract Morphogenesis."
- [6] S. V. Biechler V. *et al.*, "The impact of flow-induced forces on the morphogenesis of the outflow tract," *Front. Physiol.*, vol. 5 JUN, no. June, pp. 1–14, 2014.
- [7] E. Steed, F. Boselli, and J. Vermot, "Hemodynamics driven cardiac valve morphogenesis," *Biochim. Biophys. Acta - Mol. Cell Res.*, vol. 1863, no. 7, pp. 1760–1766, 2015.
- [8] P. R. Buskohl, M. L. Sun, R. P. Thompson, and J. T. Butcher, "Serotonin potentiates transforming growth factor-beta3 induced biomechanical remodeling in avian embryonic atrioventricular valves.," *PLoS One*, vol. 7, no. 8, p. e42527, Jan. 2012.
- [9] H. Tan *et al.*, "Fluid flow forces and rhoA regulate fibrous development of the atrioventricular valves," *Dev. Biol.*, vol. 374, no. 2, pp. 345–356, Feb. 2013.
- [10] A. E. Ehret, K. Bircher, A. Stracuzzi, V. Marina, M. Zündel, and E. Mazza, "Inverse poroelasticity as a fundamental mechanism in biomechanics and mechanobiology," *Nat. Commun.*, vol. 8, no. 1, p. 1002, 2017.
- [11] X. Li, M. K. Jolly, J. T. George, K. J. Pienta, and H. Levine, "Computational Modeling of the Crosstalk Between Macrophage Polarization and Tumor Cell Plasticity in the Tumor Microenvironment," vol. 9, no. January, pp. 1–12, 2019.
- [12] R. Poli, J. Kennedy, and T. Blackwell, "Particle swarm optimization: An overview," *Swarm Intell.*, vol. 1, no. 1, pp. 33–57, 2007.
- [13] G. J. Mahler, C. M. Frendl, Q. Cao, and J. T. Butcher, "Effects of shear stress pattern and magnitude on mesenchymal transformation and invasion of aortic valve endothelial cells.," *Biotechnol. Bioeng.*, vol. 111, no. 11, pp. 2326–37, Nov. 2014.

- [14] L. M. Goddard *et al.*, “Hemodynamic Forces Sculpt Developing Heart Valves through a KLF2-WNT9B Paracrine Signaling Axis,” *Dev. Cell*, vol. 43, no. 3, pp. 274-289.e5, 2017.
- [15] A. Williams, S. Nasim, M. Salinas, A. Moshkforoush, N. Tsoukias, and S. Ramaswamy, “A ‘sweet-spot’ for fluid-induced oscillations in the conditioning of stem cell-based engineered heart valve tissues,” *J. Biomech.*, vol. 65, pp. 40–48, 2017.
- [16] R. R. M. and R. P. V. Hajdu Zoltan , Vladimir Mironov, Agnes Nagy Mehesz, Russell A. Norris, “Tissue spheroid fusion-based in vitro screening assays for analysis of tissue maturation Zoltan,” *J. Tissue Eng. Regen. Med.*, 2010.
- [17] M. Midgett and S. Rugonyi, “Congenital heart malformations induced by hemodynamic altering surgical interventions.,” *Front. Physiol.*, vol. 5, no. August, p. 287, Jan. 2014.
- [18] P. R. Buskohl, J. T. Jenkins, and J. T. Butcher, “Computational simulation of hemodynamic-driven growth and remodeling of embryonic atrioventricular valves,” *Biomech. Model. Mechanobiol.*, vol. 11, no. 8, pp. 1205–1217, Nov. 2012.
- [19] N. Cannata, F. Corradini, E. Merelli, and L. Tesei, “Agent-based models of cellular systems.,” *Methods Mol. Biol.*, vol. 930, pp. 399–426, Jan. 2013.
- [20] A. Chakrabarti, S. Verbridge, A. D. Stroock, C. Fischbach, and J. D. Varner, “Multiscale Models of Breast Cancer Progression,” *Ann. Biomed. Eng.*, vol. 40, no. 11, pp. 2488–2500, Nov. 2012.
- [21] F. Boselli, J. B. Freund, and J. Vermot, “Blood flow mechanics in cardiovascular development,” *Cell. Mol. Life Sci.*, vol. 72, no. 13, pp. 2545–2559, 2015.
- [22] M. M. Noel, “A new gradient based particle swarm optimization algorithm for accurate computation of global minimum,” *Appl. Soft Comput. J.*, vol. 12, no. 1, pp. 353–359, 2012.

APPENDIX A.

METHOD FOR MEASURING TISSUE DEPTH USING BRIGHTFIELD MICROSCOPY AND APPLICATION TO LIVE EMBRYONIC VALVE CUSHIONS

I supervised this work which was conducted by Rishabh Singh as an undergraduate researcher in the lab. This work was enabled by the microscope automation software found in Appendix D. The scope automation class was used to set up and run Z-stacks, allowing the user to reproducibly find the height difference between the top and centerline of a cushion.

3D COMPACTION (HH25)

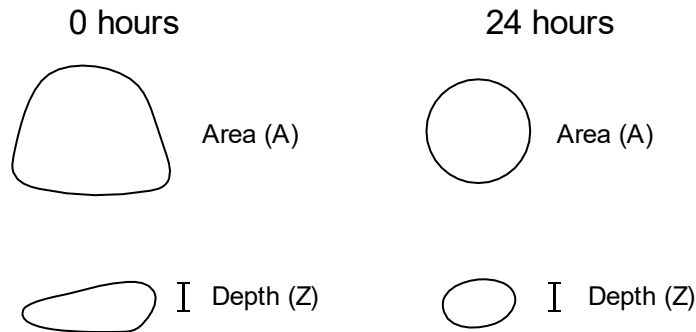


Figure 1. Area and Z-Height for morphologies at 0 and 24 hours of culture

3D compaction of HH25 cushions was calculated using two different approximations for $V/2$ between $t = 0$ hours and $t = 24$ hours. At the initial time point,

the cushions are flatter and their upper volume was approximated as their 2D area (A) multiplied by their calculated Z-height (Z) as represented in Figure 1:

$$\frac{V_o}{2} = A_o Z_o$$

At the 24-hour time point, however, cushions form an ellipsoid. While the volume of an ellipsoid is given by $V = \frac{4}{3} \pi abc$, where a, b, and c represent the axial radii, compacted HH25 cushions have relatively similar radii on their x- and y-planes under a microscope. As a result, the formula can be simplified to:

$$V_f = \frac{4}{3} \pi abc = \frac{4}{3} \pi r^2 Z_f$$

$$\frac{V_f}{2} = \frac{2}{3} A_f Z_f$$

As a result, volumetric compaction can be expected to be far more significant than the 2D compaction we've been using for quite some time. There is now a Z-axis compaction multiplied in as well as a factor of 2/3 to account for the geometry of a compacted cushion.

Measuring the volumetric compaction of HH25 cushions using darkfield Z-stacks presented one primary challenge – the orientation of the tissue inside the hanging drop. The side of a cushion facing the AVC lumen is thicker than the side attached to the myocardium, and has a distinctive surface profile that is thicker on one end and very thin towards the top. This luminal side is labeled “Up” and provides a large range in Z-heights (120-170 μm) for the 0-hour timepoint and allows for derivation of meaningful 3D compaction data. For cushions of the other orientation, “Down”, most of measured Z-heights fall between 75-90 μm . Scaling factors between 1.5 - 2 for

Down cushion Z-heights produced similar compaction numbers as Up cushions, but the factors themselves were inconsistent between cushions. This could indicate that, morphologically, the luminal side of a cushion is 1.5 – 2 times as thick, with the factor variability being partially explained by the isolation precision on the myocardial side.

An alternative approach would be to approximate the luminal side Z-height of a Down cushion using its 2D area. A scatterplot of Up cushion area vs. height is shown below in Figure 1. While there is a definite correlation between 2D area at the initial timepoint and cushion thickness, there is enough variability to make the derivation of a Z-height difficult. A down cushion of area $200000 \mu\text{m}^2$ can have a Z-height ranging from 130 – 150 μm , and any changes within this range have a large impact on the calculated volume.

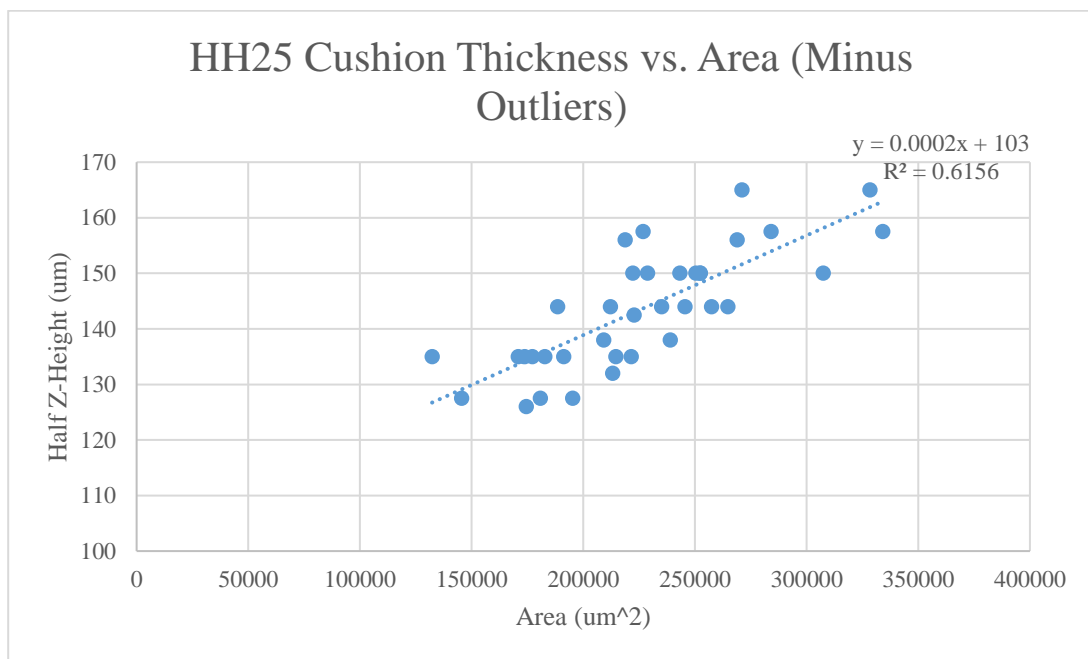


Figure 2. Scatterplot of HH25 cushion Z-height vs. 2D area. This also serves as a validation of the Z-height calculation method, as two completely isolated cushions of differing 2D sizes would be expected to also differ proportionally in Z-height.

Z-height compaction does not seem to vary significantly between conditions. No matter the treatment, Z-height at 24 hours is between 85-95% of the initial Z-height. The insensitivity of Z-height compaction to osmotic treatment would explain why the trends in volumetric compaction are so similar to those of 2D compaction.

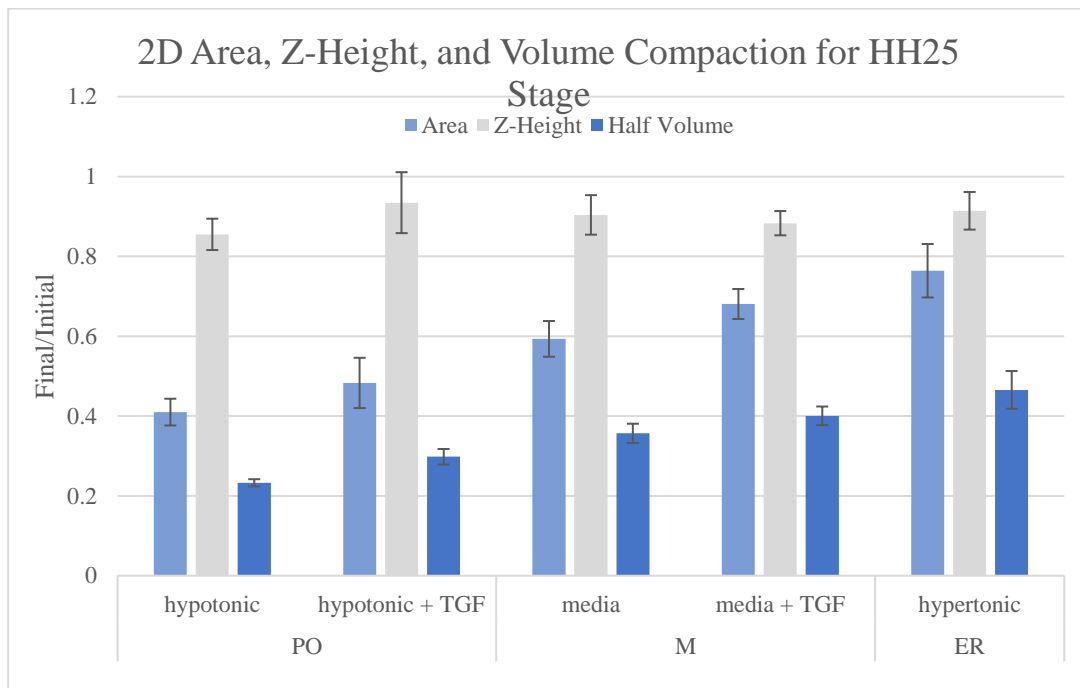


Figure 5. The compactions of HH25 cushions in 2D area, Z-height, and upper volume.

3D COMPACTION (HH34)

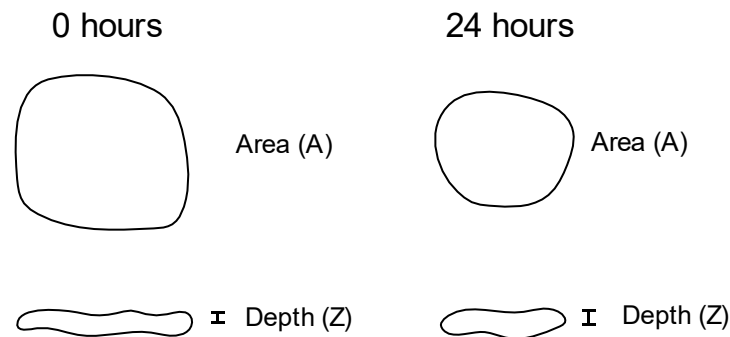


Figure 6. Area and Z-Height for HH34 morphologies at 0 and 24 hours of culture

This calculation of the volume treated the thin leaflets as prismatic and was done the same way as initial volume for HH25 cushions. Since the valve leaflets still retained a leaflet-like morphology after 24 hours of culture, the final volume was also calculated the same way.

$$\frac{V_o}{2} = A_o Z_o$$

The figure below shows the correlation between the 2D area of the isolated valves and their approximated Z-heights. The relationship is slightly weaker for HH34 valves than for HH25 cushions. One likely explanation is that the primitive valves have relatively variable (bumpy) surface profiles, and thus result in increased variability in Z-height measurement.

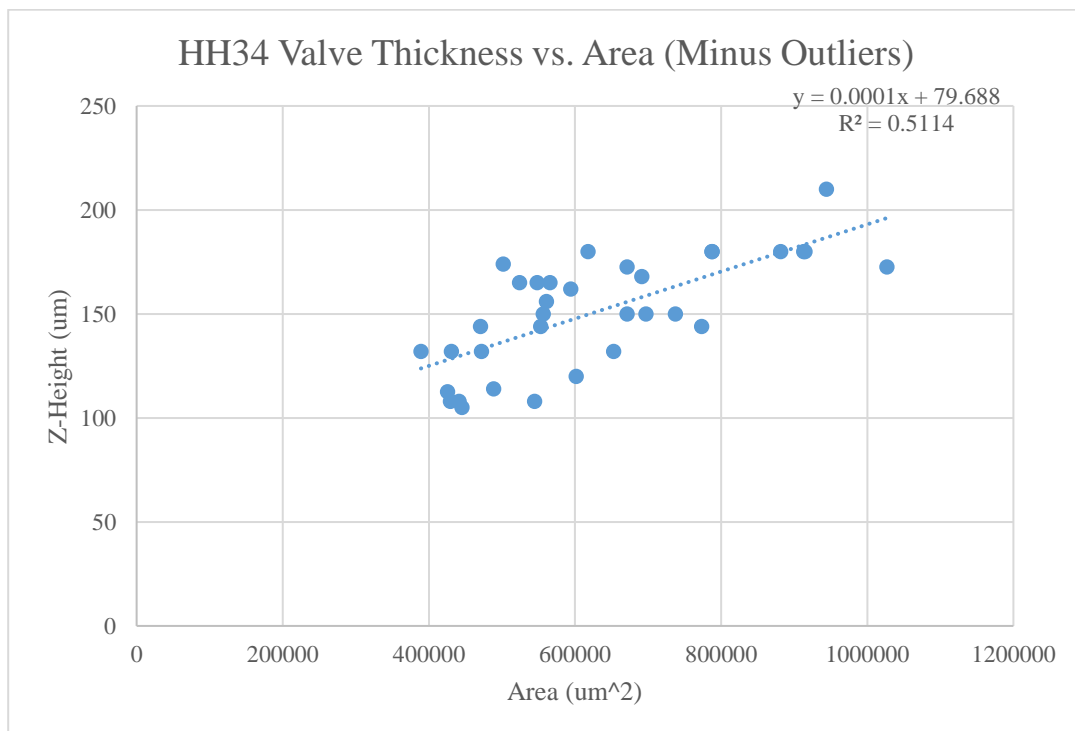


Figure 7. Scatterplot of HH34 cushion Z-height vs. 2D area

The results were similar to those of HH25 cushions in that volume compaction and area compaction trends matched. In addition, Z-compaction was relatively similar between conditions. The differences arose in actual levels of compaction. The valves under hypertonic treatment did not really compact at all in area, Z-height, or volume. On the other hand, the valves under media or hypotonic treatment had similar area compaction to their HH25 counterparts, but had significantly lower volume compaction. This can likely be attributed to the fact that compaction at this stage does not result in the tissue forming a ball shape. This behavior is attributed to collagen matrix in Chapter 2.

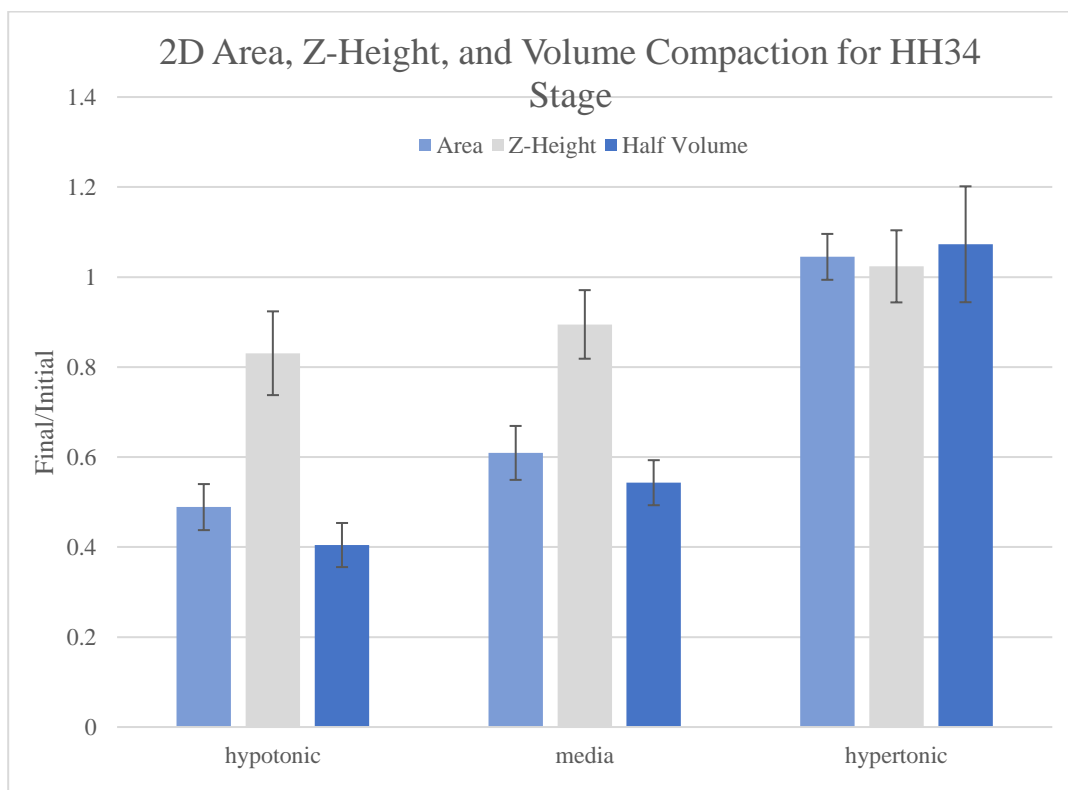


Figure 8. The compactions of HH34 cushions in 2D area, Z-height, and upper volume.

APPENDIX B.

COMPUTATIONAL MODELING TO ADVANCE PHARMACEUTICAL DEVELOPMENT IN THE AREA OF IMMUNO-ONCOLOGY

The following summary briefly describes work done during my internship at Applied BioMath (Concord, MA) in 2019, funded by the NSF (INTERN grant).

Many current advances in modern cancer therapies center on the interface of immune biology and oncology, referred to as immuno-oncology (I/O). These efforts include the development of drugs that can support a patient's immunity in the destruction of tumors or mobilize immune principles to specifically target malignant cells. A critical challenge in development of these drugs is understanding the complex relationships between the immune system, tumors and drugs in question. Quantitative systems pharmacology (QSP) models, that integrate knowledge about biological signaling process, cell phenotypes, transport and drug kinetics are poised to play a large role in decoupling this complex system. For example, dosage predictions for combination therapies and the identification of unwanted and often non-linear interactions can also benefit pharmacological development of new cancer drugs. During my internship. I gained experience in the field of immune-oncology through a literature review and implementation and analysis of models from the literature. The analysis I performed helped to both capture additional biological features without adding excess complexity and to better understand how I/O models can be parameterized. I would strongly encourage other engineering Ph.D. students to pursue internship work during their thesis. The added perspective, new skills and professional

contacts makes such an experience invaluable. In the remainder of this Appendix, you will find slides that describe multiple projects I worked during my internship.

APPENDIX C.

MECHANICAL TESTING WITH MICROPIPETTE ASPIRATION: A BRIDGE TO COLLABORATIONS

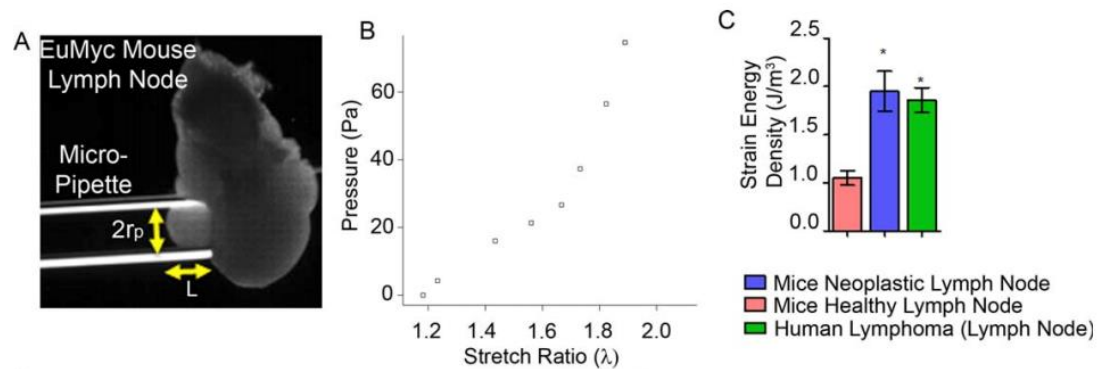
C.1 Summary

Micropipette aspiration (MPA) is a technique to test small (<1 mm) and very soft (applied pressures of 10 Pa or less) soft tissues and biological materials. It has been applied measure the stiffness of single cells (e.g. chondrocytes) to sections of adult organ tissues (e.g. mice spleen). In chapter 2, MPA was used to determine the effects of osmotically applied mechanical stress and matrix composition on chick AV valves at several stages of development. However, many other projects focused on biological material properties at Cornell required measurements of mechanical properties on substances that are too small or costly to acquire in large enough quantities to test on more traditional equipment such as rheometers or confinement testers. Here, I catalog three collaborations for graduate student projects with Dr. Ankur Singh's group, Dr. Dan Luo, as well as a fellow lab member in Dr. Jonathan Butcher's group.

C.2 Stiffness response for comparison of mouse and human lymph nodes:

Collaboration with Fnu Apoorva (Ankur Singh lab).

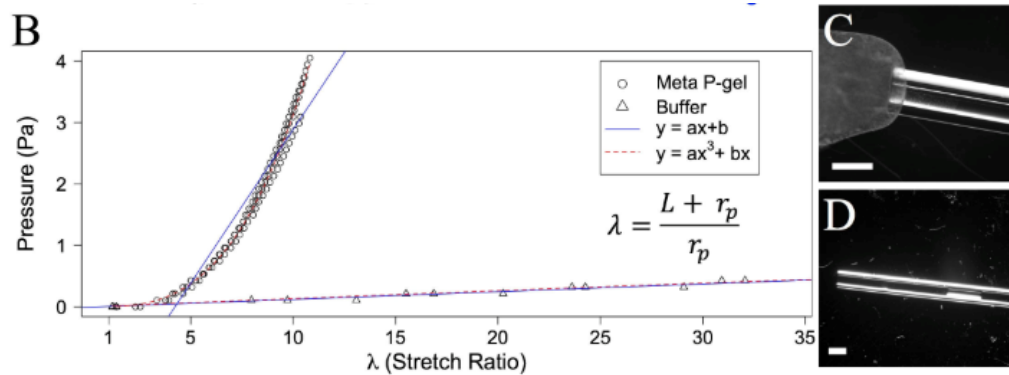
Engineering suitable microenvironments to study lymphomas is crucial to uncover the mechanisms that permit immune cells to undergo malignant transformations. It has been shown that engineered tissue scaffolds resembling lymphatic tissue can be used to mediate or even stop abhorrent immune cell activation [1]. However, in developing these systems, it is critical to match both the biological properties of the scaffold and the mechanical properties to both human and existing *in vivo* models of lymphoid disease.



In this study, we helped to demonstrate that an *in vitro* tissue engineered lymph node system based on mice neoplasms was mechanically similar to human lymphoma tissue [2]. Critically, this application of MPA enabled the testing of small samples that could not be tested using a rheometer but that ultimately allowed for a comparison between samples.

C.3 Collaboration with Dan Luo's group (Yudi Pardo, DNA meta gels)

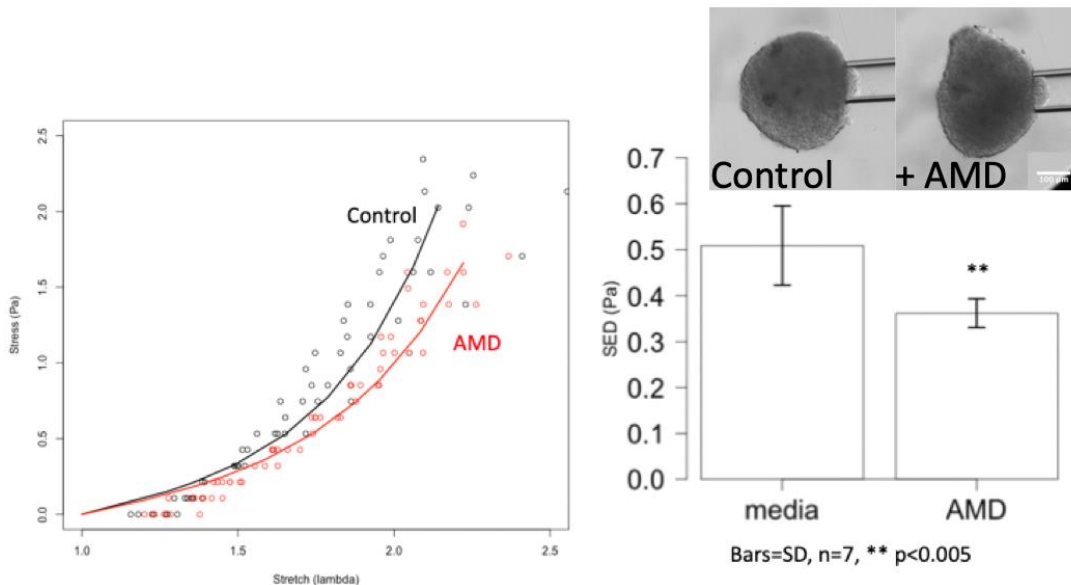
DNA hydrogels have the potential to act as substrates for the production of proteins that are difficult to produce in cells due to their toxicity or difficulties in purification [3]. In order to have enhance spatial control over protein production, it is important that such a gel be able to conform to its container, while still being reusable. Therefore, demonstrating liquid and solid like behaviors is beneficial in showing that the material can be reused and retain a predictable shape.



Here, we were able to demonstrate that a DNA hydrogel (a meta-gel called P-gel) has non-linear, solid-like material properties. In doing so, we were able to quantitatively show that in air, the gel behaves like buffer (a liquid), while submerged in aqueous medium, the gel behaves like a solid. This “meta” property allows the material to conform to and coat substrate surfaces, allowing for precise spatial production of proteins. Based on these results, we demonstrated that the Macroscale DNA hydrogels have the potential to serve as efficient, just-in-time, substrates to produce therapeutic protein products. Work from this study, including the MPA data, was presented at BMES in 2018 and is being prepared for publication.

C.4 Uncovering the side specific mechanosensitivity of CXCR4: Collaboration within the Butcher lab (Duc Pham, OFT CXCR4 project)

The CXCR4 program provides a mechanism of the trilaminar matrix patterning in the OFT valves. This has large mechanical implications for the valves *in vivo*, as the trilaminar structure is critical to producing a variety of mechanically functional modes. CXCR4 is expressed in the subendocardial cells on the ventricular side, which is under high unidirectional shear stress *in vivo*. The induction of CXCR4 expression depends on Notch1 signaling, which is a known transducer of laminar shear. In this system, CXCR4 signaling not only regulates matrix remodeling by modulating the BMP-Sox9-GAG axis, but it is also required for collagen synthesis.



Ablation of CXCR4 *in vivo* led to augmented BMP and Sox9 signaling as well as increased deposition of glycosaminoglycans. Interestingly, the MPA results showed that inhibition of CXCR4 signaling by AMD3100 *in vitro* decreased stiffness of the outflow tract valve organoids. Together, these data suggest that CXCR4 signaling is important for the matrix remodeling during outflow tract valvulogenesis.

C.5 References

- [1] A. Singh and N. A. Peppas, “Hydrogels and scaffolds for immunomodulation,” *Adv. Mater.*, vol. 26, no. 38, pp. 6530–6541, 2014.
- [2] F. N. U. Apoorva *et al.*, “Lymph node stiffness-mimicking hydrogels regulate human B-cell lymphoma growth and cell surface receptor expression in a molecular subtype-specific manner,” *J. Biomed. Mater. Res. Part A*, vol. 01, pp. 1–12, 2017.
- [3] J. B. Lee *et al.*, “A mechanical metamaterial made from a DNA hydrogel,” *Nat. Nanotechnol.*, vol. 7, no. 12, pp. 816–820, 2012.

APPENDIX D.

AUTOMATION OF DATA ACQUISITION FROM BASIC MICROSCOPY

D.1 Summary

Automating simple data acquisition tasks can lead to benefits both for personnel and scientific precision. While these automation tasks, such as automating the naming and saving of images are trivial to automate, many in the wet-lab may lack the skills or may not be familiar with the advantages beyond removing an annoyance in their protocol. Automation can save sample exposure time, reduce human errors and prevent repetitive motion injuries. A special benefit for working with live samples is a reduction in exposure time to room temperature or non-ideal culture conditions during imaging, such as during imaging of hanging drop cultures in chapter 2 of this thesis. Here, examples of two graphical user interfaces (GUI) created to assist in the capturing and saving of microscopy images are presented. Further, a modular program is provided to allow for users to take advantage of this software by coding their own interface with microscopy software using a computational robot.

D.2 Needs identification

Generally, the tasks to be addressed by this software can be described as follows:

- (1) Keeping track of the experiment name, experimental condition/timepoint
- (2) Acquiring and saving images

These lead to the following software features:

- (1) Operating other software that controls or interfaces with a camera or other

microscope components

- (2) Providing a GUI for quick and intuitive user inputs defining the current experiment, samples and image capturing commands
- (3) Providing a platform to easily interface with new image capture software
- (4) Providing a mechanism to store and recall common configurations to avoid unnecessary interaction

D.3 Cushion imaging experimental manager

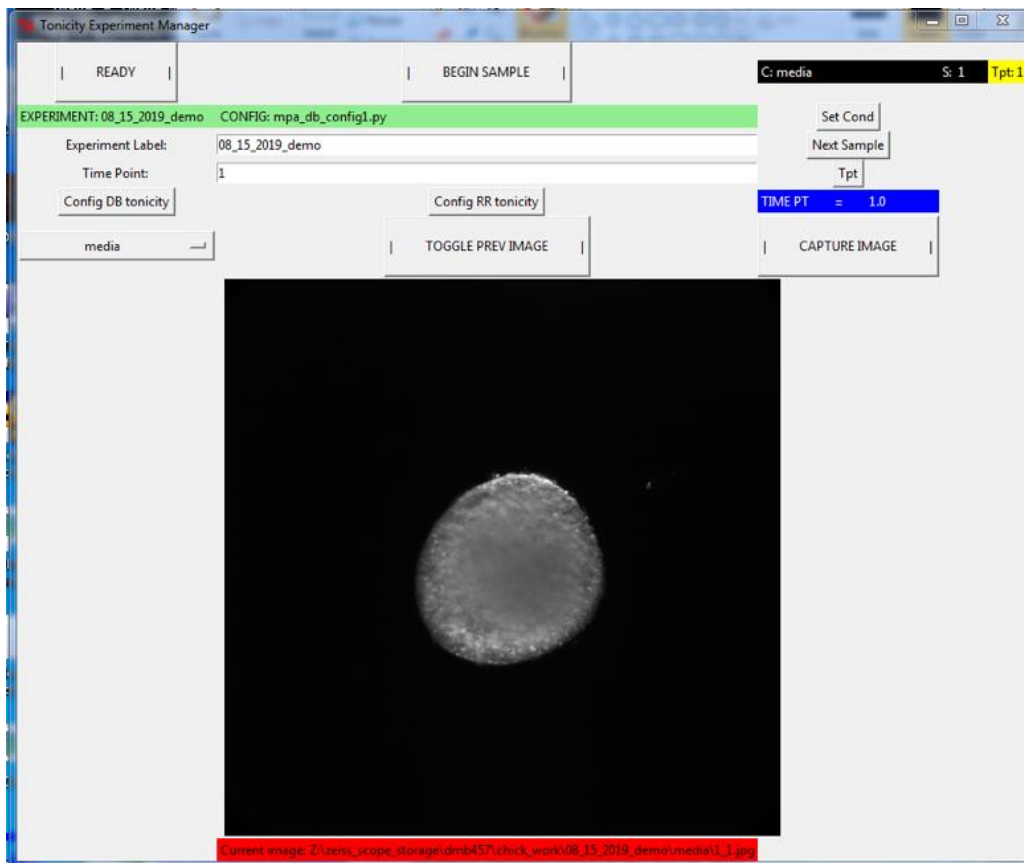


Figure D.1. Image of experimental manager during osmotic stress experiment

Features shown include the ability to add configuration files, view images and verify their location.

This application allows the user to set up an experiment with consistently defined meta data and acquire images directly from Image Pro. By automating the correct placement of files, file naming, and the several steps to acquire and save the images, this software allows for rapid acquisition of images of dozens of live valve tissues or cell cultures.

D.4 Micro-pipette aspiration experiment manager

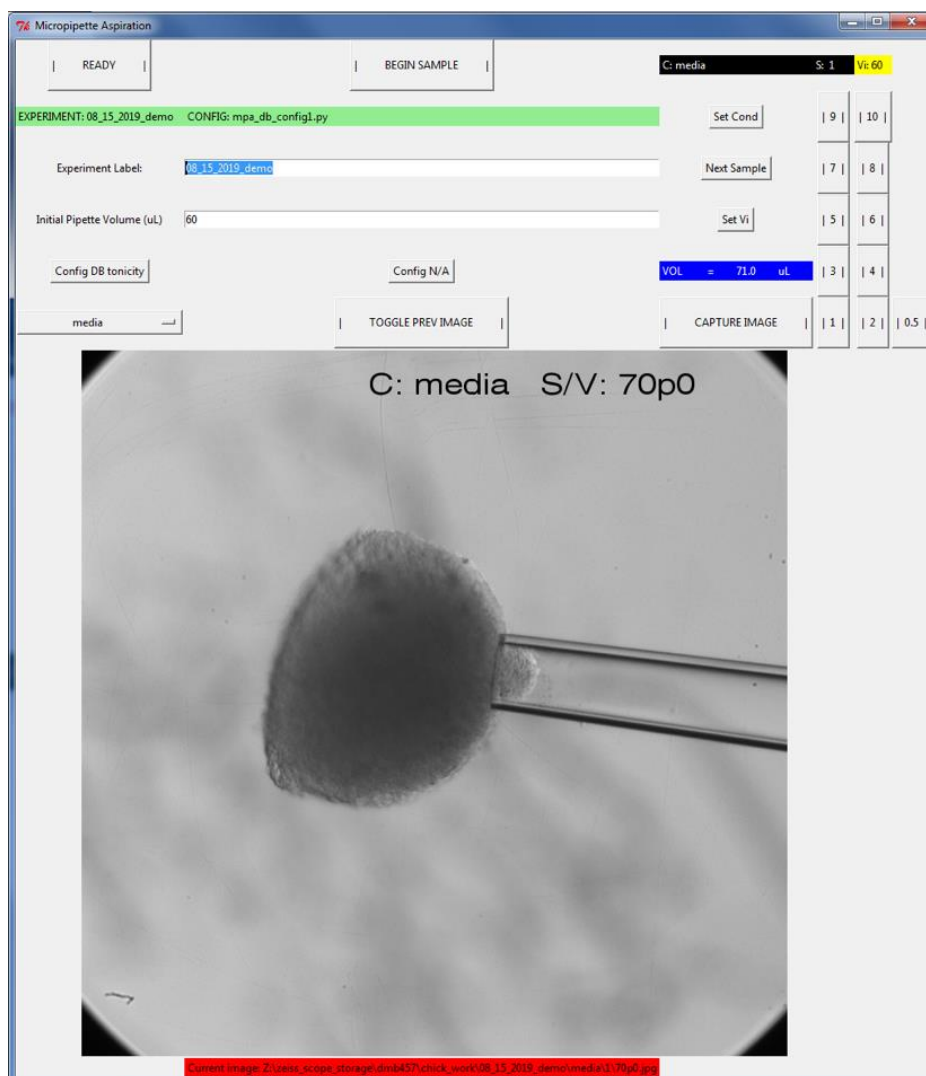


Figure D.2. **Image of experimental manager during micropipette aspiration**

Features shown include the ability to increment recording of applied pressures

(volume adjustments) and the ability to quickly toggle between the previous and current image to quickly ascertain the differential in stretching length, to help guide adjustment of the volume increments.

This iteration of the software found the greatest impact by improving the quality of mechanical testing experiments. By automating recording of volumetric measurements and by reducing image acquisition to one click, this application freed the user to carefully and consistently time the application of applied pressures to ensure a smooth and reproducible tests.

D.5 The Software

While the original code for was purpose built to perform the cushion imaging and micropipette aspiration tasks, it was straightforward to generalize the code to different operating conditions by permitting users to define certain key functions. The software provided here is implemented in Python2 using standard libraries including the Tkinter GUI package. The code can be found in appendix E.

D.6 Conclusion

This software has its greatest impact with older software that has limited, non-functional or license restricted automation features. However, it may also be useful when working with up-to-date commercial software with some degree of automation in ways that deviate from its initial design. It is my hope that students in the Butcher lab will continue to use this software for their work, and that ultimately others will be inspired to create software to support their experimental work.

APPENDIX E.

CODE FOR ANALYSIS AND APPLICATIONS

E.1 FIJI analysis code for IF quantification of image stacks

E.1.1 Main Python-FIJI analysis script

```
# batch_czi_hyperstackzc_db_v4.py
# Batch processing of czi images DB 04/26/2018
# Based off of https://www.ini.uzh.ch/~acardona/fiji-tutorial/
# INPUT: CZI files with color channels and z-stacks (can handle each
smaller case)
# DECLARE: global CHANNELS,CLAB,LOWER_PARTICLE_CUTOFF,THRESHOLDS,BLUR
# EXAMPLE SCRIPT:
#     INITIALIZATION      #
# test_flag = False
# global CHANNELS,CLAB,LOWER_PARTICLE_CUTOFF,THRESHOLDS,BLUR
#
# # THRESHOLDING OPTIONS
# nuc_thr = [64,128]
# cas_thr = [0,128]
#
# # FILE LOCATION
# rootdir = "/Users/dbassen/Desktop/CASP3/testdir" # Where are the
files located?
#
# # SET CHANNELS + PARAMS      #
# CHANNELS= [1,2] # What channels do you want to analyze?
# CLAB = ["cas3","nuc"] # What are their labels?
# LOWER_PARTICLE_CUTOFF = [10,10] # microns )^2 i.e. a square with
length sqrt(10 microns^2)
# THRESHOLDS = [cas_thr, nuc_thr ] #
# BLUR = [False,True]
#
#
# # CODE LOCATION + CALL      #
#
#
execfile("/Users/dbassen/Dropbox/code/python_stack/batch_czi_hypersta
ckzc_db_v4.py")
#
# For reading czi file as image plus object
from loci.plugins import BF
# several tools used from IJ
```

```

from ij import IJ#, ImagePlus, ImageStack#, WindowManager
#from ij.io import FileSaver

# most imports below are self explanatory (EDM is for watersheding )
from ij.plugin import ZProjector, ChannelSplitter, Thresholder,
ImageCalculator#, Filter #, LutLoader#, filter
from ij.process import ImageConverter # ImageProcessor,
from ij.plugin.filter import EDM, ParticleAnalyzer, Binary,
GaussianBlur
#from ij.plugin.frame import RoiManager
from ij.measure import ResultsTable, Measurements
#from ij.process import LUT
import re

import os

execfile("/Users/dbassen/Dropbox/pyprgs/in_out_csv.py")

def get_filepaths(path, string=''):
    all_files = os.listdir(path)
    files_wanted = []
    for filename in all_files:
        if filename.count(string) !=0:
            files_wanted.append(path+'/'+filename)
    return files_wanted

# Debugging only
try:
    test_flag
except NameError:
    test_flag = False

def tprint(x):
    if test_flag == True: print x
#

def
main(rootdir, CHANNELS, CLAB, LOWER_PARTICLE_CUTOFF, THRESHOLDS, BLUR, BLUR
_LVLS, WATERSHED):
    TABLE_NAME
    global DIAGIMG
    try:
        DIAGIMG
        print DIAGIMG
    except NameError:
        DIAGIMG = True
    filepaths=get_filepaths(rootdir, '.czi')
    #filepaths=filepaths+get_filepaths(rootdir, '.tif')
    print(filepaths)
    all_outputs =
[["Condition", "ID", "Time", "Stain", "Slice", "NUM_CELLS", "imageScale"]]
    ##
    for filepath in filepaths:

       imps = BF.openImagePlus(filepath)

```

```

# Generate save info
filename_noext, ext = os.path.splitext(filepath)

tprint(len(imps))
tprint(filepath)

for imp in imps:
    # Get current image (there will likely only be one)
    ip = imp.getProcessor().duplicate()
    imp.setProcessor("Copy", ip)
    #imp.show()

    # Split channel via ChannelSplitter

    for channel_id,channel_i in
zip(CHANNELS,range(len(CHANNELS))):
        # channel_id used for setting the channel and
naming the files
        # channel_i used to index parameters
#
        imp_all_channels =
ChannelSplitter.split(imp)# added for subtraction, make all channels
available
        imp_cs =
ChannelSplitter.split(imp)[channel_id-1] #VAR
        clab = CLAB[channel_i]
        min_t,max_t=THRESHOLDS[channel_i]
        # imp_cs.show()
        print channel_id,channel_i
        ic = ImageConverter(imp_cs).convertToGray8()

        IJ.setMinAndMax(imp_cs, min_t, max_t); #
MAKEVAR
        IJ.run(imp_cs, "Apply LUT","stack")#,
"slice") #all

        #imp_cs.show()
        #raise
        ip_stack = imp_cs.getStack()
        #global BLUR_LVL5

        try:
            BLUR_LVL5
        except NameError:
            BLUR_LVL5 = [1.0]*len(CHANNELS)
        blur_lvl = BLUR_LVL5[channel_i]

        for i in xrange(1, ip_stack.getSize() + 1):
            ip = ip_stack.getProcessor(i)
            if FIND_EDGES[channel_i] == True:

ip.findEdges() ##

            imp_cs.setPosition(i)
            #IJ.setMinAndMax(imp_cs, min_t, max_t);

# MAKEVAR
            #IJ.run(imp_cs, "Apply LUT","slice")
            cal = imp.getCalibration()

```



```

current processor
    ip=ip_tmp # need to overwrite the

# MAKE BINARY
ip.autoThreshold()

#EDM().toWatershed(ip)
if WATERSHED[channel_i] == True:
EDM().toWatershed(ip)
    ip.invert() # invert for particle

analyzer

# SET UP PARTICLE ANALYZER
table = ResultsTable()
options =
ParticleAnalyzer.SHOW_OUTLINES | ParticleAnalyzer.INCLUDE_HOLES
    measurements = Measurements.AREA |
Measurements.CIRCULARITY | Measurements.ELLIPSE | Measurements.SLICE
| Measurements.CENTROID

upr = 2000*2000#10000
pa = ParticleAnalyzer(options,
measurements, table,lwr_b, upr)
    pa.setHideOutputImage(True)

# RUN PARTICLE ANALYZER
# imp_cs.setPosition(i) # needed here

# add mask
maskflag=False
if maskflag:
    tmp_fname_search =
fname[fname.rfind("/")+1:]
    tmp_fname_search =
tmp_fname_search.split('_')
    tmp_cond = re.sub('[^A-Z]', '',
tmp_fname_search[2])
    tmp_id= re.sub('[^0-9]', '',
tmp_fname_search[2])
    print tmp_cond+tmp_id

if maskflag and
(tmp_cond+tmp_id=="ER3"):
    print 'MASK on',"ER3"
    tmp_fname =
"/Volumes/dmb457jtb47/imaging/osmo_figure_analysis/phh3_10hr/DP67/ext
ra/mask_ER3.tif"
    imask = IJ.openImage(tmp_fname)
    #imask.
    ic = ImageCalculator()
    imp_new = ic.run("SUBTRACT
create", imask, imp_cs)

ipTMP = imp_new.getProcessor()
ipTMP.invert()
#imp_new.show()
#raise
#imp_cs = imp_new

```

```

        pa.analyze(imp_new)
    elif subtractionflag and
int(channel_i)==STAIN_TOSUBTRACTFROM:
        pa.analyze(imp_new)
    else:
        pa.analyze(imp_cs)
    ## SAVE BINARY IMAGE, OUTLINES, AND
PARTICLE ANALYSIS RESULTS
    # extract image from single image
processor
    if subtractionflag and
int(channel_i)==STAIN_TOSUBTRACTFROM:
        zp = ZProjector(imp_new)
    else:
        zp = ZProjector(imp_cs)
        zp.setStartSlice(i)
        zp.setStopSlice(i)
        zp.setMethod(ZProjector.SUM_METHOD) #
SUM is selected just because (simplest?)
        zp.doProjection()
        zp_imp = zp.getProjection()
        savetype = "png" #tif
        if DIAGIMG:
            fname = filename_noext +
            "_%s_%s_z_%s_binary.%s"%(channel_id,clab,i,savetype)
            # SAVE BINARY
            IJ.save(zp_imp,fname)

            # RETRIEVE PA OUTPUT AND SAVE
            outlines_img = pa.getOutputImage()
            fname = filename_noext +
            "_%s_%s_z_%s_objects.%s"%(channel_id,clab,i,savetype)

            ###IJ.save(outlines_img,fname)
            fname = filename_noext +
            "_%s_%s_z_%s_particles.%s"%(channel_id,clab,i,"csv")
            ## save each
            print(channel_id)
            #
            #
            table.setColumn("Stain",clab)#,table.size()*[clab])

            #table_list=table.getResultsTable()
            #table_list

            fname_search =
fname[fname.rfind("/")+1:]
            fname_search = fname_search.split('_')

            stain=fname_search[-3]#.join('_') # N/A
            slice=fname_search[-1]
            time=fname_search[1] #8

            #print fname

```

```

fname_search[2]) #9
fname_search[2])#9

#
id= re.sub('[^0-9]', '',
cond = re.sub('[^A-Z]', '',

#print id,cond
print cond,id
expname = fname_search[0][-4:]
# save individual results table
print table.getCounter()
if table.getCounter() > 0:
    table.addValue("Condition",cond)
    table.addValue("ID",id)
    table.addValue("Stain",clab)
    table.addValue("Time",time)
    table.addValue("Exp",expname)
table.save(fname)

#

numCells=table.getCounter()
count_output =
[cond,id,time,clab,i,numCells,mi]
all_outputs.append(count_output)

fname = str(rootdir)+'/'+ "results_cell_number_%s"%TABLE_NAME +
".csv"

csv.out(fname,all_outputs) # save this

# continue to the next file or exit
print "Done"
return
# provide args in script
main(rootdir,CHANNELS,CLAB,LOWER_PARTICLE_CUTOFF,THRESHOLDS,BLUR,BLUR
_LVLS,WATERSHED)
#print "Done"

```

E.1.1.1

E.1.2 Analysis code for experiment including auto threshold search

gen_image_data_p_erk_DP137_7_13_19_auto.R

```

# phospho erk

#

import os

import time

# set up directories for all experiments

```

```

point1 =    "/Volumes/dmb457jtb47/imaging/osmo_figure_analysis/"

#DP94 =     "DP94/DP94_DB"
#DP94_erk = "DP94/DP94_DB/perk"
#DP95 =     "DP95"
#
#DP101_erk = "DP_101/DP_101"
#RR_11_20_p_erk = "DP_101/RR_11_20_p_erk"

DP137_1="perk_18hrs_DP137_7_13_19"
#test = 'test'
#    INITIALIZATION    #
test_flag = False
global
CHANNELS,CLAB,LOWER_PARTICLE_CUTOFF,THRESHOLDS,BLUR,DIAGIMG #
not necessary but might be clearer to declare these

#Chose experiment to run
RUN = DP137_1
NAME = RUN
# THRESHOLDING OPTIONS
# loop
DIAGIMG = False
Lowvec  = (5,125,25)
Highvec = (125,255,25)

```

```

ta = time.time()
for erk_low in range(*Lowvec):
    for erk_high in range(*Highvec):
        print erk_low,erk_high
        nuc_thr = [5,255]
        p_erk_thr = [erk_low ,erk_high]
        # FILE LOCATION
        rootdir = point1+RUN # Where are the files located?

        #rootdir = "/Users/dbassen/Desktop/MYO" # no slash
at the end

        #      SET CHANNELS + PARAMS #
        CHANNELS= [1,2] # What channels do you want to
analyze? [1,2]
        CLAB = ["p_erk","nuc"] # What are their labels?
["p_smad","nuc"]
        # Threshold contrast
        THRESHOLDS = [p_erk_thr ,nuc_thr ] # p_smad_thr
,nuc_thr

        # Particle cutoff for analyze particles
        LOWER_PARTICLE_CUTOFF = [10,10] # microns )^2 i.e.
a square with length sqrt(10 microns^2)

        # Watershedding
        WATERSHED = [True,True]

        # Find Edges

```

```

        FIND_EDGES = [False,False]

        # Blur

        BLUR = [False,False]

        BLUR_LVL5 = [0,0]

        #

        TABLE_NAME="%s_%s"%(NAME,CLAB[0])

        #execfile("/Users/dbassen/Dropbox/code/python_stack/batch_
_czi_hyperstackzc_db_v4_cushion_area.py")

        execfile("/Users/dbassen/Dropbox/code/python_stack/batch_
czi_hyperstackzc_db_v4.py")

        print

        "rootdir"+'/'+"results_cell_number_%s"%TABLE_NAME + ".csv"

        print

        "rootdir"+'/'+"results_cell_number_%s_%s_%s"%(TABLE_NAME,erk_lo
w,erk_high) + ".csv"

        os.rename(rootdir+'/'+"results_cell_number_%s"%TABLE_NAME
+
        ".csv",rootdir+'/'+"results_cell_number_%s_%s_%s"%(TABLE_NAME,e
rk_low,erk_high) + ".csv")

        tb = time.time()

        print (tb-ta)/60, "mins"

```

E.1.3 R Analysis for IF quantification of image stacks

```
#gen_image_data_myo_count_objects

#nuc_and_p_erk <-
read.csv("/Volumes/img/DP94/DP94_DB/perk/results_cell_number_DP94_p_erk.csv",header=TRUE)

# remove first slice of first cushion due to no nuc detected
nuc_and_p_erk <-nuc_and_p_erk[c(-1,-7),]

nuc_and_p_erk <-
read.csv("/Volumes/dmb457jtb47/imaging/Aim1ImagingwithDuc/DP94/DP94_DB/perk/results_cell_number_DP94_p_erk.csv",header=TRUE)

# remove first and last slice to reduce variability

first_slice <- 1
final_slice <- max(nuc_and_p_erk$Slice)

# use_slices<-
(nuc_and_p_erk$Slice!=first_slice)*(nuc_and_p_erk$Slice!=final_slice)
#
# nuc_and_p_erk <- nuc_and_p_erk[as.logical(use_slices),]

use_slices<-(nuc_and_p_erk$Slice==3)
use_slices<-
(nuc_and_p_erk$Slice!=1)*(nuc_and_p_erk$Slice!=2)*(nuc_and_p_erk$Slice!=3)
nuc_and_p_erk <- nuc_and_p_erk[as.logical(use_slices),]

# DP 101

# path <-
"/Volumes/dmb457jtb47/imaging/Aim1ImagingwithDuc/DP_101/DP_101/results_cell_number_DP101_p_erk.csv"
#
# nuc_and_p_erk <- read.csv(path)
#

#

summed_nuc_and_p_erk <-aggregate(NUM_CELLS~Condition+ID+Time+Stain,
nuc_and_p_erk, sum)
```

```

nuc <- subset(summed_nuc_and_p_erk, Stain=="nuc")
p_erk <- subset(summed_nuc_and_p_erk, Stain=="p_erk")
# Make new data
ratio <- nuc

ratio$percCellsPos <- (p_erk$NUM_CELLS/nuc$NUM_CELLS)*100

labels_exp <- c('PO', 'M', 'ER', "ERL", "ERU")

# reorder conditions for plotting
ratio$Condition <- factor(ratio$Condition, levels=labels_exp)

hour18<-subset(ratio, Time=="18HR")
hour18.means <- aggregate(percCellsPos~Condition, hour18, mean) #
Condition+exptags
hour18.sds<- aggregate(percCellsPos~Condition, hour18, sd)

# plot 18 hours

means <- hour18.means$percCellsPos
sds <- hour18.sds$percCellsPos
lvls <- c("T", "U", "C", "C+LDN", "C+U0126")
padx <- 0.0
YTOP <- max(means+sds+padx)
name <- "18HR_DP094"
#barplotname<-
'/Users/dbassen/work/tonicity_MPA_spring_2015/morpho_data_consolidate
d/bar_morph_ratios_07_27_2015.pdf'
barcol<-c("green", "blue", "black", "gray", "gray")
mp <- barplot(means, axes=FALSE, axisnames=FALSE, , main=name,
xlab="", ylab="", ylim=c(0, YTOP), col=barcol)
#ylim=c(0, 1)
size <- 0.05
mark <- 1.5
axis(1, labels=lvls, at = mp, cex.axis=2)
axis(2, at=seq(0 , YTOP, by=ceiling(YTOP/10)), cex.axis=2, las=1)
stDevs <- matrix( sds ,5)
segments(mp, means - stDevs, mp, means + stDevs, lwd=mark)
segments(mp - size, means - stDevs, mp + size, means - stDevs,
lwd=mark)
segments(mp - size, means + stDevs, mp + size, means + stDevs,
lwd=mark)

# #####
# hour10<-subset(ratio, Time=="10HR")
# hour10.means <- aggregate(percCellsPos~Condition, hour10, mean) #
Condition+exptags
# hour10.sds<- aggregate(percCellsPos~Condition, hour10, sd)
#
#
#
# # Plot 10 hrs
#

```

```

#
# means <- hour10.means$percCellsPos
# sds <- hour10.sds$percCellsPos
# lvls <- c("T","U","C","C+LDN","C+U0126")
# padx <- 0.0
# YTOP <- max(means+sds+padx)
# name <- "10HR_DP094"
# #barplotname<-
'/Users/dbassen/work/tonicity_MPA_spring_2015/morpho_data_consolidate
d/bar_morph_ratios_07_27_2015.pdf'
# barcol<-c("green","blue","black")
# mp <- barplot(means, axes=FALSE, axisnames=FALSE, , main=name,
xlab="", ylab="",ylim=c(0,YTOP),col=barcol)
# #ylim=c(0, 1)
# size <- 0.05
# mark <- 1.5
# axis(1, labels=lvls, at = mp,cex.axis=2)
# axis(2, at=seq(0 , YTOP, by=10.0),cex.axis=2,las=1)
# stDevs <- matrix( sds ,5)
# segments(mp, means - stDevs, mp, means + stDevs, lwd=mark)
# segments(mp - size, means - stDevs, mp + size, means - stDevs,
lwd=mark)
# segments(mp - size, means + stDevs, mp + size, means + stDevs,
lwd=mark)
#
#
# # plot 24 hours
#
# hour24<-subset(ratio,Time=="24HR")
# hour24.means <- aggregate(percCellsPos~Condition, hour24, mean) #
Condition+exptags
# hour24.sds<- aggregate(percCellsPos~Condition, hour24,sd)
#
# means <- hour24.means$percCellsPos
# sds <- hour24.sds$percCellsPos
# lvls <- c("T","U","C","C+LDN","C+U0126")
# padx <- 0.0
# YTOP <- max(means+sds+padx)
# name <- "24HR_DP094"
# #barplotname<-
'/Users/dbassen/work/tonicity_MPA_spring_2015/morpho_data_consolidate
d/bar_morph_ratios_07_27_2015.pdf'
# barcol<-c("green","blue","black","gray","gray")
# mp <- barplot(means, axes=FALSE, axisnames=FALSE, , main=name,
xlab="", ylab="",ylim=c(0,YTOP),col=barcol)
# #ylim=c(0, 1)
# size <- 0.05
# mark <- 1.5
# axis(1, labels=lvls, at = mp,cex.axis=2)
# axis(2, at=seq(0 , YTOP, by=ceiling(YTOP/10)),cex.axis=2,las=1)
# stDevs <- matrix( sds ,5)
# segments(mp, means - stDevs, mp, means + stDevs, lwd=mark)
# segments(mp - size, means - stDevs, mp + size, means - stDevs,
lwd=mark)

```

```

# segments(mp - size, means + stDevs, mp + size, means + stDevs,
lwd=mark)
#
#

hour18.means$percCellsPos.sd <- hour18.sds$percCellsPos
hour18.means$EXP <- "DP94"
write.csv(hour18.means, "/Volumes/dmb457jtb47/imaging/osmo_figure_anal
ysis/combine_exps/fig_perk_18hr.csv")

hour18$EXP <- "DP94"
write.csv(hour18, "/Volumes/dmb457jtb47/imaging/osmo_figure_analysis/c
ombine_exps/fig_perk_18hr_full.csv")

```

E.2 R spatial localization analysis code

E.2.1 Single sample spatial analysis

```

# spatial_quantification.R
# Quantifies spatial distribution of histological stain
# Usage
# For each relevant slice in stack, run and quantify
# source("spatial_quantification.R")

# Distance formula with inputs (c(x1,y1) and c(x2,y2))
Dist <- function(p1,p2){
  p1x <- p1[1]
  p1y <- p1[2]
  p2x <- p2[1]
  p2y <- p2[2]
  sqrt((p1x-p2x)^2 + (p1y-p2y)^2)
}

exclude_ROI_TL <- function(slice,Xlim,Ylim){
  # top left exclusion
  newslice<- slice[slice$X>Xlim&slice$Y>Ylim,]
  newslice
}

# function to find radii to generate donuts of equal area
iso_radius <- function(A0,i){
  sqrt(((i+1)*A0)/pi)
}

# test function
area_circle <- function(r){
  pi*r^2
}

```

```

}

# find radii of all points given a center
compute_radii <- function(center,X,Y){
  radii <- c()
  for (i in 1:length(X)){
    obj_center <- c(X[i],Y[i])
    radii[i] <- Dist(center,obj_center)
  }
  radii
}

compute_radii_ofequal_area<-function(A0,max_radius){
  i<-0
  bin_edge <- 0
  break_points <- c(0)
  while (bin_edge<max_radius){
    bin_edge <- iso_radius(A0,i)
    break_points[i+2]<-bin_edge # + 1 since 0 is already in
break_points and + 1 since R indexes from 1
    i<-i+1
  }
  break_points
}

spatial_quantification <-
function(slice_nuc,slice_stain,bin_number,num_cells_maxrad) {

# remove cells from other in frame cushions
#Pmyo
#slice_nuc <-exclude_ROI_TL(slice_nuc,13.82,29)
#slice_stain <-exclude_ROI_TL(slice_stain,13.82,29)
# Specify number of bins (# will divide max radius)
#bin_number <- # 10

# Specify number of cells to consider to define outside (to compute
mean max radius)
num_cells_toconsider <- num_cells_maxrad # 50

# extract X and Y coords
X <- slice_nuc$X
Y <- slice_nuc$Y

X_stain <- slice_stain$X
Y_stain <- slice_stain$Y

# compute center
center<-c(mean(X),mean(Y))

# compute radii
radii <-compute_radii(center,X,Y)

# use center from nuclear channel
radii_stain <-compute_radii(center,X_stain,Y_stain)

```

```

# find maximum radius and
max_radius <-max(c(radii,radii_stain))

# compute radii of equal area
# compute fewest number of bins given A0 that include maximum radius
# i.e. find first iso_radius given A0 with rk larger than max_radius
A0 <- area_circle(max_radius)/bin_number#10000 #um^2

break_points<-compute_radii_ofequal_area(A0,max_radius)

# normalize

# check length
if (length(radii) < num_cells_toconsider){
stop("Too many cells considered, outside num_cells_toconsider too big
")
}
norm_rad<-mean(sort(radii,decreasing=TRUE)[1:num_cells_toconsider]) #
possible that the bin including 1 and beyond can be used as estimate
for endothelial

# Calculate normalized radii with breakpoints for bins
normalized_break_points <- break_points/norm_rad

radii_normalized <- radii/norm_rad
radii_stain_normalized <- radii_stain/norm_rad

# Generate histogram
#png("/Users/dbassen/Dropbox/Butcher
Lab/Papers/AIM1_Osmotic_Stress/writeup/Figures/fig_images/3_osmo_inh_
24hr.png", width = 500, height = 600)
PLOT <- TRUE
hist_nuc <-
hist(radii_normalized,breaks=normalized_break_points,freq=TRUE,plot=P
LOT)
hist_stain <-
hist(radii_stain_normalized,breaks=normalized_break_points,freq=TRUE,
col="red",add=T,plot=PLOT)

#dev.off()

nuc_depth_counts <- hist_nuc$counts
stain_depth_counts <- hist_stain$counts

# ratios
spatial_ratios <-stain_depth_counts*100/nuc_depth_counts

output <- list()
output$nuc_counts <- nuc_depth_counts
output$stain_counts <- stain_depth_counts
output$local_ratios <- spatial_ratios
output$breaks <- break_points
output$breaks_norm <- normalized_break_points

```

```

# add calculation of mean radii
output$m_raddi <-
c(mean(radii_normalized),mean(radii_stain_normalized))

output
}

```

E.2.2 Experimental spatial analysis

```

# spatial_analyze_experiment.R
# get spatial data for pmyo0 24hrs

#// for each experiment (source this function)

### Need to split up nuc and stain because they will e in different
files but are needed at once!
spatial_analyze_experiment<-
function(expdir,stain_fname_pattern,bin_number,num_cells_maxrad) {

  setwd(expdir)

  list.files(pattern="(nuc).*(z_7|z_6|z_5|z_4).*.csv$")

  # filelist_nuc <- list.files(pattern="(nuc).*.csv$")
  # th\

  filelist_nuc <-
list.files(pattern="(nuc).*(z_7|z_6|z_5|z_4).*.csv$")
  filelist_stain <- list.files(pattern=stain_fname_pattern)

  data_dump_nuc <- lapply(filelist_nuc, read.csv, header = TRUE)
  data_dump_stain <- lapply(filelist_stain, read.csv, header = TRUE)
  num_files <- length(data_dump_nuc)

  # make empty dataframes for results
  #df_names <- c(Condition, ID, Time, Stain, Slice)

  df_names <- c("Condition", "ID", "Time", "Stain", "Slice",
"Exp")
  labeled_outputs<-setNames(data.frame(matrix(ncol =
length(df_names), nrow = 0),stringsAsFactors = FALSE), df_names)

  all_ratios <- data.frame(matrix(ncol = bin_number, nrow = 0))
  all_rmeans <- data.frame(matrix(ncol= 2,nrow=0))
  names(all_rmeans)[1] <- "meanr_nuc"
  names(all_rmeans)[2] <- "meanr_stain"
  for (i in 1:num_files){
  # access data
  slice_nuc<-data.frame(data_dump_nuc[i])

```

```

slice_stain<-data.frame(data_dump_stain[i])
#print(slice_stain[nrow(slice_stain),])
# compute
output <-
spatial_quantification(slice_nuc,slice_stain,bin_number,num_cells_max
rad)

# build data frame for just the "data" separate and then column
join to label df
all_ratios[i,] <- output$local_ratios

# get mean radii
all_rmeans[i,] <- output$m_raddi

# grab metadata from last row of raw df
Condition <- slice_stain[nrow(slice_stain),]$Condition
ID <- slice_stain[nrow(slice_stain),]$ID
Stain <- slice_stain[nrow(slice_stain),]$Stain
Time <- slice_stain[nrow(slice_stain),]$Time
Slice <- slice_stain[nrow(slice_stain),]$Slice
Exp <- slice_stain[nrow(slice_stain),]$Exp

Condition <- as.character(Condition)
Time <- as.character(Time)
Stain <- as.character(Stain)
Exp <- as.character(Exp)
print(c(Condition, ID, Time, Stain, Slice, Exp))
labeled_outputs[nrow(labeled_outputs) + 1,] <- c(Condition, ID,
Time, Stain, Slice, Exp)

}
# build output dataframe
labeled_outputs$Stain <- as.factor(labeled_outputs$Stain)
labeled_outputs$Condition <- as.factor(labeled_outputs$Condition)
labeled_outputs$Stain <- as.factor(labeled_outputs$Stain)
labeled_outputs <- cbind(labeled_outputs,all_ratios,all_rmeans)
#labeled_outputs <- cbind(labeled_outputs,all_rmeans)

#// for each slice file
# load all slices (skip top 3 layers)
# for each slice
# run spatial_quantification function
# store normalized r values
# save ouput list and plots to folder
# # basically we need to reduce from a list of slices to a list of
samples, note that
# # all slices will be loaded together regardless of sample
# compute average of normalized r values across slices (this
represents one sample)
# create master table with average and meta data (e.g. DP94 ER 1
pERK)
# aggregate down to conditions (through slices etc.)
# includes computing average of normalized r values across slices
(this represents one sample)
# plot

```

```
# save data in experiment summary table
}
```

E.2.3 Localization analysis for single experiment

```
# spatial_psmad15.R
# get spatial data for psmad15 24hrs DP69

# load quantification for one sample
source("/Users/dbassen/Dropbox/Butcher
Lab/Papers/AIM1_Osmotic_Stress/IHC/spatial_quantification.R")
# load function to process whole experiment
source("/Users/dbassen/Dropbox/Butcher
Lab/Papers/AIM1_Osmotic_Stress/IHC/spatial_analyze_experiment.R")

expdir <-
"/Volumes/dmb457jtb47/imaging/osmo_figure_analysis/pmyo_24hrs_all/pmyo_24hrs_DP87_1/individual/"
expdir <-
"/Volumes/dmb457jtb47/imaging/osmo_figure_analysis/psmad_24hrs_DP69/individual/"
#stain_fname_pattern <- "(myo).*\.csv$"
stain_fname_pattern <- "(myo).*\. (z_7|z_6|z_5|z_4) .*\.csv$"
stain_fname_pattern <- "(smad).*\. (z_7|z_6|z_5|z_4) .*\.csv$"

# Run analysis
bin_number <- 10
num_cells_maxrad <- 50
OUTPUT<-
spatial_analyze_experiment(expdir, stain_fname_pattern, bin_number, num_
cells_maxrad)

# return to home directory
setwd("~/")

# check experiment
expmeans<-
aggregate(OUTPUT[,7:16], by=list(OUTPUT$Condition), FUN=mean)
expsds<- aggregate(OUTPUT[,7:16], by=list(OUTPUT$Condition), FUN=sd)

#par(mfrow=c(3,1)) # plot

means <- as.numeric(expmeans[1,2:11])
sds <- as.numeric(expsds[1,2:11])
lvls <- 1:10
padx <- 0.0

YTOP <- max(means+padx)
name <- "test"
#barplotname<-
'/Users/dbassen/work/tonicity_MPA_spring_2015/morpho_data_consolidate
d/bar_morph_ratios_07_27_2015.pdf'
#barcol<-c("green", "blue", "black", "gray", "gray")
```

```

mp <- barplot(means, axes=TRUE, axisnames=FALSE, , main=name,
xlab="", ylab="",ylim=c(0,YTOP))#,col=barcol)

axis(1, labels=lvls, at = mp,cex.axis=2)

## Gnuplot
OUTPUT_gnuplot <- OUTPUT
OUTPUT_gnuplot[is.na(OUTPUT_gnuplot)] <- 0
num_blocks <- length(OUTPUT_gnuplot[,1]) # num rows = num samples

df_names <- c("BIN","SAMPLE","VALUE")
plotlist<-setNames(data.frame(matrix(ncol = length(df_names), nrow =
0),stringsAsFactors = FALSE), df_names)
for (i in 1:num_blocks){
  single_row <- as.numeric(OUTPUT_gnuplot[i,7:16])
  for (j in 1:10){
    access <- 10*(i-1)+j
    value <- single_row[j]
    plotlist[access,] <- c(j,i,value)

  }

}

fname <- "psmad15_DP69_localization.tsv"
plotlist[plotlist>100] <- 100

write.table( plotlist, fname, sep=" ", col.names=FALSE,
row.names=FALSE)

##

# mean radius values
OUTPUT$Condition <- factor(OUTPUT$Condition,levels=c("PO","M","ER"))
boxplot(OUTPUT$meanr_stain~OUTPUT$Condition,ylim=c(0,1),cex.axis=2,col=c())
#
heatmap(as.matrix(OUTPUT[,7:16]))
data <- as.matrix(OUTPUT[,7:16])
heatmap(data, Colv = NA, Rowv = NA, scale="column", xlab="variable",
ylab="car", main="heatmap")

# kruskal.test(OUTPUT$X6,g=OUTPUT$Condition)
# boxplot(OUTPUT$X6~OUTPUT$Condition)

# combine each experiment
# load experiment summary table(s)
# plot

```

E.3 Additional model code for shear stress model

E.3.1 Shear transfer functions

```
# shearTransferFunc.jl

# # Shear calculations
# # Calculate shear factor
# k= 1
# a= 2
# b= 2
# K= 10
#
# X = k*(M^a)*(1/(b^(F)))
# TN= X/(K+X)
# # println("Shear factor")
# # println(X)
# # println(1-TN)
# # println(TN)
# # println("-----")
#
# TAO_1 = 1-TN
# TAO_2 = TN
#
# # TAO_1 RHOA
#
# k= 1
# a = 2
# b = 1 # was 4
# K = 10
#
# X = k*(M^a)*(1/(b^(F)))
# TN= X/(K+X)
# TAO_1 = 1-TN
#
# # TAO_2 CD31
# k= 0.1
# a = 4
# b = 10
# K = 10
#
# X = k*(M^a)*(1/(b^(F)))
# TN= X/(K+X)
# TAO_2 = TN

##
# M= 1
# F= 0
k= 0.5
a = 2
b = 1 # was 4
```

```

K = 10

X = k*(M^a)*(1/(b^(F)))
TN= X/(K+X)
TAO_1 = 1-TN

# TAO_2 CD31
k= 0.1
a = 4
b = 10
K = 10

X = k*(M^a)*(1/(b^(F)))
TN= X/(K+X)
TAO_2 = TN
#println(M, " ",F)
#println(TAO_1, " ",TAO_2)
##

# form 2

# # TAO_1 RHOA
# k= 1
# a = 1
# b = 2
# K = 1
#
#
# X = (k*(M^a)*(1/(M^(b*F))))/(K+k*(M^a)*(1/(M^(b*F))))
# TN= X/(K+X)
# TAO_1 = 1-TN
#
# # TAO_2 CD21
# k= 0.5
# a = 1.5
# b = 0.5
# K = 3
#
# X = (k*(M^a)*(1/(M^(b*F))))/(K+k*(M^a)*(1/(M^(b*F))))
# TN= X/(K+X)
# TAO_2 = TN

```

E.3.2 Model signal integration logic modifications

```

# logic_flat_file.py

### DB 6/27/18
# Logic flat file

# Ecadherin transcription
activators=['activation_Ecadherin_by_Active_NFATc', 'activation_Ecadherin_by_ecad_virus']

```

```

inhibitors=['repression_Ecadherin_by_SNAIL_SLUG','repression_Ecadheri
n_by_Active_LEF1']
GROUPS = [activators,inhibitors] # ENTER GROUPS OF CONTROL TERMS THAT
ARE TO BE INTERGRATED TOGETHER
INTEGR = ['maximum','minimum','mean'] # ENTER JULIA FUNCTION NAMES
FOR THE INTEGRATION FUNCTIONS # last one is the outer most
integration function
ACTORS =
['','','SNAIL_SLUG:SNAIL_SLUG*Active_LEF1','Active_LEF1:Active_LEF1*p
Smad*Active_YAP1'] # old:new '' means no modification
pointer.reconfigure(GROUPS,INTEGR,ACTORS)

# TGFB3 transcription

effectors=['activation_TGFB3_by_TCF4
target','repression_TGFB3_by_YREG1']
GROUPS=[effectors]
INTEGR=['minimum']
ACTORS=['','','']
pointer.reconfigure(GROUPS,INTEGR,ACTORS)

# SNAIL_SLUG transcription
activators=['activation_SNAIL_SLUG_by_pSmad','activation_SNAIL_SLUG_b
y_ss_virus']
GROUPS=[activators]
INTEGR=['maximum']
ACTORS=['pSmad:pSmad*Active_YAP1','']
pointer.reconfigure(GROUPS,INTEGR,ACTORS)

# LEF1 transcription
activators = ['activation_LEF1_by_pSmad']
GROUPS=[activators]
INTEGR=['mean']
ACTORS=['pSmad:pSmad*Active_YAP1']
pointer.reconfigure(GROUPS,INTEGR,ACTORS)
### EOF

```

E.3.3 Modify control logic (using above logic flat file as input)

```

# modify_jl_control_logic.py
# This file modifies the control file
# (1) Allows for easy editing of the control file
# (2) Allows for obvious reproducibility of control file
modifications

execfile('../pyprgs/in_out_line.py')

line_list = lin.reader('Control.jl')

#def top_definition(line):
#    global count
#    counter = 1

```

```

class file_section:
    def __init__(self,List):
        self.text = List[:]
        self.return_text = self.text[:]
        self.working_block = []
        self.working_block_index = None

    def check_in_block(self,block,string):
        flag = False
        for line in block:
            if string in line:
                flag = True
        return flag

    def set_working_block(self,locator):
        index = [i for block,i in
zip(self.text,range(len(self.text))) if
self.check_in_block(block,locator)==True][0] # finds locator string
in block and rerturns index of block in text
        self.working_block = self.text[index]
        self.working_block_index = index

    def parse_actor(self,actors,i):
        #print i
        S = actors[i]
        if S == '':
            return "", ""
        else:
            return tuple(S.split(':'))

    def reconfigure(self,GROUPS,INTEGR,ACTORS):
        # first we flatten the groups list while making sure to keep
the index of the group with the group name
        ngroups = len(GROUPS)
        # flatten GROUPS
        logic_map = []
        logic_map_raw = [[x,group_index] for x,group_index in
zip(GROUPS,range(ngroups))] # group with group indices
        for x in logic_map_raw: # flatten
            for y in x[0]:
                logic_map.append([y,x[1]])

        # Find working block (contains all logic pertaining to one
reaction)
        locator = GROUPS[0][0] # what is the first reaction name of
the first group
        #print(locator)
        self.set_working_block(locator)
        # make a transfer_function_vector_ for each group
        ngroups = len(GROUPS)
        if ngroups > 1:
            for x in range(ngroups):
                # print x

```

```

self.working_block.insert(1,"transfer_function_vector_%s =
Float64[];%x)

        # find the starting index for each logical control statement
        for line,i in
zip(self.working_block,range(len(self.working_block))):
            for j in range(len(logic_map)):
                #print logic_map
                if logic_map[j][0] in line:
                    logic_map[j].append(i)
            # logic map now contains the first line of the sub-block

            counter = 0 # we need to index each logical control
statement!
            # Rename any actors as necessary (differentiate between
activators and inhibitors for parsing purposes)
            for x in logic_map:
                group = x[1]
                start = x[2]
                #print counter, "counter"
                # handle activators (all on one line)
                if "push!" in self.working_block[start+1]:
                    # patch actors
                    A,B = self.parse_actor(ACTORS,counter)
                    #print A,B

self.working_block[start+1]=self.working_block[start+1].replace(A,B)
                # patch transfer_function_vector references
                if ngroups == 1:
                    pass
                elif ngroups > 1:

self.working_block[start+1]=self.working_block[start+1].replace("tran
sfer_function_vector","transfer_function_vector_%s"%group)

                # handle inhibitors (multiple lines!)
                elif "if" in self.working_block[start+1]:
                    # patch actors
                    A,B = self.parse_actor(ACTORS,counter)

self.working_block[start+1]=self.working_block[start+1].replace(A,B)

self.working_block[start+4]=self.working_block[start+4].replace(A,B)
                # patch transfer_function_vector references
                if ngroups == 1:
                    pass
                elif ngroups > 1:

self.working_block[start+2]=self.working_block[start+2].replace("tran
sfer_function_vector","transfer_function_vector_%s"%group)

self.working_block[start+4]=self.working_block[start+4].replace("tran
sfer_function_vector","transfer_function_vector_%s"%group)
                counter = counter +1

```

```

        # update integration functions (this method cannot handle
nesting)
        if ngroups == 1:
            eq_ind = self.working_block[-4].index("=")
            self.working_block[-4] = self.working_block[-
4][:eq_ind+2] + "%s(transfer_function_vector);"%INTEGR[group]
            if ngroups > 1:
                eq_ind = self.working_block[-4].index("=")
                phrase = "%s("%INTEGR[-1]
                for q in range(ngroups):

phrase=phrase+"%s(transfer_function_vector_%s),"%(INTEGR[q],q)
                phrase = phrase[:-1]+");" # remove comma and close
                self.working_block[-4] = self.working_block[-
4][:eq_ind+2] + phrase
                # push the changes
                self.return_text[self.working_block_index]=self.working_block

        def send(self):
            return self.return_text

sect_sep = '# -'
end_keyword = "# Modify the rate_vector"
top = []
logic_section = []
bottom = []
count = 0
active_list = top # pull out the top portion of the file (before the
logic statments)

for line in line_list:

    if end_keyword in line: # watch for end separator
        active_list = bottom

    if sect_sep in line: # find logic section
        count=count+1

    if count ==5: # start to pull logic section
        active_list = logic_section

    active_list.append(line)

# # separate control blocks

# find indices of separators
seps = [i for line,i in zip(logic_section,range(len(logic_section)))]
if sect_sep in line ]

# 2i, 2i + 1 # take ordered pairs that do not overlap
def grab_blocks_by_pair(linelist,seps):
    blocks = []

```

```

    for i in range(len(seps)/2): # we can safely divide by two since
two seps are added for each block
        #print i, (2*i), (2*i+1)
        block = linelist[ seps[2*i]: seps[2*i+1]+2]
        blocks.append(block)
    return blocks

blocks = grab_blocks_by_pair(logic_section,seps)

# Example of flat file entry
# effectors=['activation_TGFB3_by_TCF4
target','repression_TGFB3_by_YREG1']
# GROUPS=[effectors]
# INTEGR=['minimum']
# ACTORS=['','']
# pointer.reconfigure(GROUPS,INTEGR,ACTORS)
# lin.writer("block.txt",pointer.working_block)
#

#

### Theoretically, we can just stream the logic flat file here and it
will generate the modified control file
### -- but still need to write the code to recombine and generate the
final file
#

# load logic blocks into file_section object
pointer = file_section(blocks)

# load flat file that will call pointer to edit requested blocks
execfile("logic_flat_file.py")

control_block= pointer.send()

# extract and flatten working blocks back to a linelist
control_block= [item for sublist in control_block for item in
sublist]

new_control_linelist = top+control_block+bottom

lin.writer("Control_modified.jl",new_control_linelist)

# find code block and select for modification

print("WARNING -- when integrating multiple rules (e.g. mean(min,max)
MANUALLY add brackets around minimum(),maximum() inside mean()")
print("grep mean Control.jl | grep -e minimum -e maximum")
# RULE:
# sect_sep opens the entire logic section AND the first logic
block/subsection
# sect_sep then closes the first block and opens the second
# therefore there are two sect_seps between all subsequent blocks
# and one sect sep at the end of the logic section

```

```

# find existing logic structure

# need to handle the following cases
# 1 multiple transferfunction integration
# need to define more than one transferfunction vector as well as
using the two references correctly

# add modifications

# replace existing logic

# save new control filey

```

E.4 Microscope controller class

```

## Scope controller for Butcher lab V20 Discovery microscope
## PURPOSE: Allow for timelapse imaging (i.e. automation of required
## microscope systems.
## This class interfaces with Image Pro, Oasis (objective imaging)
## and MTB test (Zeiss, 2004)
## REQUIRES MACRO DEFINITIONS IN IMAGE PRO
## REQUIRES PROPER CONFIGURATION IN MTB TEST
## REQUIRES USE OF POSITION LIST IN OASIS
##
## REQUIRES THE FOLLOWING MODULES:
##
##import pyautogui as pag
##import time
##import os
##import win32gui
##execfile('c_scope_controller.py')
##
##csvpath='../..pyprgs/in_out_csv.py' #specify location of csv
reader
##execfile(csvpath)
##

class commander:
    '''sends commands to the robot'''
    def
__init__(self,snap_wait=5,move_wait=5,stage=True,direct_acq=False,shu
tter=False):
    # Window selection keywords # identify window by window text
    self.kwd = '' # initialize active window keyword variable
    self.ap_class='' # initialize active window GetClassName
variable
    self.hwnd='' #initialize active window handle

    # Keywords to get window handle from window text or window
class
    self.ip_kwd='Image-Pro Plus'

```

```

        self.oa_kwd='OASIS Position List' #position list
        self.oa_main_kwd,self.oa_main_class=('OASIS','TfrmConfig') #
Oasis is not specific enough

        self.mtb_kwd='MTB2004 Test (MTB2004 Server version: 1.8.1.1)'
        self.mtb_handle=int()# initialize
        self.qi_kwd = 'QCapture'

        # MTB button locations
        self.xy_input_focus=(405,465)
        self.xy_set_focus=(365,465)
        self.xy_get_focus=(325,465)
        self.xy_current_focus=(265,465)

        # Physical operation wait times
        self.snap_wait = snap_wait
        self.move_wait = move_wait
        self.turret_wait = 1.8 # seconds

        self.save_dir = ''
## Diagnostics
        self.img_failed = False
        self.img_failed_counter = 0
        self.diagnostic()
## User input
        self.enable_shutter = shutter # True for fluorescent imaging
        self.enable_direct_acquire = direct_acq
##
        if self.enable_direct_acquire == True: # CHANGE TO FALSE FOR
IMAGE PRO!
            self.ip_acquire = self.direct_acquire ####
            print "direct acquire mode enabled !!!!!"
def diagnostic(self):
    pass
    #: run diagnostic
    #

## WINDOWS GUI BINDINGS
#####
    # enumHandler functions are passed to EnumWindows which calls
this function with
    # all available window handles. Each enumHandler tries to find
the "right" window
    # the one matching the window text or other piece of retrievable
info (win32gui.Get...)

def enumHandler(self,hwnd, lParam):
    # find a window based on text and set as active window
    if self.kwd in win32gui.GetWindowText(hwnd):
        pag.keyDown('Alt') #override windows safegaurd to prevent
window popup
        win32gui.SetForegroundWindow(hwnd)
        pag.keyUp('Alt')
        self.hwnd = hwnd # get handle out

```

```

    def enumHandler_class(self,hwnd, lParam):
        # find a window based on text and class and set as active
window
        if self.kwd in win32gui.GetWindowText(hwnd) and
win32gui.GetClassName(hwnd)==self. oa_main_class:
            pag.keyDown('Alt') #override windows safegaurd to prevent
window popup
            win32gui.SetForegroundWindow(hwnd)
            pag.keyUp('Alt')
            self.hwnd = hwnd # get handle out

    def enumHandler_snap_check(self,hwnd, lParam):
        # Make sure an image was taken
        if 'Image-Pro Plus' in win32gui.GetWindowText(hwnd):
            self.img_failed=False
            if 'Image-Pro Plus - untitled' not in
win32gui.GetWindowText(hwnd):
                self.img_failed = True
                self.img_failed_counter +=1

    def front(self,kwd):
        # set window as main focus
        ''' argument is passed through self.kwd '''
        self.kwd=kwd
        # find window by kwd and bring to front
        win32gui.EnumWindows(self.enumHandler, None)

    def front_class(self,kwd,oa_main_class):
        # set window as main focus, but set two class variables to
use text and class
        ''' based on both kwd and class'''
        self.kwd=kwd
        self. oa_main_class=oa_main_class
        win32gui.EnumWindows(self.enumHandler_class, None)

    ## PYTHON AUTO GUI (PAG) BINDINGS
    #####

    ##     def getCenter(self,path,Region=''):
    ##         if Region == '':
    ##             return pag.locateCenterOnScreen(path)
    ##         else:
    ##             return pag.locateCenterOnScreen(path,region=Region)

    ##     def click(self,x,y):
    ##         return pag.click(x,y)

    ##     def button(self,path):
    ##         # clicks a button
    ##         x,y = self.getCenter(path)
    ##         pag.click(x,y)
    ##         return x,y

    ## IMAGE PRO
    #####

```

```

def win_ip(self):
    # set focus on Image pro
    self.front(self.ip_kwd)

def snap(self):
    # must set hotkey in Image Pro
    pag.hotkey('ctrl','shift','f8')
    time.sleep(self.snap_wait)

def save_dialog(self):
    # launch save dialog with standard save shortcut
    time.sleep(0.015)
    pag.hotkey('ctrl','s')
    time.sleep(0.015)

##     def ezsave(self):
##         pag.hotkey('ctrl','s')
##         pag.press('enter')
##         pag.hotkey('alt','f4')

def nav_save(self):
    time.sleep(0.015)
    # get the mouse to the cursor to the file name box
    pag.hotkey('shift','tab','ctrl')
    pag.hotkey('shift','tab','ctrl')
    pag.hotkey('shift','tab','ctrl')
    pag.hotkey('shift','tab','ctrl')
    time.sleep(0.015)

def save(self,name,overwrite=False):
    ''' See overwrite condition default False '''
    time.sleep(0.015)
    pag.typewrite(name)

    if overwrite == True: #moves through overwrite dialog (has no
effect otherwise)
        time.sleep(0.015)
        pag.press('left')
        pag.press('enter')
        time.sleep(0.015)

    pag.press('enter')
    time.sleep(0.015)

def close_all(self):
    time.sleep(0.015)
    pag.hotkey('ctrl','shift','f9')
    time.sleep(0.015)

## OASIS
#####

def win_oa(self):
    self.front(self.oa_kwd)

```



```

        if mode == 'stage':
            if d > 110: # top
                self.zsafe(d,unit)
            if d < 65.000:
                self.zsafe(d,unit)
        # pag.press('down') #select unit

#   pag.hotkey('shift','tab')
#   continue setting focus
TS(0.015)
#pag.hotkey('ctrl','a')
#TS(0.015)
#pag.hotkey('delete')
#TS(0.015)
print(d)
pag.typewrite(str(d))
TS(0.015)

    x,y=self.xy_get_focus # make sure MTB knows the current
position or it may not move
    #pag.moveTo(x,y)
    #TS(0.015)
    pag.click(x,y)
    TS(0.015)

    x,y=self.xy_set_focus
    #pag.moveTo(x,y)
    #TS(0.015)
    pag.click(x,y)
    TS(0.015)
    # speedup gained on 4/24/17 1.139s to 0.499s -> 0.640s or 56%
of the time ~ 2x speedup

def zoom(self,f):
    '''zoom factor ZEISS'''
    pass

##### USER INTIALIZATION OF EXPERIMENT
#####

def get_rect(self):
    hwnd = self.hwnd
    x,y,w,h=win32gui.GetWindowRect(hwnd)
    return x,y,w,h

# Interacting inside OA window using button position relative to
upper left window corner
def oa_tab_focus(self):
    # switch window to Oasis
    self.win_oa_main()
    # get initial position
    x,y,w,h = self.get_rect()
    # get translated coords (location of focus tab)
    X,Y=(x+225),(y+70)
    pag.click(X,Y)

```

```

def oa_tab_stage(self):
    # switch window to Oasis
    self.win_oa_main()
    # get initial position
    x,y,w,h = self.get_rect()
    # get translated coords (location of focus tab)
    X,Y=(x+145), (y+70)
    pag.click(X,Y)

def oa_position_field(self):
    # switch window to Oasis
    self.win_oa_main()
    # get initial position
    x,y,w,h = self.get_rect()
    # get translated coords (location of focus tab)
    X,Y=(x+95), (y+310)
    pag.click(X,Y)

def oa_set_position(self):
    # switch window to Oasis
    self.win_oa_main()
    # get initial position
    x,y,w,h = self.get_rect()
    # get translated coords (location of focus tab)
    X,Y=(x+280), (y+320)
    pag.click(X,Y)

def get_update_coords(self): # MTB+OA
    ''' formally named get_focus() '''
    # handle units manually! (default of um works with OA)
    self.win_mtb() # switch to MTB
    # MAKE SURE UNITS ARE IN MICRONS
    x,y=self.xy_get_focus # location of get focus button
    pag.click(x,y) # click focus button
    x,y=self.xy_current_focus # location of focus field
    pag.doubleClick(x,y) # commit to current field and select
    pag.hotkey('ctrl','a') # select all
    pag.hotkey('ctrl','c') # copy value

    self.oa_tab_focus() # switch tab to focus (Switches to OA
window)
    self.oa_position_field() # advance to position field
    pag.hotkey('ctrl','a') # select all
    pag.hotkey('ctrl','v') # paste focus value in position field
    self.oa_set_position() # hit the "Set to Z" button

    self.win_oa() # go to position list window
    pag.press('esc') # needed to free mouse (unknown cause, might
be because window was changed within oasis)
    pag.press('insert')# add to position list -- just click
"insert"

    self.oa_tab_stage() # return to stage tab for manual stage
control

```

```

## New
def win_qi(self):
    self.front(self.qi_kwd)

## COMPLETE OPERATIONS
#####

def check_snap(self):
    self.kwd = ''
    # check window text
    win32gui.EnumWindows(self.enumHandler_snap_check, None)
# look for Image-Pro Plus - untitled****
    # if present, continue
    # if absent, try snapping again until it is present
    while self.img_failed == True:
        print 'ACQUISITION FAILURE TRYING AGAIN....'
        pag.press('enter') # Try to clear error message
        self.snap()
        win32gui.EnumWindows(self.enumHandler_snap_check, None) #
check again

def ip_acquire(self, savename, overwrite=False):
    time.sleep(0.015)
    self.front(self.ip_kwd)
    pag.press('esc')
    self.previewoff() #
    time.sleep(0.015)
    self.snap()
    self.check_snap() # Make sure we actually get an image
    self.save_dialog()
    self.nav_save()
    self.save(savename, overwrite)
    self.previewon() #

    #self.close_all() # if closed when save dialog is open, save
will fail
def previewon(self):
    pag.hotkey('ctrl', 'shift', 'K')
def previewoff(self):
    pag.hotkey('ctrl', 'shift', 'J')

def direct_acquire(self, savename):
    # Do not steal image pro pointers as you will lose
interactive
    # functionality that you want when actually at the scope
    # this function is for z-stacks/timelapse/unsupervised work
only
    # NO OVERWRITE PROTECTION
##
    if self.enable_shutter == True:
##
        mmc.setSerialPortCommand("Port", "mm", "\r")
##
        time.sleep(1)
##
        mmc.snapImage()

```

```

        image = mmc.getImage()
        img = Image.fromarray(image)
        #print(savename)
        img.save(self.save_dir+'\\'+savename+'.jpg')
        #return img
##         if self.enable_shutter == True:
##             mmc.setSerialPortCommand("Port", "zz", "\r")

        def direct_acquire_no_save(self):
            # Do not steal image pointers as you will lose
interactive
            # functionality that you want when actually at the scope
            # this function is for z-stacks/timelapse/unsupervised work
only
            # NO OVERWRITE PROTECTION
##             if self.enable_shutter == True:
##                 mmc.setSerialPortCommand("Port", "mm", "\r")
##                 time.sleep(1)
            mmc.snapImage()
            image = mmc.getImage()
            img = Image.fromarray(image)
            #print(savename)
            return img
            #return img
##             if self.enable_shutter == True:
##                 mmc.setSerialPortCommand("Port", "zz", "\r")
        def
ip_acquire_zstack(self,name,start_position,end_position,increment,mode='stage'):
            # initialize focus plane
            self.mtb_set_focus(start_position) # included in loop
            # linespace (start, end, number of slices (depth/increment) )
            START_FOCUS = start_position
            END_FOCUS = end_position
            depth = START_FOCUS-END_FOCUS
            SLICE_NUM = (depth/increment)+1
            # condition where zstack is false (start and end are
            identical, increment is non-zero), leads to one image

            zstep = 1
            name_initial = name
            for FOCUS_AT in
np.linspace(START_FOCUS,END_FOCUS,SLICE_NUM,endpoint=True):
                name = name_initial + "_%s_%s"%(increment,zstep)
                self.mtb_set_focus(FOCUS_AT,mode=mode) # units in microns
always
                #wait for moves to complete
                com.mvwt_fast()
                # name = '%s%s_s_microns'%(counter,save_string,FOCUS_AT)
                self.ip_acquire(name)
                zstep = zstep + 1
            print 'Z-STACK FINISHED %s'%SLICE_NUM

```

```

def
ip_acquire_zstack_depth(self, save_string, start_position, increment, depth, mode='stage'):
    # initialize focus plane
    self.mtb_set_focus(start_position) # included in loop
    # linspace (start, end, number of slices (depth/increment) )

    if self._zstack == True:
        START_FOCUS = start_position
        END_FOCUS = start_position+depth
        SLICE_NUM = depth/increment

    elif self.z_stack == False:
        SLICE_NUM = 1
        START_FOCUS=END_FOCUS=start_position

    counter = 1
    for FOCUS_AT in
np.linspace(START_FOCUS,END_FOCUS,SLICE_NUM,endpoint=True):
        self.mtb_set_focus(FOCUS_AT,mode=mode) # units in microns
always

self.ip_acquire('%s%s%s_microns'%(counter,save_string,FOCUS_AT))
    counter = counter + 1
    print 'Z-STACK FINISHED %s'%SLICE_NUM

def qi_snap(self):
    pag.press('alt')
    pag.press('a')
    pag.press('s')
    time.sleep(self.snap_wait)

def qi_save_nav(self):
    pag.press('alt')
    pag.press('f')
    pag.press('s')
    time.sleep(0.015)

def qi_close(self):
    pag.press('alt')
    pag.press('f')
    pag.press('c')
    time.sleep(0.015)

def qi_acquire(self, savename, overwrite=False):
    self.win_qi()
    # SNAP
    self.qi_snap()
    # SAVE
    self.qi_save_nav()
    self.save(savename, overwrite)
    # CLOSE
    self.qi_close()

def turret_get_pos(self):

```

```

os.startfile(r"C:\Users\BUTCHERZIESS\Dropbox\code\robots\static_vb\MA
C5000_get.exe")
    time.sleep(0.1)
    success =False
    while success==False:
        try:
            with
open(r'C:\Users\BUTCHERZIESS\Dropbox\code\robots\static_vb\state.txt'
,'r') as f:
            output = f.read()
            if output == '5':
                print 'BYPASS POSITION'
                success = True # you've made it this line and can
continue
            except:
                success = False # you hit an error and must stay in
the loop (technically success will always already equal false at this
line)
                print 'Could not access state.txt trying again in 1s'
                time.sleep(1)

        #print output
        return int(output)

def turret_interative_move_to(self,desired_pos):
    cur_pos=self.turret_get_pos()
    if cur_pos == int(desired_pos):
        pass
    elif cur_pos != int(desired_pos):
        dist = int(desired_pos) - cur_pos
        if dist > 0:
            self.repeat(self.turret_move_next,abs(dist))
        if dist < 0:
            self.repeat(self.turret_move_prev,abs(dist))

def turret_move_prev(self):
    time.sleep(0.1)

os.startfile(r"C:\Users\BUTCHERZIESS\Dropbox\code\robots\static_vb\MA
C5000_set_prev.exe")
    time.sleep(self.turret_wait)
def turret_move_next(self):

os.startfile(r"C:\Users\BUTCHERZIESS\Dropbox\code\robots\static_vb\MA
C5000_set_next.exe")
    time.sleep(self.turret_wait)

def repeat(self,f,n):
    for _ in range(n):
        f()

def oa_move_next(self):

```

```

        self.win_oa()
        time.sleep(0.015)
        pag.press('esc')
        self.next_oa()

def mtb_set_focus(self,value=75,units='um',mode='stage'):
    self.win_mtb()
    time.sleep(0.015)
    pag.press('esc')
    self.focus_at(value,units,mode)

def start_system(self):
    pass

## Direct control of xy stage
def move_xy(self,x,y):
    mmc.setXYPosition("oas",x,y)

## Other #####

def mvwt(self):
    time.sleep(self.move_wait)

def mvwt_fast(self):
    time.sleep(self.move_wait/10.0)

```

E.5 Get z-stack code (used in appendix A)

```

import pyautogui as pag
import time
import os
try:
    import win32gui
except:
    print 'You need win32... GUI DEBUG ONLY'
import numpy as np
execfile('c_scope_controller.py')

csvpath='../..pyprgs/in_out_csv.py' #specify location of csv reader
execfile(csvpath)

initialize_MM = True #True

def init_shutter():
    mmc.loadDevice("Port", "SerialManager", "COM4")
    mmc.setProperty("Port", "StopBits", "1");
    mmc.setProperty("Port", "Parity", "None");

```

```

def init_retiga():
    mmc.loadDevice('Retiga','Qcam','QCamera')
    # mmc.loadDevice('L1',"Xcite","X-Citel20PC")

def init_devices():
    init_retiga()
    init_shutter()
    mmc.initializeAllDevices()

CAM_WAIT,MOVE_WAIT=3,5

com = commander(CAM_WAIT,MOVE_WAIT)

def unload_devices():
    mmc.unloadAllDevices()

from PIL import Image

if initialize_MM == True:
    import MMCorePy
    mmc = MMCorePy.CMMCore()
    print mmc.getVersionInfo()
    init_devices()
    mmc.setExposure(450) #750
    mmc.setProperty('Retiga','Gain',0.55)#5
    mmc.setProperty('Retiga','Binning',2)

global SAVE_DIR
SAVE_DIR =
'Z:\\zeiss_scope_storage\\dmb457\\cushion_zstack_test_07_30_2017'
#SAVE_DIR = 'Z:\\zeiss_scope_storage\\rah386\\'

#883
#636

name = "M_1" # FOR EACH SAMPLE
#start = 1020
#end = 610
#increment = 10

# gget one image
#com.direct_acquire(savename) # savename the simple file name
"1_preview"

# get z stack
#com.ip_acquire_zstack(name,start,end,increment)

#if closing IDLE run this first
#unload_devices()
com.z_stack = True
#name, start, end =
start = 276
end = 134
def go(name, start, end, increment=12):
#    global name

```

```
# global start
# global end
a = time.time()
print(start-end)
com.ip_acquire_zstack(name,start,end,incrim)
b=time.time()
print (b-a)/60. , 'completed in minutes'

off = unload_devices

#250, 50
# 16.4363333344 minutes to do a 432 slice stack
```

APPENDIX F.

RELEVANT PROTOCOLS

F.1 Osmotic media

Final volume m199 stock	0.25	L
	8.7	g/L

Media				1X Media (M)	
	Component	grams/L	Component	Weight	
	M199	8.7	M199	2.18	g
	NaHCO3	2.2	NaHCO3	0.55	g
	Component	ml/L	Component	Vol	
	P/S	10	P/S	2.50	ml
Hyper				Hyper [0.14]suc(E R)	
	Component	grams/L	Component	Weight	
	M199	8.7	M199	2.18	g
	NaHCO3	2.2	NaHCO3	0.55	g
	Sucrose	47.922	Sucrose	11.98	g
	Component	ml/L	Component	Vol	
	P/S	10	P/S	2.50	ml
Hypo				Hypo (Po)	
	Component	grams/L	Component	Weight	
	M199	4.35	M199	1.19	g
	NaHCO3	2.2	NaHCO3	0.55	g
	Component	ml/L	Component	Vol	
	P/S	10	P/S	2.50	ml

F.2 3D Immuno-fluorescence of AV or OFT cushions

F.2.1 Whole Mount Staining of Embryonic Cushions or Cell Spheroids

FIXING AND PERMEABILIZATION

1. Rinse sample quickly (2x PBS use 200uL pipette for speed)
2. Fix sample in 4% PFA for 30 minutes in place (hanging drop) at 4 degrees
3. Wash 2x in PBS for 10 mins each
4. Permeabilize sample 2x in 0.3% Triton-X for 10 minutes each at room temperature
5. Quickly rinse once with ample PBS

BLOCKING

6. Transfer cushions in experimental groups to wells on a 96 well plate
7. Aspirate PBS
8. Block with DucBloc overnight at 4 degrees C.

PRIMARY ANTIBODIES

9. Wash 2x PBS for 10 mins each
10. Wash 2x 0.3% triton-x 10 mins each
11. Dilute primary antibodies at 1:100 dilution in DucBloc and incubate overnight at 4 degrees C

SECONDARY ANTIBODIES

12. Wash 2x PBS for 10 mins each
13. Wash 2x 0.3% triton-x 10 mins each
14. Dilute secondary antibodies 1:100 dilution and nuclear stain (DAPI) at 1:2000 dilution, in 5% BSA in PBS. Incubate samples overnight at 4 degrees C

MOUNTING (w/ clearing)

15. Wash 2x in PBS 10 mins each
16. Wash 1x in pure methanol for 10 minutes
17. Withdraw most of methanol (otherwise samples may dry out)
18. Add 20uL of clearing solution (Viskol)
19. Withdraw most of clearing solution (can leave less behind now but be careful)
20. Add 80uL of clearing solution
21. Transfer samples to glass bottom dish (with 60-80 uL of liquid depending on dish)
22. Apply coverslip over well to seal

SOLUTIONS

Duc's special blocking solution (DucBloc)

Reagent	5ml recipe
3% BSA	150mg
20mM MgCl	9.5 mg (or 100 uL 1M)
0.3% Tween 20	15 uL
5% DK or GT serum	250 uL
0.3M Glycine	112.6mg
PBS (1x)	4735 ml (or 4635 ml w MgCl (aq))

All solutions are made with 1X PBS

For reference 1% BSA is 10mg/ml BSA in PBS

F.3 Staining protocol for collagen gel embryonic patches / shear bioreactor

F.3.1 Staining of embryonic patches in shear reactor

FIXING AND PERMEABILIZATION (if fixed start at 4)

1. Rinse sample quickly (2x TBS use 200uL pipette for speed)
2. Fix sample in 4% PFA for 30 minutes in place at 4 degrees
3. Wash 2x in TBS for 10 mins each
4. ** IF using amplification:
5. Incubate in 1% H2O2 in PBS for 40 minutes
6. Permeabilize sample 2x in 0.3% Triton-X for 10 minutes each at room temperature
7. Rinse with TBS

Primary Calculation 80uL / channel

BLOCKING

8. Block with DucBloc for 1hr at RT.
9. Prep primary antibody solution

PRIMARY ANTIBODIES

10. Wash 2x TBS for 5 mins each (skip these steps unless overnight block at 4C)
11. Wash 2x TBS (triton) for 5 mins each
12. Dilute primary antibodies at 1:100 dilution in DucBloc

13. Incubate overnight at 4 degrees C, add antibody solution to gel surface only to save antibody (can do same for secondary)

SECONDARY ANTIBODIES

14. Wash 2x TBS for 5 mins each
15. Wash 2x TBS triton for 5 mins each
16. Prepare 1:100 secondary ab in 5% BSA in TBS
17. Incubate secondary antibodies for 1hr at RT
18. ** IF using amplification
19. Prepare 0.15% H₂O₂ in amplification buffer (1:200 30% H₂O₂ into TBS)
20. Prepare 1:100 TSA reagent diluted in amplification buffer with 0.15% H₂O₂ from last step
21. Incubate in TSA solution for exactly 7 minutes
22. Wash 4x in TBS for 5 mins each (convert 1 to rinse & 2 to triton if doing Phalloidin + DAPI)
23. Apply 1:100 F-actin & DAPI 1:1000 (in TBS) for 1 hr at RT.
24. Wash samples in TBS 4x5min.

Secondary Calculation

DkxMs

DKxRb

SOLUTIONS

Duc's special blocking solution (DucBloc)

Reagent	5ml recipe
3% BSA	150mg
20mM MgCl	9.5 mg (or 100 uL 1M)
0.3% Tween 20	15 uL
5% DK or GT serum	250 uL
0.3M Glycine	112.6mg
TBS (1x)	4735 ml (or 4635 ml w MgCl (aq))

All solutions are made with 1X TBS

For reference 1% BSA is 10mg/ml BSA in TBS

F.4 Use of Zeiss Stereoscope

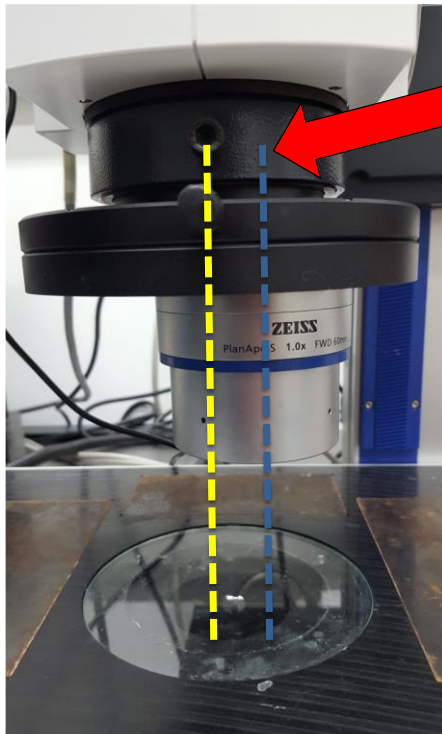
Steps for direct path imaging

- ① Unscrew the camera move it to the central camera port
- ② Move the adaptor to the side camera port to keep the port covered
(SIMPLY REST THE ADAPTOR, don't press in or screw)
- ③ Close the splitter on the side camera arm
- ④ Switch from eyepiece mode to camera mode
- ⑤ Move the Objective to the right position (will click)
- ⑥ Pull out the 2D/3D tab for best image quality (will affect eyepiece image quality and focus)

Configuration of Central Camera Port



Repositioned Objective



OBJECTIVE IN
RIGHTHAND
POSITION
(will click)

Light Path Settings

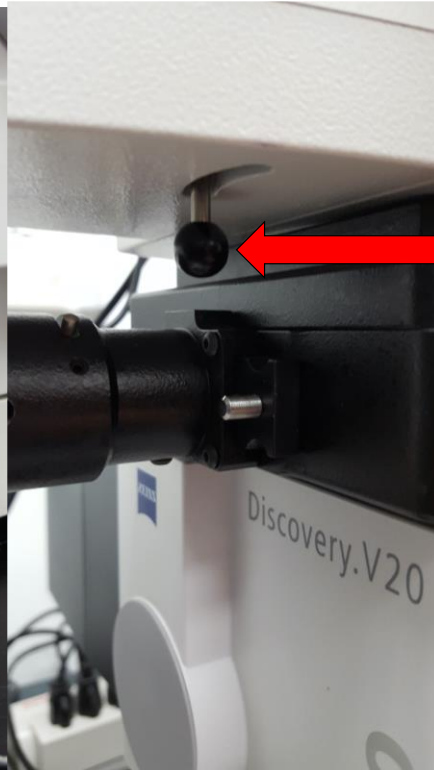
PULL OUT
2D/3D TAB
TO IMAGE*



Pushed in
will give
you a
clearer
eyepiece
image



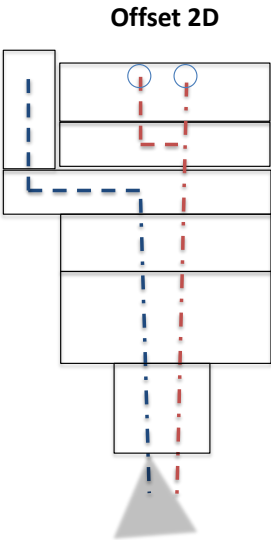
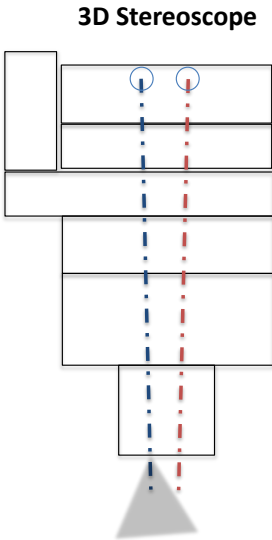
CLOSE
SIDE
CAMERA
SPLITTER



Stereoscope lightpaths

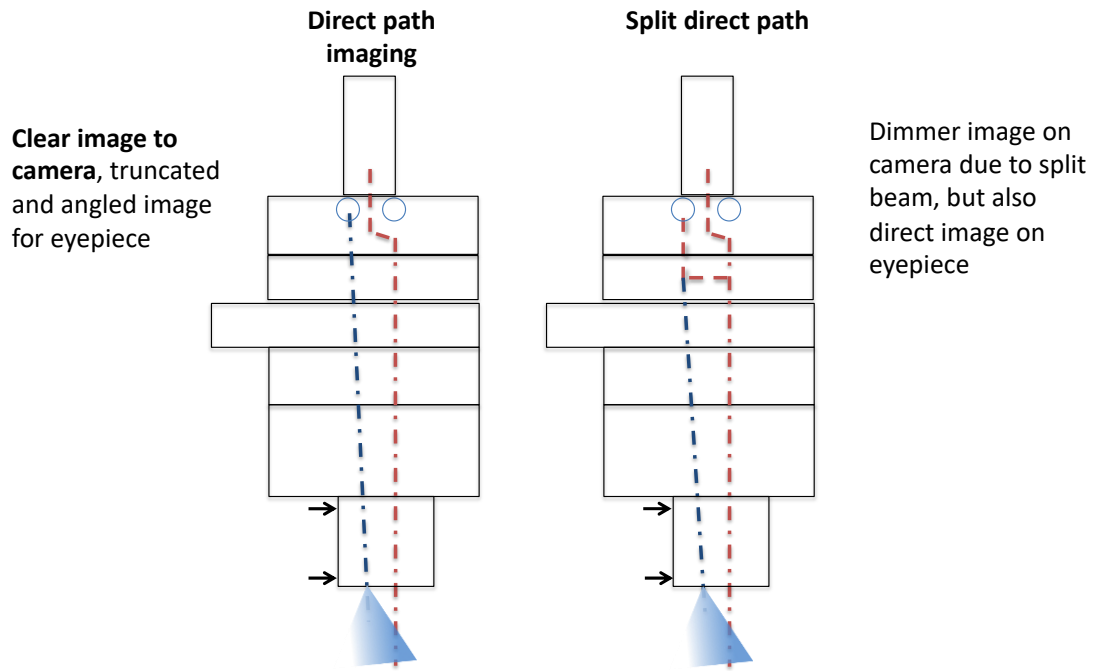
Stereo path modes

One light path to each eyepiece provides depth perception



One light path to eyepieces, one eyepiece to camera, however both images are offset by the stereoscopic angle

Direct path modes



APPENDIX G.

SUPPLEMENT FOR CHAPTER 3

G.1 Supplemental Materials and Methods

Characteristic transcription and translation parameters. We used literature based transcription and translation parameters to establish the characteristic synthesis and degradation rates for both mRNA and protein. We estimated values for the rate parameters from the Bionumbers database [31]. These parameters were then used for all gene expression calculations:

Description

cell_diameter = 12 # mu m
number_of_rnapII = 75000 # copies/cells
number_of_ribosome = 1e6 # copies/cells
mRNA_half_life_TF = 2 # hrs
protein_half_life = 10 # hrs
doubling_time = 19.5 # hrs
max_translation_rate = 5 # aa/sec
max_transcription_rate = 6.0 # nt/sec
average_transcript_length = 15000 # nt

```

average_protein_length = 5000 # aa

fraction_nucleus = 0.49 # dimensionless

av_number = 6.02 e23 # number/mol

avg_gene_number = 2 # number of copies of a gene

-----

# Description

-----

# Calculate the volume (units: L)

V = ((1- fraction_nucleus )*(1/6) *(3.14159)*( hl60_diameter )^3)*(1e -15)

# Calculate the rnapII_concentration and ribosome_concentration (units: nM)

rnapII_concentration = number_of_rnapII *(1/ av_number )*(1/ V)*1 e9

ribosome_concentration = number_of_ribosome *(1/ av_number )*(1/ V)*1 e9

# degradation rate constants (units: hr^-1)

degradation_constant_mRNA = -(1/ mRNA_half_life_TF )*log(0.5)

degradation_constant_protein = -(1/ protein_half_life )*log(0.5)

# kcats for transcription and translation (units: hr^-1)

kcat_transcription = max_transcription_rate *(3600/ average_transcript_length )

kcat_translation = max_translation_rate *(3600/ average_protein_length )

# Maximum specific growth rate (units: hr^-1)

maximum_specific_growth_rate = (1/ doubling_time )*log(2)

# What is the average gene concentration (units: nM)

avg_gene_concentration = avg_gene_number *(1/ av_number )*(1/ V)*1 e9

# Cell death constant (units: hr^-1)

```

```

death_rate_constant = 0.2* maximum_specific_growth_rate

# Saturation constants for translation and transcription (units: nM)
saturation_transcription = 4600*(1/ av_number )*(1/ V)*1 e9
saturation_translation = 100000*(1/ av_number )*(1/ V)*1 e9

```

Estimation and cross-validation of EMT model parameters. We used the Pareto Optimal Ensemble Technique (POETs) multiobjective optimization framework in combination with leave-one-out cross-validation to estimate an ensemble of TGF/EMT models. Cross-validation was used to calculate both training and prediction error during the parameter estimation procedure [97]. The 41 intracellular protein and mRNA data-sets used for identification were organized into 11 objective functions. These 11 objective functions were then partitioned, where each partition contained ten training objectives and one validation objective. POETs integrates standard search strategies e.g., Simulated Annealing (SA) or Pattern Search (PS) with a Pareto-rank fitness assignment [20, 96]. Denote a candidate parameter set at iteration $i + 1$ as k_{i+1} . The squared error for k_{i+1} for training set j was defined as:

$$E_j(\mathbf{k}) = \sum_{i=1}^{\tau_j} \left(\hat{\mathcal{M}}_{ij} - \hat{y}_{ij}(\mathbf{k}) \right)^2 \quad (\text{S1})$$

The symbol $\hat{\mathcal{M}}_{ij}$ denotes scaled experimental observations (from training set j) while \hat{y}_{ij} denotes the scaled simulation output (from training set j). The quantity i denotes the sampled time-index and τ_j denotes the number of time points for experiment j . In this study, the experimental data used for model training was typically the band intensity from Western or Northern blots. Band intensity was estimated using the

ImageJ software package. The scaled measurement for species x at time $i = \{t_1, t_2, \dots, t_n\}$ in condition j is given by:

$$\hat{\mathcal{M}}_{ij} = \frac{\mathcal{M}_{ij} - \min_i \mathcal{M}_{ij}}{\max_i \mathcal{M}_{ij} - \min_i \mathcal{M}_{ij}} \quad (\text{S2})$$

Under this scaling, the lowest intensity band equaled zero while the highest intensity band equaled one. A similar scaling was defined for the simulation output. By doing this scaling, we trained the model on the relative change in blot intensity, over conditions or time (depending upon the experiment). Thus, when using multiple data sets (possibly from different sources) that were qualitatively similar but quantitatively different e.g., slightly different blot intensities over time or condition, we captured the underlying trends in the scaled data. JuPOETs is free or charge, open source and available for download under an MIT software license from <http://www.varnerlab.org>. Details of the JuPOETs implementation, including example codes are presented in Bassen et al., [96].

O#	Species (protein)	Cell Type	Training	Prediction	Random
01	LEF1	DLD1 CC,MDCKII,A375 MC	0.54 ± 0.167	0.505 ± 0.175	1.765 ± 0.223
02	Vimentin	DLD1 CC,MDCKII,A375 MC	1.044 ± 0.668	0.783 ± 0.666	2.098 ± 0.784
03	TGF β 3	DLD1 CC,MDCKII,A375 MC	0.119 ± 0.262	0.225 ± 0.418	1.408 ± 0.732
04	E-cadherin	DLD1 CC,MDCKII,A375 MC	2.299 ± 0.449	2.154 ± 0.625	3.459 ± 0.643
05	β -catenin	DLD1 CC,MDCKII,A375 MC	0.752 ± 0.38	0.514 ± 0.351	1.025 ± 0.0
06	TGF β 3	DLD1 CC,MDCKII,A375 MC	1.662 ± 0.55	1.54 ± 0.677	3.328 ± 0.981
07	GSK3-P	DLD1 CC,MDCKII,A375 MC	0.19 ± 0.291	0.203 ± 0.292	0.756 ± 0.309
08	LEF1	DLD1 CC,MDCKII,A375 MC	0.023 ± 0.078	0.03 ± 0.11	0.937 ± 0.298
09	E-Cadherin	DLD1 CC,MDCKII,A375 MC	1.092 ± 1.228	1.412 ± 1.348	2.652 ± 1.435
010	Snail/Slug	DLD1 CC,MDCKII,A375 MC	0.019 ± 0.0	0.019 ± 0.0	1.111 ± 0.744
011	LEF1	DLD1 CC,MDCKII,A375 MC	0.005 ± 0.015	0.013 ± 0.06	0.797 ± 0.431

Figure S1. Training and prediction values as a function of condition for the 11 TGF-objective functions versus a random parameter control.

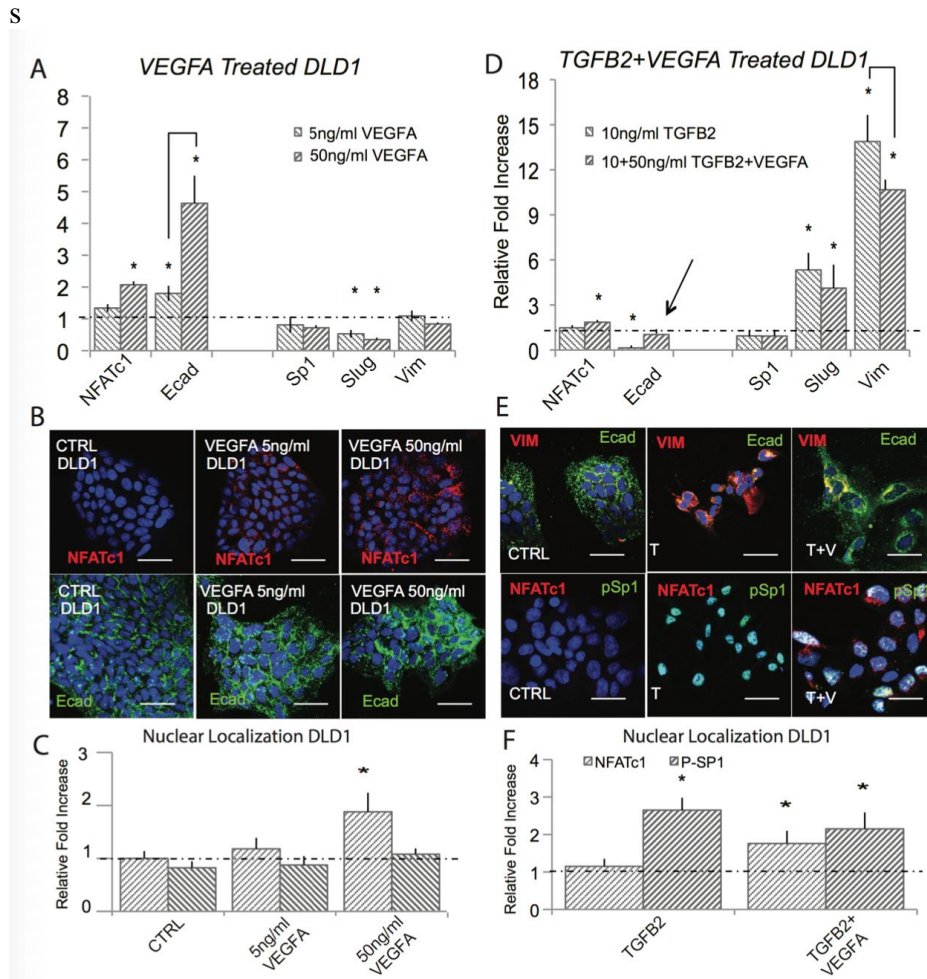


Figure S2. VEGF-A attenuates TGF-1/2 to induce phenotype heterogeneity in DLD1. (A) In DLD1, we found that 5ng/ml of VEGFA increased NFATc1 and E-cadherin gene expression via qPCR and 50ng/ml potentiated this effect at 48 hrs. (B - C) These findings were confirmed at the protein level via immunofluorescence, as ecadherin levels and nuclear localization of NFATc1 increased. (D) Treatment with (10ng/ml) TGF2 resulted in mesenchymal transformation as measured via qPCR against target genes Slug, ecadherin, vimentin, Sp1, and NFATc1. (E - F) Immunofluorescence and nuclear localization revealed a strong presence of phospho-Sp1. (G) Combination of VEGFA (50ng/ml) and TGF2 (10ng/ml) treatment resulted in increased Slug, NFATc1, and vimentin expression, while also increasing ecadherin levels compared to control. (H) Immunofluorescence confirmed these results, as both ecadherin and vimentin levels were elevated. (I) A significant increase in nuclear localization of both NFATc1 and phospho-Sp1 were also found. Magnification, 40x. Scale bars: 50µm. C=Control, T=TGF2, V=VEGFA, VI=NFAT inhibitor (VIVIT). Asterisks signify statistical differences from each other according to a one-way ANOVA with Tukey's post hoc (p<0.05).

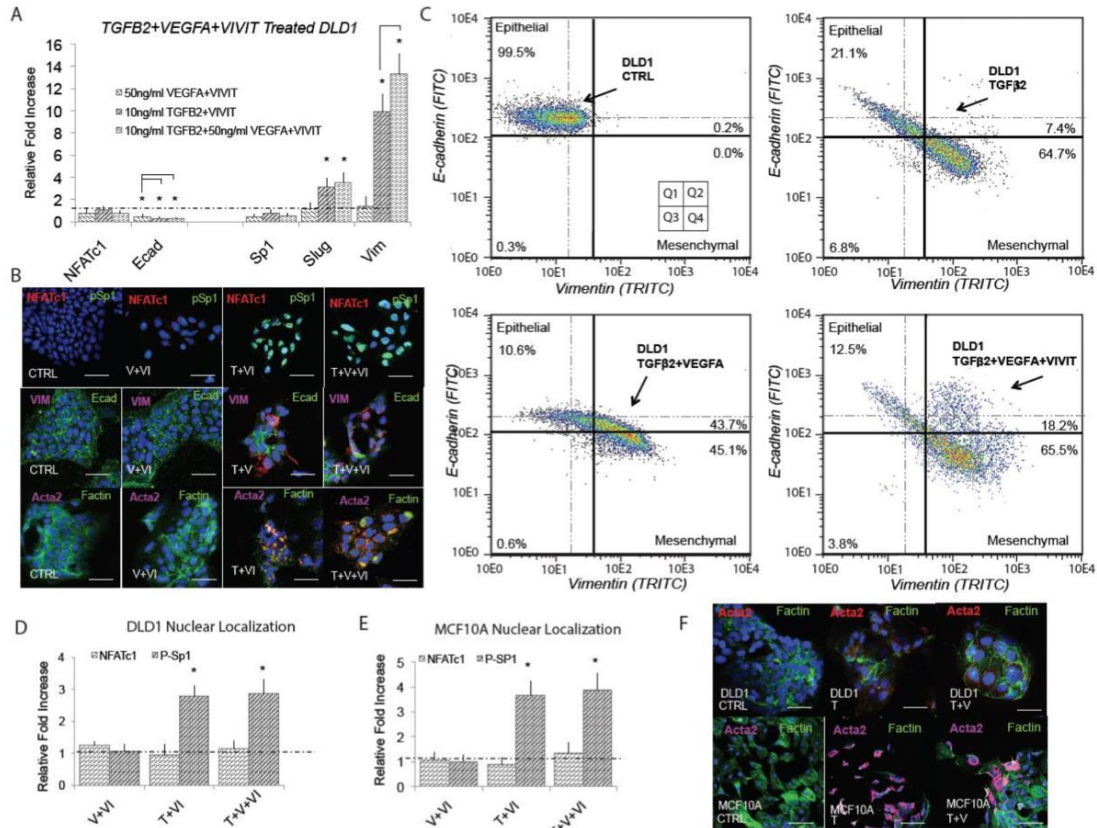


Figure S3. E-cadherin expression is dependent upon NFAT activity in DLD1. (A) Treatment with VEGFA (50ng/ml) and NFAT inhibitory peptide VIVIT (10 μ M) resulted in significantly reduced ecadherin expression (qRT-PCR at 48hrs). Addition of TGF2 (10ng/ml) and VIVIT resulted in increased Slug and vimentin expression, while inhibiting ecadherin levels. Combined TGF2, VEGFA, and VIVIT treatment resulted in target genes Slug and vimentin expression increased, while inhibiting ecadherin levels. No change in Sp1 or NFATc1 expression was found. (B) These findings were confirmed via immunofluorescence as the VIVIT inhibitors was shown to inhibit ecadherin levels in all three cases. We also found no change in gene or nuclear localization of NFATc1 in all three cases, while phospho-Sp1 was found to increase in both TGF conditions. (C) Quantitative flow cytometry also confirmed this trend. (D,E) TGF2, VEGFA and VIVIT treatment in DLD1 and MCF10A resulted in no change of Sp1 expression or NFATc1 expression. (F) Likewise, no change in nuclear localization of NFAT in all three cases, however phospho-Sp1 was found to increase in both TGF conditions. Magnification, 40x. Scale bars: 50 μ m. C=Control, T=TGF2, V=VEGFA, VI= NFAT inhibitor (VIVIT). Asterisks signify statistical differences from each other according to a one-way ANOVA with Tukey's post hoc (p<0.05).

PRELIMINARY DATA USED TO HANDFIT RESPONSE OF VEGFA WITHIN SYSTEM

MCF10A							
Values							
VEGFA	Relative mRNA			Normalized			
		Ecad	Slug	Vim	Ecad	Slug	Vim
5ng/ml	3HR	1.31	1.04	0.93	0.00	1.00	1.00
	48 HR	3.60	1.03	0.91	0.45	0.94	0.88
50ng/ml	3HR	1.37	0.92	0.88	0.01	0.25	0.71
	48 HR	6.34	0.88	0.76	1.00	0.00	0.00
Standard Deviation							
VEGFA	Relative mRNA			Normalized			
		Ecad	Slug	Vim	Ecad	Slug	Vim
5ng/ml	3HR	0.89	0.03	0.02	0.00	0.03	0.02
	48 HR	0.78	0.03	0.27	0.10	0.03	0.26
50ng/ml	3HR	0.11	0.10	0.53	0.00	0.03	0.43
	48 HR	0.53	0.21	0.19	0.08	0.00	0.00

DL1							
Values							
VEGFA	Relative mRNA			Normalized			
		Ecad	Slug	Vim	Ecad	Slug	Vim
5ng/ml	3HR	1.21	0.76	1.03	0.00	1.00	0.76
	48 HR	1.80	0.53	1.09	0.17	0.44	1.00
50ng/ml	3HR	1.54	0.46	1.03	0.10	0.27	0.76
	48 HR	4.63	0.35	0.84	1.00	0.00	0.00
Standard Deviation							
VEGFA	Relative mRNA			Normalized			
		Ecad	Slug	Vim	Ecad	Slug	Vim
5ng/ml	3HR	0.80	0.10	0.18	0.00	0.13	0.13
	48 HR	0.24	0.12	0.17	0.02	0.10	0.16
50ng/ml	3HR	0.89	0.19	0.45	0.06	0.11	0.33
	48 HR	0.87	0.06	0.05	0.19	0.00	0.00

Computer ENSEMBLE mRNA							
Values							
VEGFA	Absolute mRNA			Normalized			
		Ecad	Slug	Vim	Ecad	Slug	Vim
5ng/ml	3HR	0.94	88.12	10.23	0.00	1.00	1.00
	48 HR	2.10	55.64	5.45	0.40	0.41	0.40
50ng/ml	3HR	1.44	64.10	8.43	0.17	0.56	0.77
	48 HR	3.85	33.40	2.32	1.00	0.00	0.00
Standard Deviation							
VEGFA	Absolute mRNA			Normalized			
		Ecad	Slug	Vim	Ecad	Slug	Vim
5ng/ml	3HR	0.21	22.34	2.45	0.00	0.25	0.24
	48 HR	0.45	15.55	1.12	0.09	0.11	0.08
50ng/ml	3HR	0.38	17.87	2.23	0.05	0.16	0.20
	48 HR	1.30	9.46	0.45	0.34	0.00	0.00

Figure S4. VEGF-A qPCR data used to hand fit VEGF enhancement of E-cadherin expression. mRNA was harvested after 3hr and 48hr timepoint.